GSI-98-09
REPORT
DECEMBER 1998

HIGH ENERGY DENSITY IN MATTER PRODUCED BY HEAVY ION BEAMS

ANNUAL REPORT 1997

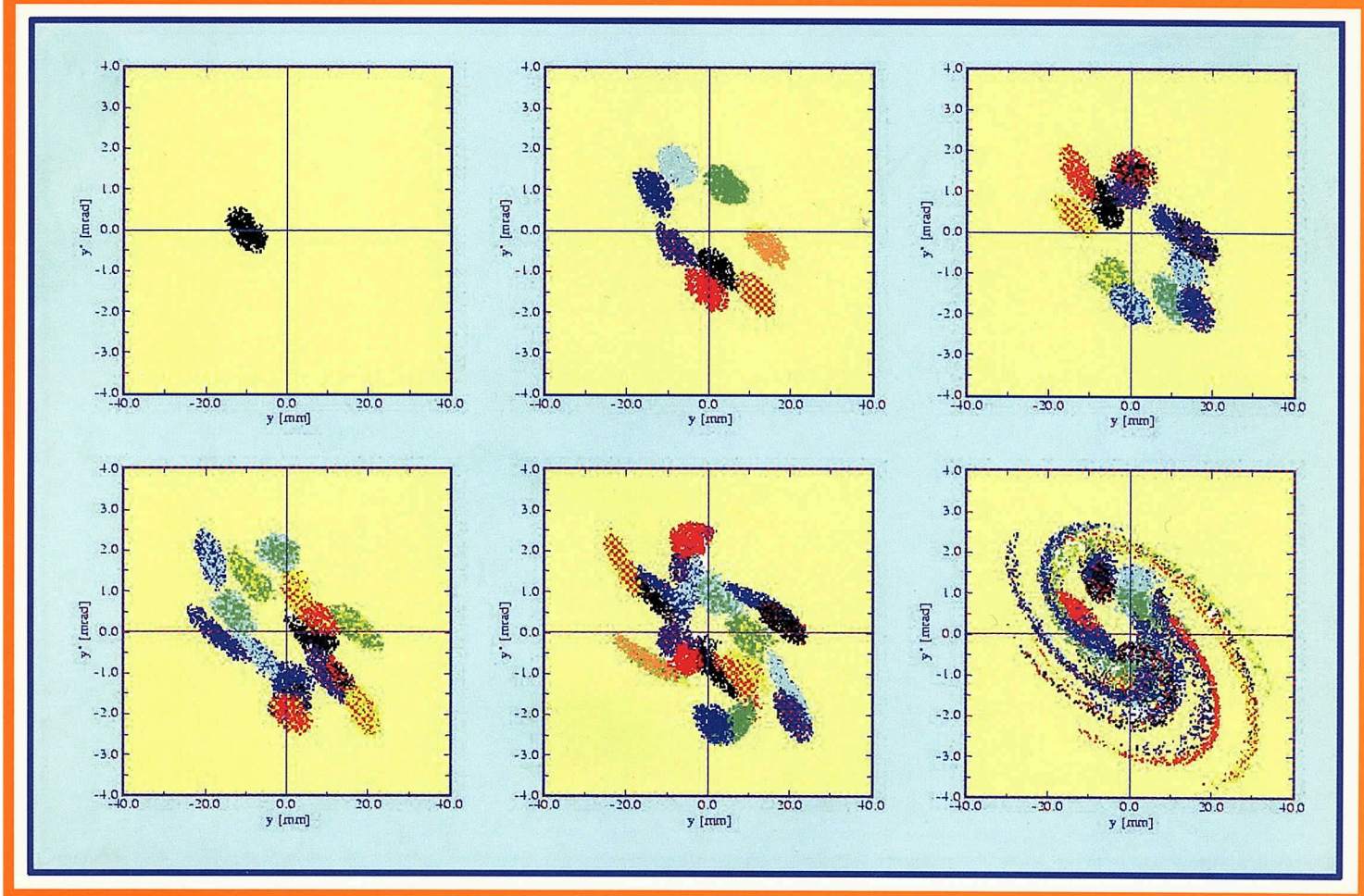

GESELLSCHAFT FÜR SCHWERIONENFORSCHUNG, DARMSTADT

Cover Picture:

Particle simulation of multiturn injection in the HIDIF accumulator storage ring calculated with a particle-in-cell-code. In order to increase the beam current to 400 mA, 20 beamlets of 20 mA each are injected successively into the lower left part at the position (–10 mm, –5 mm) with each shifted by –0.5 mm in the vertical direction. Shown is the particle distribution of the vertical phase space (from left to right and top to bottom) during the first injection, after 8, 12, 16 and 20 injections and after 20 more turns without further injection.
The spirals in the last frame result from the mismatch due to increased current. The loss of particles at the septum is below 2 %.

Picture by R. W. Hasse, see also contribution 'High Current Beams and Fusion Accelerator Studies', this report.

High Energy Density

in Matter

Produced by Heavy Ion Beams

Annual Report 1997

December 1998

Coordination and editorial works: Karin Weyrich (TU Darmstadt/GSI Darmstadt)

Preface

This Annual Report summarizes experimental and theoretical work carried out in 1997 in the framework of a basic research program on the interaction of heavy ion beams with matter. One of the main goals is the *investigation of dense plasmas* produced by heavy ion beams in rather homogeniously heated, extended volumes. An essential part of this work is devoted to issues of accelerator physics. Short high-intensity heavy-ion beam pulses with excellent beam quality are mandatory for the generation of high energy density in matter. The completion of the intensity upgrade by the year 2000 and the combination with the beam of a new Petawatt laser facility will be a milestone for the exploration of dense plasmas. This facility will be a powerful tool for the investigation of a great number of problems of basic research and also for applications, in particular *energy generation by inertial confinement fusion.*

Traditionally, the presentation of ongoing activities in this report is organized in three parts: (1) Experimental work on beam-plasma interaction, (2) Accelerator physics, and (3) Target theory. This time, in a brief introductory chapter the status of work on the long-range perspectives are briefly summarized: (a) The results of the GSI working groups 'Plasma Physics' and 'Laser facility' and (b) the achievements of the European Study Group on the HIDIF inertial fusion driver design.

Among a number of conference and workshop activities in 1997 the outstanding event was the biennial *International Symposium 'Heavy Ion Inertial Fusion'*, this time organised by GSI in Heidelberg combined with the *Workshop on 'Atomic Physics for Ion Beam Fusion'*. Results of the current program were presented at this conference and are documented in the proceedings, which already have been published.

The work presented in this report was predominantly financed from national sources. We would like to acknowledge the support by the BMBF for the collaborating University groups in the frame of the 'Verbundforschung', and support for our Russian collaborators by WTZ, ISTC and INTAS. Meanwhile, the European Commission has established a Coordinating Committee for inertial fusion activities which - with respect to potential funding by the EU - will be continued in the 5th framework program (1999 - 2003) as a 'keep-in-touch activity'. Finally, the editorial effort of Dr. Karin Weyrich for this report is gratefully acknowledged.

Darmstadt, December 15, 1998 R. Bock

CONTENTS

INTRODUCTION

Activities on Long-Range Planning and Research in the Fields of Plasma Physics and Inertial Fusion at GSI

Status by December 1998

After the deadline for the contributions to this annual report (April 1998) the long-range planing activities have undergone a rapid evolution, we therefore give here a brief update on these activities. The discussions on long-range planing, in which considerations for future facilities play the dominant role, started in 1996 and have only partially attained a final solution. The discussion on a future accelerator facility which satisfies the requirements of the various boundary conditions is still going on. With respect to *plasma physics* and to *inertial fusion* two major goals are pursued:

(1) the exploration of the future perspectives at GSI for basic research in the field of *dense plasmas* with short high-intensity *heavy ion beam* pulses and with *laser beams*, and
(2) the study of accelerator concepts based on an rf-linac with storage rings and the investigation of the corresponding key issues by theory, experiments, and simulation (HIDIF Study).

Long-range Perspectives for Research on Plasma Physics at GSI

The study of topic (1) is under consideration in the framework of a wider investigation of the *long-range research perspectives of GSI,* investigated by six working groups with national and European participation for the main fields of research at GSI. These groups were established by the Director of GSI by early 1996. *'Plasma physics with heavy ion beams'* was one of them. In addition, two more working groups were formed to study the accelerator concepts emerging from the requirements of the proposed scientific programs. The results of a first round of discussions were presented in a workshop at GSI in January 1997, and a first collection of working group reports was published in June 1997. The conclusions of the Plasma Physics Working Group report (p. 105) emphasize the enormous impact of a new accelerator facility for the research in the fields of 'Dense Plasmas' and 'Inertial Fusion' and recommend to include a laser facility into the further considerations.
After that a dedicated working group 'High Power Laser at GSI' was established to study the opportunities offered by a combination of high-power lasers and high-intensity heavy ion beams in more detail. In a series of workshops held at GSI between summer 1997 and spring 1998 it became increasingly clear that such a laser at a heavy ion beam facility, particularly if it incorporates a high-intensity femtosecond option (petawatt laser), provides exciting new and unique science opportunities not only for plasma physics but also in other fields of physics. First considerations for such a facility are documented in a contribution to this report (p.3/4). The final Project Report for this facility, *'Phelix, A Petawatt High Energy Laser for Heavy Ion Experiments at GSI'* (GSI Report 98-10), was elaborated in collaboration of GSI with German universities and research institutes and with LLNL, Livermore. A few weeks ago the decision for its construction was made. A first laser beam is expected to be delivered in the year 2001. In addition to the specific fields of plasma physics, *Physics of dense, strongly coupled plasmas, Interaction of heavy-ion beams with matter, Relativistic plasma physics* and *Ionization phenomena in dense plasmas,* the research program includes also topics of other fields, such as *X-ray laser spectroscopy*, and *Nuclear physics*, as well as the implications of such a facility for *Inertial Fusion.*

Heavy Ion Driven Inertial Fusion (HIDIF)

This subject is under investigation by a *European Study Group* in which accelerator and target groups from several European laboratories are collaborating on a detailed design study for such a facility, consisting of an rf-linac with storage rings. With respect to the target, indirect drive is assumed, and final beam as well as target requirements are discussed jointly. The Study Group was established in April 1995. A comprehensive report on the achievements of the first three years period has been published in August 1998 (GSI Report 98-06). In the introduction the authors give a resumee on the design features of driver and target and an outlook to work to be done in the next period of the study:

The Driver Study: In its early phase, the HIDIF Collaboration was oriented towards the conceptual goal of ignition, thus providing a "proof of principle" of pellet ignition by heavy ions. The chosen driver concept includes (similar to the HIBALL study) acceleration up to the desired particle energy of 10 GeV in a tree-like structure of rf linear accelerators, storage and bunching in storage rings, and final bunch compression to the short pulse duration. The energy of 6 GeV considered earlier was abandoned for space-charge reasons. As the energy needed for low-gain ignition is much smaller than for a power plant, and a test facility would need to provide only single shots, it was expected that such a facility could be considerably simpler than a full reactor driver.
The progress made during the study on pellet implosion led, however, to the conclusion that parameters are unfavorable for a heavy ion based low-gain ignition facility. While the drive energy decreases with the desired pellet gain, the drive power (the dominant factor determining the heavy ion driver) is essentially independent of gain. It was also realized that no particular advantage could be drawn from the single shot assumption; the inherent rep-rate of the rf linac and storage ring based concept would make this scheme a more appropriate choice for energy production rather than for ignition only. An upgrade of an ignition facility to energy production can be undertaken as soon as viable reactor-target design becomes available.
The bulk of detailed design and simulation studies was dedicated to the storage rings and final compression and focusing. While the linear accelerator is a substantial part of the whole driver, the task of a consistent design and checking it by detailed simulations from front to end has remained open and will be addressed in the second phase of the study. Similarly, an extensive program on experimental investigations of heavy ion beams and checking the simulation results on real machines had to be postponed for lack of funds and effort. A cost evaluation and optimization would be a further step requiring a proper choice of an optimized high-gain target.

Target Studies: The collaboration first had to advance the necessary tools for detailed multi-dimensional simulation work to describe adequately the complicated physics in the hohlraum of the indirectly driven target. Two target configurations with two and eight converters respectivly, have been considered. The latter has the advantage of more distributed final lens arrangements in exchange for reduced energy conversion efficiency. The fusion capsule for both cases was adopted from the published concept of the Livermore National Ignition Facility capsule.

The collaboration does not believe, at this stage, to have achieved an optimum match for the beam-target coupling. Innovative target geometries tailored specifically to the properties of the heavy ion beam remain a challenging issue, in particular for the energy production upgrade. The consistency between driver and target achieved in the present study is an important basis for such future work.

December 15, 1998

R.Bock

High Power Laser for Plasma Physics Applications at GSI

C. Stöckl, W. Süß, D.H.H. Hoffmann;
Physikalisches Institut 1, University of Erlangen
M. Roth, M. Geißel, W. Seelig
Institut für Angewandte Physik, TU Darmstadt
H.J. Kluge, R. Bock
Gesellschaft für Schwerionenforschung, Darmstadt

The experimental program of the plasma physics group at GSI is focused on the interaction of heavy ion beams with dense matter to achieve a better understanding of beam-plasma interaction phenomena and the properties of matter under extreme conditions of pressure and temperature.

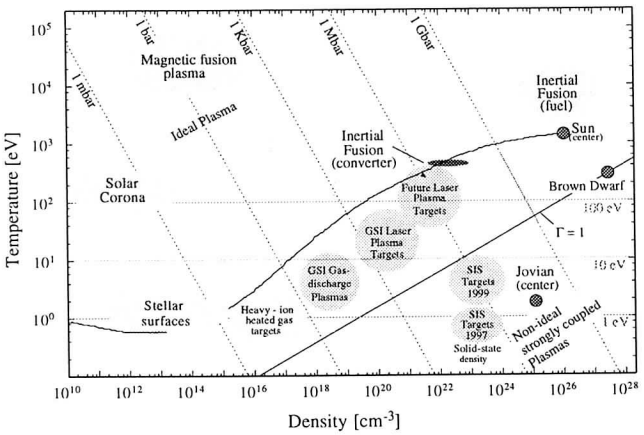

Figure 1: Density-temperature diagram of astrophysical and laboratory plasma phenomena in comparison with the present and future experimental capabilities at GSI. The solid black curve shows the state diagram of the sun with the center of the sun on the right end. The line $\Gamma = E_{pot}/E_{kin} = 1$ separates ideal and strongly coupled plasmas

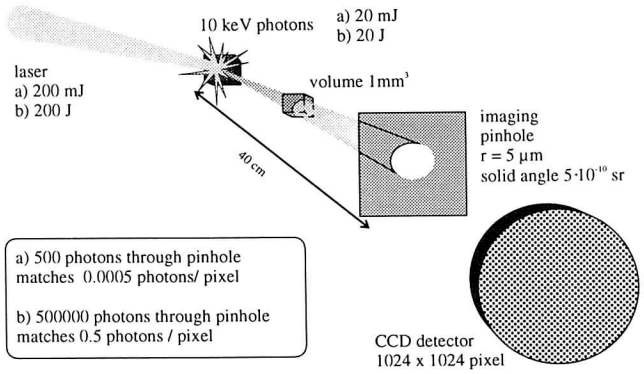

Figure 2: Schematic setup of a backlighter experiment to illustrate the calculations to determine the necessary laser pulse energy

High current mode operation of the SIS accelerator for ion beams with Z≥10 together with a new bunching mode recently allowed to demonstrate the hydrodynamic response of heavy ion heated solid Pb targets at temperatures up to 1 eV [1]. The intensity upgrade of the SIS in 1999 and the installation of a new buncher cavity will improve the capabilities of plasma generation with heavy ion beams dramatically to temperatures of up to 10 eV (fig. 1).

Recent interaction experiments with externally generated laser plasma-targets showed for the first time the enhanced stopping of dense ($n_e \leq 10^{23}\, cm^{-3}$) hot ($T_e \leq 60\, eV$) partially ionized laser-generated carbon plasma [2]. The energy of the present laser system (100 J) does not allow to produce an extended fully ionized carbon plasma for interaction experiments, which would be highly desirable because of the fundamental differences in the interaction processes of fully and partially ionized plasma [3, 4].
In order to diagnose the extended heavy ion heated plasma targets in a backlighting geometry and to widen the available density and temperature range for externally created plasma (fig. 1) the installation of a new high-power laser system is proposed.

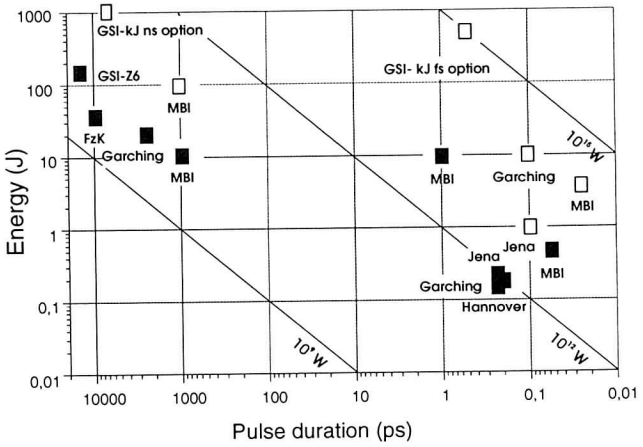

Figure 3: Parameters of the high-power laser installations in Germany. (closed squares: existing facilities, open squares: planned facilities).

A study group has been established to assess the capabilities of such a laser system and to determine the relevant laser parameters such as technology, pulse duration, energy and wavelength. To use the proposed laser system for driving an x-ray backlighter for the extended opaque heavy ion heated plasma it has to supply a sufficient amount of

energy. Fig. 2 shows an example of the calculations to determine the necessary laser energy for the backlighting experiments. Similar considerations have been made for the generation of external plasmas for interaction experiments. A fs-option for this laser system is desireable for the access into the large and exciting field of relativistic laser-plasma interaction. Consequently, three major modes of operation for the proposed laser system have been suggested:

1. 1 kJ, 1 ns at 1ω or 3ω for backlighting experiments
2. 1 kJ, 1-10 ns shaped pulse at at 1ω or 3ω for the generation of laser-plasma targets
3. 500 J, 500 fs at 1ω for relativistic laser-plasma interaction experiments

This unique combination of a high-energy and high-power laser with an intense heavy-ion beam facility will open up a large range of new experimental possibilities in fundamental and applied research and will be attractive for the German high power laser community (fig.3).

References

[1] S. Stöwe et al. *Induced Hydrodynamic Motion in Lead Targets* this report (1998)

[2] M. Roth et al. *Stopping of Heavy Ions in Laser Produced Plasma* this report (1998)

[3] K.-G. Dietrich et al., Phys. Rev. Lett. **69** (1992) 3623

[4] H. Wetzler et al., Laser and Part. Beams **15**, (1997) 449

1 THE PLASMA PHYSICS EXPERIMENTAL PROGRAM

1.1 Stopping Power Measurements

1.2 Ion Beam Induced Plasma and Plasma Lens

1.3 Atomic Processes and Ion Ion Collisions

1 THE PLASMA PHYSICS EXPERIMENTAL PROGRAM

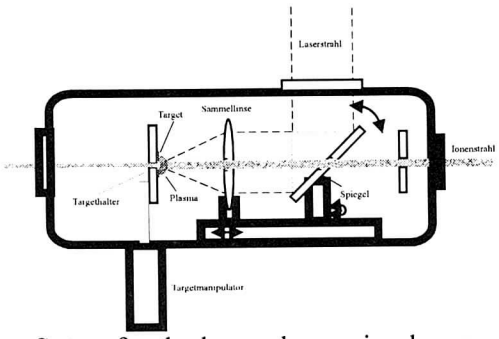

Set up for the laser-plasma ion-beam interaction experiments

The experimental activities during this report period address three topics, the interaction of heavy ions with hot, dense plasma, the investigation of ion driven plasmas and atomic processes in ion-ion-collisions.
A highlight of the beam plasma interaction program was the measurement of the stopping power of a dense laser produced carbon plasma. This experiments made use of the capabilities of a high power Nd:glass laser system to produce target plasmas in a temperature and density range that was unaccessible before.

The measured stopping power exceeds the theoretical predictions and thus points to density effects that have not been observed before.
The performance of the GSI accelerator facilities with respect to high intensities has improved considerably. At 300 MeV/u now $2*10^{10}$ Ar-ions can be deliviered in a 250 ns beam pulse to the target. Focused by the high performance plasma lens the deposition power exceeded the 1 kJ/g threshold. These beam parameters enabled experiments to observe beam induced hydrodynamic motion in lead targets.
Close international collaboration was essential to carry out the reported experimental program. The participation of research teams from Russia was supported by INTAS- and WTZ-grants. The collaboration with the Tokyo Institute of Technology is demonstrated in common experiments at GSI and TIT as well.

1.1 Stopping Power Measurements

The high power Nd:glass laser is now able to produce target plasmas in temperature and density regimes that have not been accessible for beam plasma interaction experiments before. Energy loss experiments of heavy ions in a carbon plasma ($n_e = 10^{21}$ cm^{-3}, Te = 60 eV) showed an unexpected level of energy loss. The results can only be explained if an increased charge state of the projectile ions is assumed. Increased charge states have been observed before for heavy ions traversing a fully ionized hydrogen plasma. The observed effect reported here is due to the high electronic density. Detailed modelling of the atomic processes in a dense plasma is still pending and will be corroborated by time resolved measurements of the projectile charge state evolution and the time resolved density diagnostics applying a Schlieren method with a Mach-Zehnder interferometer.
Fully ionized plasmas are known to strip heavy ions very effectively to very high charge states even at low projectile velocities. Two contributions address this topic. One experimental approach describes the performance of a CO_2-laser produced surface plasma as stripper medium. The second experiment makes use of an intense electron beam from a low pressure gas discharge to preserve the high charge states produced inside the plasma target.
Experiments using very light ions like hydrogen and helium are free of the effects due to a change in the projectile charge state during the interaction process. They are therefore experiments to determine to what extend the observed energy loss of an ion interacting with a plasma is due to the effective stopping power of the free electrons and to what extend an increased charge state of the projectiles ion plays a significant role.

A number of contributions resulting from a collaborative effort between ITEP and the Erlangen University group addresses this topic. A capillary discharge plasma was set up at the Erlangen Tandem accelerator. First results for proton energy loss are reported. A new type of plasma target, an explosively driven plasma target, is described in yet another contribution. In this type of plasma the situation is close to a strongly coupled plasma, since the coupling parameter is already $\Gamma = 0.35$.
Very clean experimental conditions are reported for a stopping power experiment with H^+ and He^{2+} projectiles in a fully ionized hydrogen plasma. The experimental results agree very well with a modified Bethe stopping theory.

1.2 Ion Beam Induced Plasma and Plasma Lens

Since intense ion beams couple very effectively to dense matter such beams are an ideal tool to produce dense, strongly coupled plasmas.
An outstanding result of the experimental efforts was the first observation of beam induced hydrodynamic response of solid lead targets. Pressure waves with an amplitude of up to 4 GPa were measured, and agree very well with 2-D-hydrosimulations. Experiments and numerical simulations are a collaborative effort of GSI, ITEP and ICP Chernogolovka. With a new two stage cryo-technique it was possible to extend the minimum temperature for cryo-targets down to 5.3 K. This enables the experimental groups to even use solid state hydrogen targets in the near future. In this report experiments with cryogenic neon targets are reported.
Of paramount importance for the experiments is the ability to focus the total beam intensity to a sub-millimeter focus diameter. The plasma lens, developed during previous years, is now in regular operation. Also this year a number of contributions address plasma lens improvements and development.
For the first time a direct observation of the argon discharge plasma of the device was attempted. Through a side-on measurement of the emitted visible light and UV- radiation the plasma temperature ($T_e = 9$ eV) and electron density ($n_e = 10^{18}$ cm^{-3}) was determined. It was also possible to reconstruct the magnetic field profile of the plasma lens from beam measurements and to evaluate the fringe field effects.

1.3 Atomic Processes and Ion Ion Collisions

This subchapter is represented by three contributions.
The TU Munich group reports about the intense emission of Lyman-α radiation from a dense Neon-Hydrogen mixture excited by an intense 100 MeV S-beam from the Munich Tandem accelerator and an effective method to produce spin-polarized ^{3}He directly at atmospheric pressure.
At the Giessen ion-ion collision facility experiments to measure electron capture cross sections in ion-ion collisions were carried out. This years report contains results on Xe^+-, Cs^+-, Hg^+- and Ta^+-ions. These data are important to assess the beam loss effects of heavy ion drivers due to intra-beam scattering processes.

(D.H.H. Hoffmann)

Stopping Power in Laser Produced Plasmas

M. Roth[1], R. Bock[3], M. Geissel[1], D.H.H. Hoffmann[4],
O. Iwase[2], C. Stöckl[4], W. Süss[4], W. Seelig[1]

[1]*Institut für Angewandte Physik, Darmstadt University of Technology,*
[2]*Tokyo Institute of Technology,* [3]*GSI Darmstadt,*
[4]*Physikalisches Institut Abt. I, Erlangen University*

To investigate the interaction processes of dense plasmas experiments with heavy ions at UNILAC energies have been performed during the last years using gas discharges [1]. To achieve parameters relevant to those of an inertial fusion converter target it was necessary to increase the plasma density and temperature by orders of magnitude. Another point of interest was to test the onset of density dependent variations of the stopping power predicted by some theories. Therefore, in the past two years a high energy laser system has been built to create plasma targets with densities of up to 10^{21} cm^{-3} and temperatures of nearly 100 eV.

In 1997 the first experiments to measure the stopping power of heavy ions in a laser generated high dense carbon plasma were performed. To compare the measured data with existing theories, it was necessary to have a detailed knowledge of the plasma parameters. Small sized, rapidly evolving laser plasmas are very difficult to diagnose, but can be described by computer-simulation programms like MULTI [2] with reasonable accuracy.

With the ion density and electron temperature derived by MULTI the electron density can be calculated under the assumption of a local thermal equilibrium (LTE) by solving the SAHA-equation self-consistently. Spectroscopic measurements in the visible, VUV- and XUV-range were performed to confirm the calculated plasma parameters.

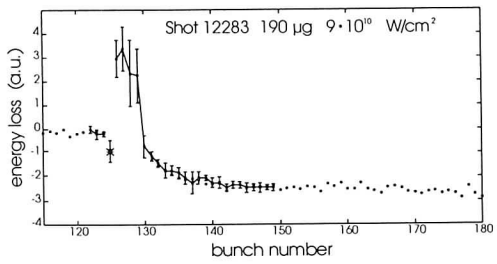

Figure 1: Signal of an energy loss measurement

The energy loss of the heavy ions in the plasma was obtained in the frame of the existing theory [3] based on the initial beam parameters by calculating the specific energy loss in each plasma layer with respect to the decreasing ion velocity. The most important parameter, the effective charge state of the beam ion, was derived by assuming a partial ionized plasma. Existing theoretical predictions as well as experiments at lower densities [1] showed that the charge state distribution in a partial ionized plasma should be equal to a cold gas distribution.

With the existing experimental setup it was possible to investigate the stopping power of the target either in the cold and in the plasma state as well as during the transition to the vacuum state. Due to the high beam quality the energy loss of different ion species in carbon plasmas of different thickness could be determined very accurately. The experimental results show a strongly increased stopping during the plasma state as seen in figure 1.

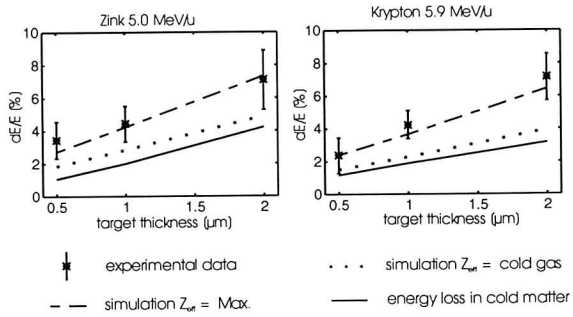

Figure 2: Results of the energy loss measurements

The experimental results revealed a significant discrepancy to the data calculated on the basis of the current theory which could not be explained by a deviation of the plasma or beam parameters. The only way to reproduce the experimental data was to assume an increased charge state like in solids. An upper limit of the charge state distribution was experimentally determined which corresponds to a maximum energy transfer at electron ion collisions and is shown in fig 2 as 'Max.' values. With this charge state distribution it was possible to get a consistent description of all the experimental results.

With these plasmas starting from solid state with densities of about 10^{21} cm^{-3} new and interesting results could be obtained which can motivate a further development of the theoretical description.

References

[1] Energy Loss and Charge State of Heavy Ions in Partly Ionized Plasmas, H. Wetzler, C. Stöckl, A. Tauschwitz, D.H.H. Hoffmann, GSI-Report 94-01

[2] MULTI, a computer code for one-dimensional multigroup radiation hydrodynamics, R. Ramis, R. Schmalz, J. Meyer-ter -Vehn, MPQ-Report 110 (1986)

[3] Energieverlust von Schwerionenstrahlen in dichten Plasmen, T. Peter, MPQ-Report 137, 1988

Charge State Distribution of Heavy Ions in Laser Produced Plasma

W. Süss[1], R. Bock[3], M. Geissel[2], D.H.H. Hoffmann[1],
O. Iwase[4], M. Roth[2], C. Stöckl[1]
[1] *Physikalisches Institut Abt. I, Erlangen University*
[2] *Institut für Angewandte Physik, Darmstadt University of Technology*
[3] *GSI Darmstadt*
[4] *Tokyo Institute of Technology*

Measurements of charge state and energy loss of heavy ions are indispensable for the detailed knowledge of physical mechanisms of the energy deposition of ion projectiles into plasma targets. The difference in stopping power of heavy ions in gases, solids and plasmas are of crucial interest for the heavy ion beam driven Inertial Confinement Fusion (ICF).

The theory of Bohr, Bethe and Bloch of the stopping power shows that the energy loss of heavy ions in the high velocity range is proportional to the square of the medium projectile charge state (compare [1])

$$-\frac{\mathrm{d}E}{\mathrm{d}z} \propto \bar{Z}^2$$

This strong dependence motivates the work for a time resolved investigation of the charge state distribution of the projectile ions in plasma.
A one micrometer thick carbon foil is placed perpendicular to the ion beam axis. The ions pass this cold foil acting as an electron stripper. So their fixed initial charge state given by the accelerator is changed to an increased charge state distribution after passing the foil. A plasma

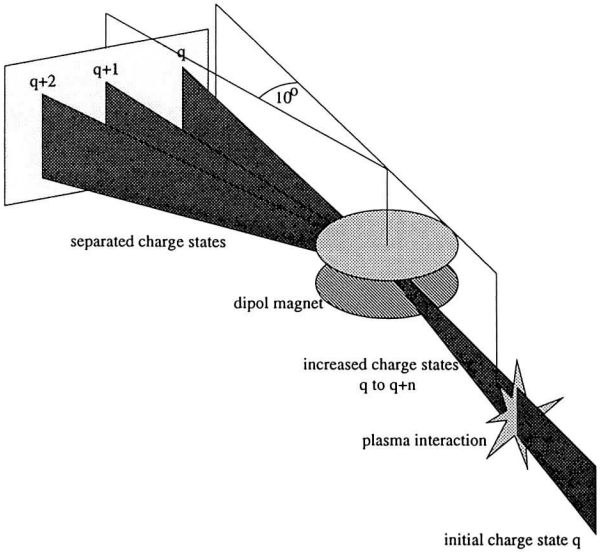

Figure 1: A magnetic dipole analyzer separates the mixture of charge states in the ion beam to different trajectories

is produced by igniting the foil by a strong laser pulse [2]. Focused to the foil the laser heats up all material in the line of sight of the ion beam. After a few nanoseconds no cold material is remaining in the ion beam/material interaction zone so the beam target is changed from solid state to plasma. The resulting charge state distribution passes a magnetic dipole analyzer (see fig.1) and is time resolved recorded by a fast MCP/scintillator detector and a streak camera. Figure 2 shows the charge state distribution of a

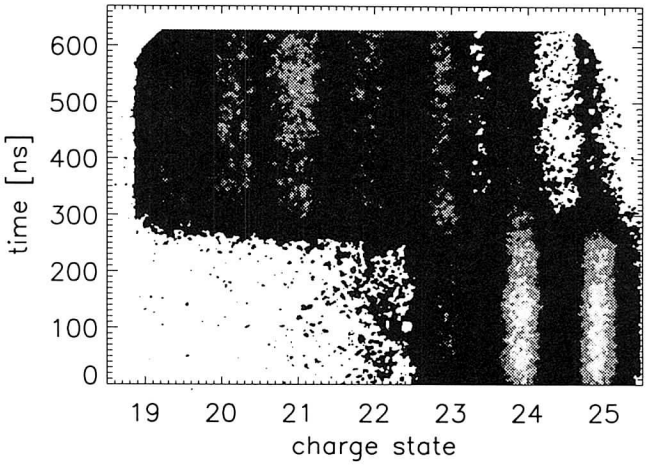

Figure 2: Charge state distribution of a ^{58}Ni beam at an energy of 5.9 MeV/u and initial charge state of 8+ in a cold carbon foil and in a carbon plasma

^{58}Ni beam in the cold carbon foil (maximum at q=24) and after the plasma evolution. The laser hits the foil at t $\approx$ 250 ns. The charge states remain high in the next 20-30 ns which corresponds to the hot plasma phase and decrease in the following plasma expansion and cooling phase. The difference of the stopping power in the cold carbon foil and the expanding gas phase at later times can be seen by the shift of the charge states 23, 24 and 25 to some percent smaller values. The reduced energy loss (the ions are faster) in the low dense gas phase corresponding to the solid state phase increases the stiffness of the beam and therefore causes a smaller deflection of the charge states by the dipole magnet. To get more details about the short hot plasma phase a better time resolution with a total streak time in the order of 100 ns is needed which will be achieved in the future beam times.

References

[1] M. Roth, PhD thesis, 1997

[2] C. Stöckl et al.,
http://www.gsi.de/~plasma/experiments/laser.html

Diagnostics of a Laser Produced Carbon Plasma

M. Geissel[1], O. Iwase[2] U. Funk[4], D.H.H. Hoffmann[4],
M. Roth[1], C. Stöckl[1], S. Stöwe[3], W. Süß[4], W. Seelig[1]
[1] *Institut für Angewandte Physik, Darmstadt University of Technology,*
[2] *Tokyo Institute of Technology,* [3] *GSI Darmstadt,*
[4] *Physikalisches Institut Abt. I, Erlangen University*

The diagnostics of the carbon plasma produced by the 100 J / 6 GW Nd:glass Laser system is essential to understand the beam-plasma interaction processes (namely the energy loss), that are examined at the Z6 experimental area of GSI. Different approaches to get information about the plasma parameters such as temperature and electron density are pursued experiments at Z6.

An optical system consisting of a Schlieren method and a Mach-Zehnder interferometer has been set up at the Z6 experimental area. Both plasma diagnostics techniques have been used only separately until now.

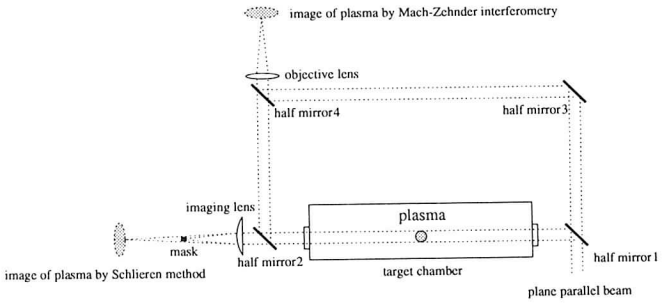

Figure 1: Schematic setup of the experiment

Figure 1 shows the setup of this method. The plane parallel uniform beam from an Ar-laser is splitted by half mirror 1. The beam penetrating the half mirror 2 is focused onto a sharp straight edge which acts as a mask (shown on the left side to block the unperturbed beams for the Schlieren method, after it passes through the target plasma. The beams which are reflected by the half mirror 2 and 3 are superposed on the half mirror 4 and generate the interference fringes of a Mach-Zehnder interferometer. Thus both methods can be used in parallel.

In figure 2 a result of the fringe shift measurements by Mach-Zehnder interferometry is presented, detected by an optical streak camera. It is seen that this method is feasible and effective for the density measurements of the laser-produced plasma.

A possibility to avoid the problems arising with the high opacity of the dense carbon plasma is the examination of soft X-rays that are emitted by the plasma. For this purpose a flat field spectrometer will be set up that can access the spectral region from 50 to 300 Å [1]. An optional second grating will allow to reach even 10 Å. The scheme of the spectrometer is shown in figure 3. The detector device is a X-ray streak unit coupled with a CCD camera, which is capable to detect photons from the VUV region up to some keV, depending on the cathode material of the streak unit.

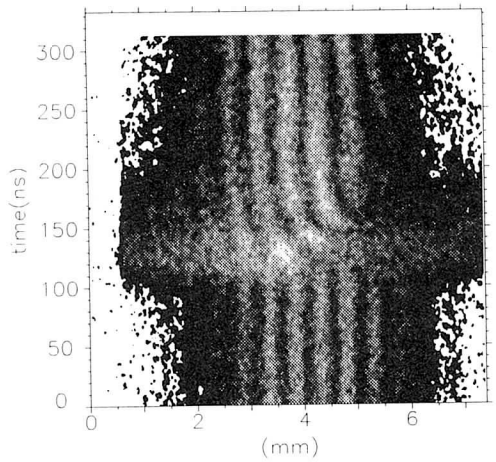

Figure 2: An example of the measured fringe shifts

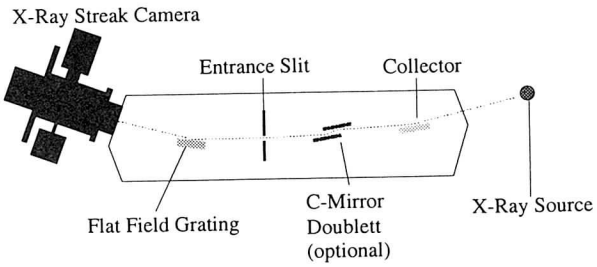

Figure 3: Schema of the flat field spectrometer

References

[1] W. Schwanda, K. Eidmann and M.C. Richardson: *Characterization of a Flat-Field Grazing Inzidence XUV Spectrometer*, Journal of X-Ray Science and Technology, **4**, 8-17 (1993)

Measurement of Energy Loss and Charge State Distribution of 900 keV Li and 2.4 MeV O in Carbon/Hydrogen- and Li-Plasmas

U. Neuner[1], M. Ogawa[2], K. Nishigori[2], M. Takizawa[2], S. Garnsomsart[3]
[1] GSI Darmstadt
[2] Research Laboratory for Nuclear Reactors, Tokyo Institute of Technology
[3] Physics Department, Faculty of Science, Burapha University Chonburi 20131, Thailand

Experimental investigations into the interaction of ion beams with plasma targets showed increased stripping as compared to cold targets, considerably effecting the energy loss.

Measurements were performed with ion beams of 900 keV $^{7}Li^{1}+$ and 2.4 MeV $^{16}0^{2}+$. The plasmas were created by irradiating the surface of polyethylene and lithium disks with a 6 J TEA CO_2 laser [1]. This produced a partially ionized surface blow-off plasma with electron densities between 10^{18} and 10^{16} cm^{-3}.

In the experiment the charge state and energy distributions of ion beams after passage through plasmas were measured. The charge state separation and energy dispersion were performed by a dipole magnet, the detection with scintillator/photo multiplier combinations (fig. 1). The magnet current was varied over several laser shots.

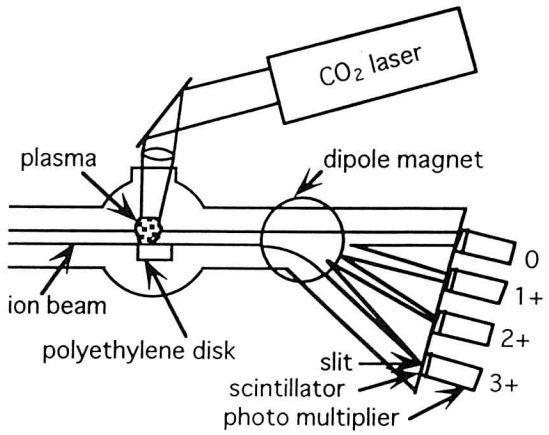

Figure 1: Experimental setup

The $Li^{1}+$ beam is stripped in the plasma, whereby the ratio of the current of 3+ to 2+ is increased as compared to the cold matter value for the first several hundred nanoseconds of the laser pulse. The plasma produced from the lithium laser target yields hereby higher values than the polyethylene target, according to its higher degree of ionization (fig. 2). Combining an oxygen beam and a polyethylene target, the effective charge state of the beam drops from initially 5 to the cold matter value of 3 within the first 1.5 μs.

Utilizing a polyethylene target, the two maxima in the energy loss at 100 and 500 ns that could already be seen with the lithium beam are much more pronounced with the oxygen beam, which has a considerably higher beam current and therefore less experimental error. Measurements with different outgoing charge states ($O^{4}+$ and $O^{6}+$) showed remarkably similar energy loss values, when calibrated to the slightly different values in cold matter (fig. 3).

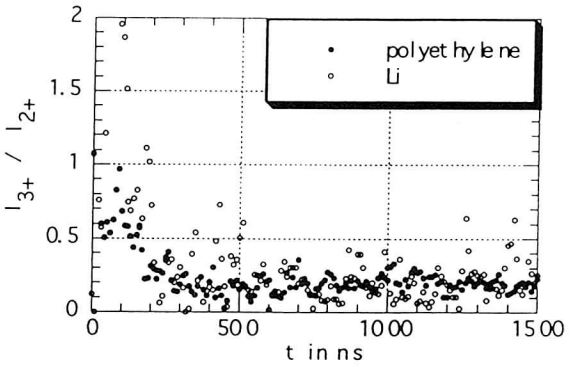

Figure 2: Stripping in different plasmas

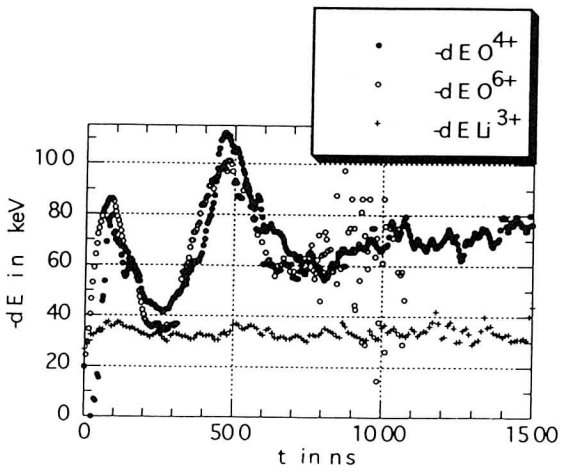

Figure 3: Energy loss of different beams

References

[1] U. Neuner, K. Horioka, M. Nakajima, M. Ogawa, Y. Oguri, M. Takizawa, S. Yamauchi, 'Performance of a Plasma Stripper for Intense Beams', accepted for publication in Fus. Eng. Design (1998)

Developement of Efficient Plasma Stripper Targets for Heavy Ion Beams

J. Kolb, E. Dewald, M. Engelbrecht, H.-P. Flierl, J. Jacoby, R. Kowalewicz, and D. H. H. Hoffmann
Physikalisches Institut I, Universität Erlangen-Nürnberg, D-91058 Erlangen

The interaction between ion beams and hot ionized matter is the subject of strained theoretical and experimental research for many years now. Several theoretical calculations [1] and simulations [2] predict a higher stripping efficiency of plasma stripper targets compared with present day cold gas strippers or stripping foils. Especially at ion energies below 1 MeV/amu there is a significant difference.
The charge state distribution of ions passing through a plasma is determined by ionization (collisional ionization by ions, collisional ionization by electrons, charge transfer ionization) and recombination (bound electron capture, radiative electron capture, dielectronic recombination, 3-body recombination) processes. The predicted higher effective charge state of ion beams in fully ionized plasma is due to the vanishing probability for bound electron capture which is the dominant process in cold targets. For an oxygen ion beam the equilibrium charge state in a cold gas target is 6+ whereas the ions will be completely stripped in a fully ionized plasma target (Fig. 1).

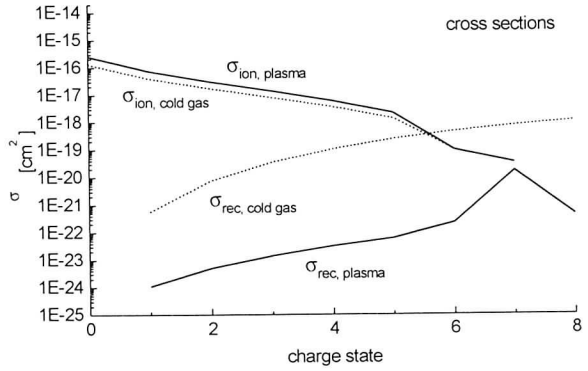

Fig. 1: Theoretical predicted cross sections for ^{16}O with 0.9 MeV/u passing hydrogen (cold gas, fully ionized plasma).

However it is very difficult to extract the high charged ions out of the plasma through the cold boundaries of a plasma column. Therefore a new technique was investigated. A system similar to the devices used in pseudospark research [3] was developed. In this device an intense electron beam is produced together with the formation of the plasma column. This electron beam allows highly charged ions to be transported out of this region. The electron beam parameters can be influenced by the gas pressure and the pre-ionization current as well as by the capacity of the electrical circuit. Free electron densities of 10^{16} cm^{-3} can be obtained for 50 ns up to 200 ns.
In previous experiments a pseudospark electron beam chamber was operated at repetition rates of 50 Hz. The higher stripping efficiency of this device could be already demonstrated [4]. Now a chamber in an "open" hollow cathode geometry was build up (Fig. 2) and operated in single shot experiments.

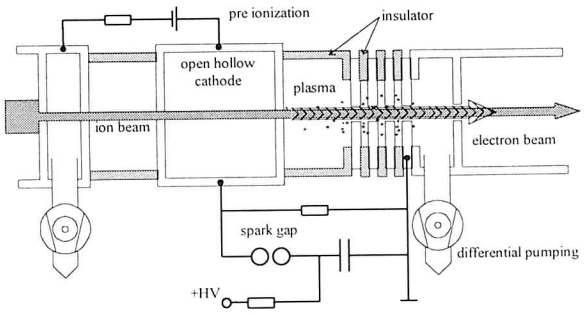

Fig. 2: Electron beam device

The interaction of the discharge with an oxygen ion beam of 0.9 MeV/amu was investigated. The initial mean charge state of the ions was 4^+. In cold gas experiments the charge state 8+ was almost negligible. During the formation of the electron beam a current signal of ions in the charge state 8+ could be detected (Fig. 3).

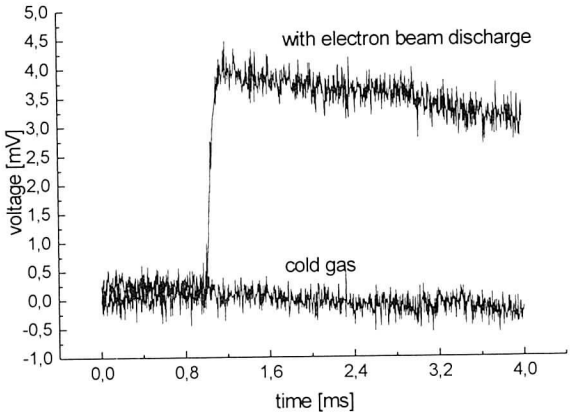

Fig. 3: Current signals of the charge state O^{8+} (initial projectile charge state was 4+) obtained with a cold gas stripper target and after the interaction with the pseudospark device described in the text.

[1] K.-G. Dietrich, D. H. H. Hoffmann, E. Boggasch, J. Jacoby, H. Wahl, M. Elfers, C. R. Haas, V. P. Dubenkov, A. A. Golubev, Phys. Rev. Lett. **69** (1992), 3623
[2] M. Engelbrecht, Diploma Thesis, March 1997 University Erlangen
[3] J. Christiansen, C. Schultheiss, Z. Phys., **A290**, 1979, 35
[4] M. Engelbrecht et al, GSI-Report-97-08 (1997), 12

funded by BMBF No. 06ER834

Energy Loss Measurements of Proton Beam in Capillary Target

A. Golubev, M. Basko, A. Fertman, V. Turtikov, B. Sharkov, ITEP, Moscow
D.H.H. Hoffmann, P. Spiller, A. Tauschwitz, GSI Darmstadt
J. Jacoby, A. Meineke, H.-P. Flierl, U. Kolb, University Erlangen
V. Mintsev, M. Kulish, V. Gryaznov, V. Fortov, ICP, Chernogolovka

Measurements of the energy losses of monochromatic proton beams in dense plasmas become a valuable method in experimental investigations of properties of strongly compressed ionized matter. The main reason for the use of the protons as projectiles is their effective charge Z_{eff} = 1+ remaining essentially the same in cold and ionized matter in wide range of plasma parameters.

The beam-plasma interaction experiments are combined with independent measurements of plasma brightness temperature or plasma pressure and numerical simulations for plasma ionization equilibrium using the computer code SAHA-4 [1]. Diagnostic method of free electron density of plasma by energy loss measurements of 3 MeV protons in plasma target was demonstrated in ITEP [2]. In new experiments the energy loss of protons in capillary discharge have been measured for a number of different projectile energies. It enables to increase the accuracy of determination of free electron density of the plasma target.

The proton beam - capillary discharge plasma target interaction experiment was set up at the Tandem laboratory of Physics Department at the University Erlangen. There is a EN tandem accelerator (maximum terminal voltage 6MV) with either a duoplasmatron ion source for hydrogen or a sputter ion source for other ion species. Proton beam was transferred by the dipole magnet from the accelerator to the experimental area. As it is shown on Fig. 1, the plasma target was integrated into the high vacuum system of the beam line.

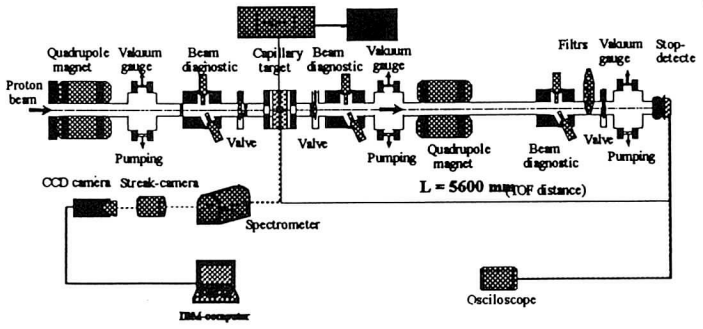

Figure 1: Experimental setup for measuring the energy loss of protons

The plasma was generated by igniting an electric discharge inside a 50 mm cylindrical capillary channel bored in a polyethylene slab . Power supply consists of a capacitor bank with a maximum stored energy up to 150 J and a triggered spark gap switch. The electrodes at both ends of capillary channel are manufactured from carbon.

The energy loss of the protons was measured with a time-of-flight (TOF) system, and the rf microstructure was used as a timer. Time structure for the proton beams is provided by the buncher (frequency $\approx$ 105 MHz) positioned in the beam line between the ion source and tandem accelerator. The stop detector based on the micro - spherical plate was used for registration of the proton beam with time resolution .

The energy loss was measured for different energies of protons: 4, 5 and 6 MeV and different diameters of the capillary target: 1.5, 2 and 3 mm. During the first 2 - 3 μs after plasma ignition the signal is not accessible for measurements, since no beam pulses reach the stop detector. The temporal behavior of the energy loss of the 5 MeV proton beam during the plasma generation in 1.5 mm capillary target is shown in fig. 2. The maximum energy loss is: ΔE = (260 $\pm$ 25) keV. Using the diagnostic method for free electron density ne of plasma which was developed in [2] we calculated the n_e from the value of energy loss: $n_e = (5.7*10^{19} \pm 0.6)$ cm^{-3} This value is in the good agreement with the results of the first 3 MeV proton beam - capillary plasma interaction experiments in ITEP $n_e = (6.4*10^{19} \pm 0.9)$ cm^{-3}.

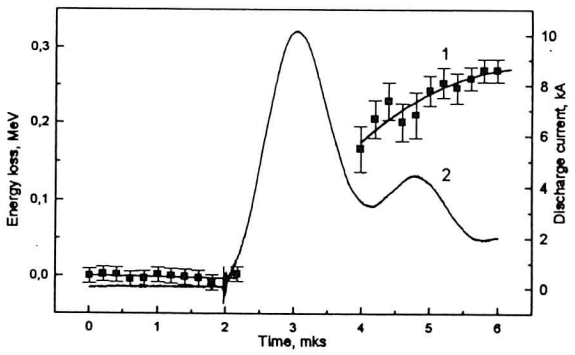

Figure 2: Time dependence of energy loss (curve 1) and discharge current (curve 2) for capillary target d = 1.5 mm

References

[1] W. Ebeling, V. Gryaznov, et al., Thermophysical Properties of Hot Dense Plasmas (Teubner, Stuttgart-Leipzig, 1991)

[2] A. Golubev, M. Basko et al., Phys.Rev. E 57, 3363 (1998)

[3] D.H.H Hoffmann, J. Jacoby et al GSI-report 97-08, 9 (1997).

Stopping Power of Helium in Hydrogen Plasma

J Jacoby, H.-P. Flierl, D.H.H. Hoffmann, J. Kolb, A. Meinecke, J. Philipps
Physikalisches Institut I, Universität Erlangen-Nürnberg, D-91058 Erlangen
A. Golubev, A. Fertman, ITEP, Moscow, Russia

The stopping power of heavy ions penetrating an ideal hydrogen plasma has been measured in varoius experiments during the last years. The final stopping power obtained in these experiments can be summarized as contribution of two different physical effects: 1. The reduced recombination rate in a fully ionized plasma causes enhanced charge states of the projectile ions, which enters the stopping power in a quadratic term. This effect is more important at low beam energies [1] close to the thermal energies of the plasma electrons. As a result a difference in the stopping power up to a factor 40 between plasma and cold gas can be observed. 2. The enhanced stopping power, due to the free electrons in a plasma causes an enhanced plasma stopping power of a factor 2 - 3 in comparison to cold gas.

To seperate the two effects, light ion beams of protons and helium beams were used in Erlangen to measure the enhanced stopping power due to the free electrons in a plasma [2]. At beam energies between 3 - 9 MeV the projectiles delivered from the EN-Tandem accelerator are fully ionized and they stay fully ionized independent whether the projectiles interact with gas or with plasma. A fast hydrogen Z-Pinch served as the plasma target. A plasma density between 10^{17} - 10^{18} cm^{-3} could be produced for a time interval from 6 - 16 μs after the start of the discharge. The energy loss of the ion beam is determined from a time of flight measurement of the projectiles. The time structure of the ion beam was provided by a fast 106 MHz buncher cavity [3], which has been placed at the low energy part of the Tandem accelerator.

Results of the stopping power measurements using a He^{2+}-beam are shown in Figure 1. Helium at beam energies of 0.75, 1.13, 1.50, 1.87, and 2.25 MeV/u has been analysed after passing hydrogen gas or plasma. The data points are shown together with the calculated dependence according to a modified Bethe formula [2, 4]. The experimental data points and the theoretical energy loss calculations are in excellent agreement in the tested beam energy and plasma density regime. The experimental ratio between the stopping power in plasma and in cold gas varies between 3.15 at 0.75 MeV/u and 2.5 at 2.25 MeV/u. This factor is now entirely caused by the enhanced stopping of free electrons in a plasma. For the beam energies used in these experiments the charge state of the helium ions is fixed to 2+, independent whether the taret is gas, partial ionized plasma or a fully ionized plasma.

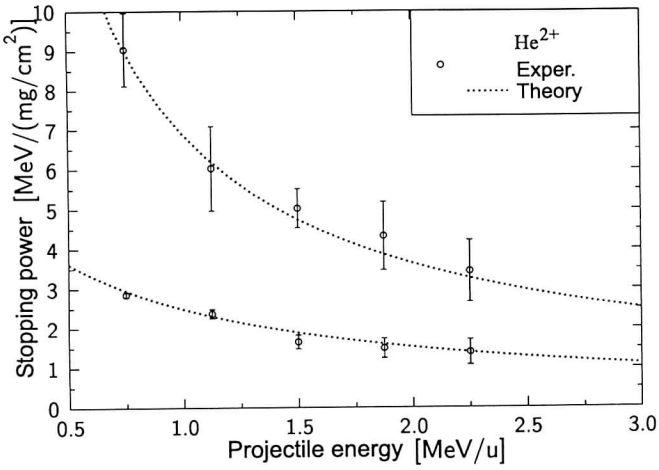

Figure 1: Stopping power of helium ions at various beam energies after passing a hydrogen gas or a hydrogen plasma. The experimental results of the measurements are marked with a circle. Theoretical calculations for gas and plasma are displayed as dotted lines. The lower data points and the lower dotted line correspond to the experiments with hydrogen gas and the upper data points and calculation correspond to the results with the hydrogen plasma.

References

[1] J.Jacoby, M.Engelbrecht, M.Engelhardt, H.-P.Flierl, D.H.H. Hoffmann, J.Kolb, R.Kowalewicz, A.Meineke, J.Philipps: *Swift Ion Plasma Interaction Experiments at Erlangen*, Nucl. Instrum. & Methods (1998) (in print)

[2] H.-P. Flierl: *Der Energieverlust leichter Ionen in einem vollständig ionisierten Wasserstoffplasma*, Dissertation (eingereicht), Universität Erlangen-Nürnberg, Erlangen (1998)

[3] R. Kölbel: *Aufbau und Inbetriebnahme eines Bunchers für variable Teilchenenergien*, Diplomarbeit, Institut für Angewandte Physik, Johann-Wolfgang-von-Goethe Universität, Frankfurt (1997)

[4] T. Peter, J. Meyer-ter-Vehn: Phys. Rev. A**43**, 1998 (1991)

*this work is funded by BMBF No 06 ER 834

Measurements of the Energy Loss of Proton Beams in Explosively Driven Xenon Plasma Targets

V.Mintsev, V.Gryaznov, M.Kulish, A.Filimonov, V.Fortov
Institute for Chemical Physics Research,
Chernogolovka, Moscow reg., 142432, Russia
B. Sharkov, A. Golubev, A.Fertman, V.Turtikov, A.Vishnevskiy, A.Kozodaev
Institute for Theoretical and Experimental Physics,
B. Cheremushkinskaya 25,117259, Moscow, Russia.
D.H.H.Hoffmann, U.Funk, S.Stoewe, M.Geisel
Gesellschaft für Schwerionenforschung, D-64220, Darmstadt, Germany
D.Gardes, M.Chabot
Institute Nacional de Physique Nucleare, 91406, Orsay, France

A new method to generate plasma targets with electron densities $n_e \geq 10^{20}$ cm^{-3} behind strong shock waves to study the energy loss of protons and heavy ions is discussed. Experimental equipment for the investigations of stopping power of proton beam in explosively driven plasma behind powerful shock waves is presented on Fig. 1. A 3 MeV 60 μs duration proton beam pulses delivered by 148.5 MHz ISTRA-36 RFQ linac at ITEP and compact metallic vacuum pumped chamber for explosions up to 150 g TNT were the main unit of this set-up. Differential pumping and fast valves proved to be sufficient for the protection of high vacuum beam line from the high pressure detonation products. Compact explosively driven linear and cumulative shock tubes were worked out to generate uniform plasma slug behind powerful shock waves with the velocities of 5-15 km/s at the initial pressure of Xenon 50-200 kPa. Shock wave velocity and brightness temperature were measured in every experiment. Plasma parameters estimated in frames of Debye approximation in grand canonical ensemble were: pressure 15-100 MPa, electron concentration 10^{19} - 10^{20} cm^{-3}. Stopping power of proton beam was defined by the displacement of the position of the spot image of the beam on the scintillator screen after it's passing through the analysing magnet.

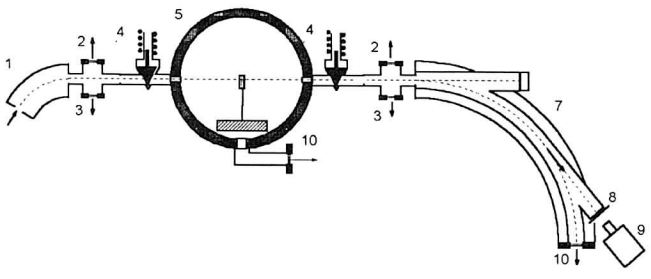

FIGURE 1. Experimental set-up.
1 - Banding magnet R=500, 2 - Differential pumping, 3 - Vacuum checking, 4 - Fast valves, 5 - Explosive chamber, 6 - Explosive generator, 7 - Analysing magnet R=707, 8 - MCP plate, 9 - PCO camera, 10 - Pumping

The position of the proton beam on a scintillator after the analysing magnet was recorded by a fast shutter camera (PCO-camera). Typical picture of the experiment is shown on Fig.2. The time gates of the PCO-camera was about 50 us in this shot. The undisturbed position of the proton beam passing through cold xenon at the initial pressure 10 kPa is seen to the right. The time about 1 us is necessary for plasma slug (D~8 km/s) to cross the beam line. The image of the proton beam interacting with the explosively driven plasma is to the left on the Fig.2. The intensity of the beam image is low because of the small time of the process and additional scattering of the beam. The estimated value of the energy loses in this experiment is ΔE_{exp} =150 keV.

The plasma temperature and shock velocity were measured in the experiment. Pressure P~50 Mpa, temperature T~4 eV, density $\rho \sim 6*10^{-3}$ g/cm^3 , electron concentration $n_e \sim 6*10^{19}$ cm^{-3} and nonideality parameter Γ~0.35 were realised. Calculated value of the energy loses (ΔE_c =200 keV) is in a reasonable agreement with the measured one.

So the first shots with the weakly nonideal xenon plasma showed a reliable operation of the experimental set-up.

This work was supported in part by INTAS Grant N94-1638.

FIGURE 2.
Image of 3-MeV proton beam in the beam-explosively driven plasma interaction experiment. (P_0=10 kPa).

Parameters of a Xenon Plasma Target in Shock Tube Created by an Explosive Source of Energy

S. Dudin, V. Fortov, V. Gryaznov, M. Kulish, V. Mintsev, N. Shilkin
Institute for Chemical Physics Research, Chernogolovka, Moscow reg., 142432, Russia
D.H.H. Hoffmann, M. Geißel, M. Roth
Gesellschaft für Schwerionenforschung, D-64220, Darmstadt, Germany

To investigate the heating of matter by particle beams detailed knowledge of the energy loss in dense plasma at high pressures and temperatures are crucial. Experiments carried out at GSI with discharge plasmas having electron densities up to $n_e \sim 10^{19}$ cc^{-1} show a considerable contribution of free electrons to the stopping. With increasing plasma density the influence of the effects of the Coulomb coupling are expected to be of great importance. Explosively driven shock wave techniques make it possible to produce plasmas with electron densities of up to $n_e \sim 10^{22}$ cc^{-1}. Standard shock wave plasma generators contain more then 500 g of high explosive, to produce shock compressed strongly coupled plasma with temperatures of 1-10 eV, pressures of 1-200 kbar and Coulomb coupling parameters of 1-5. Explosively driven plasma targets look very attractive for beam-plasma interaction experiments because of the absence of strong electromagnetic fields like in discharges, which significantly effect the beam transport.

To use standard explosive devices in beam areas of accelerator facilities it is necessary to build large-scaled explosive chambers and to solve the problems of matching high vacuum beam lines with the explosive apparatus. As the first step we suggest to use small charge (<150 g TNT) explosive generators in a vacuum pumped explosive metallic chamber with fast valves in such experiments. The performance of one type of such explosively driven generators are presented in this paper.

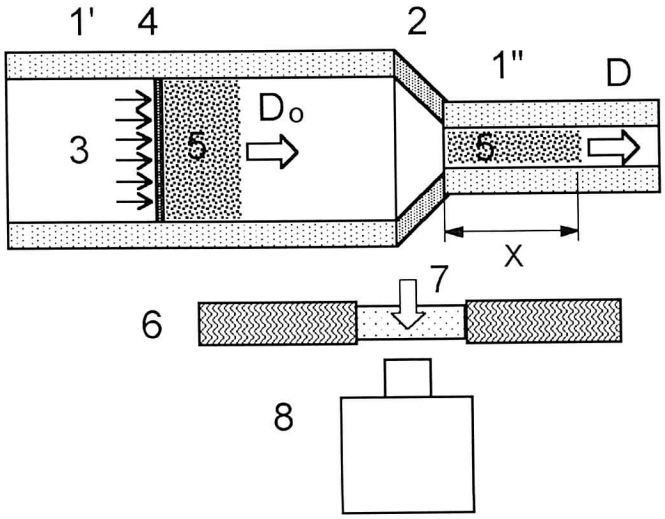

Figure 1. Experimental assembly. 1', 1"- glass tubes; 2-conical section; 3- products of detonation; 4- flying plate; 5- shock compressed plasmas; 6- protection wall; 7- optical window; 8- streak camera.

The experimental assembly is shown on Fig. 1. Through transparent tubes 1' and 1" the registration of velocities of shock waves and contact surfaces was conducted. Steel flying plate was accelerated by products of detonation (60g TNT) to values of 6.5 km/s. In the first parts of shock tube 2' velocity of shock wave in Xe was of constant value D_0=6.9 km/s. At passing of conic part the speed of shock wave grew and was increased the thickness of layer of plasma. The thickness of plasma slug was of >10 mm which provide fixed parameters for a time of 1 μs for the performance of the experiment with ion beam.

The measured velocity of shock wave in section 1" with diameter of 6 mm is shown on Fig. 2. The velocity is damped out which is connected with small diameter of tube. Calculated plasma parameters are placed in Table 1

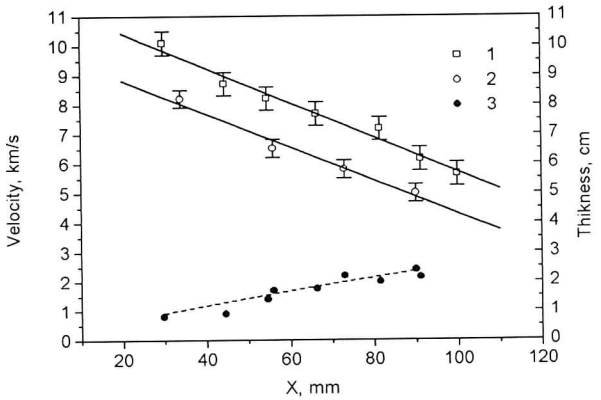

Figure 2. Velocity of shock wave and thickness of plasma slug in the direction of motion versus distance X from the cone.
1- initial density of 5.39E-04 g/cc; 2- 1.62E-03 g/cc;
3- thickness of plasma slug.

Table 1.

Initial density of xenon 5.39E-04 g/cc				
X, mm	T, K	P, bar	e, 1/cc	XeII, 1/cc
20	46700	530	6.0E+19	2.6E+18
40	40500	420	5.3E+19	5.9E+18
60	34000	320	4.5E+19	1.3E+19
80	28700	234	3.5E+19	2.0E+19
Initial density of xenon 1.62E-03 g/cc				
X, mm	T, K	P, bar	e, 1/cc	XeII, 1/cc
20	41200	1140	1.4E+20	2.9E+19
40	34800	870	1.2E+20	4.9E+19
60	29200	635	9.0E+19	6.4E+19
80	23300	430	6.5E+19	6.2E+19

This work was supported by INTAS Grant N94-1638.

Ignition Experiments with High Energy Proton Beams

M.D. Churazov, D.H.H. Hoffmann *, D.G. Koshkarev, Yu.S. Khodyrev **, B.Yu. Sharkov, P. Spiller *
Institute of Theoretical and Experimental Physics, Moscow
* *Gesellschaft für Schwerionenforschung, Darmstadt*
** *Institute of High Energy Physics, Protvino*

The unique beam parameters of high enery proton accelerators provide strong motivation to evaluate the feasibility of employing such accelerators for inertial fusion energy applications. High energy heavy ion beams (e.g. Bi at 30 GeV/u) were already considered in earlier publications for this purpose [1], [2]. A concept for ignition experiments with high energy proton beams is presented here. Proton beams at ultrarelativistic energies will be available in the near future. The LHC for example will provide a 7 TeV bunched proton beam, which has a total energy of $e_o \sim 334\ MJ$ within a pulse duration of $\sim 89 \mu s$[3]. To use this beam for the generation of dense plasma, it is necessary to compress the beam pulse ~ 2200 times, producing a single proton pulse with a duration of about $\tau \simeq 40\ ns$. This can be realized in two steps : first debunching of the accelerated beam and then rebunching the coasting beam in a single bunch. This operation will require an auxiliary low-frequency RF cavity ($11\ kHz$) with $39\ kV$ voltage amplitude. The estimated time for the bunching procedure is about $40\ sec$. Target relevant parameters, which may be achievable using the LHC as a driver, are compared in the table with other projects of this type.

	TWAC ITEP	RTTU VNIIEF	LHC CERN	GSI 2000
ion species	Co^{+27}	$Pt^{+1,-1}$	p	U^{28+}
ϵ_i GeV	40	10	7000	47
E_o MJ	0.1	10	334	0.002
τ ns	100	10	40	25
P_{ow} TW	1	1000	8350	0.08
$J_s\ TW/cm^2$	100	10^4	10^8	2.5
$J_m\ TW/g$	5	$5 * 10^4$	2500	1
$\rho \cdot l\ g/cm^2$	20	0.2	200	1.5
$\epsilon_m\ MJ/g$	0.5	500	100	0.026

Table 1 : Comparison of high energy proton beam heating with heavy ion beam projects. Anticipated LHC beam parameters were considered.

The expected very small transverse emittance of high energy proton beams (LHC : $\approx 5 \cdot 10^{-10}$ m rad) enables focusing to a spot diameter of $\sim 100\ \mu m$. Thus very high power densities of $J_s \sim 10^8\ TW/cm^2$ may be achievable in the target. In contrast to heavy ions the main process of slowing down high energy proton beams in the target matter is the process of nuclear collisions ($\rho l \sim 200\ g/cm^2$) and the development of secondary particle cascades. The latter create a wide range of energy deposition ($\Delta r \sim 0.1\ cm$ in Au) with a specific energy deposition of $\epsilon_m \sim 100.\ MJ/g$ and a specific power deposition of $J_m \sim 2500\ TW/g$ on the axis of a beam with a Gaussian distribution.
These parameters are impressive but not sufficient to obtain a highly efficient conversion of beam energy into radiation. However, magnetized targets might be considered with a scaled energy of $E_o \sim 3\ MJ/cm$.
Furthermore, the extremely small emittance of high energy proton beams, offers the possibility to create "hollow beams". In order to achieve a cylindrical illuminated target surface, a high frequency rotation ($\sim 1\ GHz$) of the needle-type beam around the target axis can be applied [4]. The rotation of the beam spot can be generated by four pairs of deflection plates at a distance of $\sim 200\ m$ from the target. Assuming a RF field strength of 30 MV/m the length of the plates must be $3\ m$ with an inter-plate distance of $10\ mm$.
To achieve the required focal spot diameter of $\sim 100.\ \mu m$ a small aperture focusing system has to be installed at a distance of $\approx 200m$ from the target.
At the described conditions of energy deposition, one can achieve an effective fuel compression by means of a cold Au-shell. In order to reach ignition parameters an initial fuel preheating ($T_o \sim 0.06\ keV$) and magnetic insulation ($B_{oz} \sim 10T$) is required. The ignition of a two-stage "cascade" DT target (see Fig.1) was obtained in 2D simulations for the geometry shown in Fig. 1. At the expected level of beam symmetry, which is of major importance, a fuel compression of $\delta \sim 1000$ [5] was obtained. In this simulations the fuel-pusher mixing was calculated to be $\leq 10^{-4}$, which is considered acceptable.

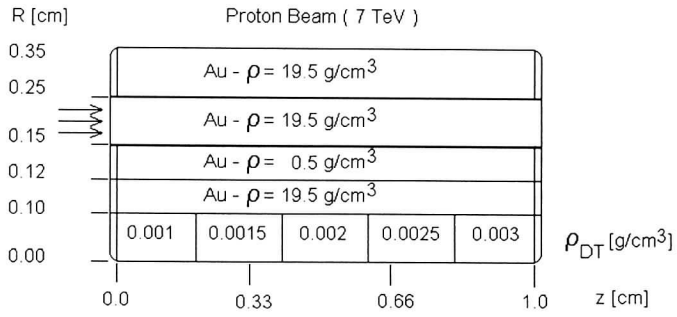

Figure 1: Fig. 1 : Magnetized cylindrical target ($B_{o,z} = 10T$).

References

[1] R,C.Arnold, R.W.Müller, GSI, Annual Report 1990, GSI-91-27, (1991)36.

[2] D.G.Koshkarev, B.Yu.Sharkov, R.C.Arnold Proc. of 12th Intern. Symp. on HIIF, Heidelberg, 1997 (to be published in NIMA 415/1-3)

[3] The Large Hadron Collider. Conceptual Design, CERN/AC/95-05(LHC)

[4] R.C.Arnold et al. Nucl.Inst. Meth. 199, (1982) 557

[5] M.D.Churazov et al. Proc. of 12th Intern. Symp. on HIIF, Heidelberg, 1997 (to be published in NIMA 415/1-3)

Heavy Ion Induced Hydrodynamic Motion in Lead Targets

S. Stöwe, R. Bock, P. Spiller, M. Stetter, *GSI-Darmstadt*
M. Kulish, A. Shutov, V. Yakushev, *Institute of Chemical Physics Chernogolovka*
B. Sharkov, S. Golubev, B. Bruynetkin, *Institute of Theoretical and Experimental Physics Moscow*
U. Funk, M. Geissel, D.H.H. Hoffmann, *Erlangen University*

One of the main topics of the plasma physics research at GSI is the investigation into dense plasmas generated by the impact of relativistic heavy ions in solid targets [1].
In recent experiments at the SIS Target Area (HHT) a maximum specific energy deposition of 1 kJ/g in an initially solid lead target was reached by stopping an intense Argon beam ($^{40}Ar^{18+}$ 300MeV/u). These experiments profit from an increase in beam current by a factor of four compared to experiments in 1996 by using the MUCIS ion source. With a new operation mode of the SIS [2], it is possible to achieve a single bunch of 250 ns pulse width (FWHM). The extracted bunch contains $2 \cdot 10^{10}$ projectiles.
For the first time it was possible to observe the hydrodynamic motion of a metal target. The time and spatial development of the hydrodynamic expansion of a lead sheet was observed by time resolved optical shadowgraphy (Fig. 1). The diagnostic setup consists of a fast multiframing camera (mimimum interframing time 1.7 µs) and an optical backlighter (xenon flash lamp). The direction of observation is perpendicular to the beam direction and parallel to the surface of the lead sheet. The beam diameter and the thickness of the lead sheet is 1 mm.

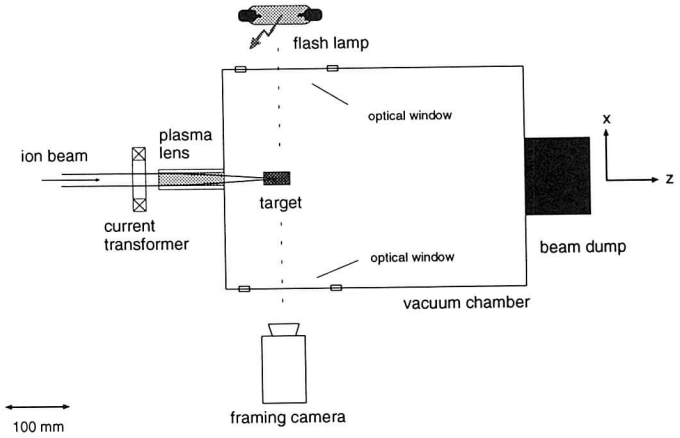

Fig. 1: Experimental setup at the HHT experimental area. Scheme of optical shadowgraphy

Fig. 2a shows the lead sheet before the beam illumination. The expansion of the heated lead 32 µs after the beam interaction phase is shown in Fig. 2b. The velocity of the transverse motion v_x of the heated matter can be extracted from the frames. It rises with the z coordinate, which is the penetration depth of the ions in the target. Due to the highest energy loss of the ions in the Bragg Peak, the velocity reaches its maximum value of about 290±20 m/s at z = 11 mm.

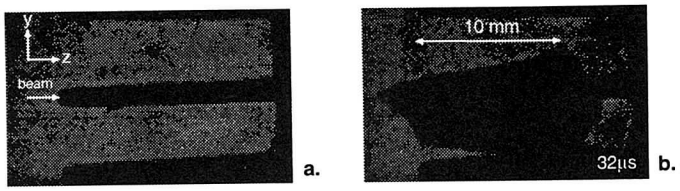

Fig. 2: Expansion of a lead sheet, heated with an intense Argon beam: a. Target before ion illumination b. 32 µs after illumination

The propagation of pressure waves in a cylindrical lead target of 17 mm diameter is measured by piezo-electric pressure gauges. The gauges are implemented in the target depth of z = 6 mm. The pressure wave passing the gauge causes a current signal in the electrical circuit of the gauges, which is recorded with a fast storage oscilloscope. The integrated signal is a measure of the pressure development in time. Fig. 3 shows the pressure signals, recorded with two gauges. Gauge 1 has a distance of 6 mm to the beam axis, gauge 2 a distance of 4 mm. The corresponding amplitudes are 0.16 GPa for gauge 1 and 0.10 GPa for gauge 2. The shape of the pressure pulse can be explained by the beam pulse structure, which is represented by the dashed curve (intensity in a.u.) and by the spatial beam intensity profile.

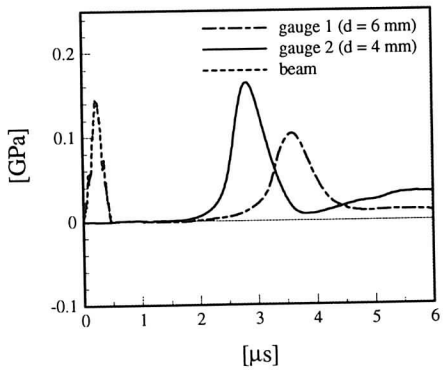

Fig. 3: Signal of two piezo-electric pressure gauges. The time resolution due to the thickness of the gauge is 10 ns

The experimental data are in good agreement with the results of a 2-D hydrodynamic code [3]. The calculated temperature at the location of the Bragg Peak is 2500 K, the pressure is up to 4 GPa.

References

[1] GSI-Nachrichten 1/97 *Plasma Physics with Heavy Ions*

[2] GSI-Nachrichten 3/97 *The Production of Intense Beam Pulses in the SIS Enables New Advances in Plasma Physics*

[3] A.Shutov et al., *2D Numerical Simulation of the Interaction of a Heavy Ion Beam with a Lead Target,* this report

2D Numerical Simulation of the Interaction of a Heavy Ion Beam with a Lead Target

A.Shutov, M.Kulish, V.Yakushev, V.Mintsev, V.Fortov - 1
S. Stöwe, M. Stetter, M.Dornik - 2
U. Funk, M. Geissel, D.H.H.Hoffman - 3
K.Hischenko- 4,

1 - Institute of Chemical Physics, Chernogolovka,RAS 142432, Russia
2 - GSI, Darmstadt, D-64291, Germany
3 - University of Erlangen, Erlangen, D-91085, Germany
4 - High Energy Density Research Center of RAS,Izhorskaya 13/19,Moscow , Russia

The numerical modeling of the hydrodynamic response of heavy ion heated lead targets is one of the topics of the collaboration between the GSI Plasma Physics Group and the ICP Chernogolovka. The numerical simulations were made by a 2D-hydrocode using a second order in space Godunov scheme [1] and an equation of state [2] developed in Chernogolovka. The experimental data of the spatial distribution of the beam power, the effect of beam focusing and the time structure of the beam were taken into account. The calculation was done both in sections of the targets along the beam and across the beam.

The beam in the experiments has an elliptical cross section. The transverse beam power density distribution has a Gaussian shape:

$$P_b = P_0 \cdot \exp\left(\frac{-(x - x_c)^2}{2 \cdot S_x^2} - \frac{-(y - y_c)^2}{2 \cdot S_y^2} \right) \qquad (1),$$

where Sx, Sy are values which characterize the size of the beam cross section. Sx, Sy are functions of the beam penetration depth in a target due to the focusing of the beam (fig.1).

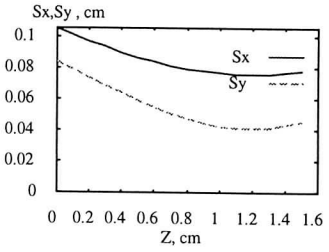

Fig.1 The dependence of Sx, Sy from the beam penetration depth

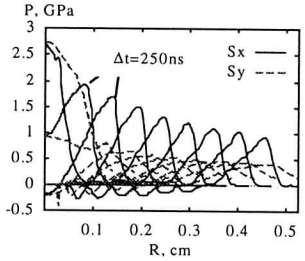

Fig.2. The pressure profiles with time step 250ns along main directions of the beam with elliptical cross section. Sy=2Sx

In spite of the 3D geometry of the real experiment it is possible to use a 2D code to determine hydrodynamic parameters in the target under beam interaction. The calculation of an infinite lead target in a plane perpendicular to the beam axis (z-) shows a circular pressure wave propagating from beam axis to outer target regions. Due to the elliptical beam power distribution the pressure amplitudes of the wave at a certain distance from the center vary with the azimuthal angle. The biggest difference occurs between the amplitudes in the main directions x and y. The pressure values in all other radial directions are between these two. The ratios of maximum pressure of the x- an y-profiles at different points in time (fig. 2) remain almost constant for distances far enough from the center:

$$P_{S_x}^{max}(z) / P_{S_y}^{max}(z) \approx S_x / S_y \Big|_{z>1.5mm} \qquad (2)$$

Thus the maximum pressure in a target caused by a beam with a circular cross section of radius $S = \sqrt{S_x \cdot S_y}$ of the same area as for an elliptical cross section must be in the range of $P_{S_y}^{max} \div P_{S_x}^{max}$. The real pressure in the direction of S_r can be approximated by:

$$P_r^{max}(z) \approx P^{max}(z) \cdot S_r / S \Big|_{z>1.5mm} \qquad (3)$$

The calculations using a plane perpendicular to the beam give almost the same results as for a plane containing the beam axis. It is possible to compare the calculated data with the pressure time development, measured with piezo-electric gauges, located at different radial positions in a finite lead cylinder. The depth z of the simulation plane is equal to the depth of the gauges in the target. Fig.3 shows the experimental data [3] and the results of the simulations.

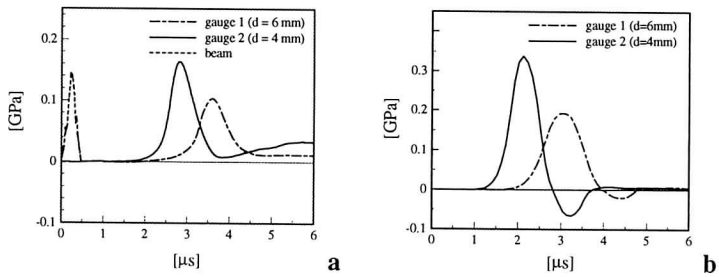

Fig.3 The experimental (a) and calculated (b) pressure development at two different radial positions in a lead cylinder, at a depth z = 6 mm

The simulation corresponding to the experiment with an expanding 1 mm plate target [3] was done at eight equidistant penetration depths z. Fig.4 shows the time development of the free surface velocity, calculated with the code.

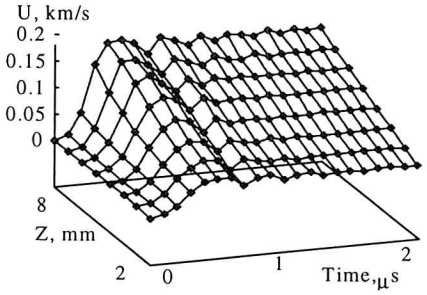

Fig 4 The history of expansion velocity of the target. For experiment

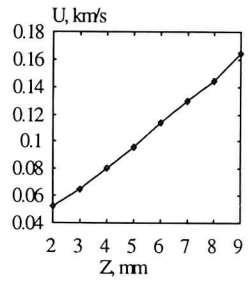

Fig. 5 The calculated velocity of the free surface

There is no acceleration of the surface in the later phase ($t > 1$ μs). The final velocities of the free surface are plotted in fig.5.

References

[1] Fortov et al., Nucl. Science and Eng. , 123,169-189(1996)
[2] Bushman A.V. et al, *Intense Dynamic Loading of Condensed Matter* (Tailor & Francis, Washington DC, London),1992
[3] S.Stöwe, *Heavy Ion Induced Hydrodynamic Motion in Lead Targets,* this report

New Cryotechnique for the Production of Rare Gas Targets and First Experiments with Neon

U. N. Funk, R. Bock, M. Dornik, M. Geissel, M. Stetter, S. Stöwe, GSI
M. Kulish, V. Yakushev, N. Shilkin, ICP Chernogolovka
D.H.H. Hoffmann, N. Tahir, Universität Erlangen

During the year 1997 the Plasma Physics Group at GSI was able to make experiments with two interesting new target materials, Lead [1] and Neon. The use of Neon was possible only after installing and implementing a new cryogenic device.
Rare gas crystals of Xenon and Krypton have been the first targets to investigate the interaction of intense heavy-ion beams with matter at GSI [2]. To expand the possibilities of growing crystals to rare gases with lower solidification points (Argon, Neon) and also Hydrogen, a new two stage closed cycle helium refrigerator was installed. It has a power of 7 **W** at 10 **K** and a minimum temperature of 5.3 **K**. The procedure of growing crystals is described in [2], but minor modifications have to be mentioned. On top of the sample holder a layer of 1 **mm** indium for sealing purposes has to be added and the growing pressure (100 **mbar**) and final height (5 **mm**) are different.
In a beamtime in October 97 the first experiments with Neon as target material were carried out with The beam a single bunch $^{40}\mathbf{Ar}^{18+}$ beam with an intensity of up to $\mathbf{1 \cdot 10^{10}}$ particles, leading to a specific energy deposition of (calculated with a simulation program) up to 1 kJ/g.
The diagnostic tools used in this beamtime were:

- A high speed framing camera capable of up to 60 exposures with a minimum interframing time of **2.2** μ**s** with a backlighter for shadowgraphie
- An image intensified CCD camera with a minimum exposure time of 5 **ns**
- A lens system for projecting the emitted light in the visible into a fiber optic to be analyzed then either by a monochromator or a photodiode
- A piezoelectric Polivenylidenflouride (PVDF) pressure gauge under the indium layer below the interaction point in the crystal

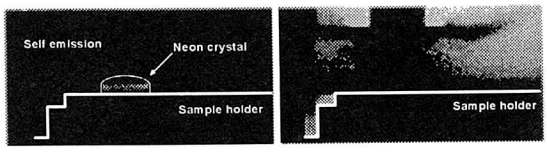

Figure 1: Two pictures showing the hydrodynamic motion of the Neon. Left: self emission; right: destruction after 120 μs.

Two selected pictures showing the hydrodynamic motion of the Neon as observed with the fast framing camera are shown in fig. 1. The left picture is taken shortly after the arrival of the beam. It shows the self emission of the crystal and gives an idea about the initial shape. The right picture is taken 120 μs later. The nearly complete destruction is visible. The cylinder in the upper part is the growing chamber for the crystal. Fig. 2 shows the signal of the photodiode and the beam intensity, measured with a fast current transformer as a function of time.

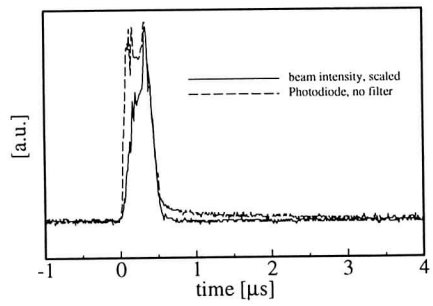

Figure 2: Signals of photodiode and beam intensity scaled to the maximum of the photodiode signal as function of time.

One can observe a very fast rise of the emission intensity with the arrival of the beam. The maximum intensity coincides in time with the maximum of the beam intensity. When the emission decreases, one can see two different time constants. First a very fast decrease, following the beam intensity and then a slower decrease with a smaller time constant, resulting in an overall emission time of up to 4 μs. With filters in front of the photodiode we could see, that the long emission originates from wavelength above 650 **nm**.
With the help of the PVDF gauges pressure waves were recorded. As the sampleholder was moveable in vertical direction, we were able to change the interaction point to pressure gauge distance. The pressure gauge signal for three different distances is shown in fig. 3. From the shift of the pressure peak with various distances we were able to calculate the sound velocity in solid Neon to $\mathbf{v_{sound}} = \mathbf{(520 \pm 50)}\ \frac{\mathbf{m}}{\mathbf{s}}$, which is in good agreement with literature values.

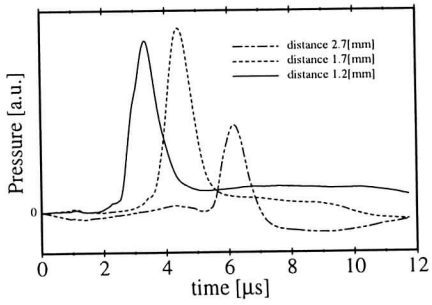

Figure 3: Signal of the pressure gauge for three different interaction point to gauge distances.

References

[1] S. Stöwe *et al.*; this report
[2] M. Dornik *et al.*; Fusion Engineering and Design 32–33 (1996) 511.

Diagnostics of the HHT Plasma Lens

M. Geissel[1], U. Funk[2], D.H.H. Hoffmann[2], M. Roth[1],
M. Stetter[3], C. Stöckl[1], S. Stöwe[3], W. Süss[2], W. Seelig[1]
[1]*Institut für Angewandte Physik, Darmstadt University of Technology,*
[2]*Physikalisches Institut Abt. I, Erlangen University,* [3]*GSI Darmstadt,*

At the High Temperature Experimental Area (HHT) of GSI a wall stabilized plasma lens is used as the final focusing device. Temporal and spatial resolved measurements of the emitted visible and UV radiation allow a detailed characterisation of the discharge. Thus the expansion dynamic, electron density and temperature of the discharge plasma have been measured for the first time.

The HHT plasma lens is an argon discharge device consisting of a 20 mm×100 mm ceramic tube, driven by six capacitor banks of together 80 μF. Charge voltages of up to 18 kV lead to maximum discharge currents of 400 kA. The duration of a discharge half wave is about 9.5 μs.
The observation of the light emission of the plasma lens in the HHT experimental area had so far not been accessible to diagnostics due to the small electrode apertures of the discharge tube. High plasma opacities had also been a reason to prevent the use of end-on diagnostics. Side-on examinations could not be done in the past, because the discharge tube consists of an aluminum-oxide ceramic. A special preparation of the discharge tube with a centered slit on one side (figure 1) allowed to observe the emitted radiation side-on from the visible up to the VUV spectral range.

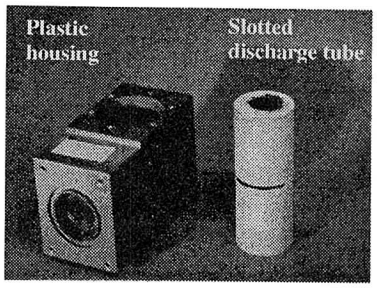

Figure 1: The diagnostic discharge tube with housing

It was shown that the discharge starts with a shock wave, which thermalizes after ca. 1 μs on the tube axis. The plasma then reaches a temperature of 9 eV, an electron density of 10^{18} cm^{-3} and a compression to four times the inital density. Temperature and density were distinguished by evaluating the spectra.
The total contraction of the current carrying plasma cylinder is reached after ca. 3 μs and reaches a minimal radius of about 4 mm. This can also be shown by the temporal variation of the inductivity of the plasma lens, which leads to a 'flat top' of the discharge characteristics. The discharge curve tends from a signal according to the 10 mm (full) discharge radius to a signal according to a 4 mm discharge radius (see figure 2).

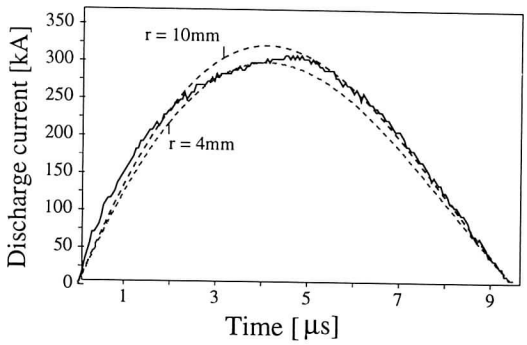

Figure 2: Variation of the plasma lens inductivity

During this time the temperature rises to almost 30 eV and the electron density exceeds 10^{19} cm^{-3} as figure 3 indicates.
It turned out that the performance of the plasma lens is optimized between 4.5 and 6 μs after the start of the discharge.

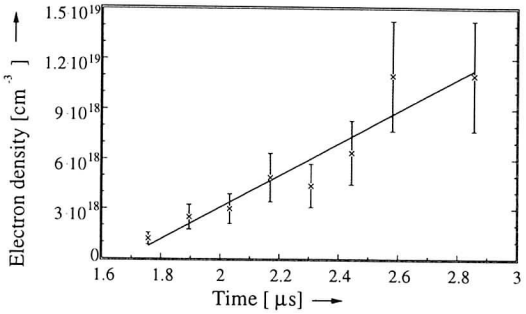

Figure 3: Development of the electron density

References

[1] M. Geißel: *Plasmadiagnostik an einer wandstabilisierten Argon-Plasmalinse*, Diploma thesis, Darmstadt University of Technology, 1997

[2] U. Neuner: *Die Plasmalinse zur Feinfokussierung hochenergetischer Schwerionenstrahlen*, PhD thesis, Erlangen University, 1995

[3] S. Stöwe: *Erster Einsatz einer Plasmalinse als Feinfokussiersystem für einen Schwerionenstrahl am SIS*, Diploma thesis, Erlangen University, 1994

Reconstruction of the Magnetic Field Profile from Beam Measurements in the SIS Plasma Lens

S. Stöwe, M. Stetter, U. Funk, M. Geissel
GSI-Darmstadt

M. de Magistris[1], A. Formisano[2]
(1) Università di Napoli Federico II, (2) Seconda Università di Napoli

The SIS Plasma Lens at the GSI - High Temperature Experimental Area - has shown a large capability in the final focusing of intense beams; this has been of primary importance in the maximisation of the beam energy deposition in solid targets (see, for example, High Energy Density in Matter GSI-Reports of past recent years).

The Plasma Lens is currently employed in high density experiments, and an accurate diagnostic of its performance is still in progress to assess and optimise the design parameters. A critical issue has been recognised in the evaluation of the field profile in the lens at the focusing time, being the lens optical properties strongly related to the profile [1]. In particular the deviation from the linear field profile has to be evaluated and controlled, in order to prevent aberrations in the focusing process. To cope with such a problem, a method, based on the evaluation of a ring beam focusing data has recently been proposed and studied [2-4]. In this report we present some results regarding the reconstruction of the field profile inside the lens based on this method, briefly exposed in the following: a ring mask is inserted on the beam line in front of the Plasma Lens; an image of the ring beam is then obtained on a set of scintillators after the lens. A series of measurements has been carried out at different radii for the ring mask, and at different time instants on the lens dynamic.

Using these data, the field profile in the lens is reconstructed by an optimisation procedure, which tries to minimise the distance between the reconstructed beam trajectories and the measured ones. The field profile is assumed to be a polynomial function (for simplicity we fix a third order one), and the corresponding coefficients are determined. At each step of the optimisation procedure the error between the measured beam trajectories and the calculated ones is evaluated:

$$err^i = \sum_{j=1}^{4} \left\| \left(\mathbf{x}_j^m - \mathbf{x}_j^c \right) / \Delta_j \right\| \qquad (1)$$

where by $\mathbf{x}_j^m$ we indicate the beam measured transverse position at the j-th scintillator, by $\mathbf{x}_j^c$ we indicate the corresponding calculated one, and by Δ_j the error bar vector on that measure.

Several standard minimisation algorithms have been tested for the determination of the field profile; in figure 1 a comparison of their performance is given for the whole set of time instants and for a fixed maximum number of iterations. From the picture two major points come to evidence. Firstly, the best performance is every time achieved with a «gradient» algorithm. Secondly, only in a late time (after the so called «pinch time»), where the plasma is presumably rather homogeneous, the reconstruction error, remaining in the order of 10%, shows a reliable field reconstruction.

The question now arises how does reconstructed field profile look like in the range of high accuracy , namely from 3 to 5.5 μs. In this range the profile is rather linear, with a maximum percentage RMS deviation from the linear profile of 14%.

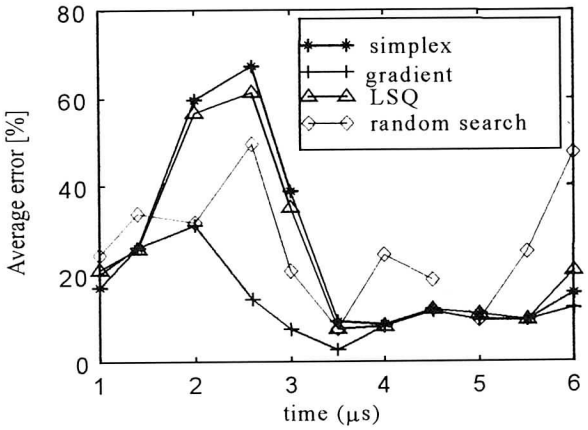

Fig. 1: Comparison of different minimisation algorithms.

An example of the reconstructed trajectories, compared to experimental points, is given in figure 2 for t=5.5 μs; one can see that the agreement is extremely good. At this time instant the RMS deviation of the field from the linear profile is below 1 %; notice that this is the time for optimal use of the lens, normally used in applications.

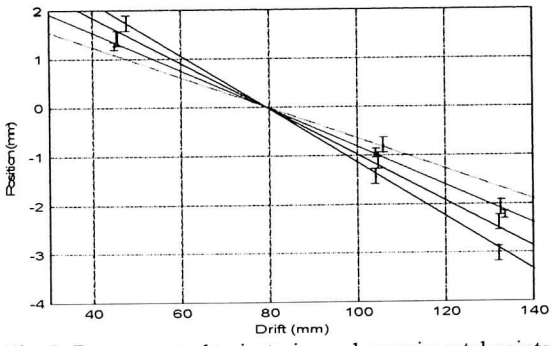

Fig. 2: Reconstructed trajectories and experimental points.

From the performed analysis we can conclude that the linearity of the lens, at the proper timing, meets satisfactory the requirements for reduced aberration, leaving to the beam emittance the main focusing limitations. A further analysis has to be performed in order to better understand early timing of the plasma discharge. This analysis will take advantage of new measurements with higher quality beams, obtained thanks to the electron cooler.

References

[1] M. de Magistris et al., *Fus. Eng. and Des.*, 32-33(1996)
[2] S. Stöwe et al., *GSI Report 1996* (1997)
[3] L.Corti et al., *GSI Report 1996* (1997)
[4] L.Corti et al., *Proc.COMPUMAG'97* (1997)

Evaluation of the Fringe Fields Effects in the SIS Plasma Lens

A. Tauschwitz
GSI-Darmstadt

M. de Magistris[1], A. Formisano[2]
(1) Università di Napoli Federico II (2) Seconda Università di Napoli

In the framework of the research activity on the SIS Plasma Lens at GSI (see this Report and GSI-Reports of past recent years), several investigation points have been recognized as crucial in the final optimization of the device. One of them is the problem of fringe field effects, often regarded as a possible source of significant aberrations, as in traditional quadrupoles. We report herein the results of our analysis of this problem.

The study is, in principle, similar to that of fringe fields of traditional quadrupoles (see, for example, [1]). The plasma current density, and magnetic field profile, have to be evaluated consistently with the electrode shapes, and the effects on the focusing compared to the ideal case, where fringe fields are neglected. From the theoretical point of view, one major difference with respect to quadrupoles has to be highlighted; as a matter of fact, a fundamental consequence of the axial symmetry of the device is that the magnetic field has rigorously only the azimuthal component [2]. This leads to simplified calculations in the particle trajectories evaluation.

Because of the typical shape of the electrodes, we expect a deformation of the current density distribution close to the lens exit. The field distribution, at least in the electrode region, will therefore depend on the longitudinal z coordinate as well as the transverse r coordinate. It has, therefore, to be determined either by measurements or by calculations. Due to the pulsed regime, direct field measurements are nearly impossible. On the other hand, a quasi-stationary calculation of the field map for a specific design is routinely obtainable with standard numerical tools. We have used, to evaluate the effects on the focusing, a field map specifically calculated, with a 2D axisymmetric FEM package, for the case of the SIS Plasma lens electrodes. The calculation, whose results are shown in figure 1, is based on the assumption of constant plasma conductivity, which seems to be reasonable at the proper discharge timing. A grid of 1800 elements has been sufficient for the prescribed accuracy of 0.01% in the field calculation. The geometrical parameters reproduce exactly the lens and electrodes shapes; the lens current has been set to 300 kA. The electrodes are considered as «ideal» conductors, thus leading to a mixed Dirichelet-Neumann problem for the plasma region. Due to the high ratio between the conductivity of the electrodes and of the plasma, this hypothesis is well established.

After determining the field map, this has been used as source for a fully 2-D tracking code, in order to evaluate the difference versus the simpler model without these effects. The results are shown in figure 2, where phase space images produced by the two models are compared for a 10π emittance, 6 Tm rigidity beam.

The substantial result of this analysis is that, as long as the final focusing is concerned and a realistic aspect ratio (length/radius) is utilized for the lens (it is around 10 in the specific case of the SIS Plasma Lens), the only appreciable effect on the focusing is a slight increase of the focal length for fixed parameters.

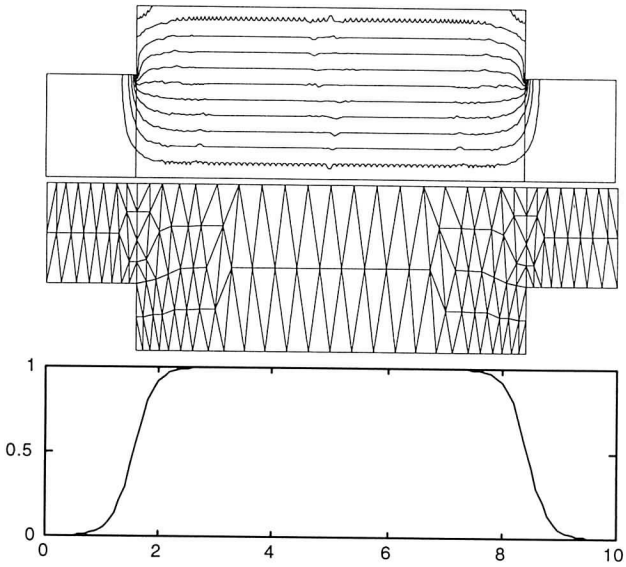

Fig. 1: Current density lines (upper), example of FEM mesh (lower), and current density field profile in the plasma lens (a.u.)

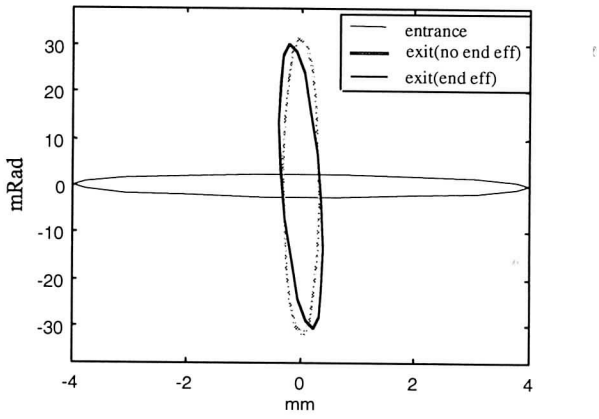

Fig. 2: phase space image of the beam with and without end effects

This behavior can be easily explained by recognizing that the region at the electrodes with distorted field is narrow if compared to the total lens length. Nevertheless, this effect has to be taken into account in the design parameters, correcting either the lens length or the plasma current. With the proper correction it is possible to reach, to any practical extent, the performance calculated with the idealized model.

References

[1] K.G. Steffen, *High Energy Beam Optics*, Interscience Publisher, 1965.
[2] M. de Magistris, A. Tauschwitz., *in preparation*

Intense Lyman-α Radiation from a Dense Neon - Hydrogen Mixture

A. Ulrich, J. Wieser, H. Shaw, TU-München
D.E. Murnick, H. Dahi, Rutgers University, Newark, NJ, USA

It is well known that excitation of dense rare gase mixtures by ionizing particles can lead to very intense spontaneous emission and laser effect on specific optical transitions via gas kinetic processes [1]. Here we describe an observation which was first made during an experiment at the Tandem accelerator in which nominally pure Neon was excited by a 100 MeV ^{32}S-beam. The VUV spectrum showed an extremely intense emission on the 121.567nm n=2 to 1 Lyman-α line. The effect was reproduced and studied in more detail using low energy (14keV) electron beam excitation as described in Ref.[2] and [3]. Small amounts of about 1mbar Hydrogen were deliberately added to Neon at atmospheric pressure in these experiments.

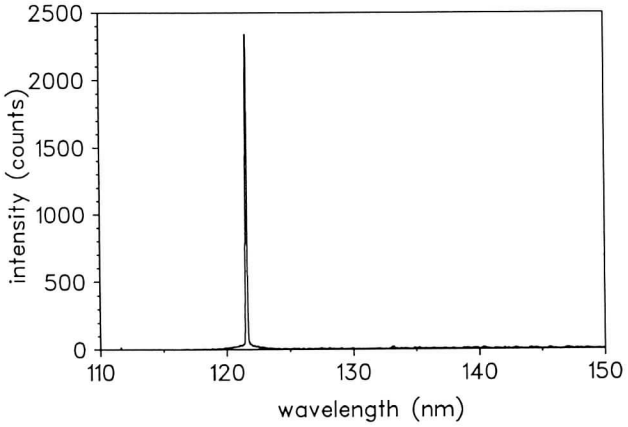

Figure 1: Emission spectrum of a mixture of 1bar Ne and 1mbar H_2 excited by a 14keV electron beam. Similar spectra can be observed using heavy ion beam excitation.

A spectrum measured using 10μA, 14keV electron beam excitation is shown in Fig. 1. A 10% conversion efficiency of beam power into Lyman-α-light could be determined. This line is essentially the only light emission observed over the entire wavelength region covered by our detection system from 110 to 800nm. In particular, emission from higher lying Hydrogen levels such as Balmer lines are completely absent. Lyman-α lamps described in the literature [4], so far, use Helium as a buffer gas. Using Helium instead of Neon in our system we find a 50 times weaker Lyman-α emission.

The gas kinetic processes leading to the observed effect have not been studied in detail up to now. There are, however, reasonable explanations for the high efficiency of Lyman-α- emission using dense Neon buffer gas and particle beam excitation: It is known that Neon excimer molecules form under these conditions[5] with strong emission on the first and second excimer continua between 75 and 90nm, corresponding to photon energies between 16.5 and 13.8eV. This is in coincidence with the sum of the dissociation energy of H_2 (4.481eV) and the excitation energy of a Hydrogen atom to the n=2 level (10.2eV). A resonant energy transfer between the decay of Ne_2^* molecules and dissociation plus excitation of Hydrogen may proceed via direct $Ne_2^* - H_2$ collisions or via photo -emission and -absorption, or both. Photodissociation of Hydrogen with fluorescence on the Lyman-α line is known from the literature[6].

Alternative kinetic processes finally leading to dissociation and excitation of Hydrogen may proceed via 3s Neon metastable atoms which are the precursors of the Neon excimer molecules. Comparing the 16.7eV excitation energy of this level with the potential energy diagram of H_2 and H_2^+ [7] one finds that a Hydrogen molecule could be ionized or excited into levels of the H(1s)+H*(2l) system in collisions with metastable Neon atoms. Molecular ions would have to undergo dissociative recombination for populating the H(1s)+H*(2l) levels. The observation that excitation of pure Hydrogen gas, or mixtures containing significantly more than 1% Hydrogen, radiate strongly on the molecular transitions suggests, however, that dissociative recombination should not be a dominant process.

A collisional transfer rate constant from Neon to Hydrogen of $3.6 \times 10^{-11} cm^3/s$ was determined from time spectra recorded on the Lyman-α line for various H_2 concentrations, a measurement which is independend of the transfer process. It is interesting to note that the Neon - Hydrogen energy transfer processes discussed above do not populate molecular levels H(1s)+H(n,l) with $n > 2$. This can explain the absence of Balmer transitions in the spectra.

Finally it should be noted that the electron beam excitation of the Neon - Hydrogen mixtures as described represents a compact, monochromatic VUV lamp emitting at 121.567nm with a high brightness of 10W per cm^2 of the entrance foil for the electron beam. The actual spectral width and shape of the line still needs to be studied.

Work supported by NSF Grant CTS 94-19440, INTAS Grant 96/351 and NATO Grant 921215.

References

[1] A. Ulrich, J. Wieser, A. Brunnhuber, and W. Krötz, Appl. Phys. Lett.6419941902

[2] J. Wieser, D.E. Murnick, A. Ulrich, H.A. Huggins, A. Liddle, and W.L. Brown, Rev. Sci. Instrum.6819971360

[3] A. Ulrich, H. Shaw, J. Wieser, and D.E. Murnick, 1996116

[4] A. Holländer and M.R. Wertheimer, J. Vac. Sci. Technol.A 121994879

[5] W. Krötz, A. Ulrich, B. Busch, G. Ribitzki, and J. Wieser, Appl. Phys. Lett.5519892265

[6] J.E. Mentall and E.P. Gentieu, J. Chem. Phys.5219705641

[7] T.E. Sharp, Atomic Data21971119

Metastable Helium Atoms in Dense Helium Gas

H. Shaw, H.-J. Körner, M. Salvermoser, J. Wieser, and A. Ulrich,
TU-München

Spinpolarized ^{3}He has become of great interest for NMR imaging of the lungs [1] and as a spin filter in neutron physics [2]. Samples of dense gas with at least atmospheric pressure are required for both applications. The most effective way for producing polarized ^3He, so far, is via optical pumping of Helium gas on the $2\ ^3S_1 - 2\ ^3P_1$ ($\lambda = 1083nm$) transition in a low pressure ($\simeq 1mbar$) discharge and subsequent compression of the gas. The discharge is used for collisional excitation of ground state $1\ ^1S_0$ Helium atoms to the metastable $2\ ^3S_1$ state.

In this report we describe a way which may avoid the complicated compressing of the gas by producing significant densities of metastable $2\ ^3S_1$ Helium atoms for optical pumping directly at atmospheric pressure. Up to now experiments were performed using ^{4}He. Densities of Helium metastables on the order of $5 \times 10^{10} cm^{-3}$ could be observed using absorption spectroscopy on the 1083nm line [3]. A low energy (10keV) electron beam is sent through a thin (300nm) SiN_x ceramic foil for collisional excitation of the dense Helium gas [4].

A schematic level diagram is shown in Fig.1. The formation rate of excimer molecules out of the $2\ ^3S_1$ level has been studied by Köymen [5] and is e.g. $1.3 \times 10^{-33} cm^6/s$ at 500°C. An estimate based on the maximum electron flux of $10^{17}/cm^2 s$ which is possible with the entrance foils used, and extrapolating cross section data results in a metastable production rate on the order of $10^{18}/cm^3 s$. This leads to a metastable density of more than $10^{11}/cm^3$ at atmospheric pressure.

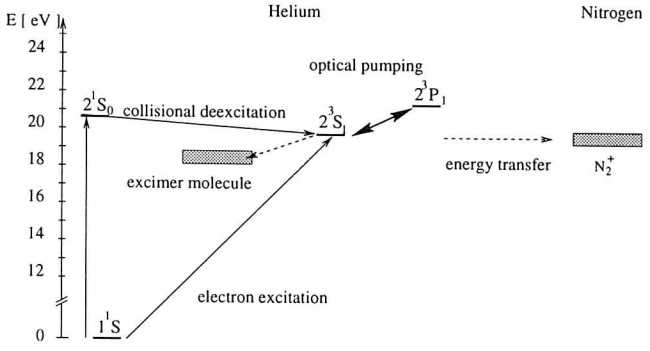

Figure 1: Schematic level diagram

Deexcitation of metastable Helium atoms by impurities is dominated by Nitrogen. This deexcitation process can be easily monitored by the B (v=0) to X (v=0,1) bands in N_2^+ around 390 and 430nm, respectively. The Helium gas was purified using an electrically heated Titanium wire which getters Nitrogen and Oxigen at about 800°C. Using this purification technique, we were finally able to reduce the Nitrogen concentration to a level at which its molecular emission was negligible.

For a direct measurement of the metastable densities in the dense gas a 10keV, $200\mu A$ electron beam was sent through a rectangular $0.7 \times 40mm^2$ SiN_x entrance window into Helium gas (e-beam flux $\simeq 4.5 \times 10^{15}/cm^2 s$). The Helium gas was contained in a stainless steel cell with optical windows for performing absorption experiments along the 40mm long region excited by the electron beam. Light from a low pressure Helium discharge lamp was sent through an optical chopper and the electron beam excited gas. The 1083nm line was selected using an interference filter in front of a Germanium photo diode detector. Absorption was measured using a lock-in technique thus suppressing 1083nm-light produced in the e-beam excited Helium gas.

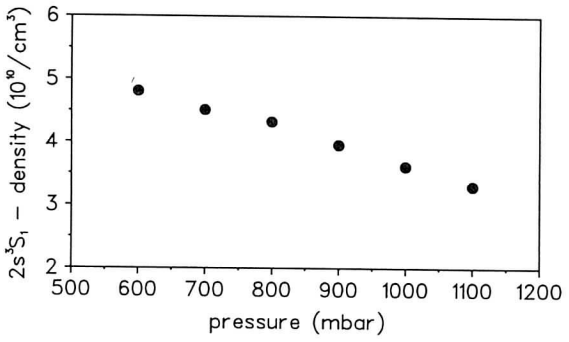

Figure 2: Pressure dependence of Helium metastable densities. Absolute values are uncertain within a factor of 2 due to systematic error.

Typically 25% absorption was observed in the experiments. Data can be interpreted using Lambert Beer's law for calculating metastable densities. The photo-absorption cross section was estimated to $2.7 \times 10^{-12} cm^2$ with an error of 50% due to limited knowledge of the linewidths of the 1083nm line in the discharge lamp and the dense gas, respectively, both being $\simeq$ 2GHz due to Doppler broadening in the first case and pressure broadening in the latter. Metastable densities obtained for various Helium gas densities are shown in Fig. 2.

Work supported by INTAS Grant 96/351 and NATO Grant 921215.

References

[1] M. Ebert et al. Lancet34719961297

[2] J. Becker et al. J. of Neutron Res.6.31995

[3] H. Shaw, Diplomarbeit, TU-München, Fakultät für Physik E12, Februar 1997

[4] A. Ulrich et al. 1996116 and J.Wieser et al. Rev. Sci. Instrum.6819971360

[5] A. Köymen et al. Chem. Phys. Lett.1681990405

Electron Capture in Collisions between Singly Charged Ions

F.Melchert, A. Pfeiffer, K. v.Diemar, K. Bajajova, C. Wohlfahrt, E. Salzborn
Institut für Kernphysik, Strahlenzentrum der Universität Giessen, D-35392 Giessen, Germany

Heavy ion induced compression of DT-pellets requires adequate accelerators and storage rings for the driving projectile ions. In the storage rings projected for the accumulation of intense beams, however, intrabeam scattering has an important effect on the lifetime and quality of high intensity heavy ion beams. In the energy region of interest, the dominating processes are

$$X^+ + X^+ \rightarrow X^{2+} + X^0 \qquad \text{(electron capture, } \sigma_C\text{)},$$

$$X^+ + X^+ \rightarrow X^{2+} + X^+ + e^- \qquad \text{(ionization, } \sigma_I\text{)}.$$

Multi-electron processes are of minor importance.The total beam loss cross section σ_L is then given by

$$\sigma_L = 2\cdot(2\cdot\sigma_C + \sigma_I) \qquad \text{(particle loss, } \sigma_L\text{)}$$

since two particles are lost per interaction in the electron capture reaction (1) and, furthermore, both ions act simultaneously as projectile and target particles. In a crossed-beams experiment, however, one ion beam is treated as the projectile ion beam where the increased charge is measured while in the target ion beam the corresponding ion in the decreased charge state is detected. σ_L contributes to the particle loss rate coefficient $\leq\sigma_L v_{rel}\geq$, where v_{rel} denotes the relative velocity distribution within the beam pulses.

A small database is available for collisions between heavy ions. By means of the Giessen ion-ion crossed-beams facility [1] we measured absolute cross sections σ_C for charge exchange in $X^+ + X^+$ collisions where $X^+ = Xe^+$, Bi^+, Cs^+, Hg^+ and Ta^+. Two momentum analyzed ion beams of adjustable energies are arranged to intersect at an angle of 17.5° in an ultrahigh vacuum region of some 10^{-11} mbar. The collision products formed in both beams are analyzed downstream from the interaction region with respect to their charge states. In order to reduce background events both ion beams are cleaned, shortly before intersection, by electrostatic deflectors from particles in other charge states which result from charge-changing collisions with the residual gas.

The measured cross sections are plotted in Fig. 1 as a function of the relative collision velocity v_{rel}. For $Hg^+ + Hg^+$ collisions, large cross sections in the order of $2\cdot10^{-16}cm^2$ which do not depend on the relative collision velocity v_{rel} are observed. In contrast, cross sections for Ta^+, Bi^+ and Xe^+ collisions are smaller and rise as a function of increasing collision velocity. The particular slopes increase from Ta^+ to Xe^+. Experimental cross sections for Cs^+ are comparably small and exhibit some deviations between results of different authors. Theoretical calculations were performed for electron capture in $Cs^+ + Cs^+$ collisions [2] and in $Ba^+ + Ba^+$ collisions [3].

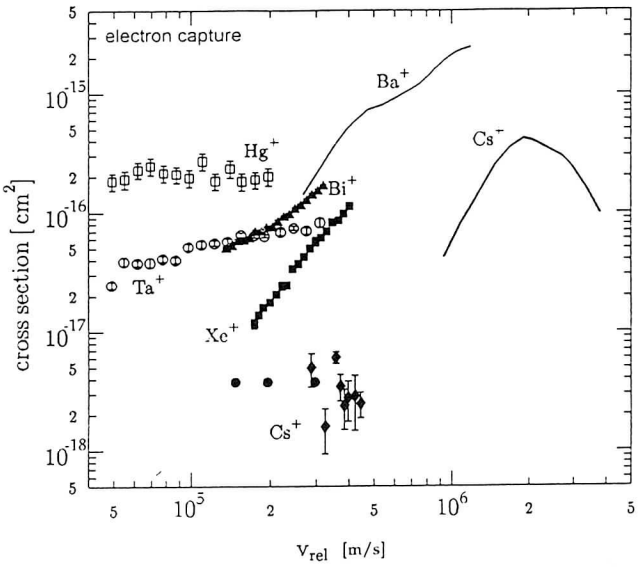

Figure 1: Electron capture cross sections σ_C in $X^+ + X^+ \rightarrow X^{2+} + X^0$ collisions where $X^+ = Xe^+$, Bi^+, Cs^+, Hg^+, Ta^+ and Ba^+

Model calculation of particle losses for stored beams of Hg^+ or Ta^+ ions [4] predicted remarkably larger particle loss rates than for stored beams of Bi^+ ions [5].

References

[1] S. Meuser, F. Melchert, S. Krüdener, A. Pfeiffer K. v.Diemar, E. Salzborn, Rev. Sci. Instr. 67 (1996) 2752

[2] A.M. Ermolaev, C.J. Noble, B.H. Bransden, J. Phys. B 15 (1982) 457

[3] S.J. Sramek, J.H. Macek, G.A. Gallup, Phys. Rev. A 22 (1980) 1467

[4] F. Melchert et al. in: Proc. of the 8th Intern. Workshop on Atomic Physics for Ion-Driven Fusion, Heidelberg, 24-27.09.97, in print

[5] D. Budicin, I.Hofmann, M.Conte, R.Schulze, F. Melchert, E. Salzborn, Nuovo Cimento, 106A (1993) 1621

2 ACCELERATOR RESEARCH AND DEVELOPMENT

2.1 The HIDIF-Study

2.2 Sychrotron and Storage Ring Experiments

2.3 Transverse Stability in Rings

2.4 Ion Sources and RFQ Funneling

2.5 Focusing and Plasma Effects

2 ACCELERATOR RESEARCH AND DEVELOPMENT

2.1 The HIDIF-study

Completion of the interim report for the HIDIF study has been a major effort in 1997/1998 in collaboration with the groups at CERN, Rutherford-Appleton Laboratory, the University of Frankfurt and FZ Juelich. The study has for the first time presented a consistent RF accelerator scheme and low-gain (ignition) fusion target, based on extended computer simulation for key areas in linac acceleration (main drift tube linac) and beam manipulations in storage rings and final compression/transport. It has been shown that there is a small but finite margin to reconcile the linac momentum spread and emittance with the pulse length and spot size at the target. Results are presented as a GSI Report (GSI-98-06).

2.2 Synchrotron and Storage Ring Experiments

The HIDIF study has shown that machine experiments on space charge dominated beams are necessary in order to obtain an experimental basis for the beam manipulations required by inertial fusion. Such experimental studies are also mandatory for the bunch compression project at GSI, which should provide short pulses of intense heavy ion bunches for plasma physics experiments.
The concept of adiabatic (slow with respect to the synchrotron frequency) pre-bunching and subsequent fast bunching has been tested for the first time in the SIS. Optimization of this procedure to obtain minimum longitudinal phase space dilution is a goal for further investigation. This forms the basis, in parallel with computer simulation for a proposal to develop a new low-frequency bunch compression cavity with 200-300 kV, which is close to completion.
The question of a direct diagnosis of the space charge density of intense beams has been investigated in the SIS by the technique of measuring the coherent quadrupolar frequency. By careful interpretation of the measurement using 2D computer simulation and noise analysis we have been able to put this new method on a firm basis.
Of continuing interest is the investigation and interpretation of the longitudinal instability of coasting beams under the effect of the RF cavity impedance, both in the ESR and SIS. Observations and simulation have confirmed that the traditional "overshoot" theorem quoted in literature must be replaced by a new one.

2.3 Transverse Stability in Rings

A computer code including the effect of nonlinear resonances and space charge has been developed. One of the applications is the study of the transverse stability of bunched beams with two momentum groups proposed as an option for the HIDIF storage rings, which has shown that a larger dispersion lattice would be required for this scheme.
Another interesting study is the possibly destabilizing effect of neutralizing electrons accumulated from the background gas. The phenomenon might be observed for very high currents and would requires cures, like feedback.

2.4 Ion Sources and RFQ funneling

A prototype Bi ion-source at Frankfurt (IAP) has recently been shown to deliver 21 mA which is close to the current required by HIDIF. The source has a seven hole extraction system with

a maximum extraction voltage of 27 kV. The fraction of Bi^{1+} in the extracted current was measured as 93 %.
The RFQ funneling concept is studied in another experiment at Frankfurt in a scaled version using two He^{+} beams from 2 identical ion sources. The ion sources have been tested and shown to fulfill the requirements needed for the funneling.

2.5 Focusing and Plasma Effects

The successful experiment in Frankfurt with a 10 keV Gabor plasma lens for He^{+} is now extended to a new 206 kV Double Gabor lens for heavy ions up to B^{+}. This lens can focus beams behind the existing RFQ.
For charge state analysis behind plasma physics targets the option of pulsed strip-line spectrometer is studied. Measured fields have shown excellent agreement with the calculations by a newly developed code.
Space charge effects between several beamlets in final focusing have been studied and applied to the HIDIF concept. They have been found to be a relatively weak but not negligible effect. For higher currents and dense gas the ionization effects in FLIBE background have been contributed by the Orsay group.

(I. Hofmann)

High-Current Beams and Fusion Accelerator Studies

I. Hofmann[1], R. Bär[1], O. Boine-Frankenheim[1], J. d'Avanzo[1], G. Franchetti[1,2], R.W. Hasse[1], R.W. Müller[1], G. Rumolo[1,3], P. Spiller[1]
[1] GSI, [2] Bologna, [3] Napoli

The theory of beam physics at high intensities and phase space densities and the interpretation of experiments at high intensities and phase space densities are directly related with the goal of developing the basis for fusion drivers. This has required a steady advancement of 2D and 3D computer simulation codes (PIC and Vlasov codes) to model as realistically as possible the results from experiments. An application of these studies is to help improve the performance of the SIS as high-current machine and to explore future accelerator scenarios at GSI.

1 HIDIF-study

The purpose of this study on Heavy Ion Driven Inertial Fusion was to find a consistent solution to the problem of driver and low-gain (ignition))fusion target. The study has been carried out on the basis of advancement in computer simulation of accelerator issues and in design of indirectly driven targets. Finalization of the HIDIF interim report with contributions from collaborators at GSI and at a number of European research centers (CERN, Rutherford and Appleton Laboratories, MPQ Garching, FZ Karlsruhe, FZ Juelich, ENEA Frascati and DENIM Madrid) and universities (Frankfurt, Erlangen, Darmstadt, Orsay, Madrid, Bologna, Naples) has been an important task in 1997/98. Most of the work was presented at the *International Symposium on Heavy Ion Inertial Fusion* held in Heidelberg (Sept. 22-27, 1997). The full HIDIF-report has appeared as GSI-report[1]. It is planned to supplement this HIDIF report, in approximately two years from now, by an upgrade of the study to high gain and to energy production.

2 Longitudinal Resistive Instability in the ESR[a]

During storage of high currents with low momentum spread beams are subject to the longitudinal instability if a resistive impedance component is present at some multiple of the revolution frequency. The problem was studied experimentally years ago in the ISR (and other machines) to check if theory was right. These earlier measurements where made above transition energy, where the space charge impedance is negligible. At the ESR we have investigated this mode in the space charge dominated regime and found some interesting new features requiring further comparison with theory [2]. The ESR electron cooling allows to carry out such experiments in the vicinity as well as far away from the stability boundary. Thus nonlinear saturation phenomena can be studied in the unstable region and compared with the findings from computer simulation. We first cooled a C^{6+} beam at 250 MeV/u and 0.3 mA current in order to obtain a very small longitudinal momentum spread near 10^{-5}. The frequency of the r.f. cavity was then shifted from an initially strongly de-tuned value towards the beam revolution frequency to obtain the expected unstable behavior. Subsequent time traces were recorded synchronously with the revolution period (waterfall diagram of Fig. 1). The diagram shows the initially

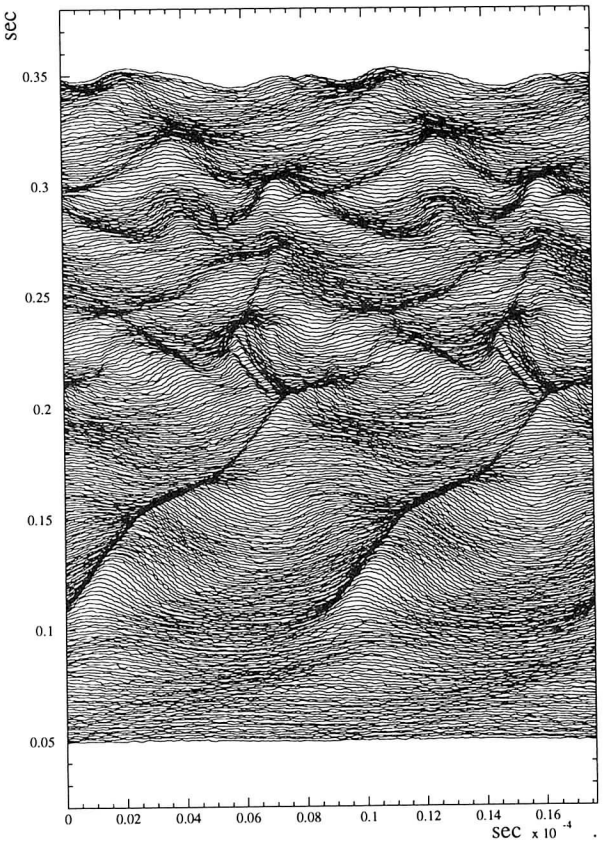

Figure 1: Exponential growth and nonlinear saturation phase of longitudinal resistive instability of cooled coasting beam in the ESR driven by the r.f. cavity on the first harmonic. The waterfall plot shows subsequent time traces from bottom to top over 350 ms (each trace is the current profile over 2 revolution periods).

exponential growth of the slow wave (moving to the right, since time is increasing from bottom to top), nonlinear saturation and decay into a fast wave moving to the left. The self-bunching effect was generally not exceeding 50% of the coasting beam current, which was found to be in excellent agreement with computer simulation. An interesting nonlinear effect is the appearance of significantly higher harmonic signals at some later time (0.2 seconds in Fig.1), which were not present if the instability on the fundamental harmonic was absent. We assume this results from a loss of Landau damping in the filamented phase space distribution of the saturated instability. It is also worth noting that the strong coherent signals persist for a long time. This is in contrast with the simplifying argument

which predicts Landau damping due to an overshoot of the momentum spread after the instability has occurred. The absence of saturation in the log-time behaviour has been explored by particle-in-cell simulation as well as a direct Vlasov code (1D), which show that after the first violent effect of the instability (exponential growth) the resistive impedance continuous to generate fluctuations in density which dissipate energy and lead to a slow growth of the momentum spread.

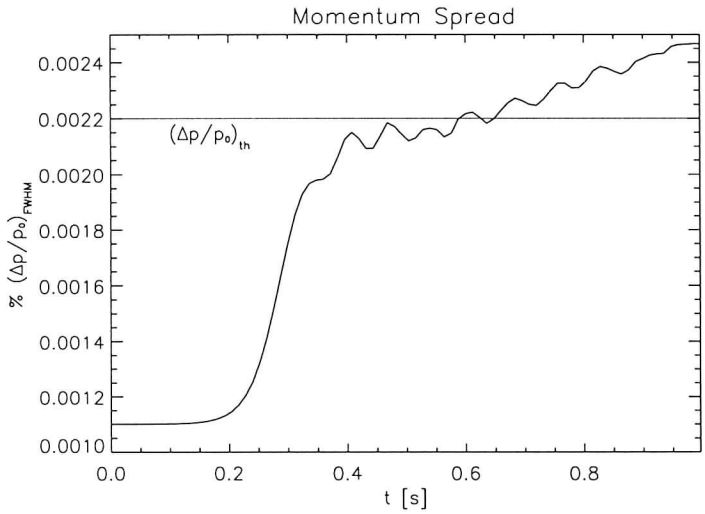

Figure 2: Vlasov simulation (1D) of longitudinal instability. The fwhm momentum spread shows the absence of real saturation of the instability. The horizontal line indicates the stability boundary of the linearized theory.

[a] supported by the ESR-group

3 Emittance Measurement in the SIS by Quadrupolar Oscillations[b]

For high-intensity heavy ion beams a non-destructive method of determining the incoherent tune shift and thus the emittance is of interest. We have implemented in the SIS a method which was for the first time studied recently at LEAR [4]. In this method (already proposed by Hardt [5]) the coherent space charge tune shift of quadrupolar oscillations is used to determine the incoherent tune shift.

The beam is excited with a signal sweeping over the envelope oscillation frequencies which are slightly shifted from $2Q_{h,v}$ due to space charge. The coherent response signal on a quadrupolar pick-up (consisting of four appropriately connected plates) is Fourier analyzed (see Fig. 3 where different side bands of these coherent lines are shown). There is a theoretical relation between the thus measured coherent frequency shift and the incoherent tune shift, which can be written approximately as

$$Q_{coh,1} - 2Q_{0,x} = -(3 - a_x/(a_x + a_y))\Delta Q_{inc,x}/2 \quad (1)$$

A second coherent frequency $Q_{coh,2}$ is obtained by simply interchanging x and y. $Q_{0,x}$, $Q_{0,y}$ are obtained from the signals in the low-current limit. The relationship can be

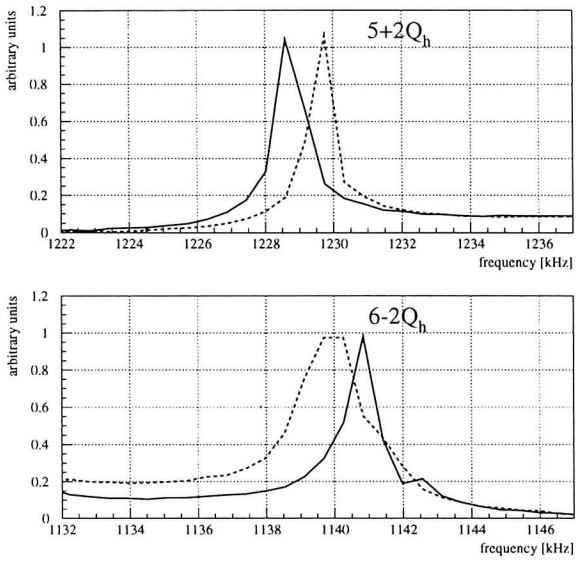

Figure 3: Measured space charge shift of quadrupolar (envelope) oscillation frequency in the SIS (dashed curve no space charge effect).

used to determine in each plane the incoherent shift and thus the rms emittances. First successful measurements at the SIS for the horizontal tune shift of a coasting Ne^{10+} beam at the injection flat-top have been carried out. The thus determined ΔQ_{inc} was used to determine the rms emittance.

The method is presently refined by using computer simulation with SCOP-XY to determine the geometry factors applying to different beam density profiles [6].

[b] supported by the SIS-group

4 Space Charge in Multi-turn Injection

Using the 2D particle-in-cell code SCOP-XY we have found that space charge in transverse multi-turn injection leads to some interesting nonlinear effects. In connection with heavy ion fusion storage rings it is of interest to study simultaneous injection into the horizontal and vertical phase space by using a corner septum and bumping the equilibrium orbit away from the injection septum in both planes. Such a scheme has been calculated for a working point of Q_h=8.858 and Q_v=8.73 as shown in Fig. 4. This working point is found after a fine-tuning to minimize loss (by a factor 3 compared with an earlier working point 8.78/8.65).

The method is found to allow 15 turns of injection without any loss on the septum if space charge is ignored. In this case the center of the phase space distributions (in x,x' and y,y') is void. The choice of the working point in the tune diagram must be re-optimized for high space charge, hence for the corrected working point the injection loss at low current is expected to be bigger than with full space charge. The intrinsic incoherent space charge tune shift of the injected beam is 0.03. Calculations including space charge show that the nonlinear space charge forces lead to

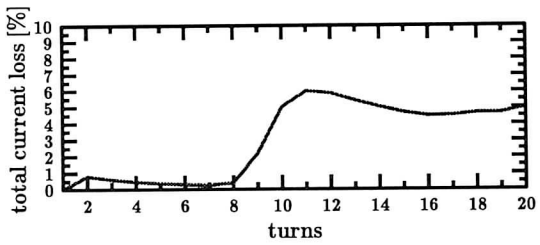

Figure 4: Total current loss in two-plane multi-turn injection of 20 injected turns using a working point Q_h=8.858 and Q_v=8.73 optimized for minimum loss in the presence of space charge.

spiraling structures in phase space and some kind of halo after additional turns beyond the injection cycle. With the optimized working point we have found that the septum losses can be kept as low as 5% for a 20-turn injection. The finally achieved coasting beam tune shift is about 0.05. An extension of this study to fully 3D simulation (including the linac bunch structure) is under way [3]. Application of this computer program to multiturn injection into SIS with the goal of improving the injection efficiency is under preparation.

5 Space Charge Effects on Multipole Oscillations and Anisotropy

The effect of space charge on higher order beam oscillations is of interest with respect to nonlinear resonances in circular machines and the subject of "equipartitioning" in intense proton linacs. We have derived a self-consistent analytical theory to calculate the coherent tune shift of beams with different oscillation energies in two degrees of freedom ("anisotropic beams") [7]. Based on the coupled Vlasov and Poisson equations we have obtained the dispersion relations of multipole oscillations of quadrupolar, sextupolar and octupolar symmetry. Numerical results applied to anisotropic ("non-equipartitioned") linac beams show that such beams can be stable in spite of considerable anisotropy. Only for space charge tune depressions considerably stronger than what one practically has in high-current linacs the theory predicts instability of sextupolar or octupolar modes. The expected consequence would be an exchange of the oscillation energy and a full or partial removal of the anisotropy (see Fig. 5)

We are presently using 2D and 3D particle-in-cell simulation to explore the practical consequences of such anisotropy effects with respect to high-current linacs. Another potential application is longitudinal laser cooling of bunched beams. There it is of interest to explore the possibilities of indirectly cooling the transverse degrees of freedom as a result of this energy exchange.

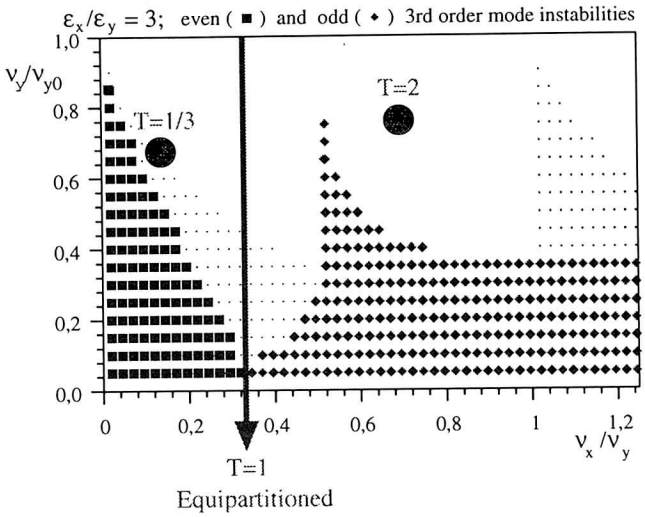

Figure 5: Instability charts indicating regions (shown by markers) where the anisotropy instability would lead to emittance exchange. The points T=1/3, 2 (with T the ratio of longitudinal to transverse oscillation energies) are examples for working points of linacs where non-equipartitioning is stable.

References

[1] "The HIDIF-study" (eds. I. Hofmann and G. Plass), GSI-98-06 (1998)

[2] G. Rumolo et al., to be published in Proc. XII Intern. Conf. on Heavy Ion Inertial Fusion, Heidelberg, Sept. 22-27, 1997

[3] G.W. Hasse et al., ibid.

[4] M. Chanel, Proc. European Particle Accel. Conf., Sitges, June 10-14, 1996, p. 1015

[5] W. Hardt, CERN internal report, ISR/Int 300 GS/ 66.2 (1966)

[6] R. Bär et al., to be published in Proc. XII Intern. Conf. on Heavy Ion Inertial Fusion, Heidelberg, Sept. 22-27, 1997

[7] I. Hofmann, *Stability of Anisotropic Beams with Space Charge*, GSI-Preprint-97-27 (1997), Phys. Rev. E **57** 4713 (1998).

Bunch Compression in the Heavy Ion Synchrotron SIS at GSI

K. Blasche, O. Boine-Frankenheim, H. Eickhoff, M. Emmerling
B. Franczak, I. Hofmann, K. Kaspar, R.W. Müller, P. Spiller

Heating matter by heavy ion beams is a central aim of the plasma physics group at GSI. In order to maximize the beam power deposited in the target the total number of particles has to be captured in a single bunch with a pulse length as short as possible.

In a first step adiabatic debunching of the four SIS bunches after acceleration followed by an adiabatic rebunching of the coasting beam on the first harmonic was successfully tested in March 97 [1]. This operation mode enabled the experimental plasma physics group to heat up a lead target to a temperture of 0.5 eV.

For further compression of the single bunch we consider as option further adiabatic compression using higher harmonics and fast bunch compression with a variable degree of prebunching. With respect to the required rf-voltages a fast bunch compression with a 90^o degree rotation promises to be the most effective.

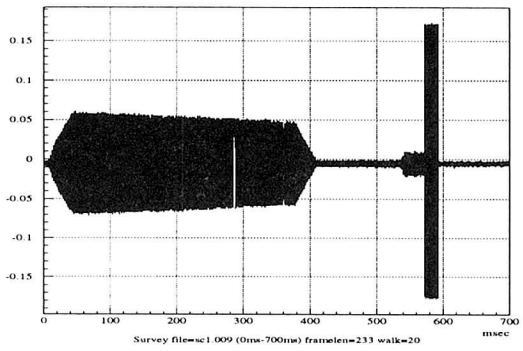

Figure 1: RF-voltage evolution over one machine cycle including acceleration, debunching, prebunching and bunch compresssion.

The fast compression is based on a rotation of the longitudinal phase space which has to be initiated by a fast jump of the rf-voltage (Fig. 1).

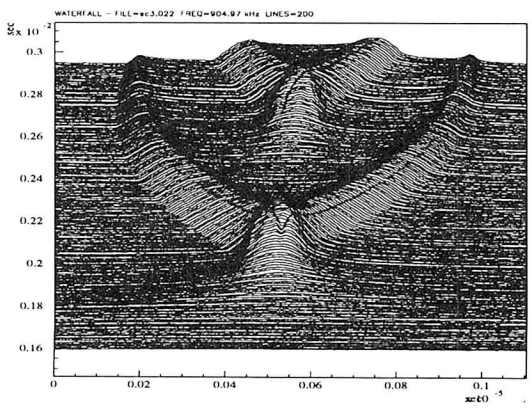

Figure 2: Evolution of the ring current at a fast voltage jump starting from a coasting beam.

The typical evolution of the ring current at fast bunch compression is shown in figure 2. Within first machine experiments the effect of different prebunching amplitudes on the final bunch length was investigated and bunches with a peak width of 100 ns were extracted (fig. 3).

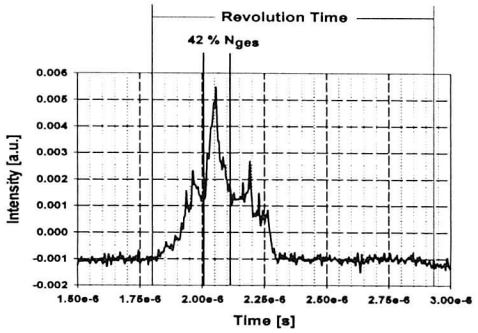

Figure 3: Beam transformer signal of an extracted single bunch after fast compression. The prebunching amplitude was 0.5 kV and the final compression voltage 14 kV.

In order to provide the maximum available rf-voltage (32 kV) for the fast compression a first test with a parallel operation of both rf-cavities was done in november 97. Beside the beam dynamics measurements important machine parameters like rise time of the rf-voltage and rf-phase stability could be studied.

With respect to the space charge coupling to the longitudinal impedances of the rf-cavities a debunched beam behaves most sensitive. Therefore we want to avoid the coasting beam phase after acceleration and envisage a bunch merging process [2] to generate the single bunch. After commissioning of the new high current injector it is planned to increase the energy deposition in the target by making use of heaviest ions at intermediate charge states e.g. U^{28+} [3]. To achieve the required 50 ns total pulse length additional rf-cavities with a total voltage in the range of 100 kV or even more have to be installed. Different concepts for the rf systems, e.g. metglas cavities were suggested and will be studied in detail. In parallel computer simulations including the effects of higher harmonics, space charge and cavity impedances are presently performed, in order to find the most adequate operation mode suitable for short bunch creation.

Acknowledgment : For supporting the measurements we thank P. Moritz, A. Tauschwitz, S. Stoewe and U. Funk.

References :

[1] GSI-Nachrichten 3/97
[2] Proc. of "Computing in accelerator design and operation", Berlin 1983(128)
[3] GSI-Report, GSI-96-07

Measurement and Interpretation of Quadrupolar Oscillation Mode Frequencies for Non-destructive Beam Biagnostics

R. Bär, I. Hofmann, P. Moritz
GSI Darmstadt

Observation of space charge phenomena is of increasing interest for high current circular accelerators, especially considering the demanding requirements of future high power machines. A nondestructive method which works particularly well for high intensity without interfering with the beam is based on measuring the frequency shifts induced by space charge of quadrupolar type envelope oscillations. This method was already proposed by Hardt [3] and successfully demonstrated at LEAR for a cooled proton beam [2].

There is a theoretical relation between the coherent frequency shift of quadrupolar oscillations and the incoherent tune shift ΔQ_{inc}, which can be derived from Sacherer's rms envelope equations. The result can be written approximately as

$$Q_{\mathrm{coh},1} - 2Q_{0,x} = -\frac{1}{2}\left(3 - \frac{a_x}{a_x + a_y}\right)\Delta Q_{\mathrm{inc},x} \qquad (1)$$

A second coherent oscillation frequency $Q_{\mathrm{coh},2}$ is obtained by simply interchanging x and y. $Q_{0,x}$ and $Q_{0,y}$ are the machine tunes measured in the low-current limit. For zero space charge one clearly has twice the betatron frequency while quadrupolare frequencies shift slightly from $2Q_{\mathrm{x,y}}$ due to space charge. In the limiting case of a round beam and symmetric focusing in both planes the two eigenfrequencies correspond to the round "breathing mode" (symmetric perturbation) and the "quadrupolar mode" frequently discussed in papers about beam halo formation. In the anisotropic case both eigenmodes have a quadrupolar symmetry.

This relationship can be used, in combination with the formulas relating the incoherent tune shifts with the emittances, to determine in each plane the incoherent tune shifts and thus the emittances (if the beam current is known precisely). It should be noted that since eqn. 1 results from the rms envelope equations valid for all kinds of particle distribution functions the measured tune shifts only depend on rms quantities, hence one strictly obtains the rms emittances by this method.

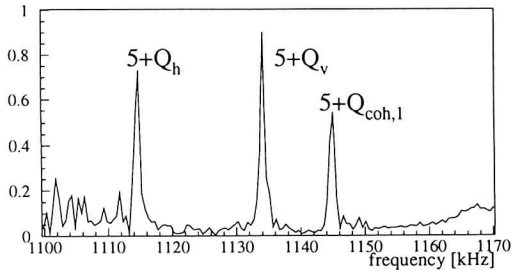

Figure 1: Measured frequency spectrum showing $5+Q_{\mathrm{h}}$ and $5+Q_{\mathrm{v}}$ normal betatron sidebands and $5+Q_{\mathrm{coh},1}$ quadrupole frequency.

Measurements [1] have been carried out at the heavy ion synchrotron SIS. Due to lack of beam pickups and exciter with quadrupolar symmetry needed already existing beam diagnostic instrumentation was used. We therefore have summed the signals on the vertical rsp. horizontal PU/exciter plates for the suppression of dipole modes and subtracted the two signals for the suppression of longitudinal modes. The measurement is of BTF-type with a excitation signal sweeping over the envelope oscillation frequencies and the response signal discriminated in the frequency domain.

The measurements have been made with a coasting Ne^{10+} beam at the injection flattop energy of 11.4 Mev/u with beam currents of up to 25 mA in order to obtain stong incoherent tune shifts. The beam current was monitored by a beam transformator coil. Quadrupolar mode oscillation frequencies have been successfully measured with typical sweep times of ~1 s and 40 dB rf power on the exciter. Fig. 1 shows a spectrum of a horizontal ($Q_{\mathrm{coh},1}$) mode sideband. As the beam is never perfectly centered neither in the pickup nor in the exiter, some other frequency lines appear at the dipole mode frequencies. The frequencies of the $Q_{\mathrm{coh},1}$ mode are strongly pronounced and comparable in signal strength to betatron sidebands of the dipole modes which are strongly suppressed by the detection scheme. $Q_{\mathrm{coh},2}$ lines are usually faint and broad and are not easily distinguishable from the background causing difficulties in locating them precisely. Computer simulations have shown that this is due to different hardware geometry and the much smaller vertical emittance as quadrupolar signals drop with distance and beam size.

Shifts of the quadrupole mode frequencies due to space charge forces have been observed (as shown in Fig. 2) clearly proving the nature of these lines. Systematic measurements with beam currents of up to 25 mA beam current (shown in Fig. 3) show a linear progression as predicted by theory. The gradient of the linear fit is a function

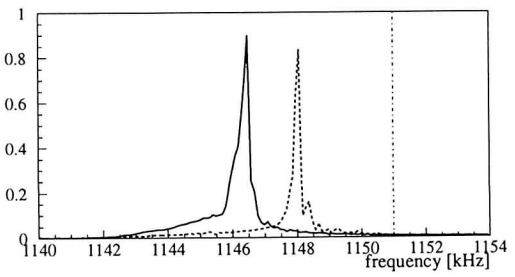

Figure 2: Frequency shift of a quadrupolar sideband $5+Q_{\mathrm{coh},1}$ due to space charge. The frequency shift corresponds to a reduction in beam current of 4.5×10^{10} (full line) to 2.9×10^{10} particles (dashed). The vertical line marks the position without space charge.

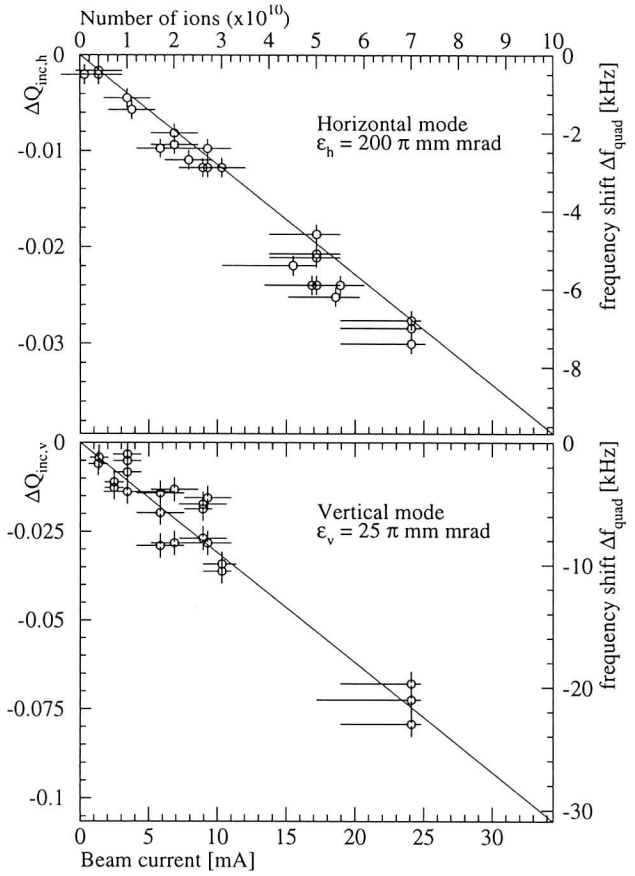

Figure 3: Measured frequency shifts of quadrupolar beam envelope oscillations in SIS with a coasting Ne^{10+} beam. Upper picture: horizontal mode, lower picture: vertical mode. The left axis shows the resulting (calculated) incoherent tune shift. The line is a fit to the data, representing beam emittances of $\varepsilon_h = 200$ mm mrad and $\varepsilon_v = 25$ mm mrad.

of the beam emittances in both planes and influenced by a geometric particle distribution factor for the incoherent tune shift. The obtained values for the beam emittances from the experimental data are in good agreement with expected values and emittance measurements assuming an almost homogeneous beam distribution function for this high current operation mode.

The scope of the SIS experiments in particular was to carry out a detailed comparison with computer simulation to reproduce the experimental data and clarify the relationship between coherent and incoherent signals. To that end we perform computer simulation with a particle in cell (PIC) code SCOPXY [4]. Coasting beams are simulated by following the trajectories of N macro particles in a two-dimensional (x–y) transverse field of a lattice and in the self-consistent electric field obtained by solving the Poisson equation on a grid with rectangular boundary condition. In order to determine the dominant eigenfrequencies of the system the electric potential of the beam is picked up at horizontal and vertical positions, which then are Fourier transformed.

Among the results we have found, for instance, that in spite of a spread in incoherent frequencies typical for

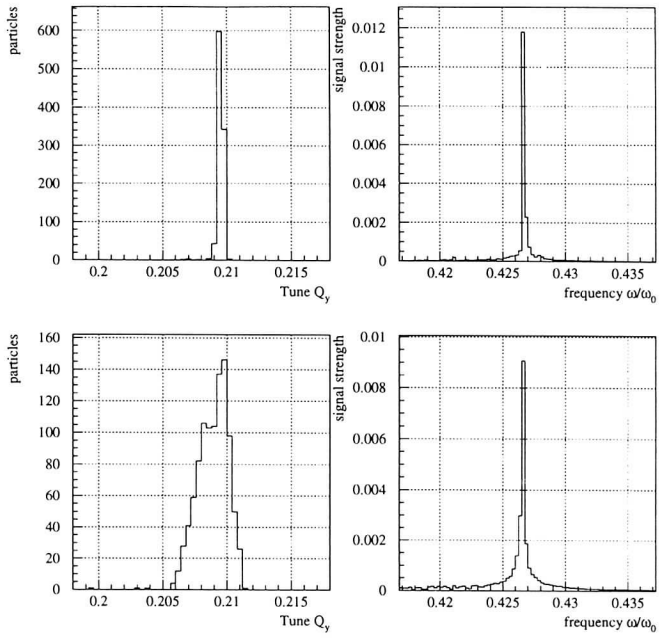

Figure 4: Comparison of a KV- (top) with a Waterbag-distributed beam (lower pictures) in the computer simulation. Left are the distributions of the incoherent tunes, the pictures to the right show the coherent quadrupolar frequencies (same frequency scale in all pictures).

non KV-distributions, there is no visible broadening of the coherent quadrupolar frequencies (which was claimed for the LEAR experiment [2]). This is shown in Fig. 4 which compares the single particle tunes and coherent quadrupolar oscillation lines of a space charge dominated KV- and Waterbag-beam.

References

[1] R. Bär et al., to be published in Nucl. Instr. Meth. **A**, 1998

[2] M. Chanel, Proc. European Particle Accel. Conf., Sitges, June 10–14, 1996, p.1015

[3] W. Hardt, On the incoherent space charge limit for elliptic beams, CERN internal report, ISR/Int 300 GS/66.2 (1966)

[4] I. Bozsik and I. Hofmann, Nucl. Instr. Meth. 187, 305 (1981)

A Warm-fluid Model for Longitudinal Instabilities

G. Rumolo*†, I. Hofmann*, G. Miano†‡

*GSI, *Gesellschaft für Schwerionenforschung, Darmstadt*

†*Dip. d'Ing. Elettrica, Università "Federico II" di Napoli*

‡INFN, *Istituto Nazionale di Fisica Nucleare, Sezione di Napoli*

The linear warm-fluid model for the longitudinal dynamics of a coasting beam hereafter proposed is able to accurately predict the rise time of a longitudinal instability and its slow wave frequency shift when the working point of the machine lies out of the stability region. This model takes into account the effects of the beam momentum spread by means of the fluid kinetic pressure.

After integration of the Vlasov equation for the beam longitudinal motion over the velocity space with the method of the distribution function moments, one obtains in the limit of adiabatic process (vanishing "heat flux") the following set of differential equations

$$\begin{cases} \frac{\partial \lambda}{\partial t} + \frac{\partial}{\partial s}(\lambda V) = 0 \\ \frac{\partial V}{\partial t} + V\frac{\partial V}{\partial s} + \frac{q}{\lambda}\frac{\partial P}{\partial s} = -\frac{q}{C_0 m^*}\phi(s,t) \\ \frac{\partial}{\partial t}\left(\frac{P}{\lambda^3}\right) + V\frac{\partial}{\partial s}\left(\frac{P}{\lambda^3}\right) = 0 \end{cases} , \qquad (1)$$

where the electric driving voltage $\phi(s,t)$, according to the sharp impedance formalism, can be expressed in the following way:

$$\phi(s,t) = \sum_m \dot{Z}(m\omega_0) I_m(t) \mathrm{e}^{-\mathrm{i}mk_0 s} + \phi_{\mathrm{ext}}(s,t) \qquad (2)$$

The impedance $\dot{Z}(\omega)$ seen by the beam consists in general of the space charge impedance of the beam itself and the impedance of its surroundings. For the ESR the only significant contribution to the impedance of the beam surroundings comes from the cavity [1].

If we linearize the Eqs. (1) (by assuming the small perturbations $\lambda = \lambda_0 + \delta\lambda$, $V = \delta V$, $P = P_0 + \delta P$), it soon becomes clear that the influence of the pressure term in the linear regime may be regarded as a further contribution to the space charge impedance seen by the beam. In other words, one could take into account the fact that our beam has got a finite spread in the velocities by considering in the classical fluid equations a modified space charge impedance in the form ($\mathrm{k}T_0 \stackrel{\mathrm{def}}{=} \Delta v_\sigma^2$):

$$X_{\mathrm{eq}} = X_{\mathrm{sc}} + X_{\mathrm{kin}} = X_{\mathrm{sc}} + 6\pi\frac{\mathrm{k}T_0}{qI_0} \qquad (3)$$

The well-known formulae for the evaluation of rise times and slow wave frequency shifts correspondingly to a given working point [2] remain applicable with the only difference that in the total impedance acting on the beam one must take into account the contribution of this "kinetic reactance", too. In Fig. 1 one might see how different the predictions of the fluid models with finite and with zero longitudinal temperature look like for the instabilities driven by cavity detuning at the ESR [3]. The very good agreement between warm-fluid model and PATRIC simulations shows the improvement introduced by such

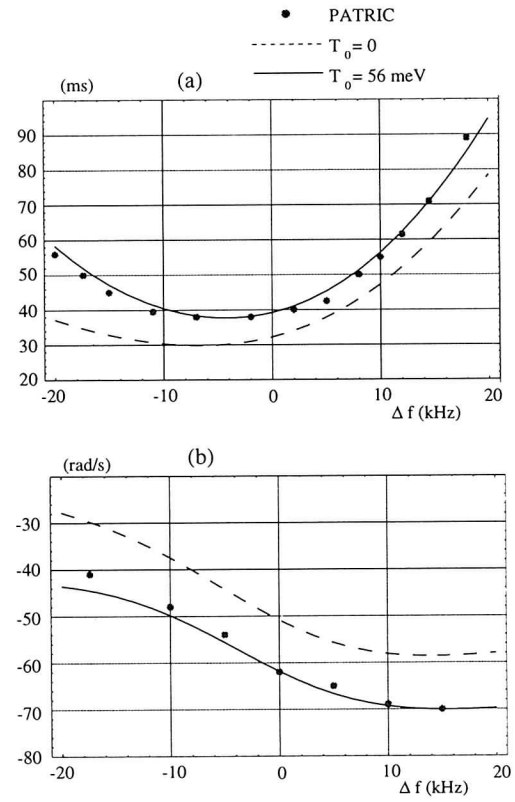

Figure 1: *Rise times (a) and slow wave frequency shifts (b) evaluated by means of the warm fluid model compared with those extrapolated from PATRIC simulations and those predicted by the cold fluid model.*

a model. After reminding the definition of Keil-Schnell impedance [2], it is possible to see that Eq. (3) can be conveniently rewritten as:

$$X_{\mathrm{eq}} = X_{\mathrm{sc}} + 3.1|\dot{Z}_{\mathrm{KS}}| \qquad (4)$$

Expression (4) clearly shows that for impedances which reach up to $10|\dot{Z}_{\mathrm{KS}}|$ (but larger than $|\dot{Z}_{\mathrm{KS}}|$ as the beam must be unstable), the effects of momentum spread must be always taken into account (via (3) or (4)) if we want to give a correct prediction of rise times and frequency shifts relative to beam instabilities.

References

[1] G. Kalisch: Dissertation **GSI**-Darmstadt 1993.

[2] M. Reiser *Theory and Design of Charged Particle Beams* (1994) 514-515.

[3] G. Rumolo, I. Hofmann, G. Miano and U. Oeftiger, to be published in Nucl. Instrum. Meth. (1998)

Off-Momentum Particle Dynamics for the HIDIF Telescoping Scenario

G. Franchetti, I. Hofmann

GSI, *Gesellschaft für Schwerionenforschung, Darmstadt*

In the HIDIF scenario the accumulation of the required total number of heavy ions is an important issue [1]. The linac beam is injected into storage rings by using a multiturn injection scheme suitable to avoid that the recirculating beam hits the septum [2]. In the HIDIF telescoping issue one option (not included in the standard scenario) for reducing the number of storage rings was the accumulation of ions with different longitudinal momentum in the same storage ring.

After injecting ions at the design momentum, new ions with $\delta p = \Delta p/p_0 = 0.01$ are injected. The space charge due to the bunched beam causes a tune shift in the off-momentum particle that in one turn could hit the septum. Here we present a preliminary investigation on the effects that the bunched beam has on the off-momentum particle. Since the off-momentum particle is moving fast with respect to the lattice, it feels in average a space charge force as if the bunch envelope weren't changed by the betatronic motion. Since the longitudinal dynamics is not considered we approximate the bunch shape to a frozen ellipsoid uniformly filled of ions, we neglect also the effect of the image charges. Under these guesses the three semi axes of the ellipsoid are kept constant. Horizontal and vertical size have the same value a and the longitudinal length c is assumed throughout to be $c > a$. The electric field E_x, E_y is found out by integrating the analytical expression [4] of the electric field generated by an ellipsoidal bunch. Since bunch reference frame is supposed orthogonal, in a bending magnet an error in E_x, E_y due to the geometric approximation is introduced. The analytic expression of the integrated transverse electric field is $E_x = M(x,y,z)x$ and $E_y = M(x,y,z)y$, where x,y and z are the transverse and longitudinal coordinates and

$$M(x,y,z) = \frac{qn}{2\epsilon_0}\frac{a^2}{c^2}\left[\frac{\beta}{\alpha(1-\alpha\beta^2)} - \frac{1}{2\alpha^{3/2}}\ln\left(\frac{1+\sqrt{\alpha}\beta}{1-\sqrt{\alpha}\beta}\right)\right]$$

$\alpha = 1-(a/c)^2$, $\beta = 1/\sqrt{1+s_0/c^2}$, n is the ions density, q the charge state and $s_0 = s_1\Theta(s_1)$ ($\Theta(s)$ is the Heavside function) and s_1 is the solution of the equation $(x^2+y^2)/(a^2+s_1) + z^2/(c^2+s_1) = 1$. We simulate the transverse electric field generated by the bunched beam on the off momentum particle with the field E_x and E_y generated by its nearest bunch. This approximation introduce a discontinuity in $\partial E_x/\partial z$, $\partial E_y/\partial z$ when the particle crosses the border of a bucket. We describe the transverse single particle dynamics in a magnetic lattice by using the micromap technique [3]. The final form of the transverse micromap is

$$\mathbf{x}(s+\Delta s) = L_{s,s+\Delta s}\mathbf{K}(\mathbf{x}(s)) + \mathbf{D}_{s,s+\Delta s}\delta p$$

where $\mathbf{K}(\mathbf{x}(s)) = (x, x' + \Delta s\tilde{f}_x, y, y' + \Delta s\tilde{f}_y)$, $\mathbf{x}(s) = (x,x',y,y')_s$, $\tilde{f}_\zeta = f_\zeta + qE_\zeta/(v_0p_0)$, $\zeta = x,y$ and v_0 is the design longitudinal speed, p_0 is the design momentum. $\mathbf{D}_{s,s+\Delta s} = (D_{s,s+\Delta s}, D'_{s,s+\Delta s})$ is a particular solution of the horizontal transverse equation of motion correspondent to the initial condition $\mathbf{x}(s) = 0$ and $\delta p = 1$. Assuming the single particle dynamics linear within one turn, we use each of the periods of the HIDIF ring to evaluate the tune. In one period the initial coordinates $\mathbf{x}_0$ are changed in $\mathbf{x}_1$ and in the next period they become $\mathbf{x}_2$. Since Courant-Snyder theory shows that the trace of the transfer matrix is $2\cos[\psi_x(l/3)]$ where $\psi_x(l/3)$ is the phase advance in one period, one finds $\cos(2\pi q_x/3) = 0.5(x_0x_2' - x_2x_0')/(x_0x_1' - x_1x_0')$ and then q_x. When $\delta p \neq 0$ the coordinates (x,x') are meant with respect to the new closed orbit. We considered the existing beam made of ellipsoidal bunches with transverse size of 2.5 cm and longitudinal length 17.36 cm filled with $1.32\cdot 10^{13}$ ions each with $\delta p = 0$. We choose the transverse size of 2.5 cm since considering a frozen ellipsoid the bunch feels an average beta function of $\beta_x = \beta_y \sim 11$ m. The ion dynamics has been computed with a micromap of length $\Delta s \sim 14.7$ cm. In order to check the code we have used first a constant focusing lattice of length $L = 442,8$ m and $q_x = 8.715$. A test particle with initial coordinates $x_0 = y_0 = 15$ mm and $p_{x,0} = p_{y,0} = 0$ mrad and $\delta p = 10^{-3}$ has been tracked for two overtaking evaluating the tune (Fig. 1a), we consider such an off-momentum as to show the physics involved in the process. The test particle moves from the border of the bucket and since it is far from the bunch it doesn't feel a strong space charge therefore the tuneshift is zero. Moving ahead the particle's motion begins to be effected by the bunch space charge that grows reaching the maximum when the particle enters inside the bunch. Since the electric field inside the bunch is linear the tuneshift $\Delta q_x = \Delta q_y = 0.0375$ is constant. Fig. 1b shows the tuneshift evolution for the test particle with $x_0 = y_0 = 50$ mm and $p_{x,0} = p_{y,0} = 0$ mrad and $\delta p = 10^{-3}$. Since the particle is outside the bunch the space charge is reduced and consequently maximum tuneshift ($\Delta q_x = \Delta q_y = 0.008$). The fluctuations at the values 0.2 and 0.65 ms are due to the nonlinearity of the space charge ($E_x \propto x/r$ where $r = \sqrt{x^2+y^2}$), they are reduced when the particle is far from the center of the bunch. Fig. 1c,d show the strong influence of the betatronic motion of the test particle on the evaluation of the tune for the HIDIF lattice. The tune behaves like Fig. 1b but now it depends on the initial transverse condition of the particle. The betatronic motion makes $\sqrt{\beta_x\epsilon_x}$ of the test particle oscillate each 11 m (β_x wavelength) while a,c are constant and the wavelentgh in space charge intensity is ~ 18.45 m. As consequence the tuneshift exhibits fast oscillation of amplitude proportional to the space charge and with wavelength $\propto \delta p$. The difference in the spread

of the tunes in the two planes is due to the effect of the bending. The same case has been considered for a test particle with $\delta p = 0.01$ in 20 overtaking (Fig. 1e,f). The tune oscillation for a strong off-momentum stays limited, the parabolic-like shape of Fig 1c,d is lost and the tune footprint (Fig. 1f) shows the spread of the tunes. The change of the dynamics due to the space charge on the off-momentum particle can be analyzed looking at the orbits on the Poincare´ section correspondent to the septum. We consider the $x - x'$ plane. The test particle with $\delta p = 0.01$ and initial coordinates $p_{x,0} = p_{y,0} = 0$ mrad, $x_0 = y_0 = 2 \cdot n, n = -50, ..., 50$ mm has been tracked for 20 turns (correspondent to $\sim$ 20 overtake). In Fig. 1g the continuous line represents the final position of the particle without the interaction with the bunched beam. The dashed line shows what is obtained when the effect of the bunched beam is included. The new closed orbit is in $x_{co} = D \cdot \delta p = 10.6$ mm ($D_x = 1.06$ m). Composing the average linear force generated by the lattice $-\bar{k}x$ with the centrifugal force due to the off momentum $\delta p/\rho$ one finds the equilibrium point x_{co}. The effect of the bunched beam moves the closed orbit outward. Considering these two contributions to the dynamics, the average potential V felt by the test particle is a parabola-like that in the bottom has either three stationary points ($\partial V/\partial x = 0$) two stable with one unstable in between (strong space charge) or simply one stable point (weak space charge). When the particle is injected on the closed orbit ($x = 0$), since this is not the closed orbit, the transverse oscillation has a different tune form $q_{x,0}$. As the initial conditions are moved outward ($x > 0$) we approach the minimum of the potential and beyond the same physical situation is repeated until $V(x) = V(0)$. Moving further outward the particle feels completely the nonlinearity of the space charge, this effect is shown in the big deformation of the dashed line in Fig. 1g. Furtheron the effect of the nonlinearity in the potential is reduced with respect to the quadratic-like shape and the deformation of the dashed line is reduced. Fig 1h shows the horizontal and vertical shift $\Delta x, y$ with respect to the unperturbed case, we see that for positive value of x the particle is beyond the septum since $x + y > x_0 + y_0$.

These results give a first indication that the space charge effect of the on-momentum beam on the off-momentum ions is significant. Hence a new optimization is required to make the off-momentum multiturn injection (nearly) loss free. Possibly the space charge effect could be reduced by choosing a lattice with a significant large dispersion.

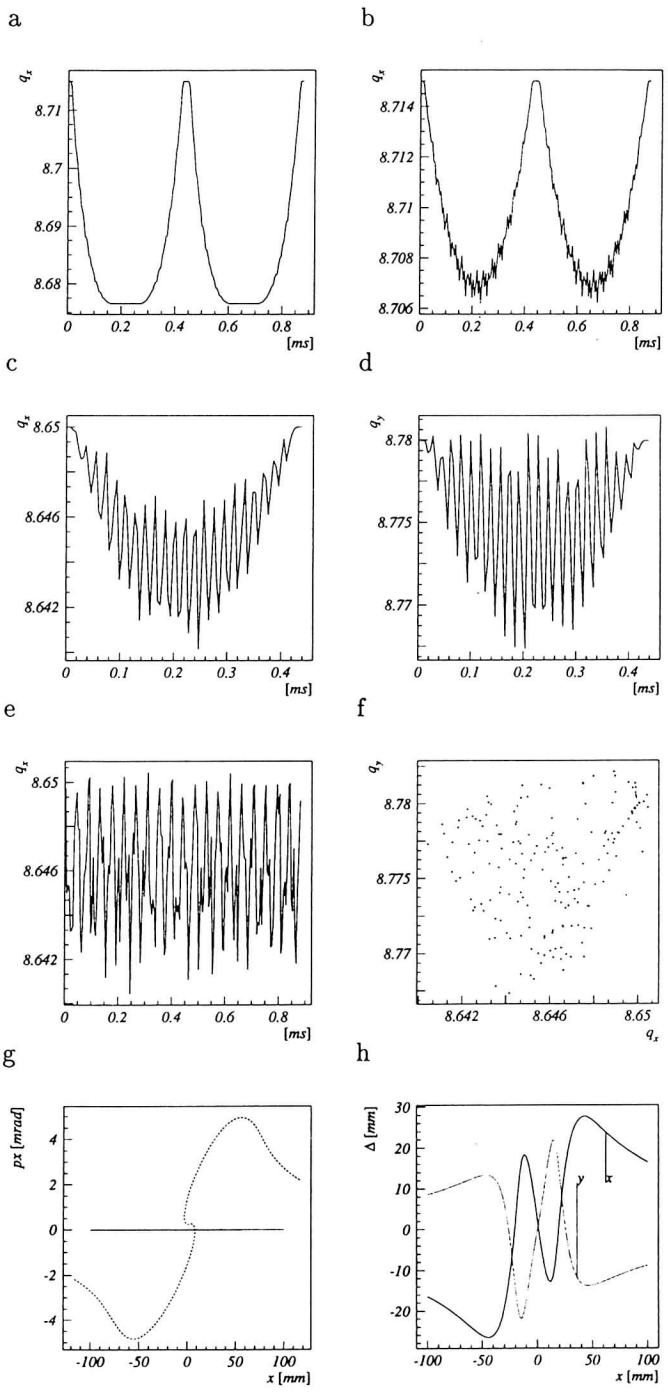

Figure 1: a) Tuneshift of a test particle crossing two bunches in a constant focusing lattice; b) Tuneshift of a test particle which is never inside any bunch; c) Tuneshift of a test particle in the HIDIF lattice; e) Evolution of the tuneshift in 20 turns; f) Tune footprint for the 20 turns case; g) Poincare´ section on the septum of a line of initial conditions for the test particle; h) Shift of the horizontal and vertical position with respect to the case without beam interaction (picture correspondent to the data of Fig. 1g).

References

[1] I. Hofmann, Proc. European Particle Accel. Conf., Sitges, June 10-14, 1996, p. 255;

[2] C. Prior et al., to be pubblished in Proc. XII Intern. Conf. on Heavy Ion Inertial Fusion, Heidelberg, Sept. 22-27,1997;

[3] G. Franchetti et al., to be pubblished in Proc. XII Intern. Conf. on Heavy Ion Inertial Fusion, Heidelberg, Sept. 22-27,1997;

[4] R.W. Garnett and T.P. Wangler, IEEE Particle Accelerator Conference, San Francisco, CA, May 6-9, 1991, IEEE, New York, p. 330.

Electron-Ion Transverse Instability in SIS(GSI) and TWAC

P.R Zenkevich
Institute of Theoretical and Experimental Physics, Moscow

The transverse coupling instability of a coasting circular beam due to an interaction with opposite sign particles stored inside the beam was examined in our previous paper [1]. This note is directed to estimation of the electron-ion instability thresholds for two facilities: 1) SIS (GSI); 2)constructed ITEP heavy ion complex (TWAC). The list of their parameters is given in Table 1.

Facility	*ITEP*	*GSI*
Kind of the ions	$^{59}Co^{27+}$	$^{238}U^{27+}$
Kinetic energy (MeV 1u)	677	11
Ring radius R (m)	40	34
Ion betatron frequency	9.7	3.4
Chamber radius (cm)	4	7
Horizontal beam emittance (mm·mrad)	80	100
Vertical beam emittance (mm·mrad)	50	25
Space charge transverse impedance $Z_{\perp}^{sc}(M\Omega/m)$	21.2	1100
Ion beam current (A)	50	0.1
Electron frequency	282	94.8

Table 1:

In accordance with paper [2] we introduce 'two-stream transverse impedance', which may be included in the standard scheme of transverse stability analysis [3].

A value of this impedance $Z_{\perp}^{1,2}$ depends on a form of the electron distribution function on the incoherent frequencies, 'space charge' transverse impedance of the ion beam Z_{sc}, beam neutralization degree η (η is a relation of the electron charge density to the ion charge density), beam size a , vacuum chamber radius b and relativistic factor γ. We limit ourselves to the simple case of 'hemicircle' distribution on electron incoherent frequencies: For this case two-stream impedance is defined by the following expression:

$$Z_{\perp}^{1,2} = -iZ_{\perp}^{1,2}\Lambda \qquad (1)$$

Here Λ is the pure real factor depending on the electron beam characteristics. We see that the electron-ion interaction results in appearance of the additional active impedance, proportional to pure imaginary space charge impedance. Factor Λ is defined by the formula :

$$\Lambda = \gamma^2 \frac{k}{\sqrt{1-k^2}} k = \eta \frac{1-a^2}{2(1-\eta)\Delta q/q} \qquad (2)$$

Here $\Delta q/q$ is the electron spread on the incoherent frequencies for the hemicircle distribution. For investigation of two-stream impedance influence on the stability threshold we used Gaussian ion distribution on the incoherent frequencies. Using Eqs. (1,2) and standard methods of stability analysis we calculated (for $\Delta q/q = 0.1$) a dependance of the ion momentum spread $\Delta p/p$ on η plotted in Fig. 1 .

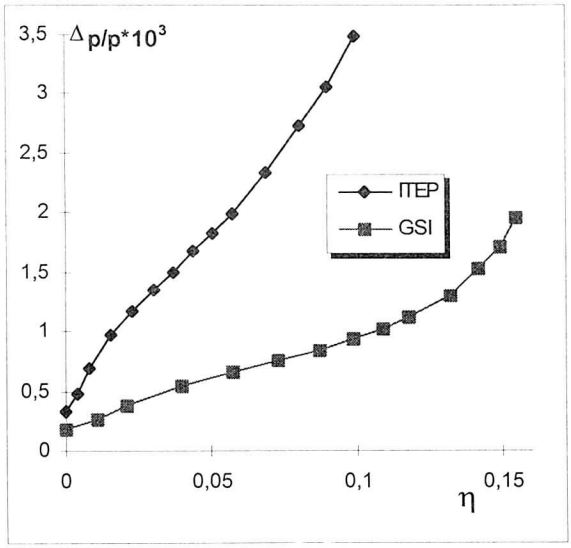

Figure 1:

We see from this figure that two-stream instability significantly enhanced the necessary momentum spread for comparatively small neutralisation degree. To avoid the instability we should decrease the electron concentration by reduction of pressure in the vacuum chamber, or by use of clearing electrons and (or) beam shaking. The alernate way for the instability subpression is a construction of high frequency damping system.

References

[1] P.R.Zenkevich and D.G.Koshkarev, 'Coupling Resonances of the Transverse Oscillations of two Circular Beams', preprint ITEP-1060 (1970); 'Particle Accelerators', 3 (1972), p.1

[2] P.R. Zenkevich, 'Transverse Impedance of the Circular Beam due to Two-Stream Instabilities, preprint ITEP6-98, Moscow, 1998

[3] B.Zotter and F.Zacherer, 'Transverse Instabilities of Relativistic Particles Beams in Accelerators and Storage Rings', CAS, CERN 77-13, p.175, Geneva, 1987

The Frankfurt Bismuth Source for HIDIF

M. Weber, K. Volk, P. Beller, R. Hollinger, A. Maaser, H. Klein
Institut für Angewandte Physik, University of Frankfurt

An ion source prototype has been developed for the conceptual design of a "Heavy-Ion-Driven Ignition Facility" [1]. Within the scenario, a beam with a current of 35 mA Bi^+ and low emittance have been demanded. Fig. 1 shows a schematic drawing of the ion source. The plasma generator is of the volume type and driven by an arc discharge between a tungsten cathode and the chamber walls which serve as an anode. The bismuth is supplied by an internal oven. A more detailed description is given elsewhere [2].

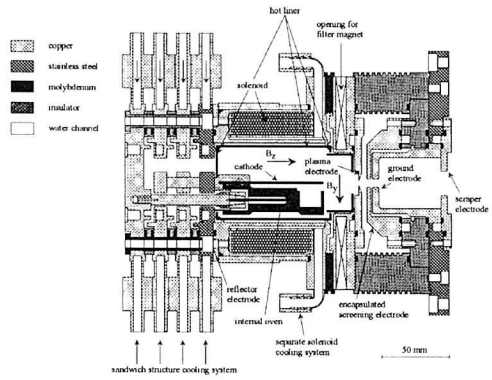

Figure 1: Schematic of the source and the extraction system.

Recall that with this ion source and a seven hole extraction system, a total current of 70 mA has been extracted with a fraction of singly ionized bismuth of 93 %. However, the relevant mode of operation for ion sources is the matched case, i.e. when the beam has the minimum divergence angle upon leaving the extraction system. It was determined (both experimentally and using the computer code IGUN ©R.Becker) for a Bi^+ current of 38.5 mA, well within the HIDIF requirements [3].

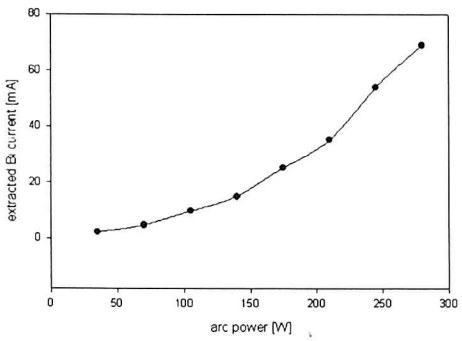

Figure 2: Bi current as function of arc power

At the same time, the ion source operates very power efficient, an arc power of less then 300 Watts is sufficient for a bismuth current of 70 mA. In Figure 2, the relation between arc power fed into the source and the extracted current is depicted. The arc power was controlled by leaving the arc voltage at a constant 30 Volts and tuning the arc current. The curve shows that the slope of this curve is increasing for larger arc powers.

Another crucial beam parameter is the emittance. Here, the HIDIF parameter list foresees a normalized rms-emittance of $\epsilon = \mathbf{0.04}\pi$ mm mrad. The measurement - on the other hand - is a difficult task because of the high power loads involved. Furthermore, even minor high voltage breakthroughs cause problems with the emittance measurement device. Nevertheless, the emittance (80 %,n,rms) of a 18.2 keV, 21 mA Bi^+ beam could be determined. As shown in Figure 3, it amounts to $\epsilon = \mathbf{0.067}\pi$ mm mrad.

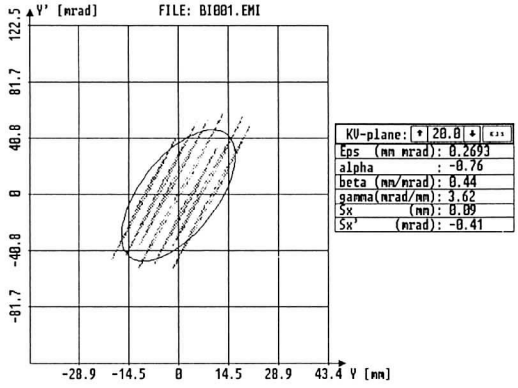

Figure 3: Emittance of a 21 mA Bi^+ beam at 18.2 keV beam energy

It is obvious that the emittance is dominated by the geometry of the multi aperture extraction system. For a single hole, it amounts to only $\mathbf{0.0043}\pi$ mm mrad. The design chosen for the used extraction system was rather conservative - seven holes, each with a diameter of 6 mm on a bolt circle of 20 mm. For example, the spacing between the holes is quite large to guarantee an appropriate lifetime disregarding the high thermal loads. Therefore, an extraction system with a "denser" arrangement has been built (smaller holes - 5.5 mm - and a bolt circle of 18 mm). From that, a further reduction of the emittance can be expected. In a subsequent step, the feasibility of this ion source for other elements will be tested. The reason is that the foreseen telescoping requires three different ion species which differ in mass between 2 and 10 %. Besides bismuth, possible candidates are mercury and rhenium, for example.

This work is funded by BMBF No. 06OF841.

References

[1] G. Plass and I. Hoffmann, Status of the HIDIF Collaboration, GSI-Report, GSI-96-02,(1996)

[2] M. Weber et al., Rev. Sci. Instrum., **69**, 1066, (1998)

[3] M. Weber et al., GSI-Report, GSI-97-08, 43, (1997)

First Results of the Two-Beam Experiment

H. Zimmermann, A. Firjahn-Andersch, A. Schempp, J. Thibus, E. Winschuh
Institut für Angewandte Physik, Johann Wolfgang Goethe-Universität
Frankfurt am Main

Because of the small values of the current limits of linear accelerators in the low energy part, Heavy Ion Inertial Fusion (HIIF) injectors start with a set of low frequency Radio-Frequency Quadrupoles (RFQs). For a higher ion energy, the frequency is increased to reach a better accelerator efficiency. The accumulation of ion beam current in such a driver linac is done by multiple stages of funneling: in each stage the accelerator frequency is doubled and the beams of two accelerators with 180 degrees phase shift are combined to fill all the r.f. buckets of the higher frequency accelerator stage. In the ideal case, there is no change of the emittance and the beam current and brightness are doubled [1]. While first funneling experiments have been done with systems of discrete elements like quadrupole-doublets and -triplets, debunchers, deflectors and bending magnets, we have proposed for the Heavy-Ion Driven Ignition Facility (HIDIF) the use of an accelerator structure which provides two beams within one cavity and a single r.f. deflector structure which bends the two beams to one common axis. In our experimental set-up we use convergent incoming beams and a short r.f. funneling structure, operating at low voltages, which will be placed around the beam crossing position. Figure 1 shows the experimental set-up of the experiment.

The modulated electrodes of the two-beam RFQ, shown in figure 2, have been mounted and aligned. With these electrodes a resonance frequency of 54.5 MHz, a Q_0-value of 1850 and an Rp-value of about 80 kΩm was measured. For high power tests and beam operation the 12 kW amplifier is in preparation. In first tests with a smaller amplifier, the RFQ has been operated with 400 W c.w. for several hours.

The measuring of the ion-sources has been finished. Fig. 3 shows a drawing of the multicusp ion-source. The emittances of the two ion-sources at a beam current of 0.8 mA, which scales to a beam current of 40 mA Bi^+, demonstrates Fig. 4. The difference between the emittances including the neutral beam is 0.5%. The comparison without the neutral beam indicates fig. 5. The ion-sources are mounted to the RFQ. They are ready to send the first beam into the RFQ.

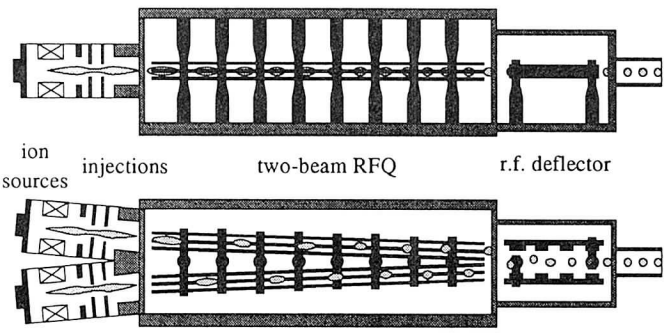

Fig.1: Experimental set-up of the two-beam funneling experiment.

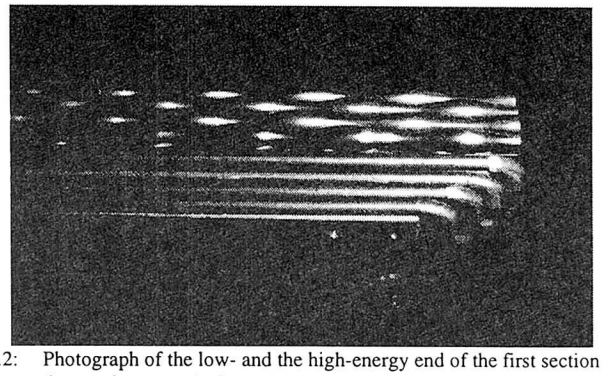

Fig.2: Photograph of the low- and the high-energy end of the first section of the two-beam RFQ electrodes.

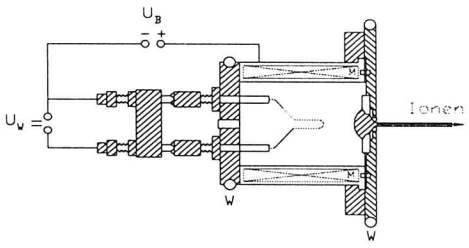

Fig.3: Scheme of the multicusp ion-source. U_w is the cathode voltage, U_B the arcvoltage, M are the magnets and W is the watercooling.

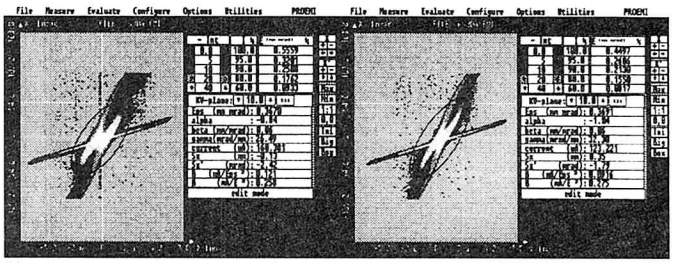

Fig. 4: Measured emittances of the ion-sources

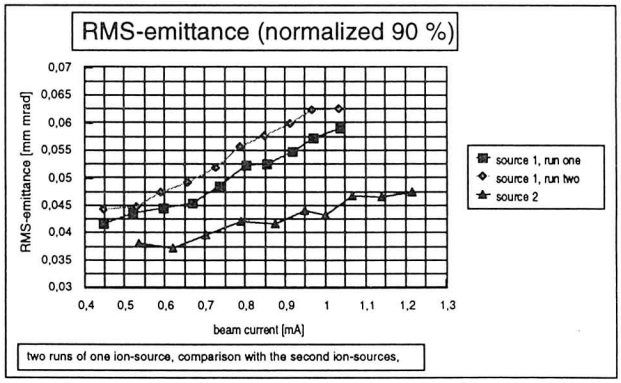

Fig. 5: RMS-emittance of the ion-sources, excluding neutral beam

References

[1] A. Schempp, A HIIF Funnel Injector System, GSI-Rep., GSI-95-06 (1995) p. 26

[2] A. Firjahn-Andersch, A. Schempp., J. Madlung, H. Zimmermann, "Progress of the Two-Beam Funneling Experiment",Proc. International Symposium on Heavy Ion Inertial Fusion, Heidelberg, Germany, 24.09.-27.09.1997

A Double Gabor Plasma Lens System for HIDIF

J. Pozimski, R. Dölling, A. Jakob, A. Lakatos, L. Wicke and H. Klein
Institut für Angewandte Physik der J. W. Goethe-Universität Frankfurt
60054 Frankfurt am Main, Germany

Transport of low energy high perveance ion beams is a crucial subject for a future HIDIF project. Electrostatic focussing systems suffer from the high beam energy, the space charge forces and the emittance requirements. Magnetic LEBT systems enable space charge compensated transport [1] but suffer from high ion mass (209 ± 10 %) and for pulsed beams from rise time of space charge compensation [2]. The strong cylindersymmetric electrostatic focussing of a **G**abor **P**lasma **L**ens [3] has experimentally and theoretically been investigated with encouraging results [4].

Numerical selfconsistent calculations of the charge density distribution in a **GPL** under assumption of an equilibrium state can be performed using a local radial enclosure criteria, thermalized electrons and longitudinal electron losses. The results of the calculations are in good agreement with beam measurements (He^+, 10 keV, 3.5 mA, $K=6.3*10^{-3}$). To extend the basis of experimental data to high ion masses at an RFQ injection energy of 206 kV and a beam current of 37 mA ($K=3.6*10^{-3}$) a **D**ouble **GPL** using the available solenoids in Frankfurt is under construction (see fig. 1).

Calculations of charge density distribution inside the new **DGPL** have already been performed. One result for an anode voltage U_A of 40 kV and a maximum B_z field of 0.2 T is shown in fig. 2. The predicted maximum net charge density of $\rho_{net} = 4.9*10^{-4}$ Cb/m^3 is able to focus a divergent (r=5 mm, r´= 50 mrad) Bi^+ beam of 156 kV and 26 mA ($K=4*10^{-3}$) and fulfil the injection requirements of an RFQ (see fig. 3) using a LEBT of appr. 30 cm length. The estimated emittance growth (normalized) due to lens aberrations (can be corrected by the lens geometry) and redistribution of beam ions due to space charge forces is $\Delta\varepsilon$=0.0065 πmmmrad.

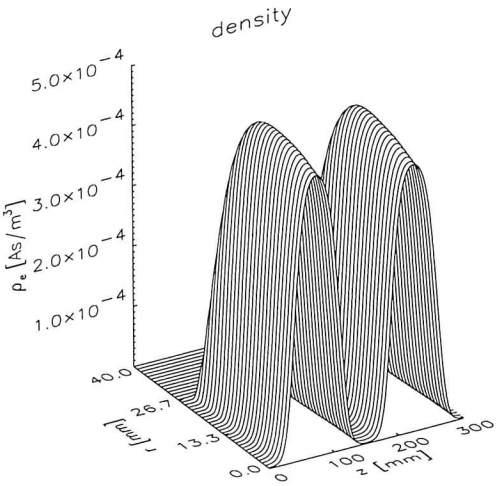

Figure 2 : Calculated net charge density distribution in the proposed double Gabor plasma lens for U_A = 40 kVand B_z = 0.2 T.

References

[1] R. Dölling, Dissertation, Institut für Angewandte Physik, Univ. Frankfurt (1994)

[2] A. Jakob, Proc. 17th. PAC conference (1997), Vancouver, Canada

[3] D. Gabor, Nature 160(1947) 89

[4] J. Pozimski, Dissertation, Institut für Angewandte Physik, Univ. Frankfurt (1997)

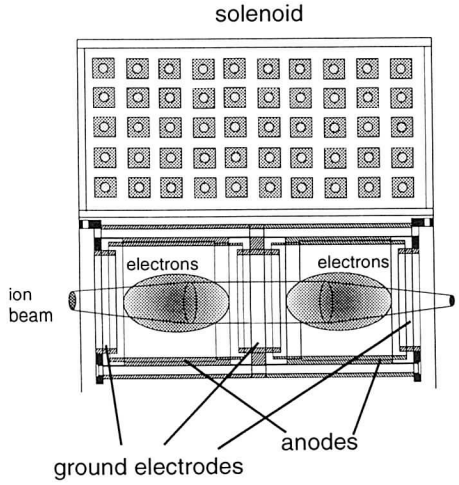

Figure 1: Set up of the proposed double Gabor plasma lens using solenoids available in Frankfurt.

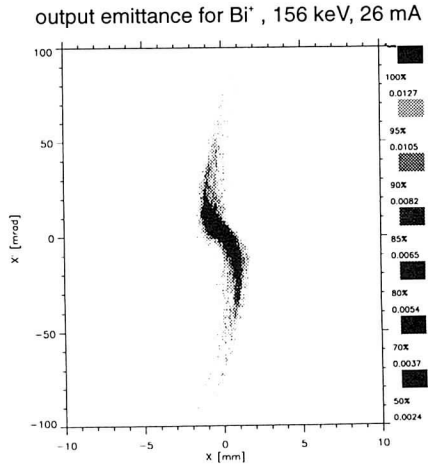

Figure 3: Calculated output emittance (normalized) at RFQ entrance for a Bi^+, 156 kV, 26 mA ion beam.

A Fast Pulsed Strip-Line Spectrometer for Plasma Physics Experiments

D. Varentsov[1], H. Eickhoff[2], U. Funk[2], P. Spiller[2], S. Stöwe[2]
[1]S.-Petersburg State Technical University, Russia
[2]GSI, Darmstadt, Germany

The energy loss and charge state distribution of the heavy ion beams interacting with dense plasma serves as an excellent diagnostic tool. The aim of this work is the development of a spectrometer for the experimental plasma physics activities at the GSI. The spectrometer will finally be installed behind the target which will be heated by the ion beam. By making use of a streak camera time-resolved energy loss and charge state distribution spectra will be measured.

The spectrometer is based on the a new generation of fast, high current pulsed magnetic lenses [1, 2]. With this type of lenses strong magnetic fields (exceeding several Tesla) and strong field gradients ($> 10^2$ T/m) can be achieved. The spectrometer consists of a capton foil with copper strip-lines glued on it (Fig. 1) and a drift space. The foil is wrapped around the plastic tube which is also used as a part of the beamline. The special layout of the copper striplines that are connected to the pulse power generator (30 kA and 10 kV) produces a quadrupole- and dipole field distribution.

The construction of the spectrometer is extremely unexpensive and compact: the length of the field region (both quadrupole and dipole) is 40 cm and the weight including the support devices is about 10 kg. This is of special advantage because of the limited spatial extension of the plasmaphysics experimental area at HHT.

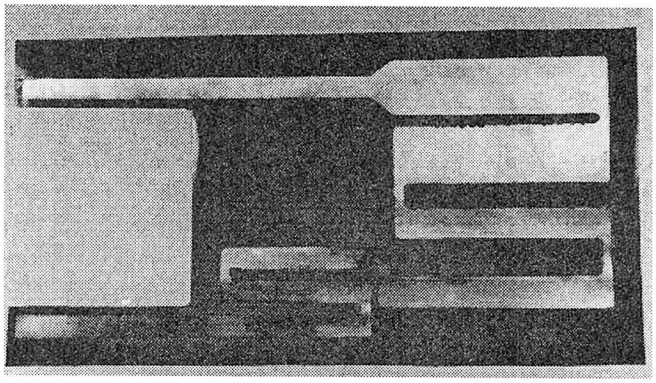

Figure 1: Stripline foil of the pulsed spectrometer.

A new ion optical simulation code was written based on differential algebra [3] formalism in order to simulate the beam dynamics. The simulation code called **DAVRAY** allows the computation of arbitrary order transfer matrices taking into account the 3D magnetic flux density distribution and fringing-field effects. With this code the spectrometer design and the stripline layout was optimized.

Two test experiments were performed with the spectrometer. In the first experiment the generated magnetic flux density distribution was measured inside the spectrometer by a small pickup coil. The result of these measurements shows only a small deviation from an ideal field distribution and is in a good agreement with the field simulations (Fig. 2). The electrical properties of the pulsed spectrometer were determined from the driving current pulse.

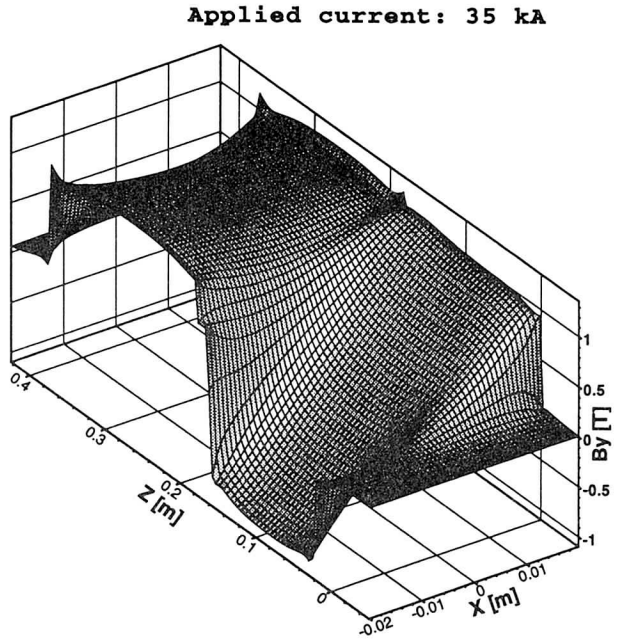

$\mathbf{B_y = B_y(x, z)}$ at $\mathbf{y = 0}$

Figure 2: The magnetic flux density inside the real pulsed spectrometer calculated by **FLUX** code.

The second experiment was performed with a $150 MeV/u\ Ni^{28+}$-beam. In order to test the spectrometer three aluminum targets with different thickness were installed on the beam axis. The energy loss of Ni-beam in these targets was calculated using the TRIM code. The deflection and focusing properties of the spectrometer were used to resolve the beam energies after the targets. The energy resolving power of the spectrometer was determined by the light emission of a fast plastic scintillator. The comparison of the obtained images with the results of ion optical simulations has demonstrated the accuracy of the code and proved the spectrometer's capability to resolve ion energies.

To achieve a higher resolving power we plan to improve the optical properties of the spectrometer construction by enlarging the deflection angle.

References

[1] P. Spiller et. al., GSI Report 1995(96), GSI-96-02
[2] M. Winkler et. al., GSI Report 1995(96), GSI-96-02
[3] M. Berz, Particle Accelerators, 24 (1989) 109

Ballistic Propagation in the HIDIF Target Chamber

J. D'Avanzo, I. Hofmann, P. Spiller - GSI Darmstadt

Final focusing and chamber transport are key issues in Heavy Ion Fusion as they determine the matching between the requirements needed on the fusion target and the beam parameters obtainable from the accelerator.

The power necessary to ignite a fusion target and to obtain a reasonable energy gain out of it ($\sim 500 - 1000$ TW) can be achieved by focusing on the target a high beam current ($\sim 50 - 100$ kA). Due to performance limitations in the storage ring and to beam transport and focusing, this current can be obtained by using a certain number of small emittance beams which are arranged in matrices at the entrance of the target chamber and then focused on each converter of the target (matrix focusing). The number of beamlines needed and the matrix geometry are directly dependent on the target design.

The high beam peak current ($\sim$ 1 kA per channel) and the relatively small target size (converter cross section ~ 9.1 mm^2 [1, 2]) considered for the HIDIF scenario can be responsible on one hand for space charge effects in a single beamlet, and on the other hand for beam-beam space charge effects within the individual matrices and for bundle-bundle mutual interaction as well. The latter depends on the overall target geometry. It is therefore necessary to understand if space charge effects along the HIDIF final focusing system and in particular in the target chamber are strong enough that beam charge neutralization has to be considered.

Our study is based on three main points: *a*) ballistic propagation, *b*) matrix focusing and *c*) beam-beam space charge effects. Here we overview the main results obtained. For details we refer to [3].

a) Estimates based on the envelope equation model and on 2D PIC simulations show that for HIDIF the upper beamlet current limit which allows ballistic transport is $\sim 1.2 - 1.4$ kA, larger than the beamlet peak current ($\sim$ 1 kA). Beam neutralization is therefore not a key issue for the HIDIF target chamber design.

b) Concerning matrix focusing, the main problem is to correctly focus all the beamlets within a matrix on the target in order to obtain the maximum beam-ion coupling. Small errors in aiming the target can cause in fact large losses in the transmission of the beam energy to the target.

c) The issue of beam-beam interaction within a matrix turns out to be negligible for HIDIF [4].

Here we show some results related to a HIDIF 3 m long drift length propagation in the target chamber. For details we refer to [4, 3].

Fig. 1 shows a 3×3 matrix as it enters the target chamber. This would the matrix geometry to be focused on one of the converters of the "octopus" target [1]. The distance between two neighbouring beamlets is 35 cm, which accounts for the realistic situation when stripline quadrupoles are used as the last lens in the HIDIF final focusing system [5].

In Fig. 2 the overall matrix transmission (continuous line) and the single beamlet ones (dashed lines) is plotted as a function of the drift length. The transmission is defined as the number of beam ions that hit the target, in this case the 9.1 mm^2 cross section converter. Notice that the whole bundle of beamlets is focused in the position where the transmission of the central beamlet of the configuration is maximum. Notice also that the overall transmission is a quite narrow function of position.

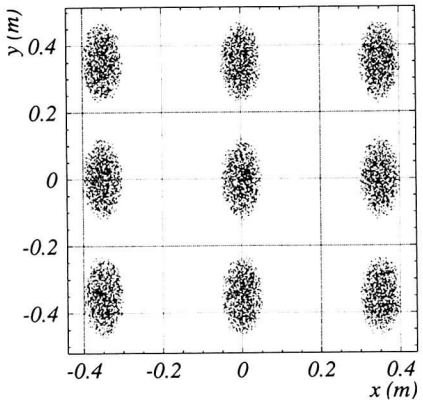

Figure 1: Example of beam matrix geometry as it appears at the entrance of the target chamber.

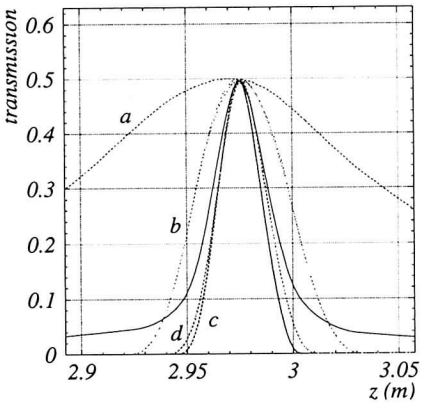

Figure 2: Particle transmission to the target for the matrix geometry shown in Fig. 1. Continuous line: overall matrix transmission; Dotted lines: single beamlet transmission: *a*) central beamlet; *b*) the two beamlets above and below the central one; *c*) beamlets at the four vertices of the matrix *d*) the two beamlets on its left and right side.

References

[1] M. Basko, Proc. of the "12th Int. Symp. on Heavy Ion Inert. Fus.", Heidelberg (Germany), Sept. 24-27, 1997;

[2] R. Ramis, as in [1];

[3] J. D'Avanzo et al., The HIDIF Interim Report (1998);

[4] J. D'Avanzo et al., as in [1];

[5] P. Spiller et al., Il Nuovo Cimento A **106** (1993) 1719.

Charge Dependence of Nonlinear Stopping Power

J. D'Avanzo, I. Hofmann - GSI, Darmstadt
M. Lontano - IFP, Milano

The interaction process between an ion (characterized by its velocity v_p and charge state Z_p) and a classical plasma (with unperturbed electron density n_0 and temperature T) is usually studied by defining the ion-plasma coupling strength $Z = Z_p/N_D$, where N_D is the number of electrons in the Debye sphere. The possibilty that heavy ions can reach high charge states [1] pushes effort in understanding the nonlinear regime of interaction, i.e. $Z \geq 1$, where the standard dielectric [2] and binary collsion [3] theories fail in their description.

Recent measurements [4] of the longitudinal stopping force dE/dx of medium and heavy ions in electron cooling experiments in a regine where $Z \geq 1$ show deviations from the predictions of the linear theories. For low ion velocities and high charge states these experiments show a scaling of dE/dx with the ion charge as $\sim Z^{1.7}$, weaker than the $Z^2 \ln Z$ dependence known from the theory. It is of interest to understand the origin of this deviation.

We study the interaction of a heavy ion with a classical plasma in conditions of strong nonlinear ion-plasma coupling by means of Particle-in-Cell (PIC) simulations in $r - z$ geometry.

Fig. 1 shows $(dE/dx)/Z^2N_D$ as a function of v_p/v_{th} for $Z = 10$. Our PIC results (filled rhombs) are compared with Vlasov simulations (open circles) (taken from [5]). In Vlasov simulations the nonlinear Vlasov-Poisson system of equations is solved within a splitting scheme. The dash-dotted line is a simple fit to the numerical results. The dieletric [2] (continuous line) and the binary collision [3] (dashed line) theories are also indicated for comparison.

In Fig. 1 we notice that when $Z > 1$ there is a big discrepancy between the numerical simulations and the linear theories. These latter overestimate the Bragg peak. Nonlinear collective plasma phenomena cause a reduction of the stopping power in the velocity range where the maximum energy transfer to the plasma target occurs. Notice also the good agreement between our results and Vlasov simulations. This proves that the lowering of the stopping power for $Z > 1$ is due to collective effects.

In Fig. 2 $(dE/dx)/Z^2N_D$ (in scaled units) is plotted as a function of Z, for different values of the ion velocity v_p. For high velocities ($v_p = 10v_{th}$) there is good agreement between dielectric theory and simulation, as expected. In fact even if $Z > 1$, the projectile interacts only with the tail of the electron distribution. The perturbation is weak and the linear theory applies. For low ion velocities ($v_p \leq 2v_{th}$) we find deviations from the $Z^2 \ln Z$ dependence due to the strong interaction with the bulk of the electron distribution. Our results show rather a scaling as $dE/dx \sim Z^{1.5}$, in agreement with the Vlasov simulations and close to the experimental data. This scaling law is due to nonlinear screening of the plasma free electrons nearby the ion core which causes a local decrease of the electron density and therefore a weakening of the stopping power [7].

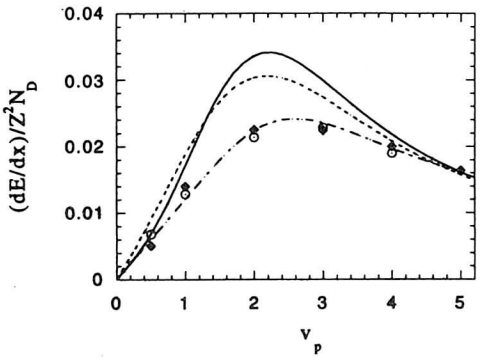

Figure 1: Normalized stopping power *vs.* the ion velocity v_p/v_{th} for $Z = 10$. Continuous line: dielectric theory [2]; Dashed line: binary collision theory [3]; Rhombs: PIC simulations; Circles: Vlasov simulations (from [5]); Dash-dotted line: numerical fit.

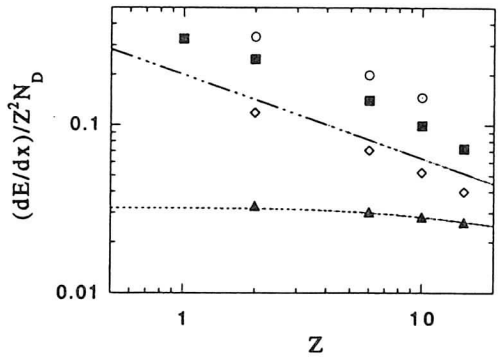

Figure 2: Normalized stopping power (in scaled units) *vs.* Z for different values of the projectile velocity. Circles: $v_p = 2v_{th}$; Boxes: $v_p = v_{th}$; Rhombs: $v_p = 0.5v_{th}$; Triangles: $v_p = 10v_{th}$; Dotted line: dielctric theory; Dash-dotted line: $Z^{1.5}$.

The authors acknowledge Dr. O. Boine - Frankenheim from GSI and Prof. P. F. Bortignon from the University of Milano for valuable discussions. This work has been partly developed in the Institute of Plasma Physics in Milano.

References

[1] J. Jacoby et al., Phys. Rev. Lett. **74**, 1550 (1995).
[2] Th. Peter et al., Phys. Rev. A **43**, 1998 (1991).
[3] P. Sigmund, Phys. Rev. A **26**, 2497 (1982).
[4] T. Winkler et al., Nucl. Instr. and Meth. A **391**, 12 (1997).
[5] O. Boine-Frankenheim, Phys. of Plasmas **3**, 1585 (1996).
[6] J. D'Avanzo et al., Phys. of Plasmas **3**, 3885 (1996).
[7] J. D'Avanzo et al., to be published in Nucl. Instr. and Meth. A (1998).

Propagation in FLIBE

J.L. Vay, C. Deutsch, LPGP, Bât. 210, Université Paris XI - 91405 Orsay

A/ PIC-Monte-Carlo Codes

In order to simulate the ion beam interaction with Flibe gas in reaction chamber, we have to take into account the random behavior of a collection of noninteracting particles (within themselves) with a background gas through short range potentials. Technically, those requirements are achieved by complementing the above PIC codes with a Monte Carlo (MCC) code [1-4]. PIC codes all share the same time step Δt. However, in MCC, every particle trajectory is independently tracked with its own Δt relying on its mean free path randomly sampled in terms of short ranged cross-sections σ_i. for the i interaction with species j with density n_j. Then, the corresponding mean free path is $L_{ij} = \ell / n_j \sigma_i$.

A beam ion with velocity V_b travels a distance $\ell = V_b \Delta t$ during time step $\Delta\tau$. Let R_0 a random number between 0 and 1, then the number N_{ij} of interactions experienced with species j writes as

$$N_{ij} = I_{nt}\left(\frac{\ell}{L_{ij}}\right)+1 \ , \ R_0 \le \left[\frac{\ell}{L_{ij}} - I_{nt}\left(\frac{\ell}{L_{ij}}\right)\right]$$

$$N_{ij} = I_{nt}\left(\frac{\ell}{L_{ij}}\right) \quad ,\text{otherwise} \qquad (1)$$

with $I_{int}(x)$, largest integer in x.

B/ Ionization Cross sections

Flibe gas consists of 90% Be F_2 and 10% LIF. It is produced by vaporization of the corresponding liquid shielding the chamber walls from the thermonuclear neutrons.

Typical parameters [1-3] for ion beam propagation in the reaction chamber are given in Table I. Here the heavy atomic species selected is lead, usually considered in heavy ion fusion scenarios andetty close to Pt. So, the beam-Flibe gas interaction is essentially monitored by Pb^+ stripping and BeF_2 ionization.

Table I- Beam characteristic for uncompensated transport in reaction chamber

Ion charge	+1
Ion mass	210 a.m.u.
Peak intensity	4.688 kA
Mean intensity	3.125 kA
Initial beam shape	revolution hyperellipsoid
Initial radius	5.2 cm
Thermal velocity	0.0001 c
Focalisation distance	2.6 m
Final radius	0.3 cm in void

Large uncertainties are still plaguing the corresponding cross sections. Hopefully, they have been recently re-estimated [4] out of the Pb ionization cross sections through BeF_2 and LiF collisions in a Thomas Fermi-type approach with appropriate pseudopotentials. Therefore, the present results for Pb do not differ by more than 7% from the Pt ones. A linear weighting procedure is used, keeping in mind that Flibe is made up of 90% BeF_2 and 10% LiF, yields a total gas ionization cross section that may be taken as

$$\sigma_{ion}^{gas} = 0.9\times\sigma_{ion}^{B_eF_2} + 0.1\times\sigma_{ion}^{L_iF} \qquad (2)$$

out of the linear approximations $\sigma_{ion}^{B_eF_2} = \sigma_{ion}^{B_e} + 2\sigma_{ion}^{F}$, and $\sigma_{ion}^{L_iF} = \sigma_{ion}^{L_i} + \sigma_{ion}^{F}$.

We found it here convenient to plot Flibe ionisation cross sections by stripped Pb^{n+} in terms of ionicity n (Fig. 1) in the range $(0.2\text{-}16)\times10^{-16}$ cm^2 with a 1×10^{-16} cm^2 step for five series of plausible initial atomic data. The quality of ion beam charge increases with Flibe gas ionization. A complete neutralisation is achieved for a beam radius $\simeq$ 2 mm. In this connection, it should be appreciated that the neutralizing electron background demonstrates a rather high mobility. Corresponding electron trajectories are constantly wiggling randomly around the ion beam. As a

consequence, the average electron beam radius appears significantly larger than that of the ion beam which explains that its neutralization can handly be a complete one.

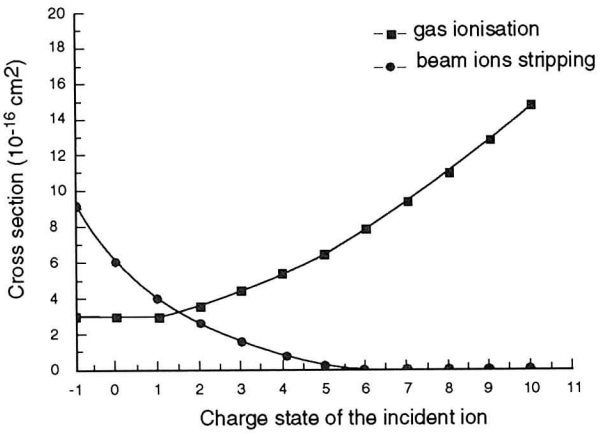

Figure 1- Flibe ionisation cross section in terms of projectile ionicity n with $Pb^{n+} + BeF_2 \rightarrow Pb^{n+} + e^- + BeF_2^+$, ion beam stripping cross sections in terms of ionicity n with $Pb^{n+1} + BeF_2 \rightarrow Pb^{(n+1)} + e^- + BeF_2$.

C/ Semianalytic model

In order to get a direct physical insight into the charge state dependence of ion beam focalisation, we consider a separate envelope equation for every ion beam ionicity with corresponding electron background. Gas ions taken as fully neutralized are thus excluded from the present treatment. So, the entire ion beam appears as a superposition of several coaxial subbeams (Fig. 2). Population N_i of i-cylinder (ionicity i) evolves in time according to the scheme

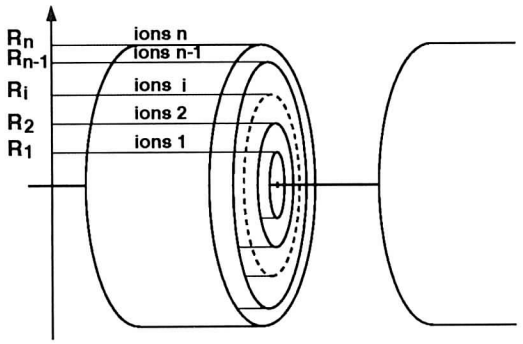

Figure 2- Envelopes model. Each cylindrical envelope is associated to a single ion beam charge state with its corresponding neutralization electron beam.

$$\bullet \quad \frac{dN_1}{dt} = -N_1 n_g \sigma_{St}(1 \rightarrow 2) v_{rel} \quad ,$$

$$\bullet \quad \frac{dN_2}{dt} = N_1 n_g \sigma_{St}(1 \rightarrow 2) v_{rel}$$

$$\bullet \qquad -N_2 n_g \sigma_{St}(2 \rightarrow 3) v_{rel}$$

$$\bullet$$

$$\bullet$$

$$\bullet \quad \frac{dN_i}{dt} = N_{i-1} n_g \sigma_{St}(i-1 \rightarrow i) v_{rel}$$

$$\bullet \qquad -N_i n_g \sigma_{St}(i \rightarrow i+1) v_{rel} \qquad (3)$$

in terms of Flibe gas density n_g and V_{rel}, relative beam-gas velocity. σ_{St} $(i \rightarrow i+1)$ accounts for the stripping of charge state i through collisions with residual gas. Then, a given beam charge state i may be given the envelope equation

$$\frac{\partial^2 R_i}{\partial t^2} = \frac{K_i}{R_i} + \frac{v_z^2 \varepsilon^2}{R_i^3} \qquad (4)$$

with V_z, constant longitudinal beam velocity, constant emittance ε and

$$K_i = \frac{iq}{2\pi\varepsilon_0 L m_0} \sum_{j=1}^{n} \left[q \cdot N_j \cdot (1 - f_j) \cdot \right.$$

$$\left. \cdot \begin{pmatrix} \left(\frac{R_i}{R_j}\right)^2 & , \; R_i \le R_j \\ 1 & , \; R_i \ge R_j \end{pmatrix} \right] \qquad (5)$$

sum of all electrostatic fields acting upon subbeam i where f_j denotes a j beam neutralisation factor.

Every subbeam is given same length L.

References

[1] J.L. Vay and C. Deutsch, *Fus. Eng. Des.* **32-33**, 467 (1996).

[2] D. Callahan, *Fus. Eng. Des.* **32-33**, 441 (1996).

[3] N. Barboza, *Fus. Eng. Des.* **32-33,** 453 (1996)

[4] J.L. Vay and C. Deutsch, *Phys. Plasmas*, **5**, 1180 (1998).

3 TARGET THEORY

3.1 Heavy-Ion Target Design and Simulations

3.2 Fast Ignitor and Laser Studies

3.3 Equation of State and Fundamental Plasma Physics

3 TARGET THEORY

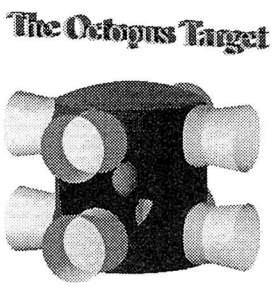

The discussion about acquiring a high-intensity laser system for GSI as well as the continued interest in the fast ignitor scenario have led to an increase in the laser-related contributions to the annual report, which take up almost half of the total. Target studies for heavy-ion beams are reported only in a small number of contributions motivated by the HIDIF study, while the rest of the work may be broadly classified as fundamental plasma physics and equation-of-state investigations.

3.1 Heavy-Ion Target Design and Simulations

A significant contribution by the Spanish-MPQ group is devoted to integrated simulations of a two-converter target, which is somewhat reminiscent of the old "Frankfurt target", but much more highly developed in detail. They show that sufficient symmetry can be achieved to make the target work, but the efficiency still needs improvement.
The Frankfurt group has performed studies concerning the "Octopus" target. A three-dimensional view factor simulation demonstrates ist high degree of symmetry even when the azimuthal symmetry is given up, but also shows the low efficiency of this approach. In a more fundamental analytic study the symmetry of irradiation in three dimensions by multiple beams was investigated in a more general setting than usual; new preferred beam arrangements and hints for the stability of the symmetry in a given geometry resulted. L. Vasina from Sarov also showed how to do view factor calculations more efficiently.
The simulation of experiments with simple cylindrical targets is still an important topic for experiment design and future planning at GSI, especially since it was seen that estimates, e.g., of the effective heating time based on the speed of sound are not very reliable N. A. Tahir and collaborators did a systematic series of studies for various beams and target materials. In related work the popular code "Multi 2D" that is being used for many such studies, performs quite well in comparison with the highly developed VNIIEF codes, at least in such simple situations.
A new result on ion beam-target coupling is presented by the Erlangen group, who report calculations of the transient effects in ion stopping, leading to a strong initial increase in the stopping power. Nersisyan and collaborators investigated ion stopping in magnetized plasmas and derive an energy loss that under certain conditions is many times that expected with the Bohr formula.

3.2 Fast Ignitor and Laser Studies

As mentioned above, these topics take up a dominating part of the contributions. It is fortunate that two competing codes can be used for calculations: the Vlasov code at TU Darmstadt and the PIC code at MPQ. New code developments include LPIC++ (MPQ), a one-dimensional PIC code written in C++ for optimum flexibility, and a tree code (Darmstadt) which allows a complete treatment of correlations and many effects neglected in other approaches but can be run only for small problems at present.

A number of contributions treat the interaction of the laser with the plasma. Ruhl studied the formation of wake fields and also found a surprising strong dependence of pulse transmission on the deformation in thin irradiated foils. The MPQ group, on the other hand, calculated the production of fast electrons and the associated nuclear radiation and investigated the case of intersecting laser pulses. They also extended the LPIC++ code for multiple ionization stages and the found the surprising and important result that strong ionization is generated at the rear surface of irradiated layers. A related study demonstrates the role of a strong azimuthal magnetic field in accelerating particles, while C. Deutsch shows important effects of correlations on the stopping of relativistic electrons in the compressed fuel.
A number of other contributions concern details of the processes caused by the laser in the plasma:breaking of electron plasma waves, the correct calculation of the Coulomb logarithm and the collision frequency, as well as the proper generalization of Ohm's law. Two reports concern the use of thin foil targets for generating very short pulses or harmonics.
Using a laser to accelerate a pellet to velocities of the order of 5×10^8 cm/s is a new idea proposed by Hain and Mulser that could lead to a new scenario of fast ignition by the impact of a macroparticle. Finally, Sheng and Meyer-ter-Vehn derived a solitary-wave solution for self-focussing of a laser.
The number and breadth of topics in these contributions show that laser physics at GSI can rely on solid theoretical support for future experimental programs.

3.3 Equation of State Theory and Fundamental Plasma Physics

Kemp and Meyer-ter-Vehn show that the MPQ implementation of the QEOS equation of state, which will certainly be important for simulations by many target theorists, gives good results for Hugoniot curves. The properties of Hydrogen under extreme conditions are studied in two reports: the Erlangen group report progress with the wave-packet molecular dynamics approach, while the Rostock group calculated the conductivity, reproducing the transition to metallic conduction.
The interest in the properties of strongly correlated plasmas has also remained constant and led to a variety of new results based on sophisticated many-body techniques. The groups in Erlangen, Greifswald, and Rostock studied such properties as the dielectric function, energy relaxation, and collective modes.

(J.A. Maruhn)

Target Design for HIDIF

R.Ramis[1], J.Ramirez[1], J.Meyer-ter-Vehn[2], and J.Honrubia[3]
1 - E.T.S.I.Aeronáuticos, Universidad Politécnica de Madrid, Spain
2 - Max-Planck-Institut für Quantenoptik, Germany
3 - DENIM, Universidad Politécnica de Madrid, Spain

INTRODUCTION

We present an indirect target designed specifically for the parameters proposed for the HIDIF. A number of beam lines incide on a closed cavity producing a cuasi-isotropic radiation field in its interior. This field drives the implosion, to ignition conditions, of a sphere filled with DT fuel situated inside the cavity. The analysis of such a target can be divided in two quite independent parts: the spherical capsule, and the cavity.

CAPSULE

The coupling between cavity and capsule is only through radiative transfer. This fact allow us to took as starting point one of the capsules proposed for the laser-driven NIF facility [1]. The capsule consists in a berylium shell with an external radius of 1.19 mm, 0.16 mm of thickness, and filled with 0.14 mg of solid DT forming a 0.05 mm shell; the central hole if filled with DT gat at 0.3 mg/cm^3. The required time depencence of incident radiation can be schematized (see figure 1) as follows. During the 80 eV prepulse (foot), a relativelly weak shock wave (1-4 MBars) tranverses ablator and fuel layers. After 5 ns, temperature increases smoothly producing additional shocks that converge in the inner surface of the fuel at 10 ns. This multishock compression guaranties the acceleration of the shell with low entropy. Finally temperature reaches its maximum (peak) at 13 ns accelerating the shell up to 300-350 Km/s. Ignition conditions are reached at 16.4 ns, and a yield of 16 MJ is produced. We perform systematic one-dimensional simulation of these processes by using our codes Multi-1D [2] and Sara-1D [3]. Figure 1 shows gain sensitivity on radiation temperature profile: continous line is the nominal profile, dashed lines produce marginal yield (1 MJ). After 15.5 ns, the nominal profile can be switched out without apreciable degradation of the yield. The required radiation fluence is 1.63 MJ/cm^2, and the absorbed energy by the capsule 170 KJ in agreement with available data in [1]. Influence of ablator doping on the fuel preheating is presented by a paper of J.J.Honrubia in this GSI report.

CAVITY ENERGETICS

The configuration we consider is schematized in figure 2: an axialy symmetric cavity with two oposite Be converters [5]. The irradiation is produced by two arrays of beam lines (each in a 4x6 matrix) arriving with an incidence of up to 30 degrees with respect to the axis [4]. Ions are Bi+ with 10 GeV, pulse duration is 4 ns FWHM and focus diameter is 4.2 mm. The irradiation conditions force us to use free expanding converters; hydrodynamic expansion will change the mass distribution inside the cavity as times goes on. We simulate this target with code Multi-2D [6],[7]. The present version includes tabulated equations of state (one temperature), electronic heat flux with a limiter, frequency integrated radiation transport with angular

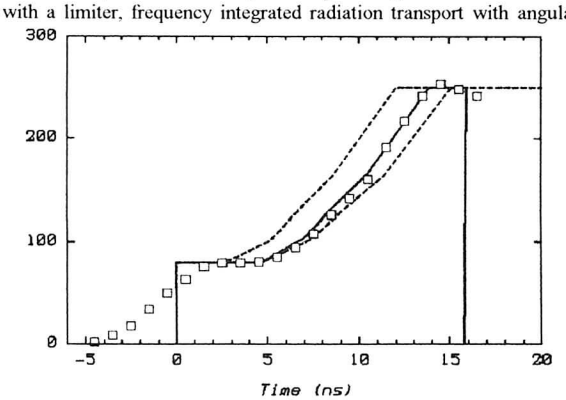

resolution, and lagrangian hydrodynamics with an non-structured grid formed by triangles. Ion beam beposition is modelled in a very crude way; range is assumed constant and equal to 0.1 gr/cm^2. Figure 3 shows grid and material evolution in a typical simulation. Succesive simulations are carried on with the following objetives:

i) Avoid direct irradiation of the capsule by the ions. This is accomplished by seting the thickness of a stopping gold shield to 100 microns and situating the beam envelopes below the border of this shield.

ii) Reproduce inside the cavity the nominal radiation temperature profile as close as posible. We divide the available energy of the beam in three groups (each with 4 ns FWHM) and adjust the relative delay and energy. This can be implemented in practice by designing the final bending lines with diferent lengths. Although the

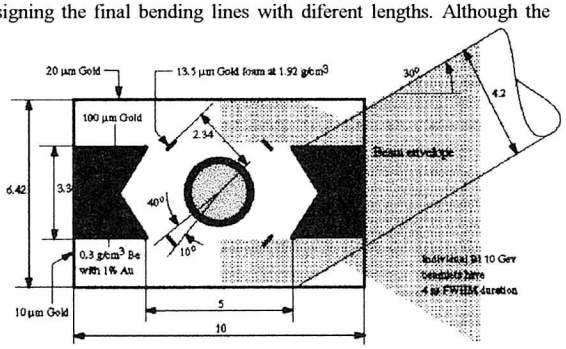

FUEL CAPSULE

0.98 mm DT gas at 0.3 mg/cm^3
0.05 mm DT solid (0.2 mg)
0.16 mm Be ablator dopped with Na and Br

PULSE SHAPING

Energy	Delay
0.46 MJ	-
0.46 MJ	8 ns
2.08 MJ	13.75 ns

prepulse can be adjusted easily, the reachable peak radiation is limited by the total available energy. Around nominal design, 25 KJ are needed to increase peak temperature 1 eV. Figure 1 shows as dots the temperature profile reached in the 2D simulations in comparison with the nominal one.

iii) Optimize. For a given input energy, the peak radiation temperature in a fixed point inside the cavity gives a good measure of the coupling efficiency. We perform its optimization by variing the following parameters: thickness of gold at entrance of beams (optimum ~ 5 microns), cavity diameter (optimum ~ 6.5 mm), converter density (optimum <0.33 g/cm3), and converter doping with gold (optimum > 1%). Due to the relative large CPU time (1-2 hour each run), we changed only one parameter at time and perform its

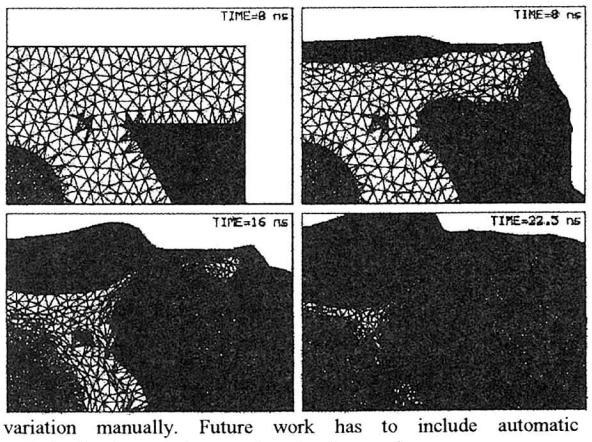

variation manually. Future work has to include automatic optimization in several parameters simultaneously.

iv) Sensitivity to physical parameters. Values of gold opacity (based on [8]), and ion range, are subject to big uncertainties

or order unity. First we decrease/increase a factor 2 the opacity we are using. That decreases/increases the peak temperature about 20eV. To compensate this effect, the input energy would have to be changed from 3 MJ to 3.5 MJ/2.5 MJ. We consider also ion ranges from 0.06 to 0.12 g/cm2, variations in this case are smaller than 8 eV.

IMPLOSION SYMMETRY

A cavity with high-Z walls produces intrinsically a very symmetric radiation field in its interior. Newertheles this can be not enough to fit the requeriments of capsule implossion. The radiation is initially produced in beam heated matter: converters and their neighbourhood. Reemision transfers energy to walls around the capsule. Because converter and capsule zones are coupled through an annular hole, more intensity is received by the capsule at a polar angle of about 45 degrees. To compensate this fact we introduce symmetry shields around the capsule at this angle. We can control low legendre modes is two ways: mode l=2 by changing sligtly the aspect radio of the whole cavity, mode l=4 by changing the thickness of the symmetry rings. We monitor the position of the fuel-ablator interface as a function of time and develop it in Legendre series. The resulting values gives a good idea of pressure non-uniformities integraded in time. Figure 4 shows legendre coefficients at one half of initial radius as a function of control parameters (normalized values can be obtained by taking into account that initial capsule radius is 0.119 cm). Both modes can be canceled by choosing a cavity diameter of 0.64 cm and a shield thickness of 0.0019 cm. The residual asymmetry is around 0.7 % RSM. This is due partially to higher Legendre modes, but also to the accuracy of the code (due to the limited number of directions taken into account in radiation transport, and to grid non-uniformities).

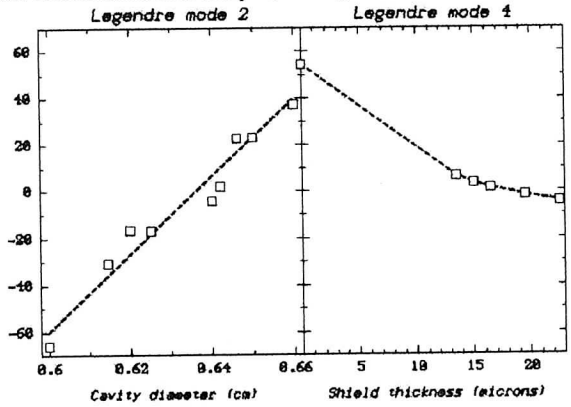

ION BEAM DEPOSITION

Alfer the design has been adjusted we realize that only a relativelly small part of beam energy (30 %) is deposited in the Be converters. The rest is dumped into stopping shield (32 %), entrance walls (20 %) and lateral walls of the cavity (18 %). The target designed initially with "localized converters", is working in fact as a "foam converter", with the ablated plasma playing the role of the foam. This sugest to evolve the actual design adding Be foam also in other parts inside the cavity.

CONCLUSIONS AND FUTURE WORK

The presented target configuration is working with the current physical and mumerical modeling. Future improvements on both will surelly change the current design point. The inmediate changes to be done are:

i) Use more realistic stopping power for ions, including range shortening.

ii) Use a gausian transversal profile for ion beams, instead a "top hat" profile.

iii) Put material converter also inside the cavity. This will give additional parameters to be optimized and to be used to control symmetry.

iv) Improve hydrodynamics and radiation transport, so that numeric and physical non-uniformities can be apropriatelly separated.

v) Use multigroup transport.

ACKNOWLEDGMENT

This work has been partially supported by the Comisión Interministerial de Ciencia y Tecnología of Spain

REFERENCES

[1] J.Lindl, *The Physics of Plasmas* **12**, 3933, (1995).

[2] R.Ramis, R.Schmalz and J.Meyer-ter-Vehn, *Computer Physic Communications*, **49**, 475, (1988)

[3] J.J.Honrubia, *Journal of Quantum Spectroscopy and Radiation Transfer* **49**, 491, (1993)

[4] P.Spiller, *Optics of Final Beam Transport and Focusing for HIDIF, Proc. of the 12th Int. Symp. on Heavy Ion Inertial Fusion*, Heidelberg (Germany), Sept. 24-27, (1997)

[5] R.Ramis et al. *"HIF target design", Proc. of the 12th Int. Symp. on Heavy Ion Inertial Fusion,* Heidelberg (Germany), Sept. 24-27, (1997)

[6] R.Ramis and J.Meyer-ter-Vehn, *A Computer Code for Two Dimensional Radiation Hydrodynamics,* Report MPQ-174, Max-Planck-Institut für Quantenoptik, Garching (Germany), (1992)

[7] J.Meyer-ter-Vehn, J.Ramirez and R.Ramis, *Fusion Engineering and Design.* **32-33** (1996) 585-593

[8] - WorkOp-II:94, *Third International Opacity Workshop and Code Comparison Study*, Report-204, Max-Planck-Institut für Quantenoptik, August 1995.

Three-dimensional Viewfactor Simulations for the Octopus Target

K.-J. Lutz, F. Illenberger, and J. A. Maruhn
Institut für Theoretische Physik der Johann Wolfgang Goethe-Universität, D-60054 Frankfurt a. M.

The symmetrical implosion of a spherical shell of D-T-fuel comprises the central issue of a working ICF target. As indirect drive targets with a small number of converters usually need a number of radiation shields to guarantee initial symmetrization (which may be spoiled by hydrodynamical expansion of the target components), different concepts using a larger number of converters are of interest now.

One of the prime candidates for such a hohlraum target is the so-called 'Octopus'-Target which has been proposed (in different versions) in ITEP and VNIIEF, consisting of two rings of converters in an almost cylindrical hohlraum illuminating a pellet with 1.11 mm radius, resembling the NIF-target (see fig. 1 for a schematical overview).

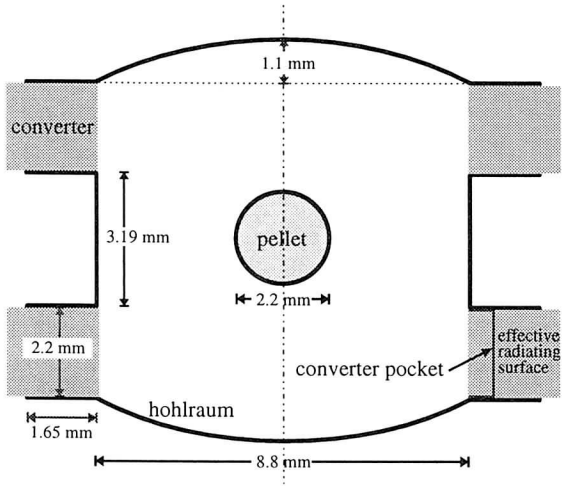

Figure 1: Schematical overview of the Octopus ICF target used in the simulations

In our simulations we use the 3D-viewfactor code HOLCON [1] which is capable of simulating arbitrary 3D configurations. While the Octopus target is 'almost' axially symmetric, the effect of the discrete converters is important as it feeds nonaxial asymmetry modes into the hohlraum. As there are no radiation shields inside the hohlraum target, the effect of hydrodynamical expansion on the applicability of the statical results is diminished. Even the severe expansion of the – optically thin – converters may be neglected as the effectively radiating surface may be controlled – e. g. by proper choice of the material density – to stay in a constant position through time.

We use the model of Basko [2] for the reemission of the walls. The source x-ray radiation pulse which is uniformly radiated by all converter surfaces consists of a 10 ns prepulse, followed by an exponential rise of 5 ns length to a 2 ns main pulse with tenfold power compared to the prepulse.The total energy injected into the target is 1.2 MJ. The hohlraum length is adjusted to give best symmetrization – the converters are not exactly placed in the minima of the quadrupole mode.

Fig. 2 shows the time evolution of the root-mean-square (rms) and the peak-to-valley (ptv) asymmetry of the absorbed flux on the pellet's surface for a target with four converters per ring. The solid lines include all spherical harmonics modes while the dashed lines are restricted to the modes with $l < 7$. Even for the full expansion, the rms-asymmetry stays well below 1 % in this case after the initial heating up. The difference to the modified case shows that most of the asymmetry is carried in higher modes which are more sensitive to numerical noise and cannot be readily resolved with the number of area elements feasible in three dimensional simulations.

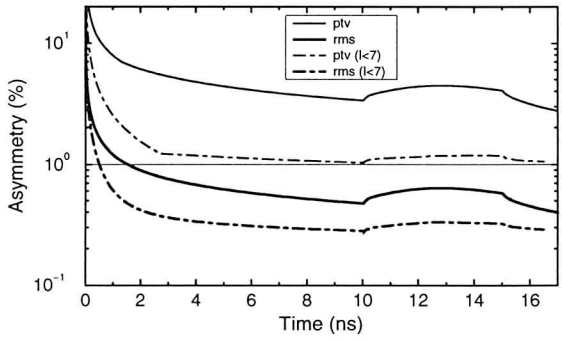

Figure 2: Time evolution of the rms- and the ptv-asymmetry of the absorbed flux on the pellet surface

The efficiency of such a hohlraum target is quite poor (see fig. 3. The integrated transfer efficiency – the time dependent ratio of the energy absorbed on the pellets surface to the total energy injected so far – stays well below 15 % in this case. Even by bringing more energy into the hohlraum, the efficiency is enhanced by a small amount only.

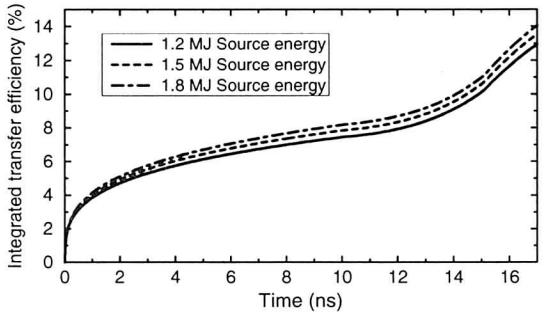

Figure 3: Time evolution of the integrated transfer efficiency to the pellet

While the octopus target may give an opportunity for a test installation target as its illumination seems to be manageable, its bad performance seems to exclude it from application in a fusion power plant. Reduction of the hohlraum size may enhance the transfer efficiency, but symmetrization is accordingly reduced.

References

[1] K.-J. Lutz, Inaugural-Dissertation, Frankfurt a. M. 1998

[2] M. Basko, *Phys. Plasmas* **3**, 4148 (1996)

Beam Irradiation Symmetry in 3-Dimensional Configurations

J. A. Maruhn, K.-J- Lutz, F. Illenberger, and S. Bernard
Institut für Theoretische Physik, Universität Frankfurt

Recently target designs based on a larger number of beams have been considered as alternatives to the simpler situation of essentially two-sided illumination. Examples are the target proposed by the VNIIEF group, the *Octopus* target and the P2 and P4 configuration proposed by Basko. The optimum polar angles of the beam groups in these cases are based on simple symmetry arguments using an expansion of the deposited energy into Legendre polynomials or spherical harmonics. In this work we have reexamined the mathematical foundations of such arguments and investigated their limitations. It should be pointed out that the basic mathematics has been described before (see, for example, [1]); this work adds some additional information and critical comments.

In a general 3-dimensional situation the expansion of the beam intensity $f(\theta,\phi)$ into spherical harmonics with coefficients given by

$$\alpha_{lm} = \int f(\theta,\phi) Y^*_{lm}(\theta,\phi) \mathrm{d}(\sin\theta)\mathrm{d}\phi \qquad (1)$$

is the natural way to analyze symmetry. It should be noted, however, that while the angular momentum l groups the amplitudes into invariant subspaces, for the stability of compression the wave length of the perturbation on the surface of the pellet is the important quantity, and this is shortest for the components α_{l0} and $\alpha_{l,\pm l}$. Systematic studies of the stability with respect to arbitrary combinations lm are not yet available.

Point Beams: for an ideally thin beam impinging of total intensity A_i along the direction (θ_i,φ_i) the intensity if given by

$$I_i(\theta,\phi) = A_i\, \delta(\cos\theta - \cos\theta_i)\delta(\phi - \phi_i \qquad (2)$$

and for a number of such beams trivially leads to amplitudes

$$\alpha_{lm} = \sum_i A_i Y^*_{lm}(\theta_i,\phi_i) \cdot \qquad (3)$$

This already gives the simplest initial consideration: the beams should be arranged such that the sum of the spherical harmonics over the beam directions, weighted with the beam intensities, vanish for as many moments as possible.

Beam Bundles: usually beams will be arranged in *bundles* of equally intense beams under the same polar angle but spaced evenly in azimuthal angle. Performing the sum of the spherical harmonics over the bundle leads to the simple result that such a bundle contributes only to $m=0$ and for m a multiple of the number of beams in the bundle. In a situation where the lowest nonvanishing amplitude is at angular momentum l, it is thus reasonable to take l (and only l) beams also in each bundle.

Polyhedral Configurations

The following table shows the amplitudes for the configurations corresponding to beams impinging in the geometry of the regular polyhedra. The numbers given are the invariant amplitudes

$$\sum_m |\alpha_{lm}|^2 \Big/ N, \quad \text{N=total number of beams.} \qquad (4)$$

For comparisons the *P2* and *P4* configurations are also shown.

l	3	4	5	6	7	8
Tetrahedron	7.00	5.41	0	8.03	8.40	3.11
Cube	0	8.12	0	4.52	0	10.50
Octahedron	0	5.41	0	8.03	0	3.11
Dodecahedron	0	0	0	8.48	0	0
Icosahedron	0	0	0	4.71	0	0
P-2	0	4.14	0	2.84	0	2.23
P-4	0	0	0	0	0	4.27

Table 1: Invariant amplitudes for the regular polyhedra and the P2 and P4 targets.

It is noteworthy that while the regular polyhedra seem the mathematically most satisfying symmetric configurations, the possibility of using beams of different intensity opens an additional parameter space that allows much more general situations.

Sample Configurations: it is now a simple matter to study a number of highly symmetric configurations under various assumptions about the number of bundles and their relative intensities. The principle is simply that the number of free parameters equals the number of multipoles that can be made to vanish. In all cases, the situation is assumed symmetric about the equatorial plane, which makes the odd multipoles vanish trivially. Thus, for the P4 configuration, there are two free angles and one intensity ratio, so that one may try to have the amplitudes for l=2,4,6 vanish. In the following, for each such configuration we give the bundles above the equator only, with the angle relative to the equatorial plane and the percentage of the total intensity allocated to each bundle. The total number of beams N is based, however, on the full space and assumes that the number of beams in each bundle is equal to the lowest$l$ with nonvanishing amplitude, which is denoted by $l_{\min}$

- *P2:* in this case one bundle is located at the zero of Y_{20}, i.e., at 35°. $l_{\min}$ =4, N = 8.
- *P4:* two bundles with adjustable intensity ratio. The optimal configuration is 60° (34%) and 20° (66%). $l_{\min}$ =8, N = 32.
- *P4':* also with three free parameters, like P4, but replaces intensity ratio by an additional beam bundle. Bundles at 60°, 25°, and 15°, all of same strength. $l_{\min}$=8, N = 48.
- *P3:* this is intermediate between P2 and P4: two bundles of equal intensity. Angles: 53° and 11°, $l_{\min}$ = 6, N = 24.
- *P3':* here the intensity of the two bundles was allowed to vary in order to get the beams as close to the equatorial plane as possible, while staying with $l_{\min}$=6. The bundles result as 51° (55%) and 2.4° (45%), N = 24. This shows that free parameters can be used to fulfill other conditions than symmetry requirements, for example to produce a more easily realizable beam arrangement.

- *P5:* three bundles with variable intensities at 69° (17%), 41° (36%), and 14° (47%). The five parameters allow l_{min}=12 while $N = 72$.

These examples have shown that it is easy to calculate the optimum configuration under a variety of subsidiary conditions, taking into account technical constraints in addition to the symmetry desiderata.

Stability: one aspect that has received little attention up to now is the question of stability. Since nonlinear effects (see below) may distort the optimum angles, it is important to check how critical the precise positioning of the beams is. To that end we have investigated the stability of the P4 configuration with respect to small changes of 1° in the bundle angles and to changing the intensity ratio from 1.87 to 2 (which may well be desirable for technical reasons). The results are given in Table 2, and show that the amplitudes (for the magnitudes, cf. Table 1) do change quite drastically even under such small perturbations. This clearly indicates that the mathematical theory presented here must be supplemented by more detailed numerical studies.

Amplitudes	l=2	l=4	l=6
$\Delta\theta_1$=1°	0.15	0.31	0.18
$\Delta\theta_2$=1°	0.10	0.29	0.46
Ratio→2	0.11	0.00	0.11

Table 2: multipole amplitudes for small perturbations in the P4 configuration. For the unperturbed configuration all these amplitudes vanish.

Extended Beams: of course a point beam is too idealized a situation. For an extended beam, the analysis may be carried over quite simply *under the assumption of linearity*, i.e., if the intensities of overlapping beams may be added up. A single beam of cylindrical symmetry in itself and impinging along the z-axis may be expanded according to

$$f(\sin\theta) = \sum_l f_l Y_{l0}(\theta) \tag{5}$$

It may be rotated to an arbitrary direction using Wigner matrices, which in this case reduce to spherical harmonics. If the beam direction is (θ',φ'), the resulting distribution on the unit sphere may be expressed as

$$f(\theta,\phi) = \sum_{lm} f_l \sqrt{\frac{4\pi}{2l+1}}\, Y^*_{lm}(\theta',\phi') Y_{lm}(\theta,\phi) \tag{6}$$

This is identical to the contribution from a point beam, Eq. (3), except that for each angular momentum the amplitude is multiplied by a *form factor*

$$c_l = f_l \sqrt{\frac{4\pi}{2l+1}}\,. \tag{7}$$

In Fig. 1 the form factors for the angular momenta up to 8 are shown for the case of a beam with parabolic profile up to a radius of d (in unit of the unit radius of the sphere), given by the formula

$$I(\theta) = A\left(1 - \sin^2\theta/d^2\right)\,. \tag{8}$$

It is clearly visible that the higher angular momenta are damped much more rapidly.

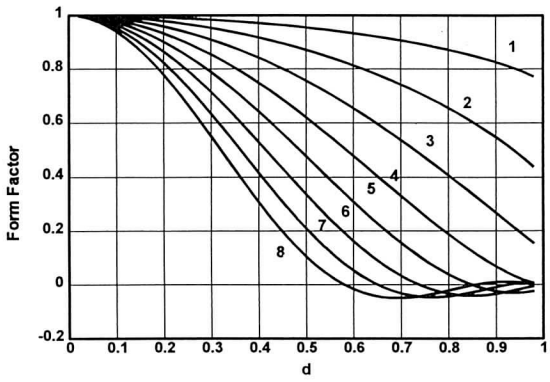

Fig. 1: Form factors for a beam with parabolic radial intensity profile as given in Eq. 8.

Limitations: the inherent weakness of the foregoing considerations is, of course, the assumption of linearity. In reality, there is no reason for a pellet implosion driven by two overlapping beams to be in any way linearly decomposable into the "sum" of the implosions driven by the beams individually. As an example we studied the implosion of a spherical shell driven in the P4 configuration, comparing the cases of overlapping and separate beams. The simulation was done with the code Multi-2D [2].

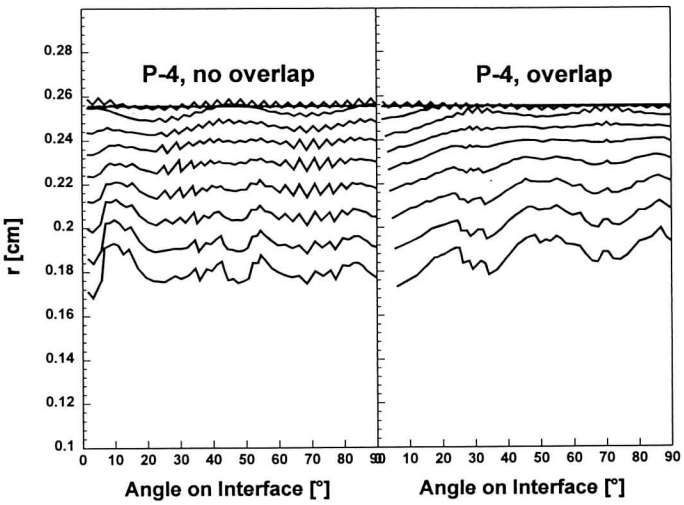

Fig. 2: Motion of the inner surface of a spherical shell driven by to beam groups in the P4 configuration, with the beams overlapping or separate. The interval between two curves is 1 ns each, and the latest curve (appearing lowest in the figure) is for 20 ns. Note that with the overlap the intensity is highest between the to beam centers, leading to a start of the compression near 45°. The structure at 0° is distorted owing to the well-known problems of the Multi-2D code at the symmetry axis.

An additional source of nonlinearities is the finite range of the beams, which leads to a deposition pattern that cannot simply be described by a function on the surface of the unit sphere.

References

[1] J. W.-K. Mark, *1984 Laser Program Annual Report, UCRL-50021-84* (1984), p. 3-24.

[2] R. Ramis and J. Meyer-ter-Vehn, MPQ Report 174 (1992).

Exact View Factors for Isotropic Sources in 2D Convex Geometries. 'Disk Algebra' Approach

E.G.Vasina
RFNC-VNIIEF, Sarov, Russia

Exact view factors are known to be very efficient for radiation transport simulation in transparent regions. They imply calculation of geometric characteristics of the modeled regions, which is a serious computational challenge in complex geometries.

For some simple geometries exact view factors are known. (see, for example, [1]).

A way was found to determine exact view factors for isotropic sources in 2D azimuthally symmetric convex geometries. According to the note made by V.G.Rogachev, their values do not depend on generatrix shape as long as the condition of convexity is met.

Consider the simplest 2D azimuthally symmetric system consisting of three surfaces: frustum of a cone 2 and two disks 1 and 3 at the cone ends (see Fig.1). determine the values of all the view factors of the system F_{ij}, ij = 1,2,3.

Using the normalization relation, depicting the physical sense of view factors (total energy emitted by the source towards all visible surfaces in all directions makes 100

$$\sum_{j=1}^{N} F_{ij} = 1 \tag{1}$$

a set of three equations for the three surfaces can be written.

Taking into account view factor reciprocity, we have

$$S_i F_{ij} = S_j F_{ji}. \tag{2}$$

This allows to exclude subdiagonal elements from the set of equations. Taking into account that view factors F_{11} and F_{33} of disks self-visibility equal zero, and that the view factor for a pair of remote disks F_{13} is well known, we get three equations for three unknowns. Thus, the problem for the simplest system (Fig. 1) is solved.

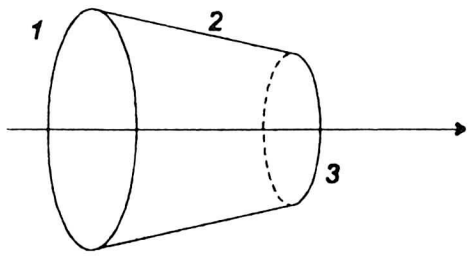

Figure 1: Simple 2D azimuthally symmetric geometry

Let view factor for a pair of two disks be denoted as D_{13}. Its value is:

$$D_{13} = \frac{1}{2}\left[X - \sqrt{X^2 - 4\left(\frac{r_3}{r_1}\right)^2}\right] \tag{3}$$

$$X = 1 + \frac{h^2 + r_3^2}{r_1^2}$$

, where r_1, r_3 are the radii of the disks 1 and 3, and h is the distance between the disk centers.

Then we have

$$F_{12} = 1 - D_{13} \tag{4}$$

$$F_{21} = \frac{S_1}{S_2} F_{12} = \frac{S_1}{S_2}(1 - D_{13}) \tag{5}$$

and similar formulas for the pair cone 2 - disk 3:

$$F_{23} = \frac{S_3}{S_2}(1 - D_{31}) \quad , F_{32} = (1 - D_{31})$$

and for self-visibility of the conic surface:

$$F_{22} = 1 - \frac{S_1}{S_2}(1 - D_{13}) - \frac{S_3}{S_1}(1 - D_{31})$$

$$= 1 - \frac{S_1 + S_3}{S_2} + 2\frac{S_1}{S_2} D_{13} \tag{6}$$

Consider now a general case of convex 2D azimuthally symmetric geometry: two remote conic elements (see Fig. 2). According to the above said, the generatrix of the surface of rotation may be substituted by the straight line without loss of generality.

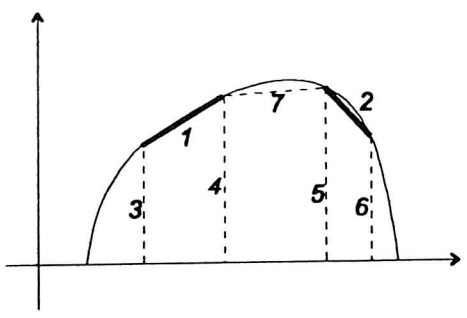

Figure 2: General case of two elements in convex 2D azimuthally symmetric geometry

In order to find the view factor F_{12} , let us build dummy closing surfaces: disks 3, 4, 5, 6 and conic surface 7. Then we may write:

$F_{12} = F_{15} - F_{16}$.

To determine view factors F_{15} and F_{16} , we use normalization relations for the surfaces 5 and 6:

$F_{57} + F_{51} + F_{53} = 1$, and $F_{62} + F_{67} + F_{61} + F_{63} = 1$.

Considering the closed contour 5-7-4, the following relation may be written: $F_{57} + F_{54} =$, which yields the value of $F_{57} = 1 - D_{54}$.

So F_{51} = 1 - D_{53} - $(1 - D_{54})$

Therefore, $F_{15} = \frac{S_5}{S_1}(1 - D_{53} - (1 - D_{54}))$

Similar considerations for contours 6-2-7-4 and 6-2-5 yield

$F_{16} = \frac{S_6}{S_1}(D_{64} - D_{63})$.

Finally, after evident rearrangements, we get

$$F_{12} = \frac{S_4}{S_1}(D_{45} - D_{46}) - \frac{S_3}{S_1}(D_{35} - D_{36}) \quad (7)$$

The formulas for degenerate cases, when one of the cones (or both) are substituted with disks or disk rings, may be readily obtained either from the above formula, or directly with the help of similar 'disk algebra' considerations.

Note, that view factor for the pair of one complete element of rotation and a part of another element of rotation limited by certain values of rotation angle, equals (of course, for the same convex case without occlusion)

$$F_{ij} = \frac{\Delta\alpha}{2\pi} F_{ij}^{total} \quad (8)$$

The work was done in the framework of the ISTC Project #154.

References

[1] R. Siegel, J.R. Howell 'Thermal Radiation Heat Transfer', McGraw-Hill, 1972, p. 814

Heating Solid Cylindrical Targets Using SIS Beam

N.A.Tahir and D. H. H. Hoffmann, TU Darmstadt ;
K. -J. Lutz and J. A. Maruhn, Universität Frankfurt;
R.Bock, GSI Darmstadt;

We have simulated one-dimensional hydrodynamic response of solid cylindrical targets made of different materials including hydrogen, neon and lead. The target and beam geometry for these different cases is shown in Fig.1 - Fig.4. According to the present accelerator parameters, the space charge limit for Ar^{+10} ions allows acceleration of about $3x10^{11}$ ions, with energy 300 MeV/u. However in most of the experiments done so far the total number of ions in the beam was $2x10^{10}$. This leads to a specific energy deposition of 1 kJ/g in solid lead.

It is expected that by the end of 1999 the SIS facility will be updated to accelerate $2x10^{11}$ ions of U^{+28} with energy 200 MeV/u. This would lead to a specific energy deposition of the order of 100 kJ/g in solid lead. We have simulated the hydrodynamic response of these targets using various values of specific energy deposition, including 1 kJ/g, 10 kJ/g, 50 kJ/g and 100 kJ/g whereas for each of these values of the specific energy, we have considered four different values of pulse length, namely, 10 ns, 50 ns, 100 ns and 200 ns respectively. In most of the cases, we assume that the beam radius is smaller than the cylinder radius whereas in some cases we allow for the beam radius to be equal to the target radius. The former type of the beam-target arrangement can be used to study the ion beam induced shock waves in solids (see Fig.5) while he latter can be used to study the heating and hydrodynamic expansion of solid matter irradiated by heavy ion beams. Moreover a Gaussian as well as a rectangular (uniform) energy deposition profile along the target radius have been considered. One important conclusion drawn from this study is that the pulse length should not be longer than 50 ns otherwise the energy deposition will be substantially reduced due to the hydrodynamic expansion.

These calculations have been carried out using a one-dimensional hydrodynamic Lagrangian computer code MEDUSA-KAT[1]. For details about these calculations see Re.[2].

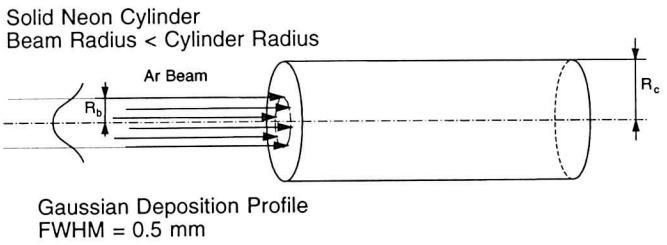

Figure 1: Target and beam geometry

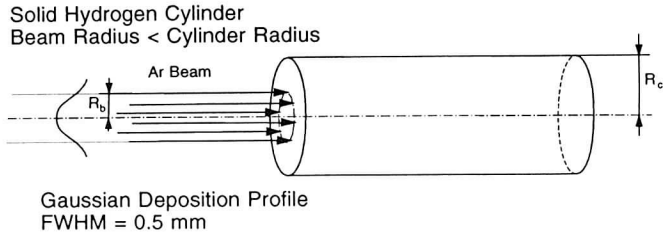

Figure 2: Target and beam geometry

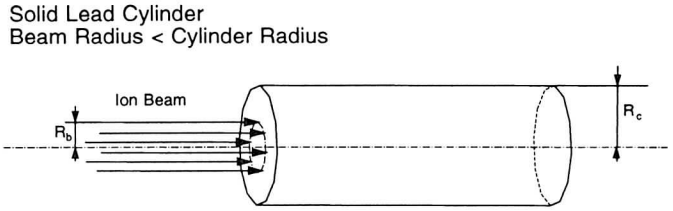

Figure 3: Target and beam geometry

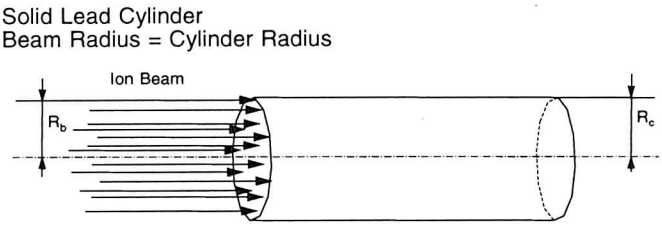

Figure 4: Target and beam geometry

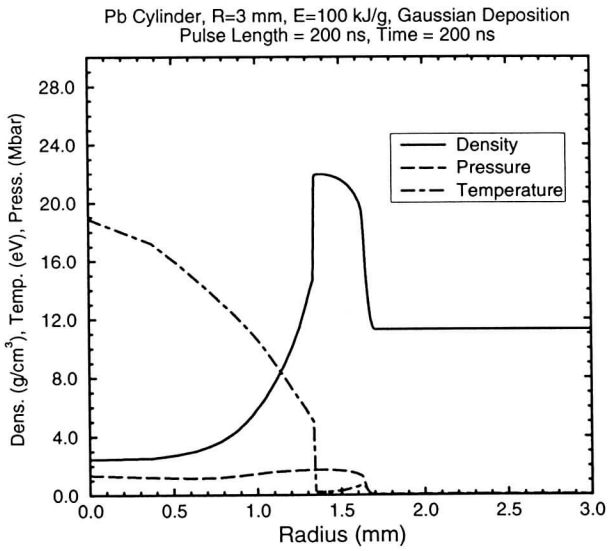

Figure 5: Density, pressure and temperature vs radius for target shown in Fig.3

References

[1] N.A.Tahir, K.A.Long and E.W.Laing, J. Appl. Phys. 60 (1986) 898.

[2] N.A.Tahir, D.H.H.Hoffmann, J.A.Maruhn,K.-J.Lutz and R.Bock, Phys. Plasmas, December 1998, to be published.

Possibiltity of Creating Metallic Hydrogen at the SIS Facility

N.A.Tahir and D. H. H. Hoffmann, TU Darmstadt ;
K. -J. Lutz and J. A. Maruhn, Universität Frankfurt;
R.Bock, GSI Darmstadt;

Because of its special properties and important applications, the possibility of creating metallic hydrogen has been of considerable interest for the past few decades. A number of techniques including the use of diamond anvil cell that generates static pressure and gas guns that provide transient pressures via shock compression, have been used to compress hydrogen. We propose to study this problem by imploding sophisticated multi-layered cylindrical targets that contain a layer of frozen hydrogen using the heavy ion beam that will be produced at the GSI Darmstadt SIS facility. It is expected that by the end of 1999, the SIS facility will be updated to accelerate $2x10^{11}$ ions of U^{+28} to energies of 200 MeV/u with a pulse length, τ, of about 50 ns. These beam parameters would lead to a specific energy deposition of 50 - 200 kJ/g in solid matter.

The target is shown in Fig.1. It consists of an inner lead cylinder that has a radius of 0.6 mm and that is coated with a layer of solid hydrogen having a thickness of 0.2 mm. This is followed by another lead shell whose outer radius is 2.0 mm. The ion beam is incident on one face of the target and the length of the cylinder is assumed to be shorter than the ion range. The ions will lose part of their energy in the target and emerge from the second face of the cylinder with a substantially reduced energy. Since in such an arrangement, the Bragg peak will not lie inside the target, the energy deposition will be fairly uniform and one may employ a one-dimensional model to treat this problem.

We have simulated the hydrodynamic response of this target to heavy ion beam using a specific energy deposition of 100 kJ/g and a pulse length of 70 ns. The beam deposition profile along the target radius is assumed to be Gaussian and the FWHM of the Gaussian deposition is considered to be 0.6 mm.

In Fig.2 we plot the coordinates of different material interfaces. It is seen that the shock generated in the heated region arrives at the inner lead-hydrogen boundary at about t = 50 ns and the shock then moves into the hydrogen layer compressing the material. The peak compression occurs at about t = 95 ns when the thickness of the hydrogen layer becomes about 15 micron while the corresponding density is 1.12 g/cm^3, the temperature is 0.13 eV and the pressure is of the order of 2.45 Mbar. The results using different values of pulse lengths are shown in Table I. We have also done calculations using a deuterium layer and the results are presented in Table II. This shows that one may achieve physical conditions necessary for the hydrogen and deuterium metallization. For further details see Ref.[2,3].

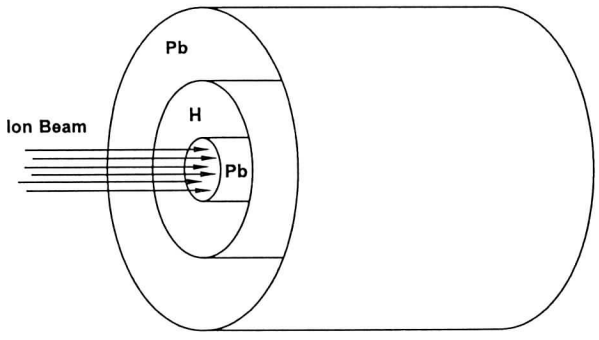

Figure 1: Target and beam geometry

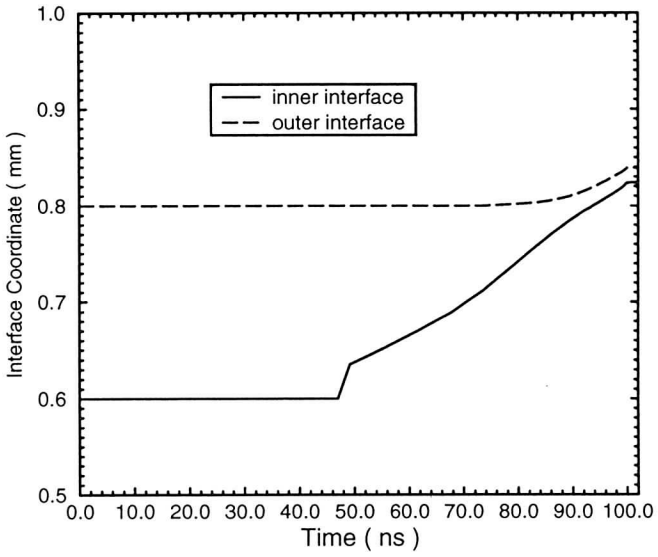

Figure 2: Interface coordinates as a function of time

TABLE I. Hydrogen physical conditions, absorbed energy 100 kJ/g, Gaussian deposition profile, FWHM = 0.6 mm

τ (ns)	ρ (g/cm^3)	T (eV)	P (Mbar)
30	1.29	0.21	3.10
50	1.25	0.17	2.75
70	1.12	0.13	2.45
100	0.88	0.11	2.34

TABLE II. Deuterium physical conditions, absorbed energy 100 kJ/g, Gaussian deposition profile, FMHM = 0.6 mm

τ (ns)	ρ (g/cm^3)	T (eV)	P (Mbar)
30	2.34	0.25	2.88
50	2.34	0.22	2.72
70	2.00	0.16	2.51
100	1.70	0.13	2.29

References

[1] N.A.Tahir, K.A.Long, E.W.Laing, J. Appl. Phys. 60 (1986) 898.
[2] N.A.Tahir, D.H.H.Hoffmann, J.A.Maruhn,K.-J.Lutz, R.Bock, Phys. Plasmas, December 1998, to be published.
[3] N.A.Tahir, D.H.H.Hoffmann, J.A.Maruhn,K.-J.Lutz, R.Bock, Phys. Lett. A, 1998, to be published.

Test of Hydrodynamic Codes for Simple Cylindrical Targets+

J. A. Maruhn
Institut für Theoretische Physik, Universität Frankfurt
V. Ermolovich, A. Kazarin, V. Vatulin, S. Skrypnik
VNIIEF, Sarov, Russia

The hydrodynamic code most widely used at Frankfurt and GSI is *Multi 2D* developed by Ramis and Meyer-ter-Vehn [1]. While this code is very fast and flexible, there are also doubts concerning its accuracy, because the hydrodyamic phase is based on a relatively simple discretization, and the use of a triangular grid could also lead to problems.

This concern was especially raised by the finding that in *Multi 2D* simulations often unphysical behavior is observed near the symmetry axis, which is caused by increasing discretization errors with respect to the radial coordinate and usually takes the form of spurious bumps or depressions in the physical fields such as the temperature.

For this reason it was decided to investigate the reliability of *Multi 2D* simulations by means of a detailed comparison of results with those of codes developed at VNIIEF. In order to investigate purely the effects of the numerical techniques, it was decided to keep the physical situation as simple as possible: straightforward geometry, equation of state, and beam-target interaction, and to gradually increase the complexity in further series of comparisons.

The target was assumed to be a solid Gold cylinder with a radius of 2 mm and a length of 0.6 mm. Into this target a heavy ion beam of total energy 40 kJ was deposited with a time-dependent intensity given by an inverted parabola of 20 ns duration. The beam has a radial profile given by a Gaussian with 2σ=1.1 mm.

For the beam deposition in this first stage two cases were considered:

1. a uniform deposition with a range of 0.897 g/cm^3
2. a realistic deposition profile with the relative energy loss given by

$$\frac{de}{dx} = 0.566\rho \times \begin{cases} 1.51e^2 - 3.48e + 3.43, & e > 0.068 \\ 12.24\sqrt{e} & \text{otherwise} \end{cases} \quad (1)$$

where e is the fractional amount of kinetic energy remaining in the ions (starting with 1), and ρ the local density in g/cm^3.

Both calculations utitlized grids characterized by about 100 by 100 zones through the target.

From the results we show two plots with characteristic quantities as functions of the time into the simulation; Fig. 1 refers to constant deposition and Fig. 2 to the profile given by Eq. 1. There is surprisingly good agreement both in the energies and peak temperatures, differences grow to more than a few percent only in the later stages of the simulations. Especially the peak conditions attainable agree quite well and show that *Multi 2D* should be trusted at least in this kind of situation, which is, of course, a very frequent scenario for investigations of future experiments.

In the later stages of the reaction, *Multi 2D* seems somewhat more dissipative than the VNIIEF codes: the kinetic energy does not increase as much but the temperatues go down more rapidly.

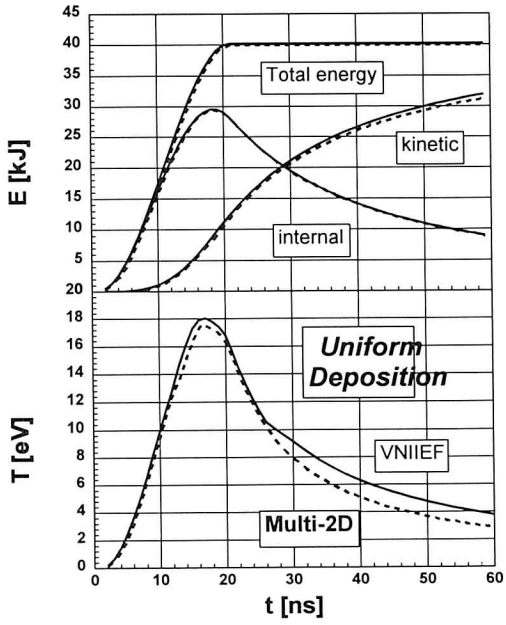

Fig. 1: Time dependence of integrated energies and of the maximum temperature in the VNIIEF (full curves) and Multi 2D (dashes) calculations. For uniform deposition.

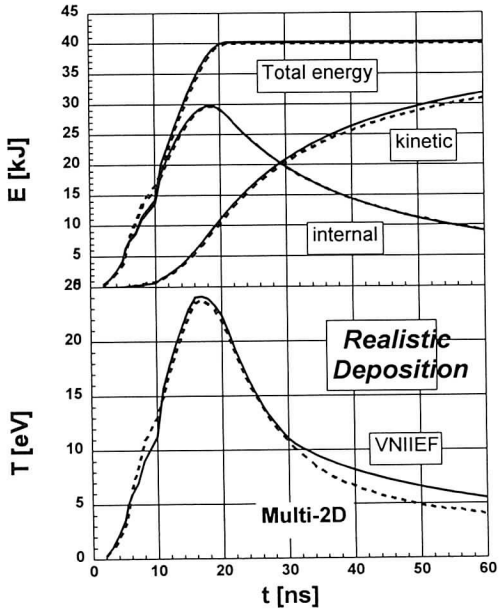

Fig. 2: Same as Fig. 1, but for the more realistic deposition profile as defined in Eq. 1.

References

+ Supported by BMBF and WTZ

[1] R. Ramis and J. Meyer-ter-Vehn, MPQ Report 174 (1992).

Time-dependent Stopping Power in Classical Plasmas

C. Seele*, G. Zwicknagel, C. Toepffer and P.-G. Reinhard
Institut für Theoretische Physik II, Universität Erlangen

Most investigations of the stopping power have so far concentrated on its long-time behavior. In many application like inertial confinement fusion or electron cooling in storage rings, however, special emphasis has to be placed on the transient properties between the onset of the external distortion, i.e. when the ion enters the target, and the stationary regime of constant stopping. We simplify this onset of the interaction of an ion with a plasma as a sudden appearance of the ion at $t = 0$ in an unperturbed homogeneous target plasma. An ion moving with velocity v_p then appears as the time–dependent external potential

$$\phi^{\rm ext}(\mathrm{r},t) \;=\; \frac{Z_p e}{4\pi\epsilon_0}\,\frac{\Theta(t)}{|\mathrm{r}-\mathrm{v}_p t|}.$$

For this perturbation of the target the stopping power on the ion reads in framework of linear response theory and expressed in Fourier-Laplace space

$$\frac{dE}{ds}(t) \;=\; \frac{Z_p^2 e^2}{i\epsilon_0(2\pi)^4}\int d^3\mathrm{k}\,\frac{i\mathrm{k}\cdot\hat{\mathrm{v}}_p}{k^2}\int_{-\infty+i\delta}^{\infty+i\delta} d\omega\,\frac{1}{\omega-\mathrm{k}\cdot\mathrm{v}_p} \times\left[\frac{1}{\varepsilon(k,\omega)}-1\right]\exp(i\mathrm{k}\cdot\mathrm{v}_p t)\exp(-i\omega t) \quad (1)$$

with $\delta \to 0^+$ and the dielectric function $\varepsilon(k,\omega)$. Evaluating Eq. (1) for $t > 0$ by closing the contour of integration in the lower complex ω-half-plane yields contributions form the real pole at $\omega = \mathrm{k}\cdot\mathrm{v}_p$ and all enclosed poles ω_j related to the zeros of $\varepsilon(k,\omega)$. These zeros provide exponentially decaying dynamic contributions to the stopping power which are damped out for large times after switching on the interaction. They describe thus the transient behavior towards the asymptotic, undamped contribution from the real pole $\mathrm{k}\cdot\mathrm{v}_p$ which yields the usual constant stopping

$$\frac{dE}{ds}(t\gg\tau_p) = \frac{Z_p^2 e^2}{\epsilon_0(2\pi)^3}\int d^3\mathrm{k}\,\frac{\mathrm{k}\cdot\hat{\mathrm{v}}_p}{k^2}\,\mathrm{Im}\left[\frac{1}{\varepsilon(k,\mathrm{k}\cdot\mathrm{v}_p)}\right] \quad (2)$$

To obtain the full time evolution of the stopping power for $t < \tau_p$ a numerical determination of the poles ω_j of the dielectric function for a classical free electron plasma and a subsequent evaluation of Eq.(1) have been performed. The results are shown in Fig.1 for different target conditions characterized by the number of electrons in a Debye sphere $N_D = 4\pi n\lambda_D^3$ and ion velocities. As the main result we found a typical transient time period of approximately a quarter of a plasma period τ_p for all studied targets and velocities. For small v_p there appear additional features like damped oscillations about the stationary value (2). To check and compare these results we also performed MD computer simulations. The simulation results for the time-dependent stopping power agree well with the linear response prediction (1) in cases of weak coupling, i.e. for $Z_p/N_D(1+(v_p/v_{th})^3) \ll 1$ as presented in Fig.1. For strong, nonlinear coupling where the linear response description is beyond its limit of validity, a quite different behavior has been revealed by the MD simulation results as shown in Fig.2. Here nonlinear effects yield an strong excess in the stopping power near $0.5\tau_p$ which decreases only slowly. For a detailed discussion of these considerations and results see Ref.[1].

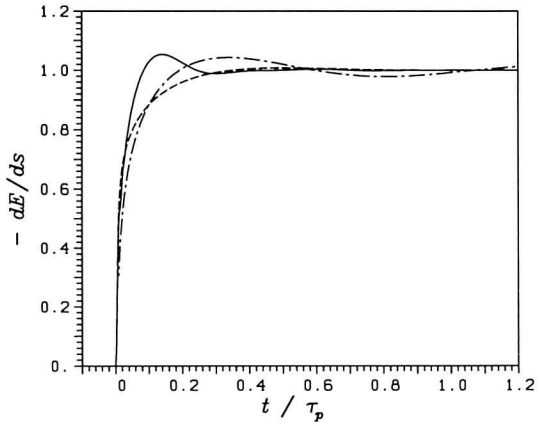

Figure 1: Time-dependent linear response stopping power (1) in units of the asymptotic stopping (2) for different target conditions and velocities in units of $v_{th} = (k_B T/m)^{1/2}$: $Z_p/N_D = 19.4$,$v_p = 12$ (solid curve), $Z_p/N_D = 0.03$ $v_p = 4$ (dashed) and $Z_p/N_D = 0.03$,$v_p = 1$ (dash-dotted).

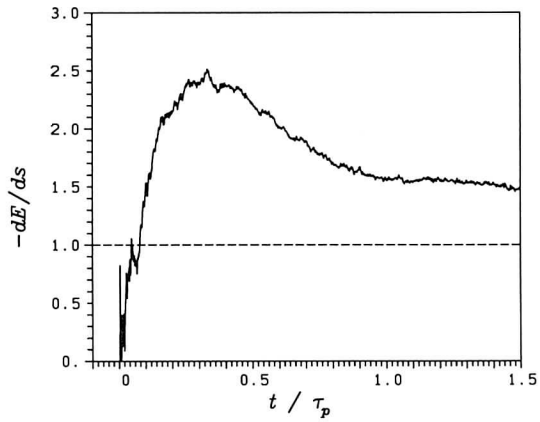

Figure 2: MD simulation result for the time-dependent stopping power (solid curve) in units of its asymptotic value (dashed) for $Z_p/N_D = 19.4$,$v_p/v_{th} = 1$.

References

[*] Present Address: Max-Planck-Institut für Aeronomie, Max-Planck-Str. 2, 37191 Katlenburg-Lindau, Germany.

[1] C. Seele, G. Zwicknagel, C. Toepffer and P.-G. Reinhard, Phys.Rev.E **57** (1998) 3368.

Stopping of Gyrating Fast Particle in Magnetized Cold Plasma

H.B. Nersisyan, H.H. Matevosyan, IRE,
Division of Theoretical physics, Ashtarak-2, 378410, Armenia
C. Deutsch, LPGP, Université Paris XI, 91405 Orsay

A uniform plasma is considered in the presence of a homogeneous magnetic field B_0 (directed in the positive z-direction) which is assumed sufficiently small so that $\lambda_B << a_c$ (where λ_B and a_c are respectively the electron de Broglie wavelength and Larmor radius). From these conditions we can obtain $B_0 < 10^5$ T (T is the plasma temperature), where T is measured in eV and B_0 in kG. We start with the scalar potential [1-4]

$$\phi(\mathbf{r},t) = \frac{4\pi Ze}{(2\pi)4}\int d\mathbf{k} \int_{-\infty}^{+\infty} d\mathbf{k}\ \frac{\exp[i(\mathbf{kr} - \omega t)}{k^2\varepsilon(\mathbf{k},\omega)} \cdot$$

$$\cdot \int_{-\infty}^{+\infty} d\tau\ \exp[i\omega\tau - i\mathbf{kr}_0 - (\tau)] , \qquad (1)$$

where $\mathbf{r}_0(t)$ is the radius-vector of the test particle having components $\chi_0(t) = a\sin(\Omega_c t)$, $y_0(t) = a\cos(\Omega_c t)$, $z_0(t) = 0$ ($\Omega_c = ZeB_0/Mc$, $a = v/\Omega_c$, Ze and v are the Larmor frequency, the Larmor radius, the charge and the velocity of the test particle respectively). $\varepsilon(\mathbf{k},\omega)$ is the longitudinal dielectric function of a magnetized cold plasma

$$\varepsilon(\mathbf{k},\omega) = \varepsilon(\omega)\cos^2\alpha + h(\omega)\sin^2\alpha \qquad (2)$$

with

$$\varepsilon(\omega) = 1 - \frac{\omega_p^2}{\omega(\omega + i\nu)} , \qquad (3)$$

$$h(\omega) = 1 + \frac{\omega_p^2(\omega + i\nu)}{\left[\omega_p^2 - (\omega + i\nu)^2\right]\omega} . \qquad (4)$$

Here, α is the angle between the wave vector $\mathbf{k}$ and the magnetic field, $\omega_p = \sqrt{4\pi n_0 e^2/m}$, ω_c and ν are the plasma frequency, Larmor frequency and the effective collision frequency of the plasma electrons respectively.

From eq. (1) it is straightforward to calculated the electric field $\mathbf{E} = -\nabla\phi$, and the stopping force acting on the particle. Then, the rate of energy loss of the test particle becomes

$$S = \frac{2Z^2e^2\Omega_c^2}{\pi v}\sum_{n=1}^{\infty} nQ_n(s)\,\mathrm{Im}\left[\frac{-1}{\varepsilon(n\Omega_c)T(n\Omega_c)}\right] , \qquad (5)$$

where

$$T(\omega) = \sqrt{\frac{|P(\omega)| + \mathrm{Re}\,P(\omega)}{2}} + i\,\mathrm{sgn}[\mathrm{Im}\,P(\omega)]\sqrt{\frac{|P(\omega)| - \mathrm{Re}\,P(\omega)}{2}} , \qquad (6)$$

where

$$Q_n(s) = \pi\int_0^s dx J_n^2(\chi) , \qquad (7)$$

$P(\omega) = h(\omega)/\varepsilon(\omega)$, $J_n(\chi)$ is the n_{th} order Bessel function and $s = k_{max}a$ with $k_{max} = 1/r_{min} = 2mv/\hbar$, where r_{min} is the effective minimum impact parameter. Here k_{max} prevents the divergence of the integral caused by an incorrect treatment of the short-range interactions within the linearized Vlasov theory.

The function $Q_n(s)$ is exponentially small at $n > s$. Therefore the series in the eq. (5) is cut at

$n_{max} \cong s$ and the rate of energy loss is determined by harmonics with $n<n_{max}$.

In the case of weak magnetic field ($\Omega_c<\nu$) one may substitute the summation in expression (5) by integration in $\omega=n\Omega_c$. Since also $Q_n(s) \cong \ell n(s/n)$ when $s>n$, in the limit $\Omega_c \to 0$ eq. (5) is transformed into well known Bohr's expression.

For strong magnetic field with $c= \omega_c/\Omega_c$ non-integer one has

$$S \cong \frac{Z^2 e^2 \omega_p^2}{\pi v} \frac{\nu}{\Omega_c} \sum_{n=1}^{\infty} \frac{1}{n^2} Q_n(s) \left[1 + \frac{n^4}{(n^2-c^2)^2} \right]. \qquad (8)$$

From eq. (8) follows, that energy loss decreases inversely proportional to the magnetic field. In the case when c=1 (electron test particle), eq. (5) shows

$$S \cong \frac{Z^2 e^2 \omega_p^2}{\pi v} \frac{\Omega_c}{\nu} Q_1(s) \ . \qquad (9)$$

Note that the rate of energy loss increases proportionally to the magnetic field.

These examples of asymptotic dependence of energy loss rate on the value of magnetic field show how strong the energy loss relies on mass of the test particle.

From eq. (5) one sees the behavior of energy loss rate as a function of magnetic field in the general case. The rate of energy loss is maximal for those values of magnetic field for which $\varepsilon(n\Omega_c)$ remain small. This means, that maxima at integer values of parameter $b=\omega_p/\Omega_c$ can be observed. They correspond to the case, when a test particle's Larmor orbit includes an integer number of plasma oscillation wavelengths ($\lambda_p = 2\pi v/\omega_p$).

Fig. 1 shows the ratio $R=S/S_B$ (where S_B is the well-known Bohr result [5]) as a function of parameter b in two cases; for electron test particle (solid line), and for proton test particle (dotted line). The parameters are: $v/\omega_p = 0.01$, $n_0 = 10^{18}$ cm^{-3}, $T = 100eV$ and $v/v_T = 10$. The rate of energy loss oscillates as a function of magnetic field and exceeds the usual Bohr energy losses many times.

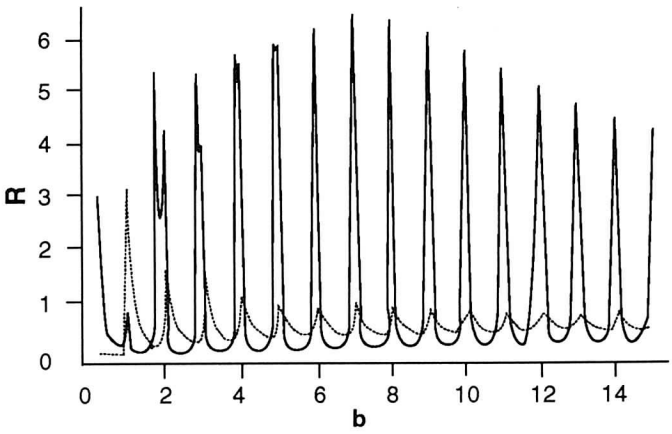

Figure 1- The dimensionless rate of energy loss $R=S/S_B$ as a function of parameter b in two cases; for electron test particle (solid line), and for proton test particle (dotted line). The parameters are : $v/\omega_p=0.01$, $n_0=10^{18}cm^{-3}$, $T=100eV$ and $v/v_T=10$.

References

[1] N. Honda, O. Aona and T. Kihara, *J. Phys. Soc. Jpn*, **18**, 256 (1963).

[2] R.M. May and N.F. Cramer, *Phys. Fluids*, **13**, 1766 (1970).

[3] G.G. Pavlov and D.G. Yalovlev, *Soc. Phys. JETP*, **43**, 389 (1976).

[4] S.V. Bozhokin and E.A. Choban, *Sov. J. Plasma Phys.*, **10**, 452 (1984).

[5] N. Rostoker and M.N. Rosenbluth, *Phys. Fluids*, **3**, 1 (1960).

Correlated Fast Ion Stopping in Magnetized Classical Plasma

H.B. Nersisyan, H.H. Matevosyan, IRE,
Division of Theoretical physics, Ashtarak-2, 378410, Armenia
C. Deutsch, LPGP, Université Paris XI, 91405 Orsay

The stopping power of the ion pair can be computed by summing up the forces acting on two ions, due to the electric field induced in the plasma; it reads [1-4]

$$S \equiv -\frac{dW}{dz} = \left(Z_1^2 + Z_2^2\right) S_{sp} + 2Z_1 Z_2 S_c \qquad (1)$$

where

$$S_{sp} = \frac{4\pi e^2}{(2\pi)^3 u} \int d\mathbf{k} \frac{\mathbf{ku}}{k^2} \, \mathrm{Im} \frac{-1}{\varepsilon(\mathbf{k}, \mathbf{ku})} , \qquad (2)$$

$$S_c = \frac{4\pi e^2}{(2\pi)^3 u} \int d\mathbf{k} \frac{\mathbf{ku}}{k^2} \, \mathrm{Im} \frac{-1}{\varepsilon(\mathbf{k}, \mathbf{ku})} \cos(\mathbf{k}\ell) . \qquad (3)$$

There are two contributions to the stopping power of two ions. The first one is the uncorrelated particle contribution and represents the energy loss of the two projectiles due to the coupling with collective plasma modes (first term in eq. 1). Both terms are responsible of the irreversible transfer of the two-ion energy to plasma through resonant electrons.

Let us begin with the evaluation of the stopping power of two ions with the same effective charge Ze. For an arbitrary relative position of the two test ions, the expressions of the uncorrelated (proportional to S_{sp}) and correlated (proportional to S_c) stopping power of the ion pair becomes:

$$S_{sp}(\lambda) = \frac{e^2}{2\pi\lambda_D^2} \left\{ \frac{B(\lambda)}{2} \ell n \frac{B^2(\lambda) + \left(s^2 + A(\lambda)\right)^2}{B^2(\lambda) + A^2(\lambda)} \right.$$

$$\left. - A(\lambda) \left[\arctan \frac{s^2 + A(\lambda)}{B(\lambda)} - \arctan \frac{s^2 + A(\lambda)}{B(\lambda)} \right] \right\} , \qquad (4)$$

$$S_c(\ell, \vartheta, \lambda) = \frac{2e^2}{\pi\lambda_D^2} B(\lambda) .$$

$$\cdot \cdot \int_0^s \frac{k^3 dk}{\left[k^2 + A(\lambda)\right]^2 + B^2(\lambda)} Q(kL\cos\vartheta; kL\sin\vartheta). \qquad (5)$$

Here

$$Q(a,b) = \int_0^1 \cos(ax) Jo\left(b\sqrt{1-x^2}\right) x dx , \qquad (6)$$

$J_0(z)$ is the Bessel function of zero order, ϑ is the angle between the interionic vector ℓ and the velocity vector $\mathbf{u}$, $L=\ell/\lambda_D$, $\lambda=u/v_T$, $s=k_{max}\lambda_D$ with $k_{max}=\ell/r_{min}$, where r_{min} is the effective minimum impact parameter. The value of k_{max}, will be ℓ/a_c for fusion plasma since the magnetized plasma approximation which neglects the perpendicular motion of the electrons ceases to be valid for collision parameters less than a_c.

Then, defining the *interference or vicinage function* $\chi(\ell)$ as [1,2]

$$\chi(\ell, \vartheta, \lambda) = \frac{S_c(\ell, \vartheta, \lambda)}{S_{sp}(\lambda)} , \qquad (7)$$

eq. (1) can be put in the form

$$S = 2Z^2 S_{sp}(\lambda)[1 + \chi(\ell)] . \qquad (8)$$

Here, χ describes the intensity of correlation effects with respect to uncorrelated situation. In the case of the fast ions ($\lambda >> 1$), from eqs. (4) and (5) we obtain:

$$\chi(\ell,\vartheta,\lambda) \equiv 2Q\left(\frac{L}{\lambda}\cos\vartheta;\frac{L}{\lambda}\sin\vartheta\right) . \qquad (9)$$

For two values of the orientation angle ϑ=0° and ϑ=90° the expression (9) for *vicinage function* becomes

$$\chi(\ell,0,\lambda) = 2\left(\frac{\sin(L/\lambda)}{(L/\lambda)} - \frac{1-\cos(L/\lambda)}{(L/\lambda)^2}\right), \qquad (10)$$

$$\chi\left(\ell,\frac{\pi}{2},\lambda\right) = \frac{2}{(L/\lambda)} J_1(L/\lambda) , \qquad (11)$$

where $J_1(z)$ is the Bessel function of the first order.

Fig. 1 shows χ as a function of L and ϑ-value, depending on the interionic distance ℓ (see also eqs. (10) and (11). Meanwhile the correlation effects decrease for large ϑ-value in plasma in the absence of magnetic field [1]. It should be clear that this effect is accounted by the character of electrostatic potential of test charged particles in magnetized plasma. As shown in ref. [3], in the frame of the test particle, moving in a plasma placed with strong magnetic field ($a_c << \lambda_D$), the spatially oscillatory potential has sperical symmetry over the hemisphere behind particle and is zero ahead of it. The second part has a different character, which makes the potential continuous at the plane containing the particle oscillatory in the radial direction, but decreases almost monotonically in the axial one.

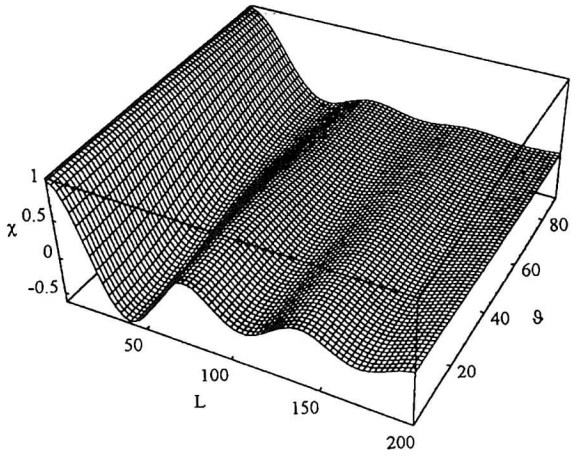

Figure 1- The *vicinage function* χ vs. $L=\ell/\lambda_D$ and ϑ (degrees). The parameters are: λ=10, s=10.

References

[1] J. D'Avanzo, M. Lontano and P.F. Bortignon, *Phys. Rev. E*, **47**, 3574 (1993).

[2] C. Deutsch and P. Fromy, *Phys. Rev. E*, **51**, 632 (1995).

[3] A.A. Ware and J.C. Wiley, *Phys. Fluids B*, **5**, 2764 (1993.

[4] C. Deutsch, *Laser Part. Beams*, **8**, 541 (1990).

Tree Code Simulations – Plasma Formation in Intense Laser Fields

R. Schneider*, TQE, TH Darmstadt

Introduction

The simulation technique of the so-called *tree code* [1,2] was originally applied in astrophysics. In the last years problems of plasma dynamics have been also solved numerically by this algorithm. Basically it is a particle code which solves the N body problem. The expense of numeric calculation reduces to $N \log N$ in contrast to the N^2 scaling of direct calculation. The code is parallelized and can run on massive parallel computers. Treating a system of $N = 32000$ particles on a machine with 2.8 Gigaflop/s (GC/PP, Paderborn) one time step needs about 30 seconds. The pictures shown in this paper are results from simulations with only $N = 512$ particles because here we want to look at the microscopic dynamics, the trajectories in phase space. The amount of data for 32000 particle is too large for that.

The advantage of this simulation technique is the exact treatment of collisions, dynamical screening and many body correlations. The calculation includes the smallest time scale of collision dynamics which is not part of the Vlasov or the Boltzmann equation. In this work we want to discuss the ionisation and the heating of matter irradiated by an intense laser beam. At intensities of $10^{16}\,\mathrm{W/cm^2}$ field ionisation plays the dominant role and can be approximately treated classically [3].

Dimensionless dynamic equations

$$\tilde{x} = \frac{x}{l_N} \;,\; \tilde{t} = t\,\frac{\omega_p}{2\pi} \;,\; \tilde{m} = \frac{m}{m_e} \;,\; \tilde{Q} = \frac{Q}{e} = Z$$

$$\Longrightarrow \quad \ddot{\tilde{\boldsymbol{x}}}_1 = \frac{Z_1 Z_2}{m_1}\pi\left(\frac{\boldsymbol{x}_1}{|\boldsymbol{x}_1 - \boldsymbol{x}_2|^3}\right)$$

Density scaling: $v \sim \tilde{v}\, n^{1/6}$, $T \sim \tilde{T}\, n^{1/3}$, $\lambda_D \sim \tilde{\lambda}_D\, n^{-1/3}$

plasma parameter $\tilde{g} \sim$ const.

As long as no more time or length scales couple in – quantum effects or external fields – the plasma parameter is constant during the evolution of the plasma.

The way towards equilibrium

At first we want to look at a cold, ionised hydrogen plasma where the electrons get an initial kinetic energy of 27 eV.

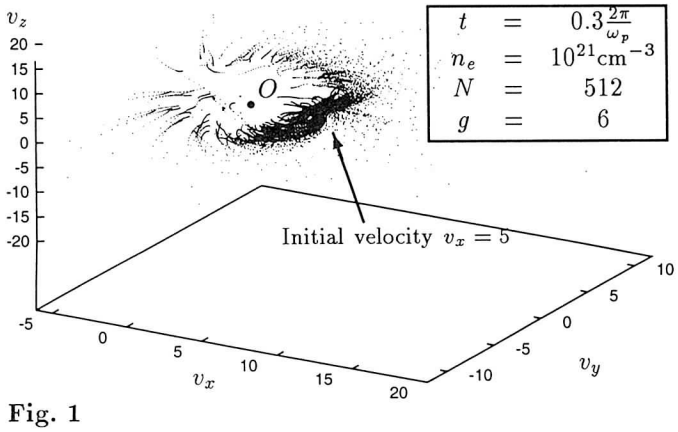

Fig. 1

Fig. 1 shows the trajectories in the velocity space. The electrons start at the point $v_x = 5$, $E_{\mathrm{kin}} = 27\,\mathrm{eV}$. Electron-ion collisions do not change the energy of the electrons because of the large mass of the ions. They only lead to isotropisation of the electron distribution. The trajectories of such collisions lie on an energy shell in velocity space. Electron-electron collisions lead to energy exchange and are neccessary to reach a Maxwell distribution. The trajectories approach the origin in v-space. The plasma parameter $g = 1/(n_e \lambda_D^3)$ is about 6, so this plasma is strongly coupled.

The formation of a hydrogen plasma

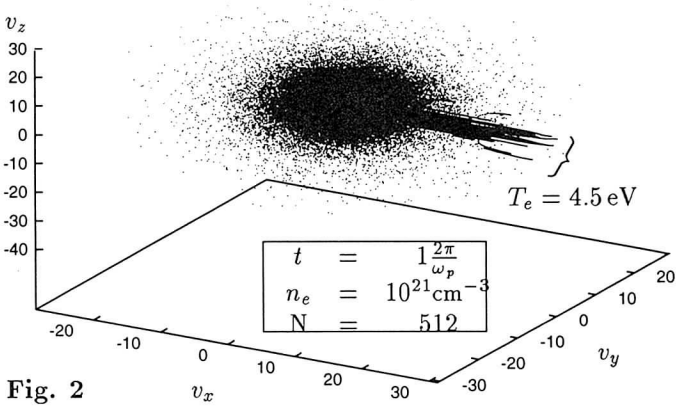

Fig. 2

We look at 256 hydrogen atoms at a density of $10^{21}\mathrm{cm}^{-3}$. The atoms are simulated classically by distributing the electrons microcanonically in the potential of the protons with the energy of the hydrogen ground state. This is the large cloud in Fig. 2. The system is driven by a gaussian laser pulse with a width of about 6 fs, a time period of about 3 fs (Nd) and a maximal intensity of $10^{16}\,\mathrm{W/cm^2}$. Field ionisation is the main mechanism at this intensities and the classical simulation agrees very well with quantummechanical calculations. The freed electrons assume a temperature larger than zero. It is about 4.5 eV which is in agreement with analytical calculations of D. Bauer [4] who gets a third of ionisation energy as a lower limit for the ejection energy.

Furthermore, the simulation has shown that collisional heating is effective only at low oscillation velocities of the electrons. This is because of the v_e^{-3} dependency of the collision frequency. The temperature at the maximum of the pulse after 6 fs amounts to a total of 145 eV.

This work has been supported by the European Comission through the TMR Network SILASI (Super Intense Laser Pulse-Solid Interaction), No. ERBFMRX-CT96-0043.

[1] A. W. Appel, J. Sci. Stat. Comput. **6**, pp. 85-103 (1985)
[2] J. Barnes, P. Hut, Nature **324**, pp. 446-449 (1986)
[3] S. Augst, D.D. Meyerhofer,D. Strickland and S.L. Chin, J. Opt. Soc. Am. B **8**, pp. 858 (1991)
[4] D. Bauer, Phys. Rev. A **55**(3) (1997)

*email: ralf@tqe2.iap.physik.th-darmstadt.de

Exact Field Ionization Rates in Intense Laser Fields

D. Bauer, P. Mulser, TQE, TU Darmstadt

In order to treat the plasma formation process in intense laser pulse-solid interaction correctly the knowledge of field ionization rates is of importance. Already for laser intensities about 10^{16} W/cm^2 the electric field of the laser light is as strong as the Coulomb attraction between electrons and atomic core. Thus, a perturbative treatment of the ionization process is not possible.

In this contribution we present numerically determined ionization rates obtained by solving the time-dependent Schrödinger equation (TDSE) for hydrogen (or hydrogen-like ions) in linear polarized laser light [1]. The TDSE reads (in cylindrical coordinates and electric laser field in z-direction)

$$\mathrm{i}\frac{\partial}{\partial t}\psi = -\frac{1}{2}\left(\frac{1}{\rho}\frac{\partial}{\partial\rho}\left(\rho\frac{\partial}{\partial\rho}\right) - \frac{m^2}{\rho^2} + \frac{\partial^2}{\partial z^2}\right)\psi$$

$$+(zE(t) - \frac{Z}{\sqrt{\rho^2+z^2}})\psi.$$

For a laser field strength $E = 0.15$ atomic units (a.u.) (1 a.u.$= 5.1\times10^9$V/cm) even a classically treated electron (on a planetary-like orbit of correct binding energy $\mathcal{E} = -0.5$ a.u.) is able to escape from the nucleus [2]. This is so-called "barrier suppression ionization" (BSI) [3] since the effective potential formed by the Coulomb-potential and the external laser field exhibits a barrier which lies below the ground state energy level, i.e., the electron need not to tunnel.

In the literature several tunneling ionization formulas are known. Among these, the Landau formula [4], ADK- [5] or KFR-theory [6, 7] are the most prominent ones. Recently, ionization rate formulas for the BSI regime were proposed [8, 9].

In Fig. 1 numerically determined ionization rates W for atomic hydrogen in the BSI region are compared with rates predicted by the theories mentioned above. The numerical data points were obtained for various pulse shapes, lengths, and frequencies. Agreement with the analytical curves is not good. In the tunneling models depletion of the ground state is not accounted for while in the classical model by Posthumus *et al.* it is the influence of the laser field on the inner-atomic dynamics (i.e. before ionization) which is neglected. However, both assumptions are not true in the BSI regime.

Once the ionization rate is of the order of the laser frequency, almost complete ionization occurs within a few half laser cycles. Thus, the region $W \approx 0.1$ a.u. is of particular interest (one atomic frequency unit is 4.1×10^{16} s^{-1}). In that region the numerically obtained results can be nicely fitted by $W = 2.4E^2$. In a recent publication [10] we show that this simple rate is indeed capable of reproducing the ground state populations during the course of the laser pulse for a wide range of peak field strengths, pulse lengths and shapes, and laser frequencies.

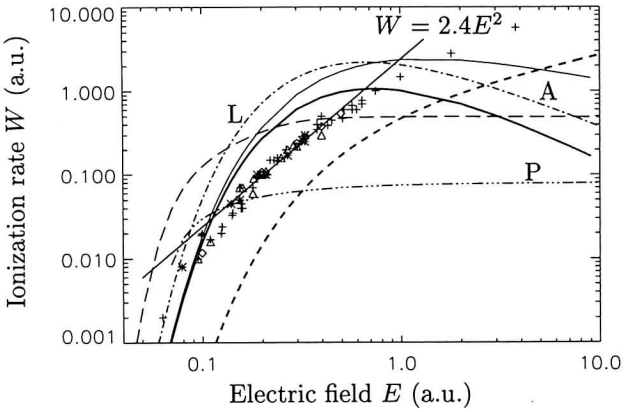

Figure 1: Numerically determined ionization rates compared with several analytical models (e.g., Landau formula L, ADK result A, and the classical rate by Posthumus *et al.* P). Agreement is rather poor. The ionization rate in the region of interest can be fitted by $W = 2.4E^2$ (in a.u.).

We conclude that even for the simplest atom we can think of, i.e., atomic hydrogen, none of the well-known theories cited predict correctly the ionization rate in short intense laser pulses reaching the BSI regime. Extrapolation of tunneling theories to BSI is not permitted. From the numerical results we deduce that a successful theory must take depletion effects into account. In classical approaches the influence of the external field on the electron's inner atomic dynamics must not be neglected.

An empirical formula for the BSI rate has been proposed. This formula is not sensitive to pulse shapes and laser frequencies in a wide parameter range.

This work was supported in part by the European Commission through the TMR Network SILASI (Super Intense Laser Pulse-Solid Interaction), No. ERBFMRX-CT96-0043 and by the Deutsche Forschungsgemeinschaft (DFG).

References

[1] D. Bauer, Ph.D.-Thesis, TH Darmstadt, 1997, (in german)
[2] D. Bauer, *Phys. Rev. A* **55**, 2180 (1997)
[3] S. Augst et al., *J. Opt. Soc. Am. B* **8**, 858 (1990)
[4] L. D. Landau and E. M. Lifshitz, *Quantum Mechanics*, 3rd revised edition, (Pergamon, Oxford, 1977), p. 294
[5] M. V. Ammosov et al., *Sov. Phys. JETP* **64**, 1191 (1987), [Zh. Eksp. Teor. Fiz. **91**, 2008 (1986)]
[6] L. V. Keldysh, *Sov. Phys. JETP* **20**, 1307 (1965), [Zh. Eksp. Teor. Fiz. **47**, 1945 (1964)]
[7] Howard R. Reiss, *Phys. Rev. A* **22**, 1786, (1980); F. H. M. Faisal, *J. Phys. B* **6**, L89 (1973)
[8] V. P. Krainov, in *Multiphoton Processes 1996*, edited by P. Lambropoulos and H. Walther, Inst. Phys. Conf. Proc. No. 154 (Institute of Physics and Physical Society, Bristol, 1997), p. 98
[9] J. H. Posthumus et al., in Ref. [8], p. 298
[10] D. Bauer and P. Mulser, submitted for publication in Phys. Rev. A

A Simulation-supported Simple View of Intense Laser-solid Interaction

S. Hain, P. Mulser; Theoretische Quantenelektronik (TQE), TU-Darmstadt, Hochschulstr. 4A, 64289 Darmstadt

A relativistic 1D Vlasov simulation for $I = 10^{19}\,\mathrm{Wcm}^{-2}$, $\lambda = 0.8\,\mu\mathrm{m}$ has been used to get some insight in the creation process of fast electrons in intense laser-solid interaction at perpendicular incidence. By the support of test particle calculations we obtain the following physical picture:

- Fast electrons are generated every half a laser cycle in the matter-vacuum interface (see Fig. 1). The mechanism is strongly related to the Brunel effect [1]. Furthermore, the generation process also seems to have a stochastic feature as can be seen from the comparison with test particle calculations: in this context the main signature is the chaotic motion of electrons in a standing wave.

- The fast electrons represent a ballistic energy transport into the solid. In the solid only a small fraction of the particles are fast electrons ($\sim 1\%$). Their current is compensated by a return current. Therefore, in 1D there is no evidence for the fast electrons in the particle current. However, they can be clearly detected in the energy current (see Fig. 2b). The absorbed laser energy ($\sim 50\%$) goes completely into fast electrons and large secular electric (and as to be expected in 2D also in magnetic) fields (see Figs. 2).

- A strong backholding electric field builds up near the critical surface ($\sim 0.5\,E_L$) and binds most of the electrons which results in a hydro-like behavior of the bulk plasma. Here, test particles show regular motion and collective behavior. Furthermore, as a typical hydrodynamic process shock formation can be observed.

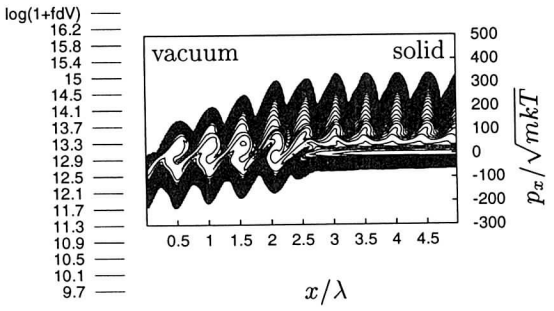

Fig. 1: Contour plot of the distribution function $f(x,p)$: electrons are extracted from the critical surface into vacuum, gain energy in the partially standing wave and are sent back into the solid supported by the space charge field ($E_{\mathrm{kin}} \simeq 2$ MeV). There, they build only a small fraction of the whole electron ensemble ($\sim 1\% \approx n_c/n_o$); parameters: $I = 10^{19}\,\mathrm{Wcm}^{-2}$, $\lambda = 0.8\,\mu\mathrm{m}$, $kT = 1$ keV, $n_o = 10^{23}\,\mathrm{cm}^{-3}$. The vacuum-solid interface is located at $x/\lambda \simeq 2.5$.

These results have been obtained by solving the Vlasov-Maxwell system for the fields $E_x(x,t), E_y(x,t), B_z(x,t)$ and the electron distribution function $f(x,p_x,p_y,t)$. Due to the conservation of the transverse canonical momentum one can write $f(x,p_x,p_y,t) = \tilde{f}(x,p_x,t)\,\delta(p_y - eA_y(x,t))$ with $E_y = -\partial_t A_y$, which leads to a 1D1V-Vlasov equation for the reduced distribution function $\tilde{f}$:

$$\frac{\partial \tilde{f}}{\partial t} + \frac{p_x}{p^0}\frac{\partial \tilde{f}}{\partial x} - \left(eE_x + \frac{e^2}{2p^0}\,\partial_x A_y^2\right)\frac{\partial \tilde{f}}{\partial p_x} = 0$$

with $p^0 = (m^2 + p_x^2 + e^2A_y^2)^{1/2}$. The ions are treated hydrodynamically as an electrically charged cold fluid.

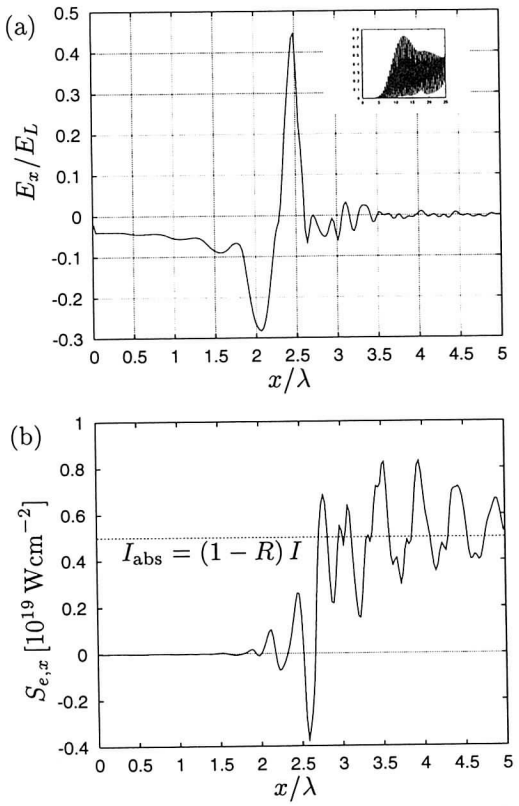

Fig. 2: Longitudinal electric field E_x with its peak that is pulsating with frequency $2\omega_L$ (see upper right corner) at the critical surface (a) and energy flow of the electrons (b), reflection $R = 50\%$. In the solid and at the interface the electron current density j_x has a shape similar to E_x. One can see a plasma wave with $\omega_{\mathrm{es}} \simeq 8\omega_L$ which has been generated at the vacuum-solid interface by the oscillating part of the force $-ev_yB_z$ and is just able to propagate into the solid. However, no contribution of the fast electrons are visible which could be identified by a $\lambda/2$-modulation in j_x.

[1] F. Brunel, Phys. Rev. Lett. **59**, 52 (1987)

Relativistic Vlasov Simulations of Short Laser Pulse Interaction with Underdense Plasma

H. Ruhl, TQE, TU Darmstadt

Introduction

Numerical simulations of laser-plasma interaction in the nonlinear relativistic regime are of importance for the study of topics such as the Fast Ignitor scheme for ICF or electron acceleration. With the advent of massively parallel supercomputers, Vlasov codes which require very large memory can now be developed as an alternative to the widely used PIC codes in the field. Due to the absence of numerical noise and high resolution Vlasov codes allow to follow the nonlinear plasma evolution on long time and small spatial scales in detail and thus help to obtain a deeper understanding of the interaction physics.

Numerical results

To show the features of 2D relativistic Vlasov simulations on parallel supercomputers, we report results on electron acceleration in a laser wakefield performed on a Cray T3E with 128 processors at the CINECA supercomputing centre (Bologna, Italy). Use is made of a novel numerical scheme which gives a linear performance scaling with the number of processors used and which can handle shocks[1]. In the simulations reported the laser pulse parameters are $I_L = 1.0-3.0\cdot10^{18}$W cm^{-2}, $\lambda = 1\mu$m and $\Delta t_L = 5$fs. The laser pulse has been injected into a preformed uniform plasma with $n_e = 5\cdot10^{19}$cm^{-3}. Figures 1 and 2 show contours of the electric wake field obtained behind the laser pulse. Figures 3 and 4 give the magnetic wake and electron current. The magnetic field oscillations along z are related to the fast electon spectrum. They are a deeply nonlinear effect [2, 3]. In the laser wakefield electrons are accelerated forwardly and laterally. The forward acceleration yields energies up to 9 MeV for the $3.0\cdot10^{18}$W cm^{-2} case. Longitudinal and lateral electron acceleration is shown in Figures 5 and 6.

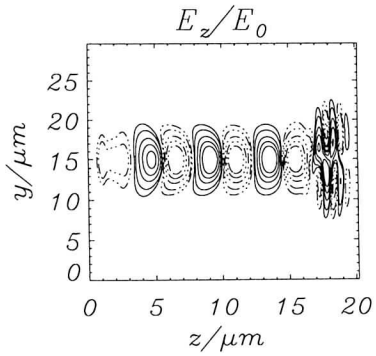

Figure 1: Laser produced E_z-wake at $\tau = 70$fs. Solid lines represent positive values.

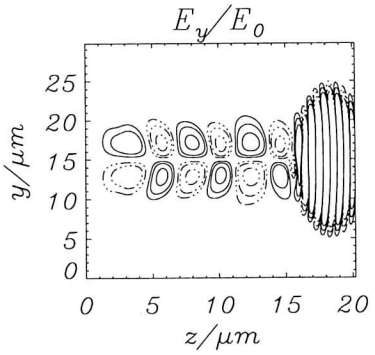

Figure 2: Laser produced E_y-wake at $\tau = 70$fs. Solid lines represent positive values.

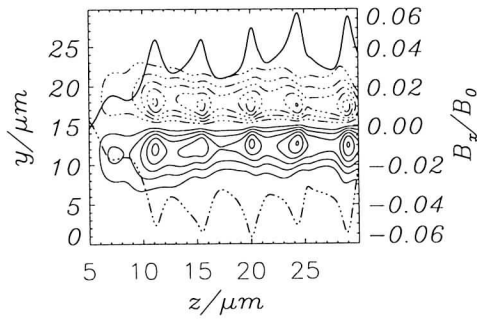

Figure 3: Laser produced B_z-wake at $\tau = 150$fs. Solid lines represent positive values. The parameter is $B_0 = 4.37\cdot10^2$ Vs/m^2.

Acknowledgements

This work has been supported by the European Commission through the TMR network SILASI (Super Intense LAser-pulse Solid Interaction), contract No. ERBFMRX-CT96-0043, and by INFM and CINECA, Italy, through a Supercomputing Project.

References

[1] H. Ruhl, F. Califano, J. D'Avanzo, and A. Macchi, submitted to Phys. Rev. E (1998).

[2] H. Ruhl, Jpn. J. of Plasma and Fusion Res. **74**, ISSN: 0918-7928, 322 (1998).

[3] F. Califano, F. Pegoraro, S. V. Bulanov, A. Macchi, R. Prandi, H. Ruhl, *Magnetic field generation by the Weibel instability in a laser plasma*, presented to LASERS 97, New Orleans (USA), Dec. 1997.

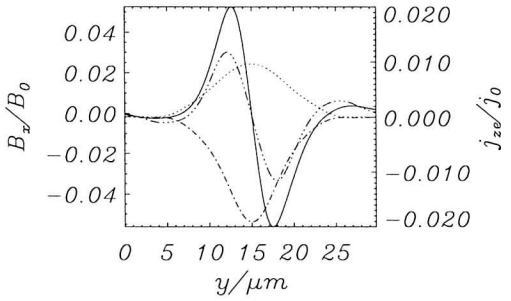

Figure 4: Radial variation of B_x at $z = \mathbf{15.0}\mu$m (dot dot dashed) and at $z = \mathbf{20.0}\mu$m (solid). The right axis gives j_{ze} at $z = \mathbf{15.0}\mu$m (dot dashed) and at $z = \mathbf{20.0}\mu$m (dotted). The parameters are $B_0 = \mathbf{4.37 \cdot 10^2}$ Vs/m^2 and $j_0 = \mathbf{4.57 \cdot 10^{16}}$ A/m^2.

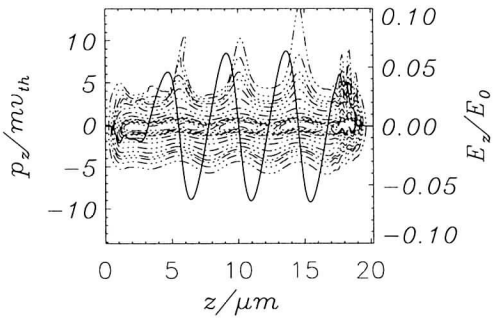

Figure 5: The zp_z-phase space projection of the electron distribution function. Fastest electrons obtain up to **10** MeV. The parameter is $E_0 = \mathbf{2.74 \cdot 10^{12}}$V/m.

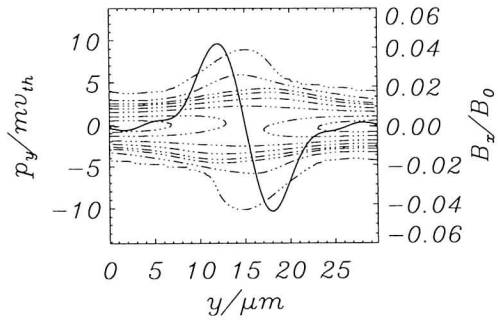

Figure 6: The yp_y-phase space projection of the electron distribution function indicating lateral currents. The parameter is $B_0 = \mathbf{4.37 \cdot 10^2}$ Vs/m^2.

Quasi-steady Electric and Magnetic Field Generation in Coronal Laser Plasmas

Hartmut Ruhl, TQE, TU Darmstadt,
Yasuhiko Sentoku and Kunioki Mima, ILE, Osaka University

Introduction

The investigation of intense laser pulse propagation in coronal laser produced plasma has recently attracted great attention. This is due to its relevance for ICF related applications like the fast ignition concept [1]. It is the idea of the latter to heat high density fusion material by fast laser produced electrons. In order that the concept works a density depleted channel extending to many times the critical density has to be created. It is the hope that this can be done by intensive laser beams. Recently, experimental evidence for laser produced density channels in underdense plasma has been reported [2, 3, 4]. However, the laser related fast ignition depends on a detailed understanding of intense laser pulse propagation through plasma as well as on fast electron transport properties in highly overdense material. The latter in turn are affected by quasi-steady electric and magnetic fields. Here we report results from relativistic Vlasov simulations of an intense laser beam incident on a preformed plasma with linear density gradient.

Numerical results

The laser pulse has radial and temporal Gaussian beam envelopes. The plasma density gradient is linear and extends to 10 times the critical density. The laser beam propagates in the positive z-direction. The radial beam diameter at full-width half-maximum is 5 μm. The intensity is $I = 2.0 \cdot 10^{18}$ Wcm^{-2} and the wavelength 1 μm. The background plasma is assumed to consist of hydrogen. The boundary conditions for the simulation are such that fast electrons can escape from the simulation area at the low as well as at the high density edge. The simulation time is measured from the time when the peak intensity enters the left boundary of the simulation box.

Figure 1 shows the laser produced electron shock and plasma channel formation. The electron density depletion can be infered from the overplotted density lines. Figure 2 yields the quasi-steady electric field E_z. The electric field strength in front of the electron shock acquires $6 \cdot 10^{11}$ V/m. The largest values for the electric field are obtained inside the laser produced channel. Figure 3 gives the quasi-steady magnetic field. The topology of the field is rather complicated. The highest magnetic field amplitudes are produced at the electron shock interface. For clarity the transverse field values at the shock interface and the longitudinal ones in the middle of the simulation box are overplotted. At the shock interface we obtain a magnetic micro-lens which focuses electrons that propagate into positive z-direction. The quasi-steady magnetic field strength of the micro-lens is approximately 2200 Vs/m^2. Due to the combined impact of the quasi-steady electric and magnetic fields close to the shock interface most of the electrons propagate in lateral direction into low density plasma. Since the plasma has to remain quasi-neutral these electrons change propagation direction again. Hence, we obtain the outer large area magnetic fields seen in Figure 3.

From the modulated magnetic field in the channel itself we may deduce the ion shock velocity and ultimately the total fractional absorption. To understand this we treat the electron shock as a moving mirror for the electromagnetic radiation with constant velocity v_s. We find for the quasi-steady electric and magnetic fields

$$E_y = \frac{E_0}{\pi} \frac{1}{1-\frac{v_s^2}{c^2}} \times \left(\sin\left[\frac{\omega z}{c} - \frac{2\pi v_s}{c}\right] - \sin\left[\frac{\omega z}{c}\right] \right) , \quad (1)$$

$$cB_x = -\frac{E_0}{\pi} \frac{1}{1-\frac{v_s^2}{c^2}} \times \left(\sin\left[\frac{\omega z}{c} - \frac{2\pi v_s}{c}\right] - \sin\left[\frac{\omega z}{c}\right] \right) , \quad (2)$$

$$v_s = \sqrt{(1+|R|^2)\frac{2I}{\rho_i c}} , \quad (3)$$

where R denotes the reflection coefficient, ρ_i the mass density of the ions and v_s the ion shock speed. Inserting the value of 900 Vs/m^2 from Figure 3 we obtain $v_s/c \approx 1/28$ for the normalized ion shock speed. This value agrees with the direct measurement of the latter which yields $v_s \approx 1.0 \cdot 10^7$ m/s. Knowing the shock speed of the ions the reflection coefficient may be determined from (3). Taking $\rho_i = 1.78$ kg/m^3 for the mass density of hydrogen we obtain $|R|^2 \approx 0.5$. The simulation yields $|R|^2 \approx 0.47$ in acceptable agreement with the simple model presented.

We now look at later simulation times and turn to the highly overdense part of the simulation box (behind the magnetic micro-lens). Figure 4 gives the quasi-steady magnetic field in the range from $4n_c$ to $10n_c$ at $\tau = 200$ fs. At this time the electron shock interface is located at $z = 2.4$ μm. The field strengths of the magnetic lens at the electron shock front has values of 4500 Vs/m^2 (not shown). The figure shows quasi-steady magnetic fields with a bubble-like structure. The magnetic field bubbles acquire values of up to 2600 Vs/m^2 with the tendency to higher field strengths at higher plasma densities. Figure 5 shows the temporal evolution of the field strength of the quasi-steady magnetic field at $z = 5.5$ μm. Recalling that 3000 Vs/m^2 suffice to trap electrons with a kinetic energy close to their rest mass to gyroradii of about 1 μm, we expect that these magnetic fields affect electron as well as ion transport properties in the overdense plasma. The mean electron gyroradius around the magnetic bubbles is about 0.4 μm. This value is close to the classical skin length of the electron plasma at $10n_c$, a typical length scale for the Weibel mechanism [5, 6, 7].

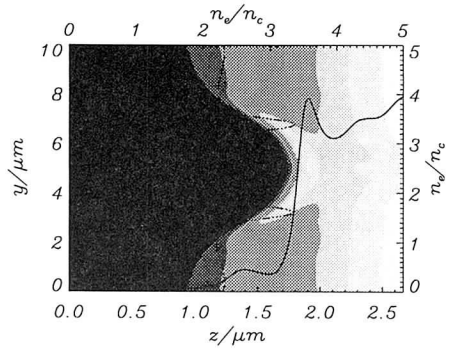

Figure 1: Laser produced electron shock. The overplotted lines give n_e at $z = 1.66$ μm and at $y = 5.0$ μm. The simulation time is $\tau = 110$fs.

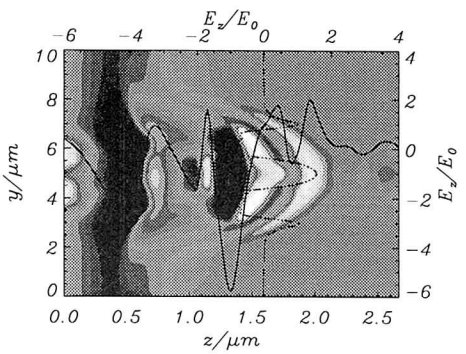

Figure 2: Quasi-steady electric field. The overplotted lines give E_z at $z = 1.66$ μm and at $y = 5.0$ μm. The parameter is $E_0 = 3.88 \cdot 10^{11}$ V/m^2. The simulation time is $\tau = 110$ fs.

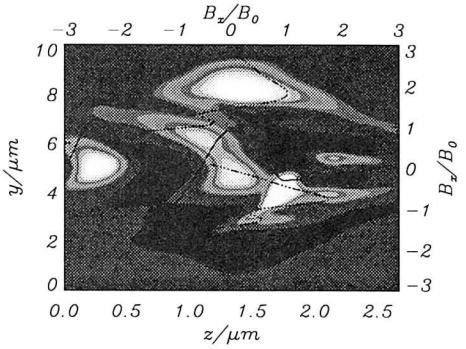

Figure 3: Quasi-steady magnetic field. The overplotted lines give B_x at $z = 1.66$ μm and at $y = 5.0$ μm. The parameter is $B_0 = 9.37 \cdot 10^2$ Vs/m^2. The simulation time is $\tau = 110$ fs.

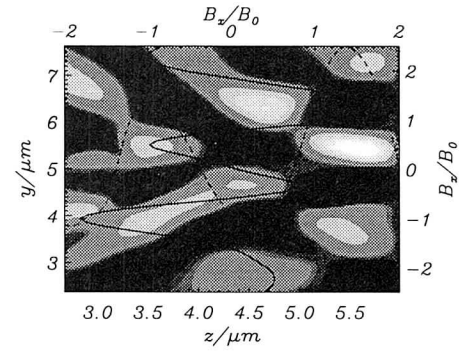

Figure 4: Quasi-steady magnetic field. The overplotted lines give B_x at $z = 4.66$ μm and at $y = 5.6$ μm. The parameter is $B_0 = 9.37 \cdot 10^2$ Vs/m^2. The simulation time is $\tau = 200$ fs.

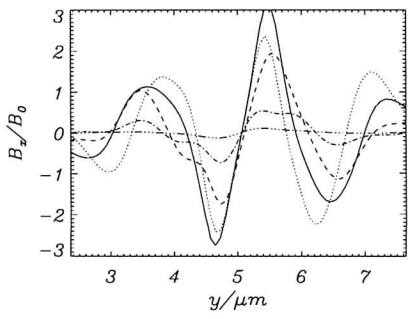

Figure 5: Temporal growth of the quasi-steady magnetic field. The times are 86 fs (dot dot dashed), 120 fs (dot dashed), 153 fs (dashed), 186 fs (solid), 220 fs (dotted). The parameter are $B_0 = 9.37 \cdot 10^2$Vs/m^2 and $z = 5.5$ μm.

Conclusion

We observed the onset and evolution of plasma filamentation instabilities at several times the critical density induced by fast electron currents. The early evolution of the latter resembles the linear growth of the Weibel instability [5]. However, at later times the quasi-steady electric and magnetic fields form islands and the field strengths of the latter saturate when the mean electron gyroradii approach the local classical skin length. After 200 fs the magnetic field strengths of the islands have grown to approximately 2700 Vs/m^2. This leads to electron gyration around the islands with a gyroradius close to the local classical skin length.

References

[1] M. Tabak, J. Hammer,M. E. Glinski, W. L. Kruer, S. C. Wilks, and R. J. Mason, Phys. PLasmas **1**, 1626 (1994).

[2] J. Fuchs, G. Malka, J. C. Adam, F. Amiranoff, S. D. Baton, N. Blanchot, A. Heron, G. Laval, J. L. Miquel, P. Mora, H. Pepin, and C. Rousseaux, Phys. Rev. Lett, **80**, 1658 (1998).

[3] M. Borghesi, A. J. MacKinnon, L. Barringer, R. Gaillard, L. A. Gizzi, C. Meyer, O. Willi, A. Pukhov, and J. Meyer-ter-Vehn, Phys. Rev. Lett. **78**, 879 (1997).

[4] V. Malka, J. Fuchs, F. Amiranoff, S. D. Baton, R. Gaillard, J. L. Miquel, H. Pepin, C. Rousseaux, G. Bonnaud, M. Busquet, and L. Lours, Phys. Rev. Lett. **79**, 2979 (1997).

[5] F. Califano, F. Pegoraro, and S. V. Bulanov, Phys. Rev. E **56**, 963 (1997).

[6] F. Pegoraro, S. V. Bulanov, F. Califano, and M. Lonatno, Physica Scripta **T63**, 262 (1996).

[7] G. Kalman, C. Montes, and D. Quemada, Phys. Fluids **11**, 1797 (1968).

Enhanced Laser Pulse Absorption and Transmission in Deformed Thin Foil Targets

Hartmut Ruhl, TQE, TH-Darmstadt,
Fulvio Cornolti, Dipartimento di Fisica, Universitá di Pisa,
Andrea Macchi, Scuola Normale Superiore, Pisa

Introduction

Recently, experimental results of sub-picosecond laser pulse interaction with thin foil targets have been reported, showing unexpectedly high levels of pulse transmission [1, 2]. Using 2D relativistic Vlasov simulations we show that if the target is not planar but has a prepared deformation, enhanced absorption and transmission is found [3]. In a real experiment such a deformation might be produced either by the intense short pulse or by spurious prepulse effects before interaction.

The numerical experiment

We use 2D2V relativistic Vlasov simulations to investigate the interaction of a **80** fs, **1** μm, $\mathbf{4 \cdot 10^{18}}$ W/cm^2 laser pulse with foils that have a Gaussian deformation (see Figure 1). We investigate three cases with deformation depths $\delta = \mathbf{0}$ μm, **1** μm, and **2** μm. The deformation widths, initial foil thicknesses, and densities for the three cases are $\gamma = \mathbf{3.6}$ μm, $d = \mathbf{0.2}$ μm and $n_e = \mathbf{15} n_c$, where n_c is the critical density for the laser light. After a finite rise time the laser beam intensity is kept constant. The radial laser beam diameter is **5** μm (FWHM). The maximum of laser intensity along y coincides with the center of the deformation.

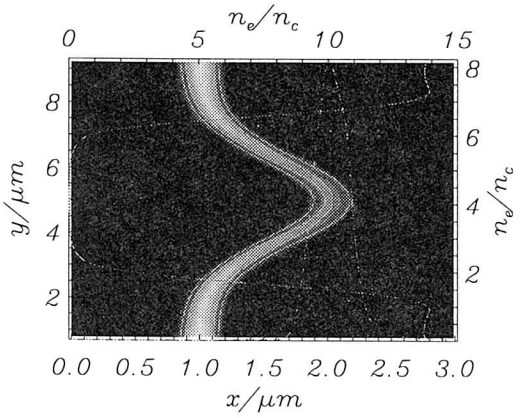

Figure 1: Contours of n_e for $\delta = \mathbf{1}$ μm, at $t = \mathbf{66}$ fs.

Absorption and transmission enhancement

Figure 2 gives fractional absorption and transmission of the laser energy as a function of time for $\delta = \mathbf{0}$ μm, **1** μm, and **2** μm. Absorption and transmission start to rise at $t \approx \mathbf{20}$ fs. Absorption tends to saturate at $t \approx \mathbf{80}$ fs at values between **40%** and **80%**. Transmission values obtained in our simulations are between **4%** and **8%** at $t \approx \mathbf{80}$ fs. Saturation of transmission is observed only for the planar target at $t \approx \mathbf{70}$ fs.

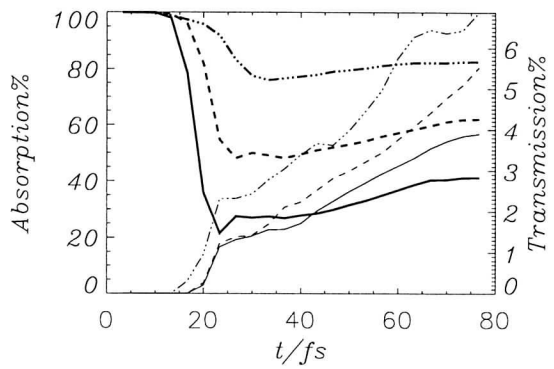

Figure 2: Fractional absorption (bold) and transmission (thin) vs. time. Planar (solid) and deformed target results with $\delta = \mathbf{1}$ μm (dashed) and $\delta = \mathbf{2}$ μm (dot dot dot dashed) are given.

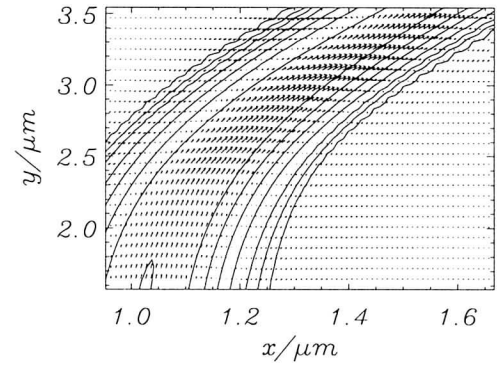

Figure 3: Vector field of electron flows on the sides of the target.

From Figure 1 we find that the electron density is depleted in the center of the foil deformation, where a high kinetic temperature of $\approx$ **500** keV is found. The density depletion increaes for deeper deformations. In the central region highest laser transmission is observed.

Figure 3 shows the quasi-steady electron density flows in the periphery of the deformation. Fast electrons generated in the laser-plasma interaction in this outer region flow parallel to the surface of the foil into the center of the deformation, and the flow velocity increases approaching the center. Qualitatively, the steady electron flows are generated on the periphery of the deformation, where the laser is obliquely incident, and electrons acquire parallel momentum from the light wave. Due to the particular deformed geometry the flows from both sides point to the central region. A more detailed investigation of absorption in a deformed density profile is in progress and will be reported elsewhere.

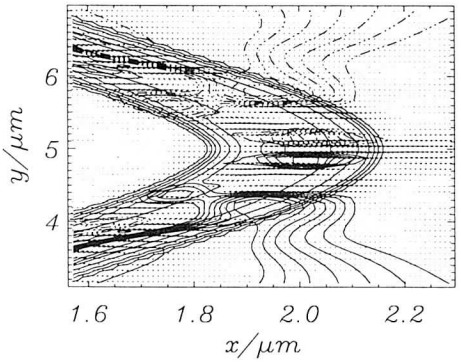

Figure 4: Vector field of electron flows and magnetic field contours in the central spot of the target.

In the central region we observe that the electron currents gyrate around magnetic filaments (see Figure 4). The magnetic field pinches electrons and redirect them into the longitudinal (x) direction. After **66** fs the quasi-steady magnetic field in the filaments begins to saturate at about **16** MG. The structure and scalelengths of the magnetic field and current patterns seem to be consistent with those generated by a nonlinear Weibel instability [5] driven by the magnetic repulsion of the counterpropagating lateral currents flowing into the central region.

Comparison with experiments

Our simulation results overlap qualitatively with many features of recent experiments, giving an indication of the important role of target deformations. In [2] high transmission in a small central spot, and correlation between transmission and high absorption are found. In [4] experimental data suggest important target deformation effects and the existence of electrons with high tangential velocity.

We point out that mechanisms leading to target deformation are not self-consistently included in our simulations, since they should occur on much longer time scales, and thus must be discussed separately. Here we focus on deformations induced by radiation pressure. The overall momentum q that the target has to gain in order to perform a displacement $\delta \approx 1$ μm during a time t_p is $q \approx \rho(2r_s)^2 d\delta/t_p$, where ρ is the mass density and $2r_s$ is the deformation width which we suppose to match the laser spot diameter. The momentum due to the radiation pressure is $i = (P_p t_p/c)(1 + R - T)$, where P_p, T and R are the mean power, the transmission and reflection coefficients of the laser pulse. By imposing $i = q$ we find the required laser intensity

$$I_p = \frac{4\rho c \delta d}{\pi t_p^2 (1 + R - T)} \qquad (1)$$

For a plastic foil with $\rho \approx 10^3$ Kgm^{-3}, $d = 0.2\mu$m, and $R - T \approx 1$, we find that intensities of $3 \cdot 10^{19}(3 \cdot 10^{21})$ W cm^{-2} are needed for short interaction pulses with $t_p = 300(30)$ fs to induce a deformation $\delta \approx 1$ μm. If we consider a long-duration, low-intensity prepulse, we find that intensities of $2.8 \cdot 10^8(2.8 \cdot 10^{10})$ W cm^{-2} for $t_p = 100(10)$ ns are sufficient to push the target as required; these values might remain below the target damage threshold. For Al targets long prepulses are needed because of higher ρ and lower damage threshold. Thus different experiments with the same short pulse interaction parameters might give very different results because of the variability of the target and prepulse conditions.

This work has been supported by the European Commission through the TMR network SILASI (Super Intense LAser-pulse Solid Interaction), contract No. ERBFMRX-CT96-0043.

References

[1] D. Giulietti *et al*, Phys. Rev. Lett. **79**, 3194 (1997)

[2] J. Fuchs *et al*, Phys. Rev. Lett. **80**, 2326 (1998)

[3] H. Ruhl, F. Cornolti, and A. Macchi, submitted to Phys.Rev.Lett. (1998).

[4] T. Feurer *et al*, Phys. Rev. E **56**, 4608, (1997).

[5] F. Califano, F. Pegoraro, and S. V. Bulanov, Phys. Rev. E **56**, 963 (1997).

Multi-MeV Electrons from Relativistic Self-Focusing in Underdense Plasmas: 3D Particle-In-Cell Simulations

A. Pukhov and J. Meyer-ter-Vehn
Max-Planck-Institut für Quantenoptik, Garching-bei-München, Germany

A laser beam propagating in underdense plasma with a plasma frequency ω_p smaller than the laser frequency ω undergoes relativistic self-focusing as soon as its total power P exceeds the critical value [1]

$$P_c \approx 17\,(\omega/\omega_p)^2 \;\; GW. \qquad (1)$$

The self-focusing is due to the relativistic mass increase of plasma electrons and the ponderomotive expulsion of electrons from the pulse region. Both effects lead to a local decrease of plasma frequency and an increase in refractive index. The medium then acts as a positive lens.

Self-focusing of a laser with $P \geq P_c$ in three-dimensional geometry leads to strong intensity enhancement on axis [2]. Simultaneously the three-dimensional self-modulation of the laser pulse sets in [4], generating high amplitude plasma waves. It is expected, that these waves break due to the 1D [5, 6] or the 2D [7] mechanism, trapping and accelerating background plasma electrons to high energies as it has been observed recently in experiments [8, 9]. Detailed experimental studies show that the fast electrons first appear above some threshold in the laser power [9] and plasma density [10], and this threshold is found to be consistent with (1).

To gain more insight in the actual mechanism of electron acceleration we have carried out a series of 3D PIC simulations [3]. We used a laser pulse of a Gaussian form with radius $r = 8.5\ \mu$m, and duration 460 fs propagating through plasma with density $n = 0.036 n_c$ over 0.6 mm distance. The laser power was varied from 0.16 to 6 P_c, where $P_c = 470$ GW in this case. The conditions of the simulations were similar to an experiment reported in [9].

A characteristic evolution of a laser pulse with $P > P_c$ is shown in Fig. 1a for $P = 4P_c$. Three regions are seen: (1) the diffracted low-power head; (2) the depleted region behind the head, where laser energy has been consumed to produce the plasma wake; and (3) the focused and modulated tail of the pulse which experiences hosing [11] at the end of interaction.

Energy spectra of accelerated electrons are shown in Fig. 1b. We observe in our simulation that the laser pulse is already strongly self-modulated even at powers much less than the critical power for self-focusing. The energetic electrons, however, appear only for $P > P_c$. Although the self-modulation process at $P < P_c$ produces strong plasma waves, their amplitude is still insufficient to break longitudinally and trap background electrons. The situation changes drastically when the laser power overcomes the threshold (1). Then we observe a dramatic contraction

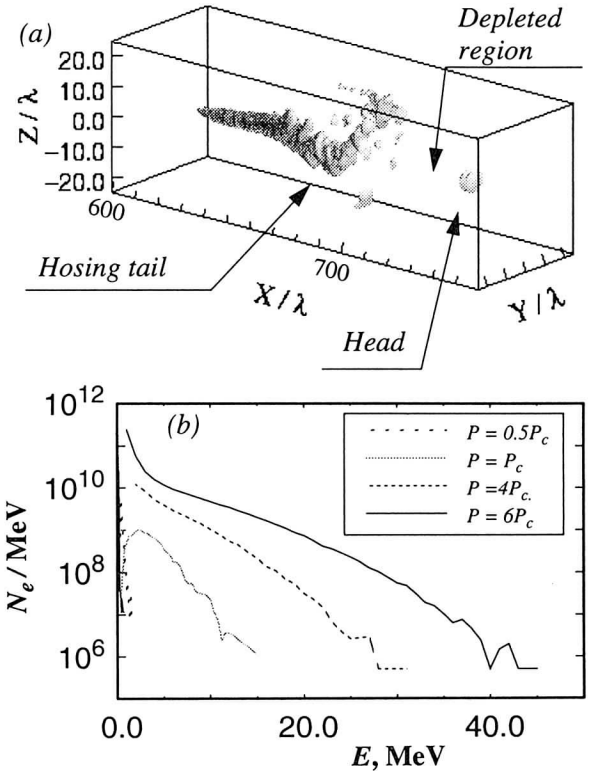

Figure 1: 3D PIC simulations of relativistic self-channeling in an underdense plasma with density $n = 0.036 n_c$ for different laser powers. (a) Laser pulse with $P = 4P_c$, when having passed 0.6 mm plasma; (b) Energy spectra of "real" accelerated electrons; each "numerical" electron substitutes 2.5×10^5 real electrons.

of the laser pulse in transverse direction due to the self-focusing. Transverse extention of the plasma waves diminishes correspondingly, and the wake breaks *transversely*. It has been shown recently [7] that the transverse wave breaking happens at significantly lower amplitudes than the longitudinal one, and the critical amplitude is the less, the narrower is the wake. Apparently, the wave breaking is *catalyzed* by self-focusing of the laser pulse.

The energy distibution of fast electrons in Fig. 1b resembles a Boltzmann one with a long smooth roll-off at high energies. The "effective temperature" T_{eff} of the distribution increases with the laser power, reaching $T_{eff} \sim 7.5$ MeV at $P = 6P_{cr}$.

Fig. 2 gives more insight in the process of acceleration for the high-power case $P = 6P_c$. It is interesting to see that only the head of the laser pulse is modulated with the

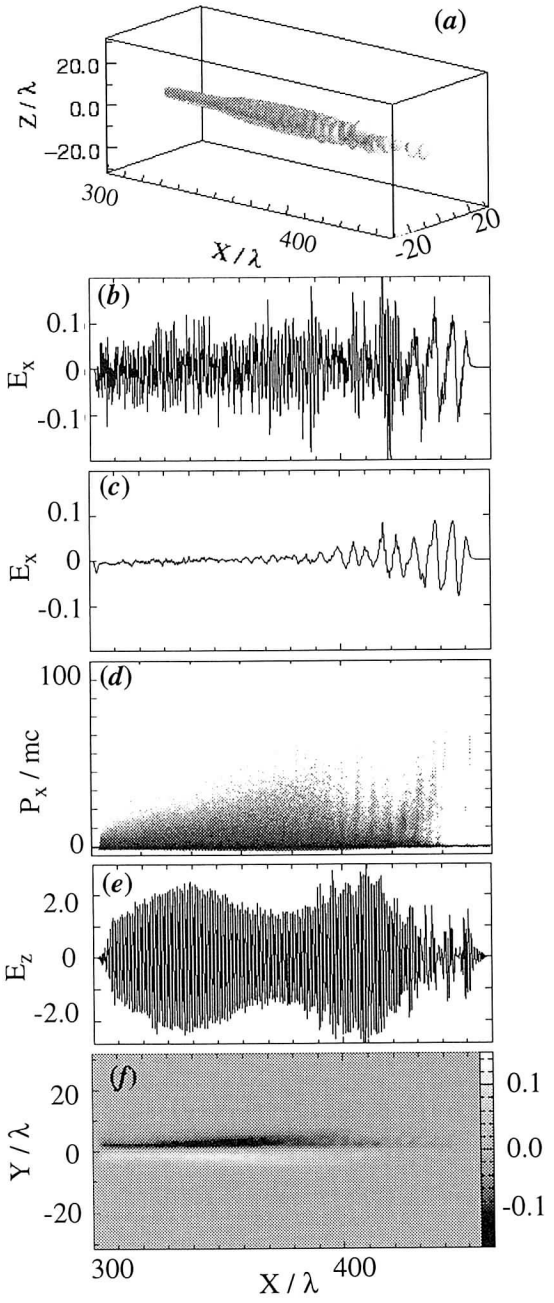

Figure 2: More details on electron acceleration mechanism (a) Laser pulse with $\boldsymbol{P = 6P_c}$, after 0.3 mm of plasma. (b) Unaveraged dimensionless electric field $\boldsymbol{E_x = e\mathrm{E}_x/mc\omega}$. (c) $\boldsymbol{E_x}$, all modes with wavelengths shorter than $\boldsymbol{\lambda}$ are filtered out. (d) Electron phase space; (e) Dimensionless laser electric field $\boldsymbol{E_z = e\mathrm{E}_z/mc\omega}$ on axis; (f) $\boldsymbol{(X, Y)}$ cut of the quasi-static magnetic field $\boldsymbol{B_z = e\mathrm{B}_z/mc\omega}$.

plasma wavelength, and only a few regular plasma wave periods exist, as it is seen in Fig. 2b,c. This agrees with the transverse wave breaking scenario [7]. The electron phase space, Fig. 2d, is also strongly modulated with the plasma wavelength in this region, corroborating the SM-LWFA acceleration mechanism acting here. This region contains electrons with the highest, up to **30** MeV, energies.

However, the phase space shows also another, *unmodulated* region containing fast electrons with energies up to $\mathbf{15 - 20}$ MeV. This region corresponds to the tightly focused high-intensity tail of the laser pulse, where *no regular wake exists*. Electron acceleration here looks more like a direct anisotropic heating by the laser pulse. Actually, this is the $\boldsymbol{B}$−loop acceleration mechanism [3, 12]. Fig.2e gives the dimensionless $\boldsymbol{E_z}$ field on the axis with the maximum amplitude $\boldsymbol{eE_{max}/mc\omega \sim 2.5}$. The azimuthal magnetic field, Fig.2f, surrounds the focused tail of the laser, and reaches up to $\boldsymbol{eB_z/mc\omega \sim 0.15}$. These parameters of the laser pulse and the magnetic field correspond to our numerical example [3, 12]. The maximum observed energies of electrons are also similar.

Aknowledgements

This work was supported by EURATOM, DFG and BMBF.

References

[1] G. Schmidt and W. Horton, Comments Plasma Phys. & Contr. Fusion **9**, 85 (1985);

[2] A. Pukhov and J. Meyer-ter-Vehn, Phys. Rev. Lett. **76**, 3975 (1996).

[3] A. Pukhov, and J. Meyer-ter-Vehn, *to appear in* Phys. Plasmas, **5**, *May issue*, (1998).

[4] E. Esarey, J. Krall, and Ph. Sprangle, Phys. Rev. Lett. **72**, 2887 (1994).

[5] A. I. Akhieser, and R. V. Polovin, JETP **3**, 696 (1956).

[6] S. V. Bulanov, F. Pegoraro, and A. Pukhov, Phys. Rev. Lett. **74**, 710 (1995).

[7] S. V. Bulanov, F. Pegoraro, A. Pukhov, A. S. Sakharov, Phys. Rev. Lett. **78**, (1997).

[8] A. Modena, Z. Najmudin, A. E. Dangor, C. E. Clayton, K. A. Marsh, C. Joshi, V. Malka, C. B. Darrow, C. Danson, D. Neely, and P. N. Walsh, Nature (London) **377**, 606 (1995); D. Umstadter, S.-Y. Chen, A. Maximchuk, G. Mourou, and R. Wagner, Science **273**, 472 (1996).

[9] R. Wagner, S.-Y. Chen, A. Maksimchuk, and D. Umstadter, Phys. Rev. Lett. **78**, 3125 (1997).

[10] R. Fedoseevs, X. F. Wang, and G. D. Tsakiris, Phys. Rev. E, **56**, 4615 (1997).

[11] G. Shvets, and J. Wurtele, Phys. Rev. Lett **73**, 3540 (1994).

[12] A. Pukhov, J. Meyer-ter-Vehn, *Magnetic Field Assisted Particle Acceleration,* This issue.

MeV Electrons and Fusion Neutrons from Deuterium Plasma Irradiated by TeraWatt Laser: 3D Particle-in-Cell Simulations

A. Pukhov and J. Meyer-ter-Vehn
Max-Planck-Institut für Quantenoptik, Garching-bei-München, Germany

A relativistically strong laser pulse drives intense currents of MeV electrons in the forward direction [1, 2]. These currents of accelerated electrons interacting with solid-state material can be used as a source of ultra-short X-ray pulses [3], γ−rays, and nuclear radiation [4]. The simplest experimental configuration is a solid state target with an ablatively preformed plasma in front of it. The scale length of the preformed plasma is one of the most crucial parameters influencing the energy spectrum of the fast electrons and the conversion efficiency into other forms of radiation. It has been shown by PIC simulations [5] that when the laser pulse directly interacts with *a sharp edge* of solid density material, the suprathermal electrons have approximately a Boltzmann distribution with an effective temperature

$$T_e = \left[\sqrt{1+\frac{I\lambda_\mu^2}{4\times 10^{18}}}-1\right] mc^2, \qquad (1)$$

where I is the laser intensity in W/cm^2 and λ_μ is the wavelength in micrometers. Applying (1) for a 1 TW laser pulse focussed on the surface up to an intensity of $I \sim 10^{18}$ W/cm^2, we estimate the temperature of the suprathermal electrons to be as low as $\sim$ 60 keV. This disappointing value is quite understandable. The interaction length at the solid state surface is too small, smaller than the laser wavelength, and even if the laser field is as large as 30 GV/cm, the electrons can not gain much energy on that distance.

To show the importance of the underdense region we have made 3D PIC simulations of plasma with an exponential density profile $n_e = n_c \exp(-x/d_p)$, where $n_c = 10^{21}$ cm^{-3} is the critical density for 1 μm wavelength laser pulse. The laser pulse had a Gaussian shape in time with a FWHM duration $T_{laser} = 200$ fs, and a FWHM diameter of the focal spot $D_{laser} = 9$ μm The spectra of accelerated electrons obtained in three runs for different density ranges d_p and peak laser intensities are presented in Fig. 1. *In the run I* the maximum intensity was $I_0 = 1.5 \times 10^{18}$ W/cm^2, and the peak laser power about 1 TW. The effective temperature of the suprathermal electrons $T_I \approx 0.83$ MeV should be compared with the "pessimistic" estimation $T_e = 0.06$ MeV according to (1). The effect of the underdense region is profound.

In the run II we have used a 10× steeper plasma density profile with $d_p = 3$ μm. The obtained spectrum of fast electrons, line *II* in Fig. 1, has an effective temperature $T_{II} \approx 0.2$ MeV, that is roughly 4 times lower than T_I. The total number of accelerated electrons was also significantly lower: $N_{II} = 3.0 \times 10^9$ electrons versus $N_I = 17.3 \times 10^9$ in the first run. *In the third run, III,* the plasma parameters were the same as in run *I*, but the laser intensity was 10 times higher, $I_0 = 1.5 \times 10^{19}$ W/cm^2. Thus, the peak laser pulse power was 10 TW. The resulting spectrum is shown as the line *III* in Fig. 1. We find the effective temperature $T_{III} \approx 3.3$ MeV, much larger than T_I.

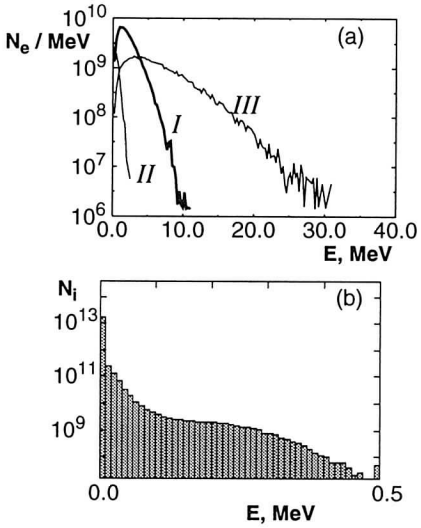

Figure 1: (a) Fast electron spectra for three runs (see text). *I*: $P = 1$ TW, $d_p = 30$ μm; *II*: $P = 1$ TW, $d_p = 3$ μm; *III*: $P = 10$ TW, $d_p = 30$ μm. (b) Deuteron energy spectrum in run *I*. Laser is incident on a nonuniform plasma with density $n_e = n_c \exp(-x/d_p)$.

As the laser pulse channels in the underdense region, it leads to electron cavitation, and then to *ion acceleration*. The ion (deuteron mass) energies obtained in the run *I*, Fig. 1b, reach up to 0.5 MeV. Deuterons with such energies make fusion reactions. Fusion neutron emission at characteristic 2.54 MeV energy has been detected experimentally at MPQ with the rate of 200 neutrons per laser shot [6].

References

[1] A. Pukhov and J. Meyer-ter-Vehn, Phys. Rev. Lett. **76**, 3975 (1996).

[2] A. Pukhov and J. Meyer-ter-Vehn, Phys. Rev. Lett., Vol 79, 2686(1997).

[3] J.D. Kmetec *et al.*, Phys. Rev. Lett. **68**, 1527 (1992); M. Schnürer *et al.*, Phys. Plasmas **2**, 3106 (1995).

[4] P. L. Shkolnikov, A. E. Kaplan, A. Pukhov, and J. Meyer-ter-Vehn, Appl. Phys. Lett., **71**, 3471 (1997).

[5] S. C. Wilks *et al.*, Phys. Rev. Lett. **69**, 1383 (1992).

[6] G. Pretzler et al., *to be published.*

Relativistic Electrons Dynamics in Intersecting Laser Pulses

Z. -M. Sheng and J. Meyer-ter-Vehn
Max-Planck-Institut für Quantenoptik, 85748 Garching

The interaction of single electrons with laser light received renewed interest owing to the recent advent of high intensity, ultrashort laser pulses. One purpose of this study is concerned with particle acceleration by use of the intense laser pulses [1]. The other aspect is that the knowledge of single electron dynamics provides an important basis for the investigation of relativistic laser plasma interaction in more complicated situation [2, 3]. The classical theory of single electrons interaction with an intense electromagnetic wave was given by Sarachik and Schappert in 1970 [4]. The present study is devoted to the interaction of electrons with two intersecting planar laser pulses. We show that the angular direction of the scattered electron is simply related to its initial and final energy. This relation is valid even for stochastic electron motion which sets in during the interaction for very intense laser pulses.

As shown in Fig.1, two laser pulses propagating at a relative intersecting angle 2α interact with an electron initially located at the origin of the given coordinate system. Assuming that the vector potential of the P-polarized planar pulses in vacuum has the form

$$\mathbf{A}_{\perp \mathrm{i}} = A_{0i}(\xi_i)\cos(\xi_i + \psi_i)(\cos\alpha\hat{\mathbf{x}} \mp \sin\alpha\hat{\mathbf{z}}), \quad i = 1, 2,$$

where $0 \le \alpha \le \pi/2$, $\xi_i = k_{0i}(z\cos\alpha \pm x\sin\alpha) - \omega_{0i}t$ is the propagation coordinate, x and z are normalized to some k_0^{-1}, t is normalized to some ω_0^{-1}, k_{0i} to k_0, and $\omega_{0i}(= k_{0i})$ to $\omega_0(= k_0 c)$, ψ_i is a constant phase, the upper and lower signs in the operation symbols $\mp$ (and $\pm$) corresponds to $i = 1$ and 2. In terms of the vector potential, the equation of electron motion is

$$\frac{d\mathbf{p}}{dt} = \frac{d\mathbf{A}}{dt} - \nabla(\mathbf{v}\cdot\mathbf{A}) + \nabla\phi, \tag{1}$$

where the momentum $\mathbf{p}$ is normalized to mc, the velocity $\mathbf{v}$ to c, the vector potential $\mathbf{A} = \mathbf{A}_{\perp 1} + \mathbf{A}_{\perp 2}$ to mc^2/e, and the first ∇ acts on $\mathbf{A}$ only, ϕ is the scalar potential normalized to mc^2/e. It is convenient to transform all variables into a frame moving with velocity $\mathbf{V} = c\cos\alpha\hat{\mathbf{z}}$, where the four-vector potential are

$$\phi_i' = \pm A_i\cos\alpha, \; A_{ix}' = A_i\cos\alpha, \; A_{iy}' = 0, \; A_{iz}' = \mp A_i,$$

assuming $\phi = 0$ in the laboratory frame, where $A_i = A_{0i}(\xi_i')\cos(\xi_i' + \psi_i)$, $\xi_i' = (\pm k_{0i}x' - \omega_{0i}t')\sin\alpha$. In the moving frame, the equation of motion reduce to

$$\frac{dp_x'}{dt'} = -v_z'\frac{\partial}{\partial x'}(A_2 - A_1), \tag{2}$$

$$p_z' = p_{z0}' + A_2 - A_1, \tag{3}$$

where p_{z0}' is the initial electron velocity in the moving frame before it interacts with the laser pulses. Equation (3) leads to a relation between the angular direction and the energy of escaping electrons. Transforming the variables back to the laboratory frame and setting $p_y = 0$ and $p_x/p_z = \tan\theta$, Eq.(3) leads to $\tan\theta = \pm[(\gamma^2 - 1)/(\gamma\cos\alpha + C)^2 - 1]^{1/2}$, with C a constant dependent on the initial conditions. For the case when the particle is initially at rest, i.e. $p_{x0} = 0$, $p_{z0} = 0$ and $\gamma_0 = 1$, it simplifies to

$$\tan\theta = \pm\left(\frac{2}{\gamma - 1} + \frac{\gamma + 1}{\gamma - 1}\tan^2\alpha\right)^{1/2}, \tag{4}$$

which is shown in Fig.2 for some given α value. Generally, the scattering angle θ ranges from α to 90° (or $-\alpha$ to $-90°$) with corresponding γ values from ∞ to 1. When $\alpha = 90°$, i.e. two pulses counter-propagate along the x-axis, one gets $\theta = \pm 90°$, i.e. $p_z = 0$. When $\alpha = 0$, i.e. two pulses co-propagate along z-axis, a well-known relation is recovered [1, 5]. For S-polarization and $p_{y0}' = 0$, the relation between p_z and p_x is the same as in P-polarization case.

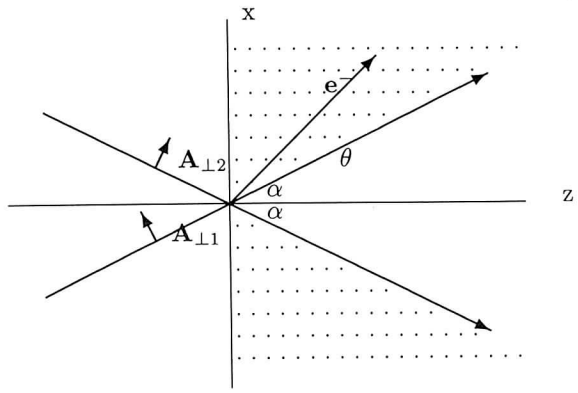

Figure 1: Electron scattering by two laser pulses. An electron is scattered in the dotted region when it is initially at rest at x=z=0.

In the moving frame, one needs only to solve the x-component of the equation of motion , then transform back to the laboratory frame. In the following, we study only the simple case when $\omega_{01} = \omega_{02} = 1$. The x-component equation of electron motion in P-polarized laser pulses is rewritten as

$$\frac{dv_x'}{dt'} = -\gamma'^{-2}(p_{z0}' + A_2 - A_1) \times \left(\frac{\partial}{\partial x'}(A_2 - A_1) + v_x'\frac{\partial}{\partial t'}(A_2 - A_1)\right), \tag{5}$$

where $\gamma'^{-1} = (1 - v_x'^2)^{1/2}/(1 + p_y'^2 + p_z'^2)^{1/2}$. This equation is solved numerically, using the Rung-Kutta-Fehlberg method with variable time-step. We assume the pulse profile in the form of $A_{0i} = a_i\sin^2(\xi_i'/\tau_i)$ for $0 \le \xi_i' \le \pi\tau_i$,

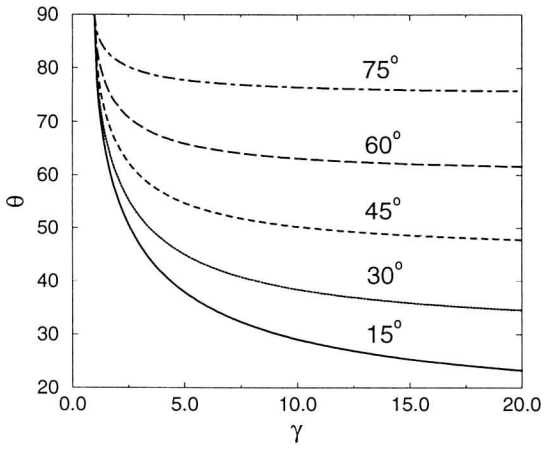

Figure 2: Scattering angles as a function of the escaping energy for $\alpha = 15°$, $30°$, $45°$, $60°$, and $75°$.

$i = 1, 2$, where a_i is the peak amplitude and τ_i is the pulse duration. At low light intensities, it is found that the energy of the escaping electrons is a smooth function of the phase difference $\psi_1 - \psi_2$. For the special case when $p'_{z0} = 0$, the results are very similar to that obtained with the guiding center equation, which is the time average over fast varying terms in Eq.(5). In the guiding center equation, the ponderomotive force appears as a function of $\psi_1 - \psi_2$. However, with the increase of the pulse intensity, the energy of escaping electrons is no longer a smooth function of $\psi_1 - \psi_2$ [See Fig.3], and the guiding center eqution is not valid any more. In some range, stochastic motion develops. When the intensities of the pulses are high enough, the electron motion is always stochastic for the whole phase difference range from 0° to 360°.

The criterion of stochastic motion may be estimated with the well-known resonance overlap theory [6]. The threshold of a_1 and a_2 is the minimum value satisfying

$$\left.\begin{array}{ll} s_1 & = \Delta_1 + \Delta_2 \geq 1, \\ s_2 & = \Delta_1 + \Delta_3 \geq 1/2, \\ s_3 & = \Delta_2 + \Delta_3 \geq 1/2, \end{array}\right\} \qquad (6)$$

where

$$\Delta_i = \left\{ \begin{array}{ll} \gamma_0'^{-1}(p'_{z0}a_i)^{1/2}, & p'_{z0} \geq a_i \\ \gamma_0'^{-1}(p'_{z0} + a_i)/2, & p'_{z0} < a_i \end{array} \right.$$

for $i = 1, 2$, and $\Delta_3 = \gamma_0'^{-1}(a_1 a_2/2)^{1/2}$ and $\gamma_0'^{-1} = (1 + p'^2_{y0} + p'^2_{z0})^{1/2}$. If the electron is at rest initially, $\gamma_0'^{-1} = \sin\alpha$. The estimated threshold is in good agreement with that observed in numerical calculations.

References

[1] F. V. Hartmann, et al., Phys. Rev. E **51**, 4833 (1995); G. Malka, et al., Phys. Rev. Lett. **78**, 3314 (1997); P. K. Kaw, et al., Phys. Fluids **16**, 321 (1973).

[2] J. N. Bardsley, et al., Phys. Rev. A **40**, 3823 (1989).

[3] J. T. Mendonca and F. Doveil, J. Plasma Phys. **28**, 485 (1982); D. Bauer, P. Mulser, and W. H. Steeb, Phys. Rev. Lett. **75**, 4622 (1995).

[4] E. S. Sarachik et al., Phys. Rev. D **1**, 2738 (1970).

[5] C. I. Moore, et al., Phys. Rev. Lett. **74**, 2439 (1995).

[6] B. V. Chirikov, Phys. Rep. **52**, 263 (1979).

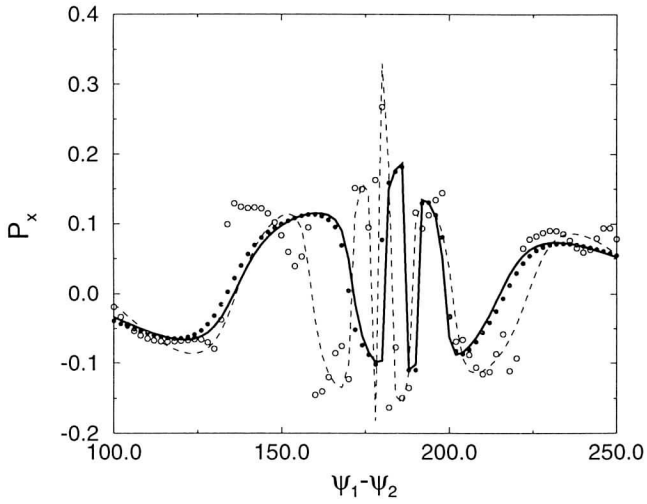

Figure 3: Dependence of the momentum of escaping electrons as a function of the phase difference of the counter-propagating pulses ($\alpha = 90°$) with $\tau_1 = \tau_2 = 50.0$. The filled circles are obtained from Eq.(5) for $a_1 = 0.1$, $a_2 = 0.5$ and the solid line is obtained from the corresponding guiding center equation; The open circles are for $a_1 = a_2 = 0.4$ and the dashed line is obtained from the guiding center equation. In the latter case, the guide center equation is not a good approximation to the equation of motion, and stochastic electron motion has set in around $\psi_1 - \psi_2 = 180°$. The test electron is initially at rest for both cases.

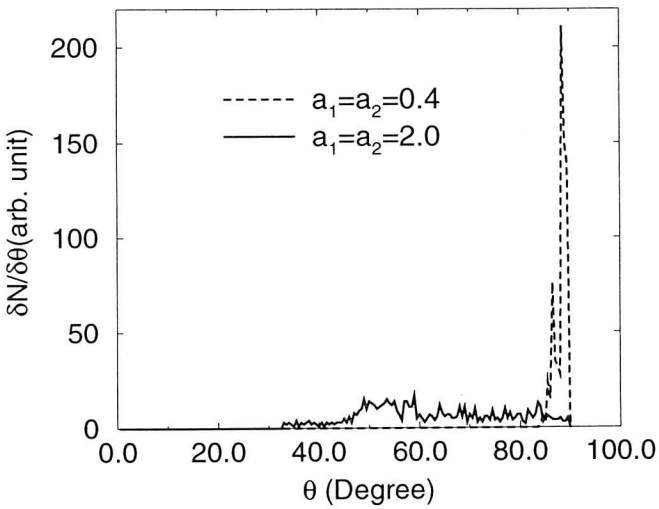

Figure 4: Number of particles per degree scattered by the pulses as a function of scattering angle for $\alpha = 30°$. The dashed line is for $a_1 = a_2 = 0.4$ and $\tau_1 = \tau_2 = 50.0$ when sotchastic motion has not developed. The solid line is for $a_1 = a_2 = 2.0$ and $\tau_1 = \tau_2 = 50.0$ when stochastic motion sets in. In the latter case, escaping electrons are found in a wide angular region.

LPIC++ a Parallel One-dimensional Relativistic Electromagnetic Particle-In-Cell Code for Simulating Laser-Plasma-Interaction

Robert E. W. Pfund, Roland Lichters and Jürgen Meyer-ter-Vehn

Max-Planck-Institut für Quantenoptik, Hans-Kopfermann-Strasse 1, D-85748 Garching, Germany

We report on a recently developed electromagnetic relativistic 1D3V (one spatial, three velocity dimensions) Particle-In-Cell code for simulating laser–plasma interaction at normal and oblique incidence. The code is written in C++ and easy to extend. It will be published and distributed freely [1].

Particle-In-Cell (PIC) codes are well established tools for kinetic simulations in plasma physics and astrophysics [2]. Recently, the progress in producing intense ($I > 10^{18}\mathrm{W/cm^2}$) ultra-short ($< 100\mathrm{fs}$) laser pulses [3] calls for a kinetic description of the interaction of such laser pulses with plasmas. It involves high intensities, short time scales and large density gradients, and conventional hydrodynamic approaches assuming nonrelativistic dynamics, local thermodynamic equilibrium, etc. become insufficient.

The code `LPIC++` presented here, is a one-dimensional, electromagnetic, relativistic PIC code that has originally been developed for kinetic simulations of high harmonic generation from overdense plasma surfaces [4, 5]. The code uses essentially the algorithm of Birdsall and Langdon [2], and Villasenor and Bunemann [6]. It is written in C++ in order to be easily extendable and has been parallelized to be able to grow in power linearly with the size of accessable hardware, e.g. massively parallel machines like Cray T3E. The parallel `LPIC++` version uses `PVM` for communication between processors. `PVM` is public domain software, that can be downloaded from the world wide web [7].

In PIC codes ionized plasmas are simulated by macro particles with positive or negative charge. Macro particles represent groups of electrons or ions containing an extensive number of real particles. `LPIC++` solves the Maxwell equations for the fields and the equations of motion for macro particles simultaneously. The relativistic equations of motion for a collisionless plasma

$$\begin{aligned} \dot{\boldsymbol{p}} &= q_s(\boldsymbol{E} + \boldsymbol{v} \times \boldsymbol{B}), & \boldsymbol{p} &= m_s \gamma \boldsymbol{v}, \\ \dot{\boldsymbol{r}} &= \boldsymbol{v}, & \gamma &= \sqrt{1 + (p/m_s\, c)^2} \end{aligned} \tag{1}$$

are solved for each macro particle once per time step Δt. The particles contribute to charge and current densities ρ and j on a spatial grid with spacing Δx. The Maxwell equations

$$\begin{aligned} \nabla \times \boldsymbol{E} &= -\partial_t \boldsymbol{B}, & \nabla \times \boldsymbol{B} &= \tfrac{1}{\epsilon_0\, c^2}\, \boldsymbol{j} + \tfrac{1}{c^2} \partial_t \boldsymbol{E}, \\ \nabla \cdot \boldsymbol{B} &= 0, & \nabla \cdot \boldsymbol{E} &= \tfrac{1}{\epsilon_0}\, \rho \end{aligned} \tag{2}$$

are then solved on this grid. This procedure is iterated leading to the selfconsistent evolution of plasma and fields.

Advantages of `LPIC++` are its clear program and data structure. The data structure is characterized by the use of chained lists for the grid cells as well as particles belonging to one cell. The parallel version of the code splits the grid into several spatial domains each belonging to one processor. Since particles can cross boundaries of cells as well as domains, the processor loads will generally change in time. This is counteracted by adjusting the domain sizes dynamically, for which the use of chained lists has proven to be very convenient. Moreover, an option for restarting the simulation from intermediate stages of the time evolution has been implemented even in the parallel version.

This code was used to simulate the generation of laser harmonics by interaction of an ultrashort laser pulse with a step boundary of a plane overdense plasma layer at intensities $I\lambda^2 = 10^{17} - 10^{19}\mathrm{W/cm^2}\ \mu\mathrm{m}^2$ [4, 5]. See figure below for an electron density plot and the power spectrum of the reflected light made with an example input file distributed with `LPIC++`.

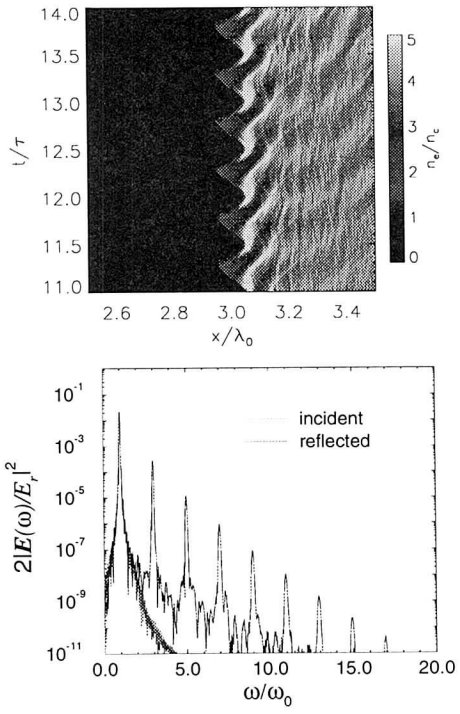

`LPIC++` is supposed to run on any Unix platform like Linux, Solaris, SunOS, AIX, etc.. It has been tested and used extensively under AIX. Program and postprocessor will be freely available together with a detailed manual describing how to install and prepare input for `LPIC++`. It includes a description of output and postprocessing, discusses several examples and presents the main structure of the code [1].

References

[1] R. Lichters, R. E. W. Pfund, and J. Meyer-ter-Vehn, **MPQ 225**, (1997).

[2] C. K. Birdsall and A. B. Langdon, *Plasma physics via computer simulation* (Adam Hilger, New York, 1991).

[3] M. D. Perry and G. Mourou, Science **264**, 917 (1994).

[4] R. Lichters, J. Meyer-ter-Vehn, and A. Pukhov, Phys. Plasmas **3**, 3425 (1996).

[5] R. Lichters and J. Meyer-ter-Vehn, in *Multiphoton Processes 1996* (Institute of Physics Publishing, Bristol and Philadelphia, 1996), p. 221.

[6] J. Villasenor and O. Buneman, Comput. Phys. Commun. **69**, 306 (1992).

[7] A. Geist *et al.*, *PVM : Parallel Virtual Machine* (MIT Press, Cambridge, USA, 1994), `http://www.netlib.org/pvm3`.

Ionization of Dense Matter by 10^{17} W/cm^2 fs-laser Pulses: 1D-PIC Treatment

Robert E. W. Pfund and Jürgen Meyer-ter-Vehn

Max-Planck-Institut für Quantenoptik, Hans-Kopfermann-Strasse 1, D-85748 Garching, Germany

The ionization of dense cold matter by ultrashort (few fs long) high-intensity (10^{17} W/cm^2) laser pulses is studied by one-dimensional Particle-In-Cell simulations. The code LPIC++ [1] has been extended to include ionization processes in materials with multiple ionization stages. The method used conserves energy. Both field and electron collisional ionization are included. Explicit results are presented for a thin layer of He gas. The spatial and temporal evolution of the ionization dynamics resulting from steeply rising pulses within the first laser cycles is highlighted. As a new and outstanding result of this study, we report on strong field ionization by electrostatic fields occuring in particular at the rear surface of the layers.

The progress in producing ultra short laser pulses (**$\sim$10fs**) [2] with high intensities leads to situations in which the time for ionizing the illuminated dense material is of the same order as the laser pulse length. In case of long laser pulses (**$\gg$100fs**), a short part of the laser pulse ionizes the material and the main part interacts with a preionized plasma. Then it is sufficient to consider the interaction of a laser pulse with a preionized plasma. In the present work, however, the evolution of plasma generation using ultra short pulses is studied, i.e., the time-dependent development of the charge state distribution, the electron density in the material and a clear identification of all different ionization processes as a function of space and time. In addition the feedback on the laser pulse is important, i.e., the transmitted and reflected signal or the corresponding spectra.

Therefore the Particle-In-Cell code LPIC++ [1] has been extended. It handles now all possible ionization stages from the neutral to the completely ionized atom. Concerning ionization processes, ionization in strong electric fields as well as electron collisional ionization are implemented. The field ionization process is based on the barrier suppression ionization model (BSI) [4] or alternatively on the ADK tunneling model [5]. The implementation is energy conserving. The ionization energy is extracted from the field by a fictitious ionization current.

The electron impact ionization process uses a Monte Carlo technique including the null collision method [6] and is also energy conserving. Recombination processes are not important on this time scale for the density considered here and are therefore not implemented as well as ionization processes from excited states.

In the following simulation results are presented for a laser pulse with an intensity of $\boldsymbol{I = 9 \times 10^{16}\mathrm{W/cm^2}}$ normally incident on a helium gas layer. The laser pulse

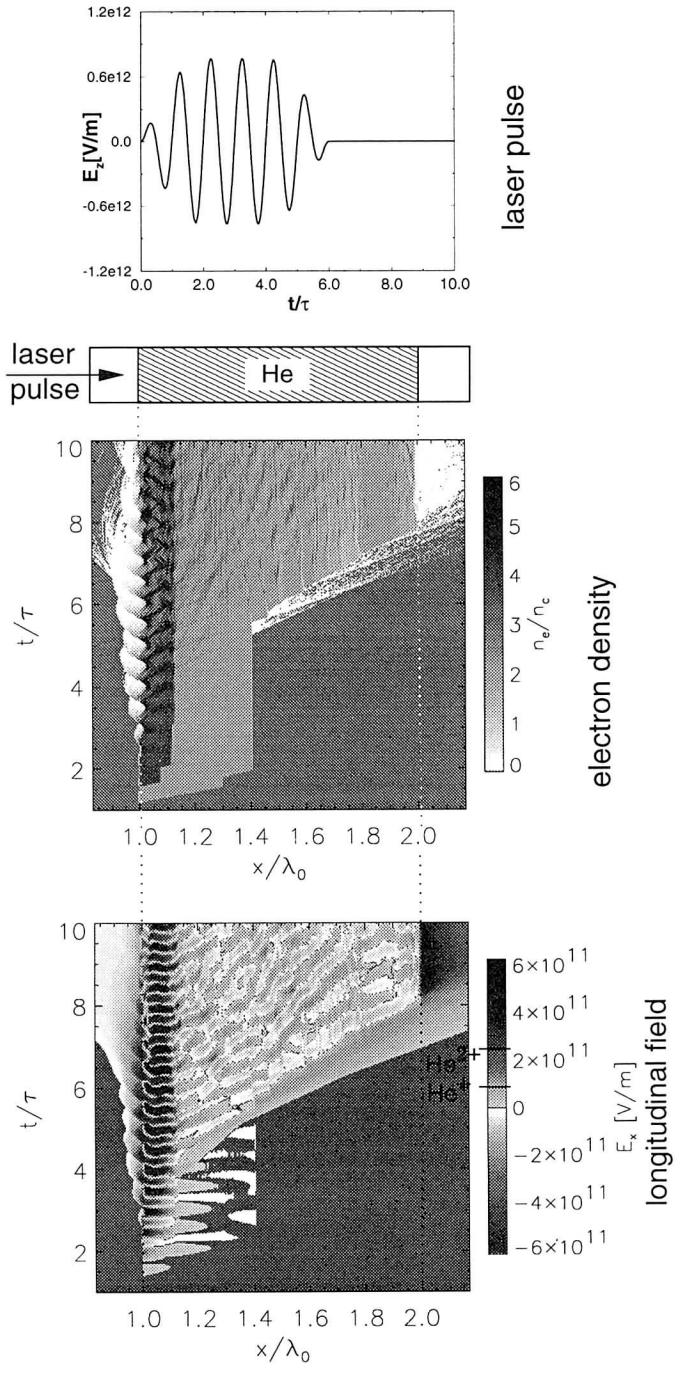

Figure 1: Laser pulse, six cycles long with intensity $\boldsymbol{I = 9 \times 10^{16}\mathrm{W/cm^2}}$, impinging on He $\boldsymbol{n_{He} = 2 \times 10^{21}\mathrm{cm^{-3}} = 2n_c}$. Spacetime plot of the electron density and the longitudinal electric field.

is six cycles long with a **sin**-envelope, see Fig. 1. The layer with a density of $\boldsymbol{n_{He} = 2 \times 10^{21}\mathrm{cm^{-3}} = 2n_c}$ (n_c is

the critical density) is $\lambda_0 = 1\mu m$ (laser wavelength) thick and centered in a $3\lambda_0$ long simulation box.

Fig. 1 depicts a spacetime plot of the electron density n_e. The space and time coordinates are given in units of the laser wavelength and the laser cycle, respectively. At $t = 0$ the laser pulse enters the simulation box on the left side and the head reaches the gas layer at $t = \tau$. In this simulation the BSI model is used, which is a threshold model in the sense that an atom or ion is ionized only if the electric field at its position is above a certain threshold. This leads to sharp ionization fronts. As soon as the field amplitude in the first half laser cycle is strong enough to ionize the gas atoms, the electron density increases to $2n_c$. The laser pulse propagates deeper into the gas layer partially using its field energy for ionizing the material. As soon as n_e exceeds n_c, the light cannot propagate anymore and starts to be reflected. This results finally in an ionized layer of finite thickness. A more realistic stochastic model like the ADK tunneling formula, which gives a field amplitude dependent ionization probability, results in an electron density continuously decreasing with penetration depth. The BSI model has been used here as a limiting model.

The second half cycle of the laser pulse impinges then on He^+ and is strong enough to ionize it to He^{2+} ($n_e = 4n_c$) with a front at $x = 1.1\lambda_0$, which corresponds to the skin depth for this electron density. Furthermore this half cycle is strong enough to shift the He^+ front deeper into the gas layer ($1.3\lambda_0 < x < 1.4\lambda_0$).

After this initial phase, the pulse impinges on fully ionized, four times overcritical plasma and is reflected. The penetration depth is given by the skin depth. Since the laser field amplitude is still increasing in the following two cycles the thickness of the He^{2+} layer at the left side is slightly growing. The region of non-ionized gas ($x > 1.4\lambda_0$) is not affected by the laser pulse anymore.

Due to the strong light pressure, plasma oscillations are excited at the front side finally producing high-energetic electrons which are injected into the plasma. These jets pass the plasma layer and enter the non-ionized gas layer ($t > 5\tau$). Thereby a strong longitudinal electrostatic field is built up, strong enough to ionize up to He^+. This strong longitudinal field is clearly visible in the spacetime plot for E_x, see Fig. 1. The field strengths needed for ionizing to He^+ and He^{2+} are labeled.

Finally the electron jets exit the plasma layer at the rear side ($x > 2\lambda_0$, $t > 7\tau$), but are returned by the space charge potential they build up. The longitudinal electric field present during this process is strong enough to create a thin layer of He^{2+} at the rear side.

In Fig. 2 three snapshots of the charge state distribution in the simulation box are depicted: at $t = 0$ when only gaseous He is present, at $t = 5\tau$ shortly before the electron jets enter the non-ionized gas layer and at $t = 10\tau$. Results are shown for the BSI and the ADK model.

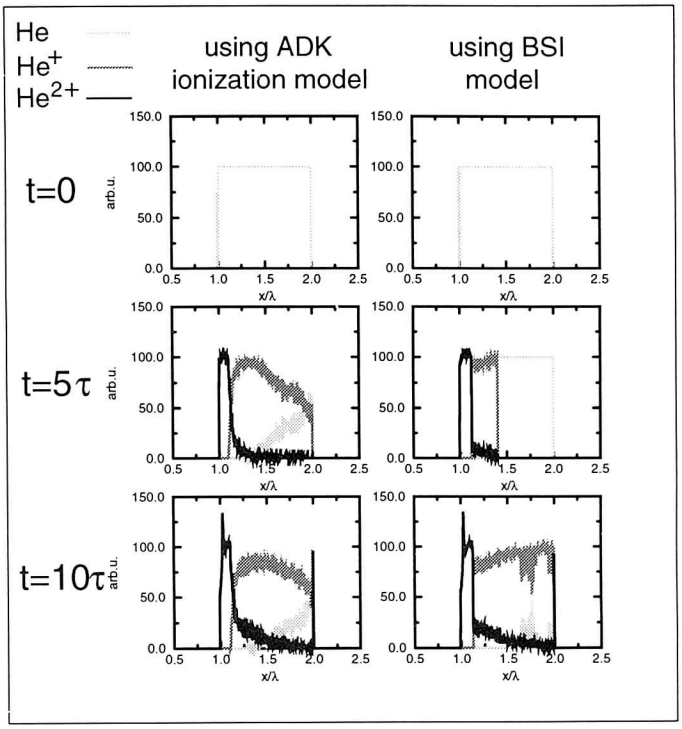

Figure 2: Snapshots of the charge state distribution using the ADK ionization and the BSI model. At $t = 10\tau$ two layers of He^{2+} can be identified, one at the front and the other at the rear surface.

At $t = 5\tau$ the difference between the threshold and the more realistic stochastic model is clearly visible. The latter does not show a distinct separation between a partially and a not at all ionized region. After ten cycles one can clearly identify in both cases two layers of fully ionized He, one at the front and the other at the rear surface. In the region in between He^+ is the dominating charge state. All He^{2+} in this region is due to electron collisional ionization and is not caused by any kind of field ionization process.

One of the most outstanding consequences of this work may be the practically instantaneous ionization of an atomic layer at the rear surface. This should become an interesting topic for spectroscopists studying the recombination radiation and for possible applications to X-ray lasers.

References

[1] R. Lichters, R. E. W. Pfund, and J. Meyer-ter-Vehn, **MPQ 225**, (1997).

[2] C. Spielmann *et al.*, Science **278**, 661 (1997).

[3] C. K. Birdsall and A. B. Langdon, *Plasma physics via computer simulation* (Adam Hilger, New York, 1991).

[4] S. Augst, D. D. Meyerhofer, D. Strickland, and S. L. Chin, J. Opt. Soc. Am. B **8**, 858 (1991).

[5] M. V. Ammosov, N. B. Delone, and V. P. Krainov, Sov. Phys. JETP **64**, 1191 (1986).

[6] V. Vahedi and M. Surendra, Comput. Phys. Commun. **87**, 179 (1995).

Magnetic Field Assisted Particle Acceleration by Direct Laser Push

A. Pukhov and J. Meyer-ter-Vehn
Max-Planck-Institut für Quantenoptik, Garching-bei-München, Germany

PIC simulations [1, 2] of laser pulse channeling in near-critical plasma show that particles are accelerated to energies much higher than the ponderomotive potential. The effect has also been observed in recent experiments [3]. At the same time, no regular plasma waves exist, thus precluding an otherwise possible explanation in terms of wake-field acceleration. In the present paper we show that a strong azimuthal magnetic field around the channeling laser pulse is sufficient to lead to net acceleration of electrons to very high energies by direct laser push [4].

The following arguments are based on the well known analytic solution for relativistic electron motion in a plane electromagnetic wave [5, 6, 7]. It is governed by two constants of motion. The first one stems from the longitudinal symmetry of a wave, progressing with phase velocity $v_{ph} = c\beta_{ph} = \omega/k$ in X−direction and depending only on the phase $\varphi = kx - \omega t$. It is given by

$$\varepsilon - \beta_{ph} c p_x = \varepsilon_0, \tag{1}$$

combining the particle kinetic energy ε and its longitudinal momentum p_x. The second one follows from 1D planar geometry and expresses conservation of the transverse generalized momentum

$$\mathrm{p}_\perp/mc - \mathrm{a} = \mathrm{P}^0_\perp. \tag{2}$$

First, we consider a plane electromagnetic wave in vacuum, propagating exactly with the light velocity, $\beta_{ph} = 1$. For an electron at rest, before it is caught by the wave, one has $\varepsilon_0 = 0$ and $\mathrm{P}^0_\perp = 0$, and therefore

$$\mathrm{p}_\perp = mc\,\mathrm{a}; \quad p_x = mc\frac{a^2}{2}; \quad \varepsilon = mc^2\frac{a^2}{2}. \tag{3}$$

Thus, the kinetic energy of the particle within a laser pulse equals the ponderomotive potential $\phi_l = mc^2a^2/2$. If, however, the laser pulse overtakes an electron with an initial momentum p_0 in the laser propagation direction, then the electron momentum inside the pulse is

$$\mathrm{p}_\perp = mc\,\mathrm{a}; \quad p_x = p_0\left(1 + \frac{a^2}{2}\left(1 + \frac{\gamma_0}{p_0}\right)\right), \tag{4}$$

where $\gamma_0 = \sqrt{1 + p_0^2}$, and in the ultra-relativistic limit $\gamma_0 \gg 1$ [8]:

$$\gamma = \gamma_0(1 + a^2). \tag{5}$$

The result (5) holds only for an electromagnetic wave propagating exactly with the vacuum speed of light c. If, however, the laser pulse propagates in a plasma, or is focused, it has $\beta_{ph} > 1$. Starting from (1,2), we find a modified form of the Eq. (4):

$$p_x = mc\cdot\gamma_{ph}\left(\sqrt{1 + a^2 + \left(1 + \frac{\varepsilon_0}{mc^2}\right)^2\gamma_{ph}^2} - \left(1 + \frac{\varepsilon_0}{mc^2}\right)\sqrt{\gamma_{ph}^2 + 1}\right), \tag{6}$$

where we have introduced a laser γ−factor $\gamma_{ph} = 1/\sqrt{\beta_{ph}^2 - 1}$.

Equation (6) can be simplified in two limiting cases of major interest. First, for electrons propagating slower than the laser pulse, $1 \ll \gamma_0 < \gamma_{ph}$, we reproduce relation (5).

The second case corresponds to fast electrons, $\gamma_0^2 > a^2\gamma_{ph}^2$ (here we assume also $a \gg 1$), and instead of (5) we have

$$\gamma \approx \gamma_0\left(1 + \left(\frac{a\gamma_{ph}}{\gamma_0}\right)^2\right). \tag{7}$$

Comparing this expression with (5) we see that the acceleration is strongly degraded. Apparently, the characteristic energy ε_c, at which this degradation sets in, scales like

$$\varepsilon_c = \Lambda a\gamma_{ph}\, mc^2. \tag{8}$$

where Λ is a factor of the order unity.

The analysis above shows that an electron can acquire a significant energy inside a plane electromagnetic wave. However, this acceleration is virtual, since according to the constants of motion the electron is falling back to its initial energy and momentum, after the pulse has passed, and the light amplitude is $a = 0$ again. *However the rigorous conservation of integrals (1)-(2) is artificial, and is violated for realistic geometries, strongly modulated laser pulses and situations when the particle interacts with other particles or fields.*

Here we discuss the case of a laser beam of finite width such that the electron can be scattered out of the beam in transverse direction. Such electrons can take away some of the energy gained in the laser field. This process has been demonstrated experimentally in [9, 10].

Now, let us assume that the escaping electron is reflected by a sufficiently large azimuthal magnetic field and is rein-

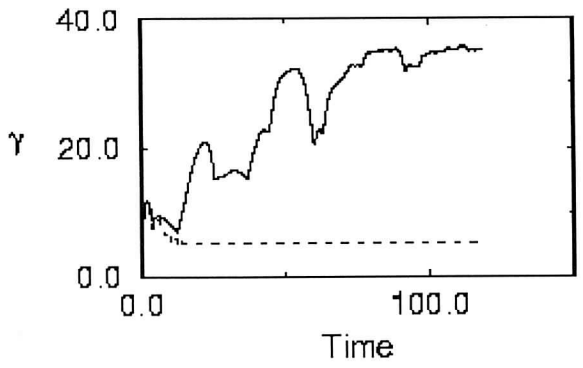

Figure 1: Maximum relativistic γ−factor of test electrons without (dashed line) and with azimuthal $\boldsymbol{B}$−field (solid line)

jected into the beam volume such that a second acceleration step can take place. This magnetic field $\boldsymbol{B}$ must have a focusing polarity, corresponding to a counter-clockwise direction when looking along the laser. Also, it must be strong enough and have a sufficiently large extent r_B in radial direction to return escaping electrons. In order to trap a relativistic electron moving forward with $p_{\|} \gg p_{\perp}$, the magnetic rigidity has to be

$$Br_B > \frac{p_{\perp}^2}{2(mc)^2\gamma} B_0 \lambda, \qquad (9)$$

where we have introduced the unit magnetic field $B_0 = mc\omega/e = 107$ MG for a laser pulse with $\lambda = 1$ μm. Magnetic fields of the order (9) are naturally produced in plasma by relativistically strong laser pulses as it has been observed in 2D [2] and 3D [1] PIC simulations. It is always accompanied by acceleration of background plasma electrons to multi-MeV energies [1, 2].

An accurate analytic description of the particle motion in this case is complicated. Therefore, we performed simplified numerical simulations, and used the results obtained above as a guideline. We followed trajectories of test electrons in a guided laser pulse with and without an azimuthal magnetic field. The laser pulse transverse profile was assumed to be Gaussian, $\mathbf{a}_{\perp}(x, r) = a_0 \exp\left(-(r/w_l)^2\right) \sin(kx - \omega t)$. It corresponds to a parabolic plasma density channel [11]. The wave vector of the laser pulse k, plasma frequency ω_p on axis of the channel and the transverse laser waist w_l are connected by the dispersion relation

$$\left(\frac{\omega^2}{c^2} - k^2 - \frac{\omega_p^2}{c^2}\right) = \frac{1}{w_l^2}. \qquad (10)$$

We also take care of the *longitudinal* component of the laser vector-potential to ensure $\mathbf{div}\ \mathbf{a} = 0$.

The laser pulse is assumed to be infinite in time, and an ensemble of 1000 test electrons was initialized at time $t = 0$ with zero initial energies at random positions *inside the pulse region*. During simulation we have recorded the maximum kinetic energy among the test particles.

An example result is presented in Fig. 1. The laser and channel parameters were $a_0 = 2.5$, $w_l = 3\lambda$, $\omega_p = 0.1\omega$. The ponderomotive potential for this laser pulse is $\phi_l = 1.55$ MeV. The dashed line in Fig. 1 represents the simple ponderomotive scattering of test electrons. The maximum energy of the scattered electrons is about 2 times the ponderomotive potential. This corresponds to electrons seeded at the peak of the vector potential.

In contrast, the solid line in Fig. 1 has been obtained with an additional azimuthal magnetic field with a magnitude $B(r) = 0.15 B_0 (r/w_l) \exp\left(-(r/w_l)^2\right)$. A very fast growth of the maximum kinetic energy about linear in time at early stages is followed by a saturation at the level ~ 17 MeV ($\gamma \sim 34$). This is 12 times higher than the ponderomotive potential. This saturation level agrees with (8) for $\Lambda \approx 2$. Simulations for different parameters show that the saturation value indeed scales linearly with the laser amplitude and γ_{ph}. This acceleration disappears for magnetic fields smaller than the estimation (9).

The $\boldsymbol{B}$−loop acceleration mechanism dominates when the regular self-modulation wake field can not grow, as it happens in plasmas with near-critical density [1], and when it disappears, e.g., due to a strong wave-breaking. Both these cases are of a key importance for Fast Ignitor physics.

This work was supported by EURATOM, DFG and BMBF.

References

[1] A. Pukhov and J. Meyer-ter-Vehn, Phys. Rev. Lett. **76**, 3975 (1996).

[2] A. Pukhov and J. Meyer-ter-Vehn, Phys. Rev. Lett., Vol 79, 2686(1997).

[3] G. Malka, et al., Phys. Rev. Lett. **79**, 2053 (1997).

[4] A. Pukhov, and J. Meyer-ter-Vehn, *to appear in* Phys. Plasmas, **5**, *May issue*, (1998).

[5] L. Landau and E. Lifshitz, *The Classical Theory of Fields*, 4th ed. (Oxford: Pergamon Press, 1975), p.118.

[6] A. I. Morozov and L. S. Solov'ev, in: *Reviews of Plasma Phys.*, ed. by M. A. Leontovich, Vol. 2 (Consultants Bureau, NY, 1966).

[7] P. B. Corkum, N. H. Burnett and F. Brunel, in *Atoms in Intense Laser Fields*, ed. M. Gavrila (New York, Academic Press, 1992)

[8] F. V. Hartemann, et al., Phys. Rev. E **51**, 4833 (1995).

[9] C. I. Moore, J. P. Knauer, and D. D. Meyerhofer, Phys. Rev. Lett. **74**, 2439 (1995).

[10] G. Malka, E. Lefebvre, and J. L. Miquel, Phys. Rev. Lett. **78**, 3314 (1997).

[11] H. M. Milchberg, et al., Phys. Rev. Lett **75**, 2494 (1995).

Correlated Stopping of Relativistic Electron Beams in Supercompressed DT Fuel

C. Deutsch, LPGP, Université Paris XI, 91405 Orsay

Recently, an intense interest for the stopping of relativistic electron beams in dense and hot plasma of thermonuclear concern has emerged from the so-called fast ignitor scenario initially advanced at Livermore [1]. This proposal is about decoupling the fuel compression through standard drivers (laser, particle or cluster beams) from the hot spot ignition in a fraction only of the DT mixture. The latter process is expected to arise through a femtosecond laser boring a hole in the corona of the precompressed material.

Here, we address the issues concerning the interaction of the laser produced relativistic electrons with the fully ionized and mostly classical electron plasma featuring the very dense compressed core. The corresponding beam-plasma collective modes are seen to be collisionaly damped.

The relativistic stopping of MeV electrons (ß=0.94) in supercompressed DT fuel (300g/cc, $n_e=10^{26}cm^{-3}$, T=5keV) has been recently demonstrated [2]. Here we address the issues of correlated effects in a dense electron beam with $n_b=10^{22}cm^{-3}$, arising from *ad hoc* funtosecond laser. For this purpose we implement numerically a classical impact parameter formalism due to Rule and Cha [3], and consider various orientations of two-electron cluster w.r.t beam velocity. A first unexpected result is that for cluster extensions much larger than target Debye length, one gets significant correlated stopping for perpendicular (Fig. 1) and parallel (Fig. 2) 2-cluster inter-distance. This effect persits over tens of target screening length (Fig. 1) for transverse orientation. Longitudinal correlated stopping (Fig. 2) is seen modulated and undamped over several mean electron beam distance, as well. In ferences to the coupling efficiency of relativistic electron beams with supercompressed DT fuel is currently under investigation.

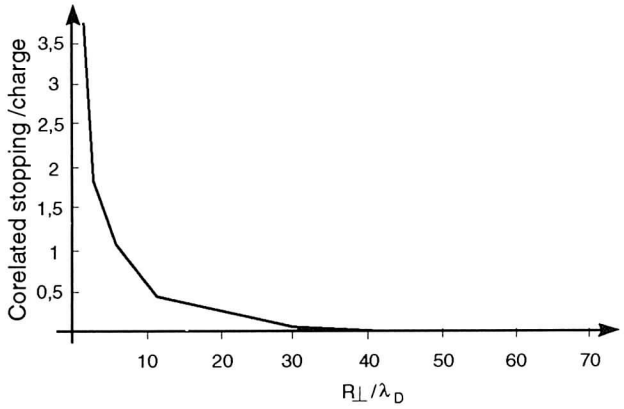

Figure 1- Correlated stopping/charge for a 2-cluster orientated perpendicular to beam velocity $V_1=V_2=0.94c$ in terms of interdistance $R_\perp=1$ given in number of target Debye length 5.25×10^{-9}cm. $R_\perp=1$ pertains to the relativistic stopping of an isolated charge.

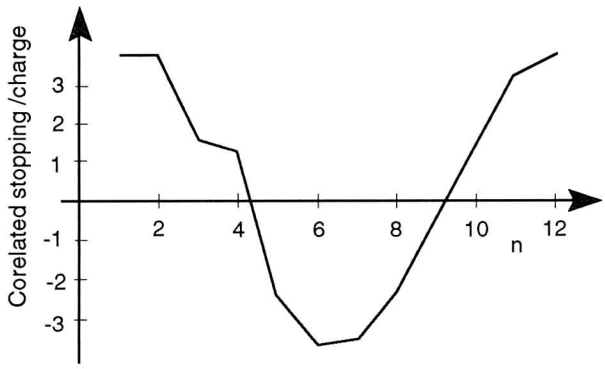

Figure 2- Correlated stopping/charge for a 2-cluster orientated parallel to beam velocity $V_1=V_2=0.94c$ in terms of interdistance $R_{//}$ given in numbers n of mean interelectron beam distance 2.88×10^{-8}cm.

References

[1] M. Tabak, I. Hammer, M.E. Glinsky, W.L. Kruer, S.C. Wilks, J. Woodworth, E.M. Campbell, M.D. Perry and R.J. Mason, *Phys. Plasma*, **1**, 1626 (1994).

[2] C. Deutsch, K. Nishihara, *Phys. Rev. Lett.*, **77**, 2483 (1996).

[3] D.W. Rule and M.H. Cha, *Phys. Rev.*, **24**, 55 (1981).

Wavebreaking of Resonantly Excited Large Amplitude Electron Plasma Waves

J. D'Avanzo - GSI, Darmstadt
P. Mulser - TUD, Darmstadt
H. Ruhl - ILE, Japan
B. Battacharrya - University of North Bengala, India

The excitation of large amplitude, relativistic plasma waves by high intensity, ultra short laser pulses is a topic of great interest in the last years. Depending on the laser characteristics (intensity, pulse shape and duration) and on the plasma conditions (density profile, temperature) the excited plasma wave propagates (in the underdense region) in a very regular way, and when its amplitude reaches some maximum value it *breaks*. At present a clear and quantitative picture of wavebreaking of plasma waves is still not available and a general criterion which defines its onset and explains the reason why the plasma itself cannot sustain a collective particle motion is still missing.

Starting from a 1D fluid model for a cold plasma, Dawson [1] derived a simple condition which defines the signature of wavebreaking: $\eta = v_{osc}/v_{ph} = 1$. Here $v_{osc} = eE_0/m_e\omega$ is the electron oscillatory velocity and $v_{ph} = \omega/k$ the plasma wave phase velocity, with E_0 the maximum electric field in the plasma, and ω and k the laser frequency and wave number respectively. Therefore wavebreaking occurs when neighbouring fluid elements cross each other (*hydrodynamical wavebreaking*). The inclusion of thermal effects leads to a more general criterion for wavebreaking of a free running wave [2]: $n_e/n_0 = (v_{ph}/s_e)^{2/(\gamma+1)}$, where n_e is the electron density, n_0 the unperturbed density, $s_e = (\gamma T_e/m_e)^{1/2}$ and γ the adiabatic coefficient.

The above crtierions are related to an *hydrodymanical* picture of wavebreaking. Kinetic effects are not accounted for and are totally washed out in this description. A general definiton would require the inclusion of kinetic effects. In this sense we define *kinetic wavebreaking* as *the loss of periodicity in at least one of the macroscopically observable quantities (i.e. n_e, E_x, j_x, ...).*

The problem of a correct definition of wavebreaking is in our feeling of great concern since in literature there is much confusion on the topic. Our aim is to give a criterion of wavebreaking within a kinetic description and to look at the signature of it. For example it is generally accepted that there is a relation between fast particle generation and wavebreaking. Fast particle generation is the signature of wavebreaking [4]. On the other hand we have indications that when wavebreaking sets in fast electrons cannot be accelerated because of the loss of periodicity in the wave structure. The fast electrons already exist in the wave before it breaks. The physical picture that we have is very simple. As the wave amplitude grows, the electrons are first trapped in the wave, the number of trapped electrons increases and these sustain the electrostatic wave until the latter collapses. These electrons gain meanwhile energy from the field and when the plasma cannot sustain the collective motion anymore, the electron plasma wave breaks. The excess of energy then accelerates the electrons.

We study wavebreaking of large amplitude electron plasma waves with the aid of a 1D2V relativistic Vlasov code [5].

In our simulations we consider a plasma with some density profile $n_e = n_e(x)$, inhomogeneous in the x-direction. For simplicity we assume a static ion background to insure the overall electrical neutrality, but ion motion can be in general included in our calculations. A p-polarized laser pulse impinges the plasma under an arbitrary angle of incidence θ. Using a boosted frame, the 2D electron distribution function can be reduced to 1D in space but 2D in velocity [6], i.e. $f_e(x, p_x, p_y, t)$, and obeys to the following relativistic Maxwell-Vlasov equation:

$$\begin{aligned}(\partial_t + v_{ex}\partial_x - e\{E_x + v_{ey}B_z\}\partial_{p_{ex}} \\ -e\{E_y - v_{ex}B_z\}\partial_{p_{ey}})\, f_e = 0,\end{aligned} \tag{1}$$

$$\partial_t \mathcal{E}_x + \frac{j_x}{\rho + C}\,\partial_x \mathcal{E}_x = 0, \tag{2}$$

$$(\partial_t \pm c\partial_x)\; E^{\pm} = -\frac{1}{\epsilon_0}\, j_y, \tag{3}$$

where

$$v_{ex/y} = \frac{cp_{ex/y}}{\sqrt{m_e^2c^2 + p_{ex}^2 + p_{ey}^2}} \tag{4}$$

is the electron velocity, $E^{\pm} = E_y \pm cB_z$ and $\mathcal{E}_x = E_x + Cx$, with $\rho + C > 0$, $C >> 1$ ($C \sim 10^3$) being a constant introduced for numerical purposes. Notice that Eq. (3) enables the solution of Maxwell's equations along their vacuum characteristics $x \pm ct = \text{const}$.

In this paper we present results related to wavebreaking within the *capacitor model* [7], i.e. the driver is localized at the resonance, around the critical density. In the following we show results related to a run for a driver intensity of $I\lambda^2 = 5 \times 10^13\text{W}(\mu\text{m/cm})^2$, with $\lambda = 0.8\ \mu$m ($\eta = 0.14$).

In Fig. 1 we show the density profile at two different laser cycles. The critical density is in $x = 0$. After 28 cycles the plasma is regular and propagates downhill in the

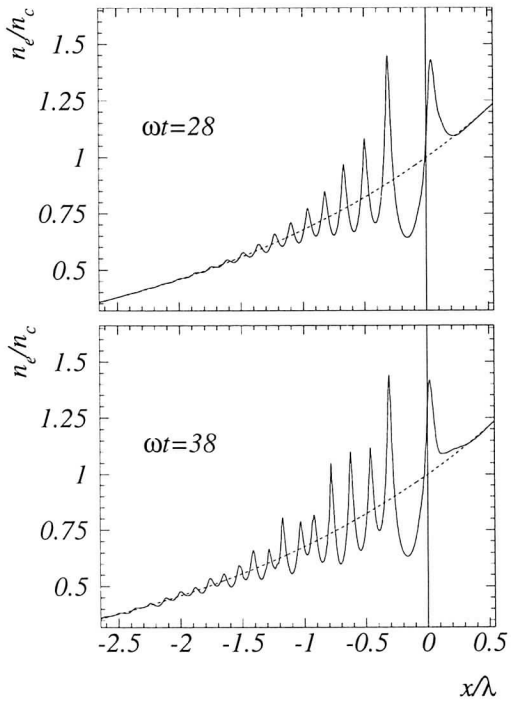

Figure 1: Electron density profile (in units of the critical density n_c) *vs.* x (expressed in units of the laser wavelength λ). Dotted line: unperturbed density profile.

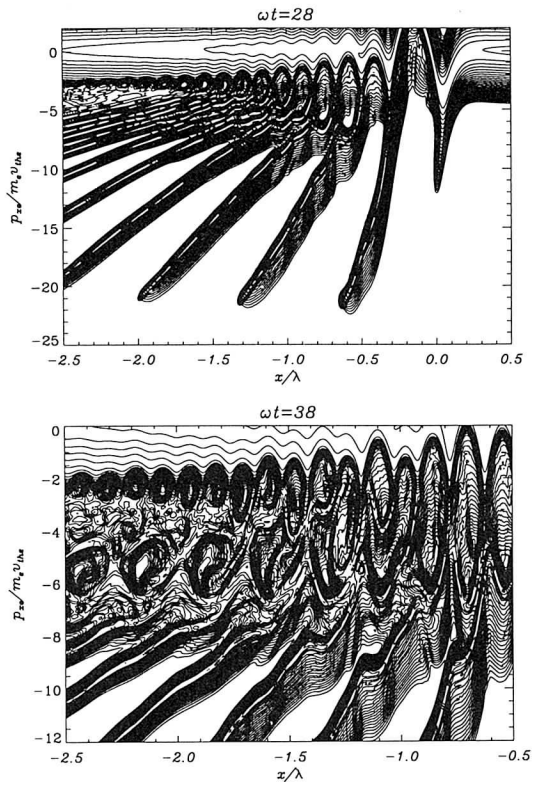

Figure 2: Contour lines of the electron distribution function related to Fig. 1

underdense region. At $\omega t = 38$ we see that its shape is not regular anymore more, i.e. the wave is *broken*. Therefore there is a transition (depending in general on the density profile, plasma temperature and laser intensity) to a state where the plasma cannot sustain anymore a collective particle motion.

A clearer picture comes out looking at the contour plots in phase space (Fig. 2). At $\omega t = 28$ we see jets of fast electrons generated by the driver applied at the resonance and they propagate downhill. Notice that the slope of the contour lines of these fast electrons decreases as they move away from the resonance, indicating that they are free running electrons, i.e. not accelerated by the electrostatic field. We also notice the slower electrons are trapped by the wave (closed structures in the plots).

At the later time $\omega t = 38$ we observe a transition (in phase space) to a turbolent state. In Fig. 2 we show a detail of the contour plot. Notice the complicated structures that build up, with phase space mixing and the coalescence of entire bunches of electrons. These results confirm on one side the ones obtained earlier [3], but also show new features due to a sofisticated numerical scheme adapted in the code. We see in fact that wavebreaking leads to the formation of superstructures and to period doubling and tripling in phase space. Furthermore, we see subsequent mixing of wave structures with the superstructures. We also never observe wavebreaking neighbourhood of the critical density where the plasma wave is resonantly driven. These results show the kinetic nature of wavebreaking.

Finally we claim that we have indications that wavebreaking is not directly related to efficient particle acceleration, but this statement has still to be confirmed by further runs.

We conclude with a few words for our future studies. Here we showed results related to the "capacitor model" approximation. We performed also runs for the full electromagnetic case, with a laser pulse propagating through the underdense plasma corona up to the critical density. We have indications that there is a stabilization effect of the electromagnetic laser field and that the wavebreaking limit is larger than the predictions of the capacitor model.

This work has been supported by the European Commission through the TMR network SILASI (Super Intense LAser-pulse Solid Interaction), contract No. ERBFMRX-CT96-0043.

References

[1] J. M. Dawson, Phys. Rev. **113**, 383 (1959).
[2] P. Mulser, H. Schnabl, Laser Particle Beams **1**, 379 (1983).
[3] A. Bergmann, P. Mulser, Phys. Rev. E **47**, 3585 (1993).
[4] S.V. Bulanov et al., Phys Rev. Lett. **78**, 4205 (1997).
[5] H. Ruhl et al. to be submitted for publication.
[6] A. Bouridier, Phys. Fluids **26**, 1804 (1983).
[7] Th. Speziale, P.J. Catto, Phys. Fluids **22**, 681 (1979).

About the Importance of Proper Calculation of the Coulomb Logarithm in Collisional Absorption

E. Bésuelle, Theoretical Quantum Electronics (TQE), Darmstadt University of Technology,
Hochschulstr. 4A, D-64289 Darmstadt, Germany.

In the collisional absorption, the *Coulomb* logarithm plays an important role – and for what we know not extensively studied – in the computation of the collision frequency (see for instead [1]). We report in this communication that it should be calculated carefully to avoid large overestimation of the collision frequency, especially in the case of strong Laser field.

We suppose oscillating electrons in a harmonic Laser field of amplitude $\hat{E}(\mathbf{r})$ with the velocity $\mathbf{v}_{os}(t) = \hat{\mathbf{v}}_{os}\ \exp(-i\,\omega\,t)$ where $\hat{\mathbf{v}}_{os} = -i\,e/(m_e\,\omega)\ \hat{\mathbf{E}}(\mathbf{r})$ and immobile ions ($T_i = 0$).

The *Coulomb* logarithm appears in the *Rutherford* collision cross-section calculation under the form, for an electron velocity v:

$$\ln\Lambda = 2\int_{\chi_{min}}^{\chi_{max}} \cot(\chi/2)\; d\;(\chi/2) = \ln\left(\frac{1+b_{max}^2/b_\perp^2}{1+b_{min}^2/b_\perp^2}\right) \quad (1)$$

with $b_\perp$ the impact parameter for the perpendicular deflection: $b_\perp = Z\,e^2/4\pi\,\varepsilon_0\,\gamma\,m_e\,v^2$, with $\gamma = \left(1-v^2/c^2\right)^{-1/2}$ and χ_{min} and χ_{max} the minimum and the maximum deflection angles, corresponding to b_{max} and b_{min}. Eq. (1) is often reduced for low velocities to the familar expression:

$$\ln\Lambda_r = \ln\left(b_{max}^2/b_\perp^2\right) \quad (2)$$

We assume that the ions are shielded by electrons and that outside the *Debye* sphere there is no electric interaction between the two charged particles. The *Debye* length we have to take into account is the *oscillatory* one, corresponding to the pseudo-atom formed by the ion and the oscillating electrons:

$$b_{max} = \lambda_0 = \sqrt{\frac{\varepsilon_0\,\gamma\,m_e\,v^2}{Z\,e^2\,n_i}} = \frac{v}{\omega_{pe}} \quad (3)$$

with $v = \|\mathbf{v}_{os} + \mathbf{v}_e\|$ where $\mathbf{v}_e$ is the individual thermal velocity on the considered electron. The minimum impact parameter is the *de Broglie* length meaning that under this length quantum effects have to be taken into account, which reduce considerably the collision cross-section, so that we set it to null value for an impact parameter under λ_B:

$$b_{min} = \lambda_B = \frac{\hbar}{\|\mathbf{p}\|} = \frac{\hbar}{\gamma\,m_e\,v} \quad (4)$$

In order to have a tractable tabulated value for the *Coulomb* logarithm, we averaged it on the velocity *Maxwellian* isotropic distribution function, in spherical coordinates. It gives, integrated on the domain $\{(v_e,\theta,\phi)\,/v_e \geq 0\,;\,0 \leq \theta \leq \pi\,;\,0 \leq \phi \leq 2\pi\}$ with symmetry along ϕ:

$$<\ln\Lambda\big(v_{os}(t)\big)> =$$

$$2\pi\int_0^{+\infty} v_e^2\,f_e(v_e)\left[\int_0^{\pi}\ln\Lambda\big(v_{os}(t)\big)\Big|_{b_{min}<b_{max}}\sin\theta\;d\theta\right]dv_e \quad (5)$$

where $f_e(v_e) = \left(\frac{1}{2\pi\,v_{th}^2}\right)^{3/2}\exp\left(-2\,v_e^2/v_{th}^2\right)$

Assuming for simplicity a harmonic electron motion in the Laser field: $v_{os}(t) = \hat{v}_{os}\cos(\omega t)$, what is not quite true in collisional regime, we obtain the one cycle time-averaged *Coulomb* logarithms $\overline{<\ln\Lambda>}$ and $\overline{<\ln\Lambda_r>}$. The exact *Coulomb* logarithm is presented in Fig. 1, for $n_i = 10^{28}\,m^{-3}$, $Z = 1$ and different k_BT_e values.

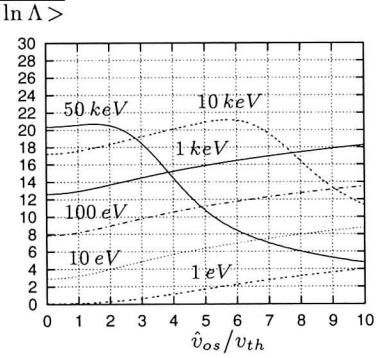

Figure 1: $\overline{<\ln\Lambda>}$ vs $\hat{v}_{os}/v_{th}$

It appears that the value of the *Coulomb* logarithm is much higher than commonly supposed for $T_e \gg 10\,eV$, since for $T_e = 100\,eV$ it reachs easily 8 for $\hat{v}_{os}$ around v_{th}. For comparison, we present in Fig. 2, $\overline{<\ln\Lambda>}$ and $\overline{<\ln\Lambda_r>}$ for $n_i = 10^{28}\,m^{-3}$, $Z = 1$ and $k_BT_e = 100\,eV,\ 50\,keV$.

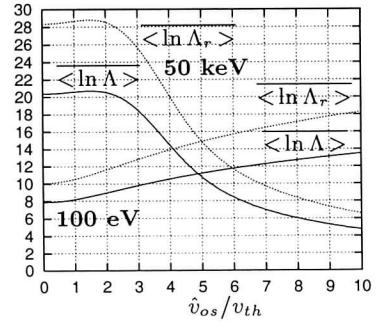

Figure 2: $\overline{<\ln\Lambda>}$ & $\overline{<\ln\Lambda_r>}$ vs $\hat{v}_{os}/v_{th}$

In this case, for $\hat{v}_{os}/v_{th} > 1$, the exact calculation is by 25% at **least** *less* than the common approximation of Eq. (2) due to the contribution of the suprathermal electrons for which $b_{min}/b_\perp > 1$ ($b_{min}/b_\perp = 1$ for $v \approx 2.10^6\,m.s^{-1}$ which correspond to the thermal velocity for a Maxwellian distribution with $T_e \approx 25eV$ only).

This work was supported by the European Commission through the TMR Network SILASI (Super Intense Laser Pulse – Solid Interaction), No. ERBFMRX-CT96-0043.

[1] C.D. Decker, W.B. Mori, J.M. Dawson, and T. Katsouleas, "Nonlinear collisional absorption in laser-driven plasmas", Phys. Plasmas **1**, 4043 (1994).

Time-dependent Collision Frequency in Strong Laser Fields and Collisional Harmonics

E. Bésuelle and P. Mulser, Theoretical Quantum Electronics (TQE), Darmstadt University of Technology, Hochschulstr. 4A, D-64289 Darmstadt, Germany.

F. Cornolti, Dipartimento di Fisica, Università di Pisa, Piazza Torricelli 2, I-56100 Pisa, Italy.

Introduction. A monochromatic laser field $\boldsymbol{E}(\boldsymbol{x},t) = \hat{\boldsymbol{E}}(\boldsymbol{x})e^{-i\omega t}$ impinging onto a plasma forces the free electrons to oscillate at the velocity $\boldsymbol{v}_{\rm os}(\boldsymbol{x},t) = -ie\hat{\boldsymbol{E}}(\boldsymbol{x})e^{-i\omega t}/m_e\omega$. It adds to the individual thermal speed $\boldsymbol{v}_e$ which we assume to know from the local distribution function $f(\boldsymbol{x},\boldsymbol{v}_e,t)$. The single electron collides with velocity $\boldsymbol{v}(t) = \boldsymbol{v}_{\rm os}(t) + \boldsymbol{v}_e$ with the plasma ions at a collision frequency $\nu_{\rm ei}(\boldsymbol{v})$ thereby undergoing irreversible deflections. At low-laser intensity $v_{\rm os} \ll v_e$ holds and $\nu_{\rm ei}$ is no longer time-dependent and reduces merely to a function of ion density n_i and electron temperature T_e (unless $T_i \gg T_e$). The well-known standard expressions of $\nu_{\rm ei}$ for this case were given by Spitzer and Braginskij. Intense laser beams with intensities up to $I = 10^{21}$ W.cm^{-2} are available now. Here, the electric field forces the electrons to oscillate at velocities of the order of the mean thermal speed $v_{\rm th} = \sqrt{kT_e/m_e}$ or considerably higher. So far time-averaged collision frequencies $\overline{\nu}_{\rm ei}$ have been presented on the basis of simple kinetimatic considerations and of the dielectric theory. The latter leads to complex integral expressions and, although the procedure is standard it is inadequate for $\hat{v}_{\rm os} \gg v_{\rm th}$. We have applied a kinematic analysis and have done the ensemble averages of $\mathbf{v}(t)$ correctly. We present $\nu_{\rm ei}(t)$ for arbitrary ratios $\hat{w}_{\rm os} = \hat{v}_{\rm os}/\sqrt{2}\,v_{\rm th}$ and show that production of intense harmonics via collisions is possible. Then we determine $\overline{\nu}_{\rm ei}$ in order to compare with the published literature.

Average time-dependent momentum loss. The momentum loss $\Delta\boldsymbol{p}$ in a Coulomb collision at velocity $\boldsymbol{v}$ is: $\Delta\boldsymbol{p} = 4\pi\, m_e\, \boldsymbol{v}\, b_\perp^2 \ln(b_{\rm max}/b_\perp)$, $\quad b_\perp = Ze^2/4\pi\varepsilon_0 m_e v^2$. This expression has to be averaged over all velocities $\boldsymbol{v}$ from $\mathbf{v}(t)$. The problem is completely analoguous to the determination of the gravitational attraction of a point mass by an isotropic distribution of mass points: $\langle \boldsymbol{v}/v^3\rangle = -\langle\partial(1/v)/\partial v_{\rm os}\rangle = -\partial\langle 1/v\rangle/\partial \boldsymbol{v}_{\rm os}$. With the distribution function $f(v_e)$ we obtain the general result

$$\nu_{\rm ei}(t) = \frac{K}{m_e|v_{\rm os}(t)|^3}\int_0^{|v_{\rm os}(t)|} 4\pi v_e^2 f(v_e)\,dv_e\ ;\ K = \frac{Z^2\,e^4\,n_i}{4\pi\,\varepsilon_0^2\,m_e}\ln\Lambda$$

In particular, in the thermal equilibrium $f(v_e)$ is a Maxwellian,

$$f_M(v_e) = \left(\frac{\beta}{\pi}\right)^{3/2} e^{-w_e^2}\ ;\ w_e = \sqrt{\beta}\,v_e\ ,\ \beta = \frac{m_e}{2kT_e}$$

and $\nu_{\rm ei}(t)$ becomes with $w_{\rm os} = \sqrt{\beta}\,v_{\rm os}(t) = v_{\rm os}(t)/\sqrt{2}\,v_{\rm th}$:

$$\nu_{\rm ei}(t) = \frac{2}{\pi^{1/2}}\frac{K}{m_e\,|v_{\rm os}(t)|^3}\left\{\int_0^{|w_{\rm os}|} e^{-w^2}dw - |w_{\rm os}|\,e^{-w_{\rm os}^2}\right\}$$

For $|w_{\rm os}| \geq 1$ this is well approximated within 4 % by

$$\nu_{\rm ei}(t) = \frac{2}{\sqrt{\pi}}\frac{K}{m_e|v_{\rm os}(t)|^3}\times$$

$$\left\{\frac{\sqrt{\pi}}{2} - e^{-w_{\rm os}^2}\left[\frac{1}{|w_{\rm os}| + \sqrt{w_{\rm os}^2 + \frac{3}{2}}} + |w_{\rm os}|\right]\right\} \qquad (1)$$

At low temperature $\nu_{\rm ei} \gg \omega$ holds and all odd harmonics in the current density $\boldsymbol{j}$ are produced due to the time-dependence of $\nu_{\rm ei}(t)$. The analysis shows that the intensity ratio $I_{3\omega}/I_\omega$ is as large as 9.5 %.

Cycle averaging of $\nu_{\rm ei}(t)$ has to be done in such a way that the true absorption per unit time is $2\overline{\nu}_{\rm ei}\overline{E}_{\rm kin}$ on the average. For a Maxwellian plasma this leads from (1) to

$$\overline{\nu}_{\rm ei} = 2\left(\frac{\beta}{\pi}\right)^{1/2}\frac{K}{\overline{E}_{\rm kin}}\overline{\frac{1}{|w_{\rm os}|}\left\{\int_0^{|w_{\rm os}|} e^{-w^2}dw - |w_{\rm os}|\,e^{-w_{\rm os}^2}\right\}}$$

Expansion in power series and averaging for purely harmonic motion, $w_{\rm os} = \hat{w}_{\rm os}\cos\omega t$, yields the result

$$\overline{\nu}_{ei} = 8\,\frac{\beta^{3/2}}{\pi^{1/2}}\frac{\overline{K}}{m_e}\bar{I}\ ,\ \bar{I} = \sum_{n\geq 1}\frac{(-1)^{n+1}\,n}{2n+1}\frac{(2n)!\,\hat{w}_{\rm os}^{2n-2}}{2^{2n}(n!)^3} \qquad (2)$$

The universal function $\bar{I}$ in presented in Fig. 1 with its best fit for $\hat{w}_{os} > 1$: $\bar{I} \approx 0.32\ln\left(\sqrt{2}\,\hat{w}_{os}\right)/\hat{w}_{os}^3$.

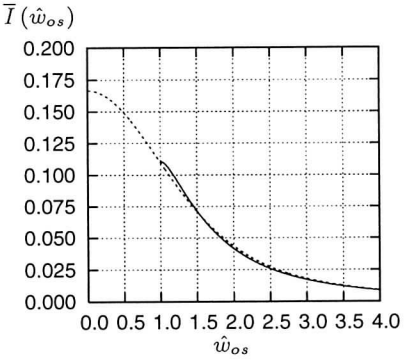

Figure 1: $\bar{I}$ vs $\hat{w}_{os}$. Solid line: fit; dashed: exact.

Expression in Eq. (2) is valid for arbitrary ratios $\hat{v}_{\rm os}/v_{\rm th}$. For vanishing $\hat{v}_{\rm os}$ the sum reduces to the constant term 1/6 ($n = 1$) and hence reproducing again Spitzer's result. In the domain $\hat{w}_{\rm os} > 1$, we obtain as a best fit to (2)

$$\overline{\nu}_{\rm ei} \approx 1.4\,\frac{Z^2\,e^4\,n_i}{4\pi\,\varepsilon_0^2\,m_e^2\,\hat{v}_{\rm os}^3}\ln\Lambda\ln\left(\frac{\hat{v}_{\rm os}}{v_{\rm th}}\right)$$

From the dielectric theory analytical formulas for $\overline{\nu}_{\rm ei}$ exist only for $\hat{v}_{\rm os}/v_{\rm th} \gg 1$. We compared with Decker *et al.* [1] and found excellent agreement in the strong field limit. If for $\hat{v}_{\rm os}/v_{\rm th} < 1$, $\overline{\nu}_{\rm ei}$ is identified with $\nu_{\rm Spitzer}$, the error does not exceed 19 %.

This work was supported by the European Commission through the TMR Network SILASI (Super Intense Laser Pulse – Solid Interaction), No. ERBFMRX-CT96-0043.

[1] C.D. Decker, W.B. Mori, J.M. Dawson, and T. Katsouleas, "Nonlinear collisional absorption in laser-driven plasmas", Phys. Plasmas **1**, 4043 (1994).

Generalized and Covariant Ohm's Law

S. Hain, P. Mulser; Theoretische Quantenelektronik (TQE), TU-Darmstadt, Hochschulstr. 4A, 64289 Darmstadt

For the study of the fast ignitor approach to inertial confinement fusion a wide density domain has to be covered ranging from the low density region inside the laser produced channel ($n_e \lesssim n_{\rm crit}$, creation of fast electrons) up to the highly overdense regime in front of the laser pulse ($n_e \sim 10^2 - 10^4\, n_{\rm crit}$, bow shock formation). Therefore, growing attention has again been payed recently to fluid and multifluid approaches [1]. While in the underdense plasma kinetic methods (PIC, Vlasov) represent the appropriate tools, in the highly overdense regime (inaccessible to PIC codes) the matter is to be expected to behave increasingly hydro-like. Here, it is desirable to reduce the hydrodynamic picture to a monofluid description with Ohm's law playing a major role. Because of the relativistic motion of electrons in superintense laser beams at intensities $I \gtrsim 10^{18}\,\mathrm{Wcm}^{-2}$, there is a need now for a covariant Ohm's law also in the physics of superintense laser-solid interaction, while in the past this was rather restricted to astrophysical plasmas [2,3].

To derive Ohm's law we start with a relativistic two fluid description. We restrict ourselves to a plasma of ions and electrons without ionization and recombination reactions, but with momentum exchange due to collisions (collision frequency ν). The continuity and energy-momentum equations for electrons and ions ($a = e, i$) then read:

$$\boldsymbol{\nabla}\cdot(m_a n_a \mathbf{u}_a) = 0, \quad \boldsymbol{\nabla}\cdot\mathbf{T}_a = q_a n_a \mathbf{F}\cdot\mathbf{u}_a + \mathbf{M}_a \qquad (1)$$

with $\mathbf{M}_e + \mathbf{M}_i = 0$ ($\mathbf{T}_a$ energy-momentum tensors, $\mathbf{u}_a$ fluid velocities, $\mathbf{F}$ electromagnetic field tensor, $\boldsymbol{\nabla}$ covariant derivative). For the tensors $\mathbf{T}_a$ we write $\mathbf{T}_a = m_a n_a \mathbf{u}_a \otimes \mathbf{u}_a + \boldsymbol{\Pi}_a$, where the $\boldsymbol{\Pi}_a$ contain all temperature, heat conduction and viscosity effects. Furthermore, we introduce the barycentric four-velocity $\mathbf{u}$ by the definition $\rho\mathbf{u} = \sum_a m_a n_a \mathbf{u}_a$ (ρ barycentric mass density) and the 'difference velocities' $\mathbf{d}_a$ by the decompositions $\mathbf{u}_a = \mathbf{d}_a + \sqrt{1+\mathbf{d}_a^2}\,\mathbf{u}$ with $\mathbf{u}\cdot\mathbf{d}_a = 0$. For a background of massive ions ($m_i \gg m_e$) one derives from the relativistic Boltzmann equation in the relaxation time approximation: $\mathbf{M}_e = -\mathbf{M}_i \simeq -\nu m_e n_e \sqrt{1+\mathbf{d}_e^2}\,\mathbf{d}_e$. Finally, we define the electric four-current density by $\mathbf{J} = \sum_a q_a n_a \mathbf{u}_a = \rho_{\rm el}\mathbf{u} + \mathbf{j}$, where $\mathbf{j}$ denotes the conductive current $\mathbf{j} = \sum_a q_a n_a \mathbf{d}_a$ which is perpendicular to the barycentric velocity $\mathbf{u}$. From the coninuity equations in (1) follows the conservation of electric charge $\boldsymbol{\nabla}\cdot\mathbf{J} = 0$.

Summing eqs. (1) over all particle species gives the law of 'mass conservation' and the energy-momentum balance of the monofluid ($\mathbf{T} = \sum_a \mathbf{T}_a$):

$$\boldsymbol{\nabla}\cdot(\rho\mathbf{u}) = 0, \quad \boldsymbol{\nabla}\cdot\mathbf{T} = \mathbf{F}\cdot\mathbf{J}.$$

Multiplying the energy-momentum equations with the specific charges q_a/m_a and taking the sum over all species yields the generalized Ohm's law. For $Zm_e/m_i \ll 1$ and also $Zm_e\sqrt{1+\mathbf{d}_e^2}/m_i \ll 1$ one obtains $\mathbf{j} \simeq -en_e\mathbf{d}_e$ and

$$\begin{aligned}
\sqrt{1+\mathbf{d}_e^2}\,(\boldsymbol{\nabla}_{\mathbf{u}}\mathbf{j} + \boldsymbol{\nabla}_{\mathbf{j}}\mathbf{u} + \mathbf{j}\,\boldsymbol{\nabla}\cdot\mathbf{u} + \nu\mathbf{j}) \quad &+ \\
+\ (\mathbf{u}\,\boldsymbol{\nabla}_{\mathbf{j}} + \mathbf{j}\,\boldsymbol{\nabla}_{\mathbf{u}})\sqrt{1+\mathbf{d}_e^2} \quad &+ \\
-en_e\sqrt{1+\mathbf{d}_e^2}\,\mathbf{u}\,\boldsymbol{\nabla}_{\mathbf{u}}\sqrt{1+\mathbf{d}_e^2} \quad &= \\
= \frac{e^2 n_e}{m_e}\sqrt{1+\mathbf{d}_e^2}\,\mathbf{F}\cdot\mathbf{u} - \frac{e}{m_e}\,\mathbf{F}\cdot\mathbf{j} \quad &+ \\
+\frac{e}{m_e}\,\boldsymbol{\nabla}\cdot(m_e n_e \mathbf{d}_e\otimes\mathbf{d}_e + \boldsymbol{\Pi}_e). \qquad (2)
\end{aligned}$$

The derivative $\boldsymbol{\nabla}_{\mathbf{u}}$ in the direction of the monofluid velocity $\mathbf{u}$ is just the derivative with respect to the proper time of the barycentric mass element $d/d\tau$. Thus, this equation represents an equation of motion for the conductive current $\mathbf{j}$. From charge conservation one obtains the equation for the time evolution of the charge density in the barycentric frame:

$$\rho\,\boldsymbol{\nabla}_{\mathbf{u}}(\rho_{\rm el}/\rho) = -\boldsymbol{\nabla}\cdot\mathbf{j}.$$

We shall get a more convenient equation, if we reformulate eq. (2) as an equation of motion for the difference velocity $\mathbf{d}_e$, that is,

$$\begin{aligned}
n_e\sqrt{1+\mathbf{d}_e^2}\,(\boldsymbol{\nabla}_{\mathbf{u}}\mathbf{d}_e + \boldsymbol{\nabla}_{\mathbf{d}_e}\mathbf{u} + \nu\mathbf{d}_e) - \mathbf{u}\,n_e\nu\mathbf{d}_e^2 \quad &= \\
= -\frac{e}{m_e}\,n_e\sqrt{1+\mathbf{d}_e^2}\,\mathbf{F}\cdot\mathbf{u} \quad &+ \\
-\mathbf{h}\cdot\left(\frac{e}{m_e}\,n_e\,\mathbf{F}\cdot\mathbf{d}_e + n_e\boldsymbol{\nabla}_{\mathbf{d}_e}\mathbf{d}_e\right) \quad &+ \\
-\frac{1}{m_e}\,\boldsymbol{\nabla}\cdot\boldsymbol{\Pi}_e + \mathbf{u}\,\frac{\boldsymbol{\nabla}\cdot\boldsymbol{\Pi}_e(\mathbf{d}_e)}{m_e\sqrt{1+\mathbf{d}_e^2}}, \qquad (3)
\end{aligned}$$

where $\mathbf{h}$ denotes the hydrodynamic projection tensor with components $h_{\mu\nu} = g_{\mu\nu} + u_\mu u_\nu$.

With the help of the tensor $\mathbf{h}$, projection of eq. (3) on the local three-space yields the equation of motion in the proper sense, i.e., in the barycentric rest frame ($\mathbf{u} = \partial_t$) it will reduce to a pure three-vector equation. Projecting eq. (3) on the local time direction (build the scalar product with $\mathbf{u}$) and obeying the normalization of the four-velocity $\mathbf{u}^2 = -1$, we obtain the first law of thermodynamics for the electron fluid:

$$\boldsymbol{\nabla}\cdot\boldsymbol{\Pi}_e(-\mathbf{u}) = m_e n_e \nu\mathbf{d}_e^2 + \frac{\boldsymbol{\nabla}\cdot\boldsymbol{\Pi}_e(\mathbf{d}_e)}{\sqrt{1+\mathbf{d}_e^2}}.$$

The first term on the right hand side represents the heating by collisional absorption while the second one describes the well-known Peltier effect. The residual terms in eq. (3) stand for the Hall and the thermoelectric effects.

[1] R.J. Mason and M. Tabak, Phys. Rev. Lett. **80**, (1998) 524

[2] F. de Hoffmann and E. Teller, Phys. Rev. **80**, (1950) 692

[3] M. Gedalin, Phys. Rev. Lett. **76**, (1996) 3340

Radiation at $\omega_p \pm \omega_0$ from short intense laser pulse interactions with thin solid targets

Z. -M. Sheng and J. Meyer-ter-Vehn
Max-Planck-Institut für Quantenoptik, 85748 Garching

Harmonics generation driven by short intense laser pulses at solid target surfaces has been shown to be a potential coherent source at XUV range [1]. The physical mechanism is the reflection of incident pulses from a oscillating surface (or a oscillating "mirror"), which is driven by the incident pulses itself. The oscillating surface is just the target surface in the case with ultrashort intense laser pulse, and it is the critical density layer in the case with long pulses when a plasma with a relatively long density scalelength is produced. More recently, with one-dimensional PIC code simulation [2, 3], strong emission at $2\omega_p$ was found from the short pulse interaction with solid targets, where $\omega_p = (4\pi n_e e^2/m)^{1/2}$ is the electron plasma frequency. Plasma waves are first driven by bunches of fast electrons penetrating through the target surface, where they are generated by the laser pulses. Then the radiation is produced due to an inverse process of two plasmon decay when the phase match condition is fulfilled.

Here, using the one-dimesional PIC code LPIC++ [3], we show the emission at $\omega_p \pm \omega_0$, where ω_0 ($\ll \omega_p$) is the incident laser frequency. The physical mechanism is coupling of the incident laser pulse with the driven plasma wave by bunches of electrons generated at the target surface. It is different from that in underdense plasmas, where emission at $\omega_0 \pm \omega_p$ (with $\omega_p \ll \omega_0$) is generated due to the parametric (Raman scattering) instabilities. As an example, in Fig. 1(a), the emission at 10 and 12 times of the fundamental frequency is clearly seen when we choose the plasma density as 121 times of the critical density. Notice that, in the normal incidence, one should only observe odd harmonics reflected from the solid surface[1] without accounting for the plasma oscillation generation in the targets. Fig. 1(b) shows the spectrum of the longitudinal current in the plasma, where the oscillation at ω_p is obvious. This kind of emission is found at high plasma densities (normally larger than $50n_c$ or at the solid density), and the radiation efficiency is high when the thickness of the solid targets is equal to $L = N\lambda_p$ where N is an integer and plasma wavelength $\lambda_p = \lambda_0/\sqrt{n_e/n_c}$, because the plasma oscillation is easy to excite in this resonant case. This radiation may serve as a useful diagnostic to the short pulse interaction with solid targets.

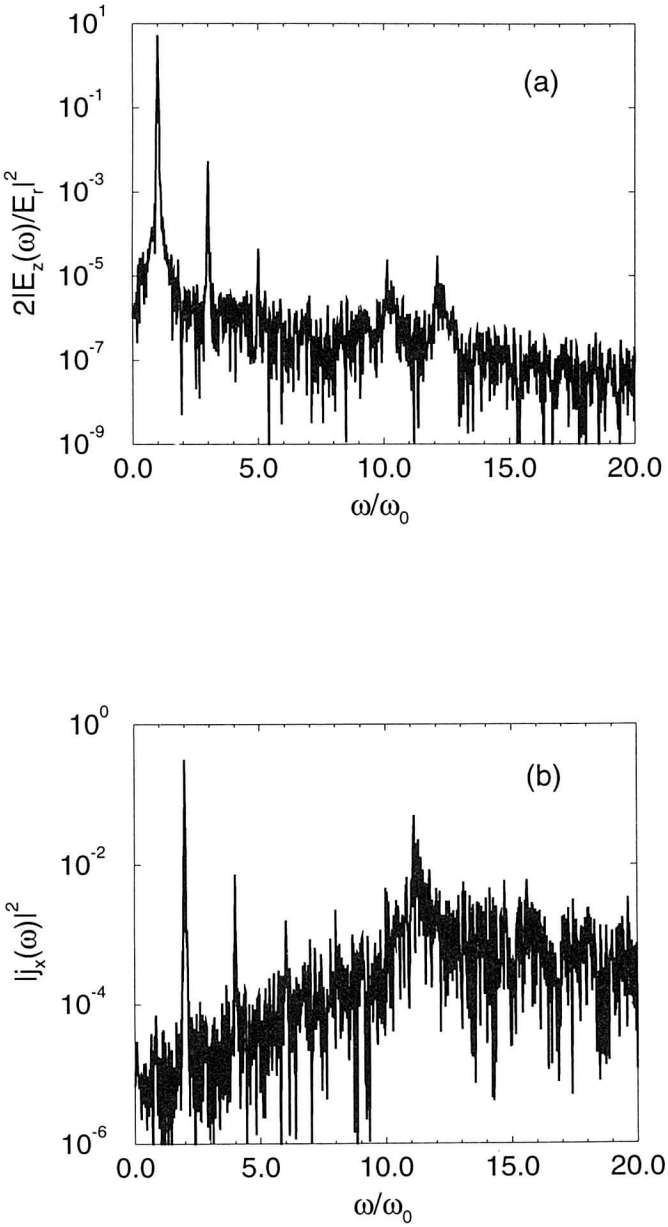

Figure 1: (a) Spectrum of light reflected from the solid target surface with parameters $a_0 = 3$, $n_e/n_c = 121$, pulse duration $\tau = 50$cycle, incident angle $\alpha = 0$ and thickness of solid target $L = 0.45\lambda_0$. (b) Spectrum of longitudinal current driven by the laser pulse with parameters as given in Fig.1. The spectrum is taken at $0.01\lambda_0$ from the plasma-vacuum interface inside the plasma.

References

[1] R. Lichters, et al., Phys. Plasmas **3**, 3425 (1996); P. Gibbon, PRL **76**, 50 (1996); S. Kohlweyer, et al., Opt. Comm. **117**, 431 (1995); D. von der Linde, et al., PRA**52**, R25 (1995); P. Norreys, et al., PRL **76**, 1832 (1996).

[2] R. Lichters and J. Meyer-ter-Vehn, in *Multiphoton Processes 1996* (IOP Publishing Ltd, Bristol 1997), p 221; R. Lichters, PhD thesis, Technishchen Universität München (1997) and MPQ Report 219 (1997).

[3] R. Lichters, et al., MPQ Report 225 (1997).

Ultra-short Light Pulse Generation by a Rapidly Field-ionized Thin Foil Target

D. Bauer[1,2], R. R. E. Salomaa[2], P. Mulser[1]
[1]TQE, TU Darmstadt, [2]Helsinki University of Technology

In recent years several mechanisms generating harmonics of electromagnetic radiation have been discovered. Among these harmonics from gases [1], harmonics from a laser pulse propagating through underdense plasma [2], and harmonics production from the plasma-vacuum boundary when a laser pulse impinges on a solid target [3] are the most prominent ones. Especially the high-order gas-harmonics, exhibiting a "plateau" instead of a rapid decrease with the harmonic order, seem to be a promising source for xuv "water-window"-radiation.

Apart from the effort to make progress towards shorter wavelengths, another goal is to achieve shorter pulse durations because the temporal resolution in pump-probe experiments clearly depends on the pulse length. One scheme proposed to generate attosecond pulses is based on phase-matching pulse trains which are produced by a laser pulse focused into a jet of rare gases [4]. Another method makes use of the fact that the efficiency of gas-harmonics generation is sensitive to the ellipticity of the incident laser light [5].

The method to generate an ultra-short *low order* harmonic laser pulse as proposed in this letter is based on the time-dependent electron density of the target material (due to ionization) in laser pulse-solid interaction. It is easy to show that the time-varying density in the wave equation produces odd harmonics [6]. The harmonic pulse duration is of the order of the density risetime and thus can be tuned appropriately by varying the intensity of the incident pulse. The mechanism is thus entirely different from those mentioned above which are based on phase-matching of nonlinear single atom-responses [4], relativistic (and thus nonlinear) electron trajectories under the influence of the surrounding plasma [2] or the oscillating vacuum-target-interface owing to the $\mathbf{v}\times\mathbf{B}$-nonlinearity in the Lorentz force. We would like to mention that in a recently published conference proceeding [7] similar studies of "ionization harmonics" were presented, but the authors did not focus on the generation of ultra-short pulses there.

A particle-in-cell code was utilized do simulate ionization harmonics-production. In Fig. 1 numerically computed spectra of the transmitted light are shown for 5 different peak field strengths $\hat{E}_0$, corresponding to intensities $I = 4.0, 4.8, 6.5\times10^{14}$ and $1.1, 1.6\times10^{15}$ W/cm^2. All other parameters were held constant: wavelength $\lambda_1 = 815$ nm, foil thickness $\ell = \lambda_1/10$, incident $\sin^2$-shaped laser pulse of duration $T = 30$ fs, and the density was the critical one with respect to the fundamental frequency, i.e., $n_0 = n_c = 1.68\times10^{21}$ cm^{-3}.

The pulse length of the harmonic radiation can be estimated by fitting the peaks in the spectrum to a Fourier transformed "test envelope" $\sim \sin^2 \pi t/T_n$. T_n is the pulse duration of the nth harmonic. For the 5 cases of Fig. 1 one finds for the pulse length of the 3rd harmonic $T_3 = 3.3, 3.0, 2.3, 2.0, 1.9$ times the fundamental period $\tau = 2\pi/\omega_1$. A lower limit for T_3 certainly is τ itself because a shorter risetime of the electron density leads to a vanishing ω_1-structure in the spectrum.

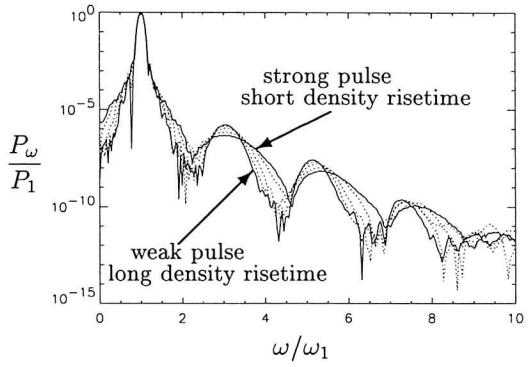

Figure 1: The spectra of the light transmitted through the thin foil target for 5 different incident pulse intensities (see text). The higher the field strength the broader are the harmonics peaks in the spectrum.

In summary, we have studied the spectrum of a perpendicularly incident laser pulse when transmitted through a rapidly ionizing foil. The pulse duration of the harmonic radiation is only a few cycles with respect to the frequency of the incident laser light. The pulse length is governed by the risetime of the electron density in the target and therefore it can be easily tuned through adjusting the peak field strength of the incident pulse. This might be a promising way towards the generation of attosecond pulses.

This work was supported by the European Commission through the TMR Network SILASI (Super Intense Laser Pulse-Solid Interaction).

References

[1] N. Sarukura et al., Phys. Rev. A **43**, 1669 (1991);
G. Farkas and C. Toth, Phys. Lett. A **168**, 447 (1992);
J. L. Krause et al., Phys. Rev. Lett. **68**, 3535 (1992);
A. L'Huillier et al., Phys. Rev. A **46**, 2778 (1992)
[2] Phillip Sprangle and Eric Esaray, *Phys. Fluids B* **4**, 2241 (1992);
J. M. Rax and N. J. Fisch, *Phys. Rev. Lett.* **69**, 772 (1992)
[3] R. L. Carman et al., Phys. Rev. Lett. **46**, 29 (1981);
R. L. Carman et al., Phys. Rev. A **24**, 2649 (1981);
Paul Gibbon, Phys. Rev. Lett. **76**, 50 (1996);
R. Lichters et al., Phys. Plasmas **3**, 3425 (1996);
H. Ruhl, R. A. Cairns, Phys. Plasmas **4**, 2246 (1997)
[4] Philippe Antoine et al., Phys. Rev. Lett. **77**, 1234 (1996);
Philippe Antoine et al., *Phys. Rev. A* **56**, 4960 (1997);
[5] P. B. Corkum et al., Opt. Lett. **19**, 1870 (1994);
M. Yu Ivanov, et al., Phys. Rev. Lett. **74**, 2933 (1995)
[6] D. Bauer et al., accepted for publication in Phys. Rev. E
[7] Enrique Conejero Jarque and Luis Plaja, in: *Superstrong Fields in Plasmas*, ed. by M. Lontano et al., (AIP Proceedings 426, New York, 1998), p. 360

Pellet Acceleration by Intense Laser Beams

S. Hain, P. Mulser; Theoretische Quantenelektronik (TQE), TU-Darmstadt, Hochschulstr. 4A, 64289 Darmstadt

The traditional concept in ICF (symmetric ignition) requires large compression ($\sim 100 - 1000 \times$ solid state density) and ignition with the same laser pulse. Furthermore, extremely high symmetry conditions are necessary. Rayleigh-Taylor and also parametric instabilities in the underdense corona (stimulated Brillouin scattering, filamentation a.o.) as well as the stagnation instability of the shell-fuel interface make this to become a nightmare. Therefore, fast ignition is a tempting alternative, because in this case compression and ignition are seperated into two working processes. Nonetheless, the question arises how variable this concept may be. Even for intensities $I \gtrsim 10^{19}\,\mathrm{Wcm}^{-2}$ it is almost impossible to thrill a channel in a precompressed target ($100 \times$ solid density) reaching the dense core within a time window of ~ 30 ps. If it were sufficient just to create a hole at the surface of the target and if it were possible to trigger a burn-off from this starting point, this would be of great advantage (release of symmetry). Therefore, the option of asymmetric external ignition of ICF-targets will become important [1].

With intense lasers the highest macroscopic accelerations can nowadays be achieved in the laboratory (e.g. $10^{17}\,g$ for $I \simeq 10^{17}\,\mathrm{Wcm}^{-2}$, Ti-Sapphire laser [2]). Can this be of practical use? May it be possible to accelerate a macroscopic piece of matter (solid) and to form with it a pellet that can be shot onto a target? After the impact such a pellet should amalgamate with the target material and deliver its macroscopic kinetic energy by conversion into ion-thermal energy. The target may then ignite asymmetrically. If we estimate the kinetic energy per baryon (ions) by using the approximate formula $v_S \simeq (2I/\rho_0 c)^{1/2}$ for the velocity of a radiation pressure-driven shock, for $I = 10^{19}\,\mathrm{Wcm}^{-2}$, $m_i = 2m_p$, $n_i = 10^{23}\,\mathrm{cm}^{-3}$, $\rho_0 = m_i n_i$ we obtain $E_{\mathrm{kin}} \simeq m_i v_S^2/2 \simeq 20$ keV. This demonstrates that, at least from the energetic point of view, ignition is not impossible, as long as the delivered energy is not spread over a too largely extended region. Fig. 1 shows the result of a hydro-simulation for a laser beam impinging on a small piece of solid with beam radius larger than the lateral extension of the pellet resulting in pellet compression and acceleration.

This example of intense laser-solid interaction is studied by using a hydrodynamic approach which is based on a monofluid model including a generalized Ohm's law. By the latter the electric current is determined which enters as a source term in Maxwell's equations. The starting point are the covariant fluid equations and the covariant generalized Ohm's law which are taken in the limit of nonrelativistic barycentric motion, whereas fully relativistic electron motion in the electric current density is considered. Detailed calculations are in progress.

[1] Stefano Atzeni, Topical Workshop on Fast Ignition of Fusion Targets, MPQ Garching, Sept. 97

[2] R. Sauerbrey, Phys. Plasmas **3**, 4712 (1996)

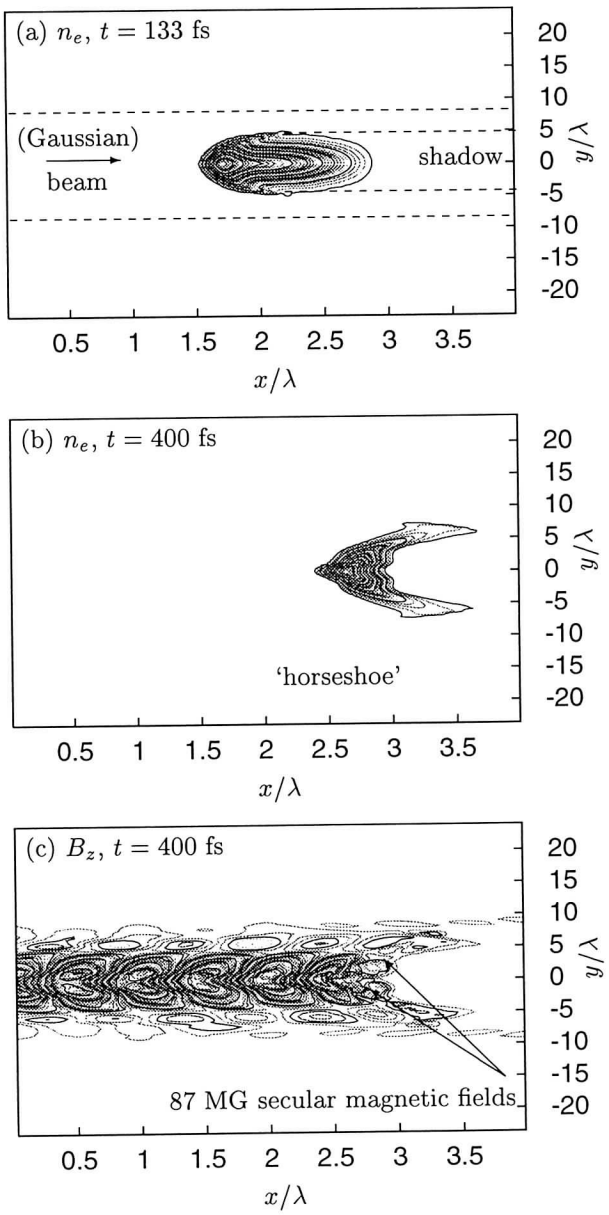

Fig. 1: Acceleration of a macroscopic piece of solid hydrogen ($n_o = 10^{23}\,\mathrm{cm}^{-3}$) by a Gaussian beam with $I = 10^{19}\,\mathrm{Wcm}^{-2}$, $\lambda = 0.8\,\mu$m; the material is compressed (compression ratio ~ 3) and partially ablated by the ablation pressure (in (a) the right half of the pellet is still unperturbed). When the shock has run through the pellet (b) it begins to move as a whole reaching a velocity of $5 \times 10^8\,\mathrm{cms}^{-1}$ after 533 fs. A strong deformation of the pellet can be observed. Nevertheless, this does not lead to a total desintegration. Fig. (c) shows the total magnetic field B_z (p-polarized case with fields B_z, E_y, E_x). In the region of the horseshoe-like deformation (b) large secular magnetic fields (87×10^6 Gauss) are generated due to an electron current starting at the outer regions of the 'horseshoe' and returning in the shadow zone near the beam axis.

Soliton Solution for Two-Dimensional Self-Focusing of Laser Beams in Plasma Including Density Caviation

Z. -M. Sheng and J. Meyer-ter-Vehn
Max-Planck-Institut für Quantenoptik, 85748 Garching

Self-focusing of laser beams in plasma is a topic of fundamental interest both for Fast Ignition of fusion targets [1] and plasma-based particle accelerators [2]. There have been a lot of studies on this phenomenum both experimentally [3] and theoretically [4]. As to the theoretical aspect, self-focusing has also been simulated with PIC codes either in two or in three-dimensional (2D/3D) version [5]. Here, we present an analytic soliton solution of self-focusing in 2D planar geometry. The most remarkable point is that it includes a full description of density cavitation.

We consider a laser beam, linearly polarized in z-direction (s-polarization) propagating in xy plane in a homogeneous plasma. The laser beam is assumed to be homogeneous in z-direction and to be finite in y-direction. In the paraxial approximation, the amplitude of the laser field satisfies

$$(\frac{\partial^2}{\partial y^2} + 2ik\frac{\partial}{\partial x})E_z + (k_0^2\epsilon - k^2)E_z = 0, \qquad (1)$$

where E_z is the transverse component of the laser field, $\epsilon = 1 - (n/\gamma)(\omega_p^2/\omega_0^2)$ with $\omega_p^2 = 4\pi N_0^2 e^2/m$, $\omega_0 (= k_0 c)$ is the laser frequency, the electron density $n = \theta[1 + \nabla^2\gamma]$ is normalized to the unperturbed density N_0, $\theta(\xi)$ is the Heaviside function, $\gamma = \sqrt{1 + |a|^2/2}$ with $a = eE_z/m\omega c$ and k is the main wave vector in plasma. For polarization in the y direction (p-polarization), an additional term $\partial/\partial y[E_y(\partial \ln \epsilon/\partial y)]$ appears in Eq.(1). Here we only concentrate on the s-polarization case. The eigen value equation representing stationary self-focusing is obtained from Eq. (1) as

$$d^2a/dy^2 + (\sigma - n/\gamma)a = 0, \qquad (2)$$

where y is normalized to k_p^{-1}, $0 < \sigma < 1$ is the eigen value associated with the laser power. Notice that Eq. (2) takes a similar form as that for circularly polarized laser beams [4], though it is derived for a linearly polarized laser beam in teneous plasma. In cylindric geometry, the second derivative is substituted with $r^{-1}d/dr(rd/dr)$, and the corresponding solution was obtained numerically [4]. But in planar geometry, Eq. (2) can be solved analytically. The first integral of Eq. (2) is

$$\frac{d\Gamma}{dy} = \pm\Gamma\left[-\sigma\Gamma^2 + 2(1-2\sigma)\Gamma + 4(1-\sigma)\right]^{1/2}, \qquad (3)$$

where $\Gamma = \gamma - 1$. The suitable soliton solution of Eq.(3) is

$$\Gamma = \frac{2\kappa^2\mathrm{sech}^2(\kappa\tilde{y})}{1 - \kappa^2\mathrm{sech}^2(\kappa\tilde{y})}, \qquad (4)$$

$$a = \frac{2\sqrt{2}\kappa\mathrm{sech}(\kappa\tilde{y})}{1 - \kappa^2\mathrm{sech}^2(\kappa\tilde{y})}, \qquad (5)$$

$$n = \frac{[1 + \kappa^2\mathrm{sech}^2(\kappa\tilde{y})]}{[1 - \kappa^2\mathrm{sech}^2(\kappa\tilde{y})]^3} \times [1 + (8\kappa^4 - 4\kappa^2)\mathrm{sech}^2(\kappa\tilde{y}) - 5\kappa^4\mathrm{sech}^4(\kappa\tilde{y})], \qquad (6)$$

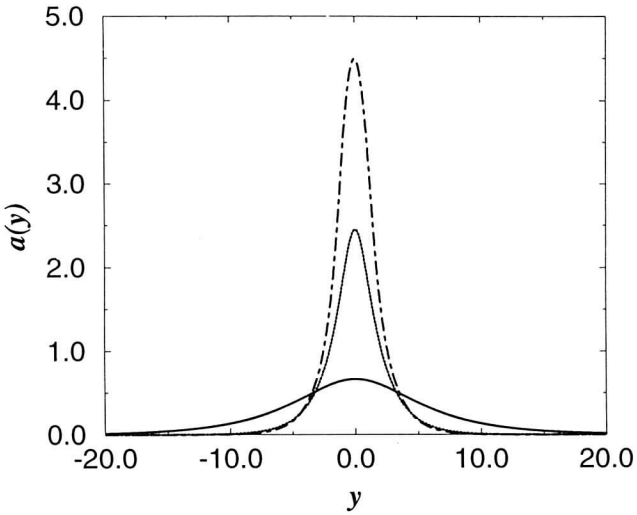

Figure 1: The transverse profiles of a self-focused laser beam in plasma for $\sigma = 0.95$ (—), 2/3 (- - -), and 0.5 (- · -).

where $\kappa^2 = 1 - \sigma$, $\mathrm{sech}(\kappa\tilde{y}) = 2/[\exp(\kappa\tilde{y}) + \exp(-\kappa\tilde{y})]$, and $\tilde{y} = |y| - y_0$ with y_0 a constant value depending on the value of σ. For $2/3 < \sigma < 1$, $y_0 = 0$, and the solution has a single peak at $y = 0$. Obviously, when $\sigma \to 1$ (or $\kappa \to 0$), Eq. (5) reduces to $a = 2\sqrt{2}\,\kappa\mathrm{sech}(\kappa y)$, which is the solution for the weak relativistic case [6]. Figure 1 shows the transverse profiles of the laser beam as given by Eq. (5) for $\sigma = 0.95$ and 2/3; while the curve for $\sigma = 1/2$ is determined by Eq.(5), as well as by Eq.(7) given below.

With the decrease of σ, the peak amplitude increases and the electron density decreases due to the ponderomotive pressure. When $\sigma \le \sigma_c = 2/3$, complete cavitation ($n = 0$) occurs in the region around $y = 0$, as shown in Fig. 2. Inside the cavitation channel ($|y| < y_c$), the valid solution to Eq. (2) is now

$$a = a_0\cos(\sqrt{\sigma}y), \qquad (7)$$

rather than Eq. (5), where the peak amplitude a_0 and the size of cavitation cahnnel y_c depends on σ. Outside the cavitation channel, Eq.(5) is still valid, but with $y_0 \neq 0$. For given σ, the constants a_0 and y_0 are found by matching Eqs.(5) and (7) with the conditions that both a and da/dy are continuous at $y = y_c$ where cavitation occurs. In general, they are not easy to obtain analytically. Here we consider two interesting cases, i.e. $\sigma \le 2/3$ and $0 < \sigma \ll 1$, where the match of Eqs.(5) and (7) at $y = y_c$ can be done explicitly. Numerical calculation shows that the solution for $n = 0$ [with n given by Eq.(6)] is near $\tilde{y} = 0$ for both cases [see Fig.(3)]. Therefore, one can use

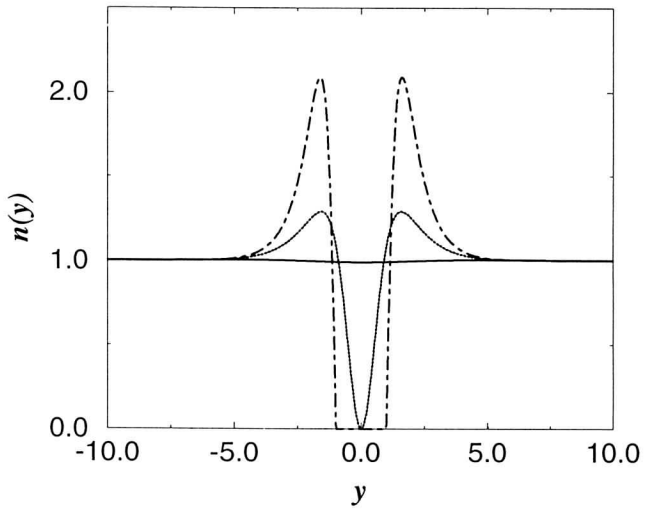

Figure 2: The transverse profiles of the electron density for $\sigma = 0.95$ (—), $2/3$ ($\cdots$), and 0.5 (- · -).

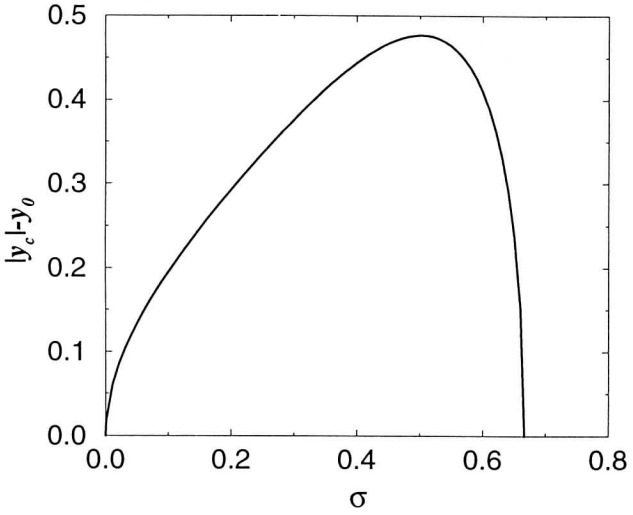

Figure 3: The root of $n(\tilde{y}) = 0$ as a function of σ. Near $\sigma = 0$ and $2/3$, the root is $\tilde{y} = 0$.

$\mathrm{sech}^2(\kappa\tilde{y}) \approx 1 - (\kappa\tilde{y})^2$. The final result is

$$\begin{aligned}
\tilde{y}^2 &= \frac{(1-\kappa^2)(3\kappa^2-1)}{2\kappa^4(\kappa^2+2)} \\
&= \begin{cases} \frac{9}{7}(1-\frac{23}{14}\tilde{\sigma})\tilde{\sigma}, & \text{for } \sigma \sim 2/3 \\ \frac{\sigma}{3}, & \text{for } \sigma \ll 1 \end{cases} \qquad (8) \\
a|_{y=y_c} &= \begin{cases} \sqrt{6}(1+\frac{4}{7}\tilde{\sigma}), & \text{for } \sigma \sim 2/3 \\ \frac{3\sqrt{2}}{2}\sigma^{-1}, & \text{for } \sigma \ll 1 \end{cases} \qquad (9) \\
\frac{da}{dy}|_{y=y_c} &= \begin{cases} -\frac{2\sqrt{6}}{\sqrt{7}}\tilde{\sigma}^{1/2}, & \text{for } \sigma \sim 2/3 \\ -\frac{3\sqrt{6}}{4}\sigma^{-3/2}, & \text{for } \sigma \ll 1 \end{cases} \qquad (10) \\
a_0 &= \begin{cases} \sqrt{6}(1+\tilde{\sigma}), & \text{for } \sigma \sim 2/3 \\ \frac{3\sqrt{6}}{4}\sigma^{-2}, & \text{for } \sigma \ll 1 \end{cases} \qquad (11) \\
y_c &= \begin{cases} \frac{3}{\sqrt{7}}(1-\frac{1}{2}\tilde{\sigma})\tilde{\sigma}^{1/2}, & \text{for } \sigma \sim 2/3 \\ (\frac{\pi}{2}-\frac{2}{\sqrt{3}}\sigma)\sigma^{-1/2}, & \text{for } \sigma \ll 1 \end{cases} \qquad (12) \\
y_0 = y_c - \tilde{y} &= \begin{cases} \frac{27}{28\sqrt{7}}\tilde{\sigma}^{3/2}, & \text{for } \sigma \sim 2/3 \\ (\frac{\pi}{2}-\sqrt{3}\sigma)\sigma^{-1/2}, & \text{for } \sigma \ll 1 \end{cases} \qquad (13)
\end{aligned}$$

where $\tilde{\sigma} = 2 - 3\sigma$. When $\sigma \to 0$, the peak amplitude increases very fast $a_0 \sim \sigma^{-2}$, while the cavitation size increases relatively slowly $y_c \sim \sigma^{-1/2}$. At $y = y_c$,

$$\sigma a = 3\sqrt{2}/2, \quad y_c\sigma^{1/2} = \pi/2. \qquad (14)$$

Alternatively, at $y = y_c$, since $n = 1 + d^2(1 + a^2/2)^{1/2}/dy^2 \approx 1+(1/\sqrt{2})d^2a/dy^2 = 0$ and $d^2a/dy^2+\sigma a = 0$, we have $\sigma a \approx \sqrt{2}$ as in Eq.(14) The relation (14) holds even for cylindrical geometry, except for the modified constants.

One can obtain the power per length analytically. In the case without complete cavitation,

$$P = \int_{-\infty}^{+\infty} a^2 dy = \frac{8\kappa}{(1-\kappa^2)^{3/2}}[\kappa(1-\kappa^2)^{1/2} + \arcsin(\kappa)] \qquad (15)$$

When $\kappa \to 0$, $P = 16\kappa$. For given P (which is a constant in 2D planar geometry), the self-focused beam size is $w = \kappa^{-1} = P/16$. To compare with the threshold power in 3D geometry, assuming the beam size in z-direction is L, one obtains

$$P_{th} = 16\kappa L \sim \left(\frac{\omega_p}{c}\kappa L\right)\frac{2}{\pi}P_0\left(\frac{\omega}{\omega_p}\right)^2, \qquad (16)$$

where $P_0 = mc^2/(e^2/mc^3) = 8.7\mathrm{GW}$. If one takes $\omega_p\kappa L/c = 2$, the resulting threshold is compariable to the obtained by numerical calculation in cylindrical geometry. For the case when cavitation occurs, in general, the power has to be calculated numerically. Specially when $\sigma \to 0$, we find

$$\begin{aligned}
P &= P(|y| < y_c) + P(|y| > y_c) \\
&= \frac{27\pi}{16}\sigma^{-9/2} + (\frac{8\pi}{3} - 2\sqrt{3})\sigma^{-3/2}. \qquad (17)
\end{aligned}$$

It shows that most of the beam energy is confined in the cavitation channel. It would be interesting to compare the 2D PIC simulation results with the above analytic solution. Finally, let us mention that Eq.(5) was obtained earlier by Turki-Suonio, et al. [7]; this we found out after completion of this work.

References

[1] M. Tabak, et al., Phys. Plasmas **1**, 1626 (1994).

[2] E. Esarey et al., IEEE Trans. Plasma Sci. **PS-24**, 252 (1996).

[3] R. Wagner, et al., Phy. Rev. Lett. **78**, 3125 (1997); G. Malk, et al., Phys. Rev. Lett. **79**, 2053 (1997).

[4] G.-Z. Sun, Phys. Fluids **30**, 526 (1987).

[5] A. Pukhov and J. Meyer-ter-Vehn, Phys. Rev. Lett. **76**, 3975 (1996); ibid **79**, 2686 (1997); J. C. Adam, et al., Phys. Rev. Lett. **78**, 4765 (1997); W. Mori, et al., Phy. Rev. Lett. **60**, 1298 (1988). D. W. Forslund, et al., ibid **54**, 558 (1985).

[6] G. Schmidt, et al., Comments Plasma Phys. Contr. Fusion **9**, 85 (1985).

[7] T. Kurki-Suonio, et al., Phys. Rev. A **40**, 3230 (1989).

Modelling MPQ-Hugoniot Results for Copper and Gold with MPQeos

A.J. Kemp and J. Meyer-ter-Vehn
Max-Planck-Institut für Quantenoptik, 85748 Garching, Germany

With MPQeos a new equation of state (EOS) code for hot dense matter, based on the QEOS description [1], is now freely available[1]. In the following, the underlying model is characterized briefly. MPQeos results for gold and copper Hugoniots are presented and compared to experimental data recently measured at MPQ [2, 3].

Underlying model

In the QEOS model [1], thermodynamic functions like pressure, energy, and entropy are computed from the Helmholtz free energy function, which is calculated as the sum of three components

$$F_{tot}(\rho, T_e, T_i) = F_i(\rho, T_i) + F_e(\rho, T_e) + F_b(\rho).$$

Ion thermal motion (F_i), electron properties (F_e) computed from the Thomas-Fermi (TF) model and a semiempirical bonding correction (F_b) contribute independently. One also obtains values for the ionization state $Q(\rho, T_e)$, which is computed within the TF-description of the electron gas. The semiempirical bonding correction is necessary to correct for the unrealistic TF-behaviour at solid density and low temperatures. It needs bulk modulus and solid density of the desired material as the only empirical parameters, aside from nuclear mass and charge that are used in the ionic and electronic EOS. For the results presented here it has been assumed that $T_e \equiv T_i$, but it is also possible to work with two different temperatures. This can be of interest for situations in laser-plasma interaction, where the electron and ion temperature may differ strongly.

Its semianalytical structure makes the QEOS description very attractive for applications in high-power beam and inertial fusion studies and may replace tabulated EOS like the SESAME tables [4].

Results

Despite its conceptual simplicity the QEOS model describes shock Hugoniots for various materials quite well. In Fig. 1 and Fig. 2, a comparison between experimental Hugoniot data for copper and gold and the corresponding MPQeos results is presented.

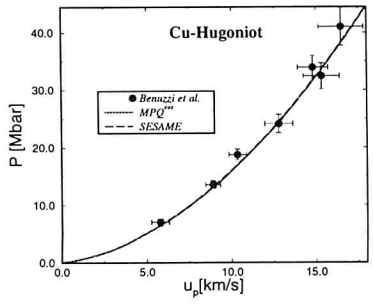

Fig. 1: *Copper Hugoniot curves. Data from Benuzzi et al. [2].*

[1]Email: Kemp@mpq.mpg.de

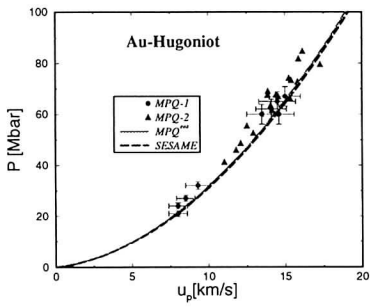

Fig. 2: *Gold Hugoniot curves. Experimental data obtained at MPQ during two European experiments [3].*

The Hugoniot data, ranging up to 40 Mbar pressures, has been determined recently from laser-driven shock experiments at MPQ [2, 3] Both results are also compared to calculations based on SESAME EOS. In Fig. 3, MPQeos results for gold isotherms at 0.1 and 100 eV are directly compared to the corresponding QEOS results [5], showing complete agreement.

A.J.K. wishes to thank Dr. Alexei Oparin for his support.

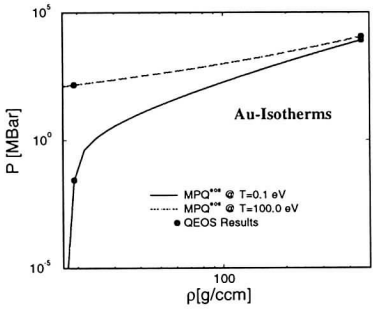

Fig. 3: *Comparison between MPQeos and QEOS results [5].*

References

[1] R.M. More, K.H. Warren, D.A. Young and G.B. Zimmerman, Phys. Fluids **31**(10), 3059 (1988).

[2] A. Benuzzi, T. Löwer, M. König, B. Faral, D. Batani, D. Beretta, C. Danson and D. Pepler, Physical Review E **54**(2), 2162 (1996).

[3] D. Batani, T. Löwer, private communication (1997). The experiments have been realised at MPQ in the framework of the E.U. "Access to Large Scale Facilities" Programe and funded through the contracts CHRX-CT93-0377 and ERB-CHCT92-0006. Results have been submitted for publication.

[4] *SESAME Report on the Los Alamos Equation of State Library, Report No. LALP-83-4* (T4 Group, Los Alamos National Laboratory, Los Alamos (1983)).

[5] D.A. Young, private communication (1997).

Hydrogen Under Extreme Conditions: Proton-proton Pair Distribution

M. Knaup, G. Zwicknagel, P.-G. Reinhard and C. Toepffer
Institut für Theoretische Physik II, Universität Erlangen-Nürnberg

We are interested in the properties of hydrogen systems at very high densities with pressures around 100 GPa, where recent experiments with multiple shock waves show a transition from nonconducting to metallic behaviour [1]. An important quantity to analyze the structure of such a hydrogen system is the radial proton-proton pair distribution function $g_{pp}(r)$. Therefore we have calculated $g_{pp}(r)$ for an atomic number density of $n = 2.02 \times 10^{29}$ m^{-3} and various temperatures. Introducing the Wigner-Seitz radius $a = (3/4\pi n)^{1/3}$ and the Bohr radius $a_B = 0.529 \times 10^{-10}$ m, the density n corresponds to $r_s := a/a_B = 2$.

As theoretical tool we employ "Wave-Packet Molecular-Dynamics" (WPMD) simulations, in which the protons are treated as classical point particles, whereas the electrons are represented by Gaussian wave packets, whose parameters follow a pseudo-Hamiltonian dynamics [2, 3, 7]. The actual WPMD simulations reported here have been done with $N = 2048$ electrons and the same number of protons in a periodically continued box. The distribution function was calculated for each particle in the simulation box. The error bars were obtained from averaging over all particles, they represent the mean error to the mean.

Fig. 1 shows the results for a temperature of $T = 2000$ K. We observe a prominent first peak at the bond length of the H_2-molecule at 1.4 a_B. The further, broader peak around 4.5 a_B is due to the next-neighbour molecules. The minimum around 2 a_B clearly indicates the molecular structure of hydrogen under this conditions. In comparison with the analytical approach provided by the "dissociation model" [4, 7], the WPMD yields a more pronounced intra-molecular correlation and a sharper inter-molecular structure.

In Fig. 2, we show the pair distribution functions for a higher temperature of $T = 5000$ K. H-Atoms from dissociated molecules contribute to the flattening of the minimum near 2 a_B in comparison to Fig. 1. The same behaviour is also observed in the dissociation model. In Fig. 2, further comparisons are made with results of "Path-Integral Monte Carlo" (PIMC) [5] and "Tight-Binding Model" (TB) [6] simulations for the same conditions. Compared with our WPMD simulation, the proton-proton pair distribution function derived from PIMC simulations is sharper peaked and the maximum of the first peak occurs at a smaller value. On the other hand, the pair distribution function derived from the TB simulation shows less structure than the WPMD result.

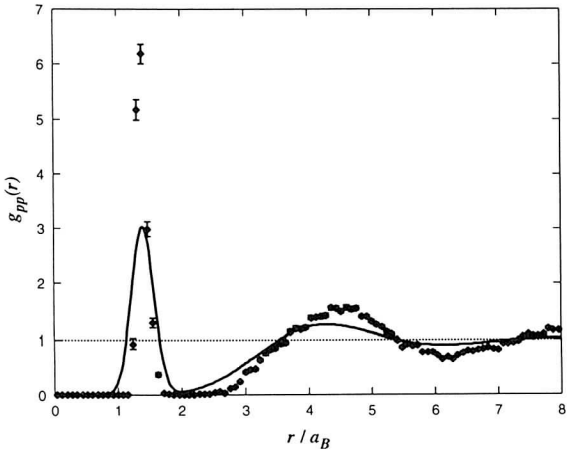

Figure 1: *Proton-proton pair distribution at $T = 2000$ K and $n = 2.02 \times 10^{29}$ m^{-3} ($r_s = 2$). The WPMD result for 2048 electrons (data points) is compared with the dissociation model [4, 7] (full curve).*

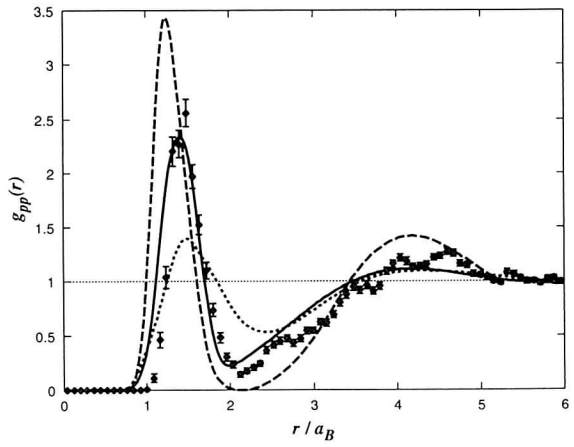

Figure 2: *Proton-proton pair distribution at $T = 5000$ K and $n = 2.02 \times 10^{29}$ m^{-3} ($r_s = 2$). The WPMD result for 2048 electrons (data points) is compared with the dissociation model [4, 7] (full curve), the PIMC simulation with 32 electrons [5] (dashed line) and the TB calculation [6] (dotted curve).*

References

[1] S. T. Weir, A. C. Mitchell, and W. J. Nellis, *Phys. Rev. Lett.* **76**, 1860 (1996)

[2] D. Klakow, C. Toepffer, and P.-G. Reinhard, *Phys. Lett. A* **192** (1994) 55-59

[3] D. Klakow, C. Toepffer, and P.-G. Reinhard, *J. Chem. Phys* **101** (1994) 10766

[4] A. Bunker, S. Nagel, R. Redmer, and G. Röpke, *Phys. Rev. B* **56**, 3094 (1997)

[5] W. R. Magro, D. M. Ceperley, C. Pierleoni, and B. Bernu, *Phys. Rev. Lett.* **76**, 1240 (1996)

[6] T. J. Lenosky, J. D. Kress, L. A. Collins, and I. Kwon, *Phys. Rev. B* **55**, R 11907 (1997)

[7] S. Nagel, R. Redmer, G. Röpke, M. Knaup, and C. Toepffer, *Proton-proton pair distribution in dense fluid hydrogen,* to be published in *Phys. Rev. E* (1998)

Pair Correlation Functions and Conductivity in Dense Fluid Hydrogen

Stefan Nagel, Ronald Redmer, Gerd Röpke
Universität Rostock, Fachbereich Physik, D-18051 Rostock

We have determined the equation of state for dense hydrogen fluid for temperatures of about $(2-3) \times 10^3$ K and Mbar pressures. Fluid hydrogen is treated as a mixture of H_2 molecules and H atoms supposing realistic pair potentials between the components [1]. The dissociation of molecules into atoms is treated via the chemical equilibrium $H_2 \rightleftharpoons H + H$. The correlation contributions to the chemical potentials of H and H_2 are taken into account in a consistent way which leads to an increasing dissociation above 0.2 Mbar [2].

We have calculated the respective pair distribution functions g_{HH}, g_{HH_2}, and $g_{H_2H_2}$ from which the proton-proton pair distribution function g_{pp} can be derived [2]. Fig. 1 shows good agreement between the present dissociation model and wave-packet molecular dynamics (WPMD) simulations [3]; results from path-integral Monte Carlo (PIMC) [4] and tight-binding molecular dynamics (TBMD) simulations [5] are also shown.

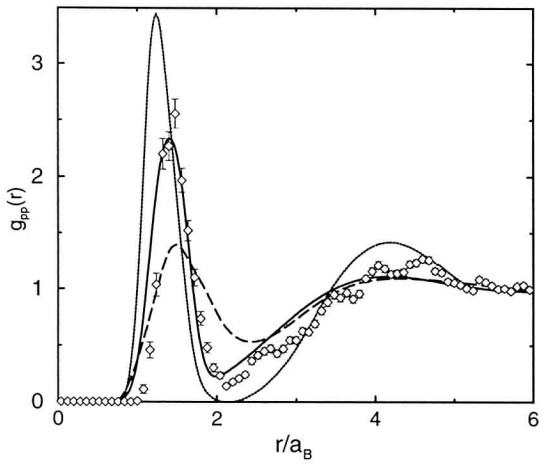

Figure 1: Proton-proton pair distribution function for 5000 K and 0.33 g/cm^3: WPMD results (data points) and dissociation model (full line) from Ref. 3, PIMC [4] (dotted line) and TBMD simulations [5] (dashed line).

The electrical conductivity was determined within linear response theory using estimates for the ionization degree derived from the ionization equilibrium $H \rightleftharpoons e + p$. The transport cross sections of (free) electrons at protons and neutral atoms were calculated on t matrix level [6]. Fig. 2 shows the respective conductivities [7] in comparison with single-shock experiments up to 0.2 Mbar [8]. The conductivity of the dense fluid shows a semiconducting behavior. The strong increase with the density results from the respective decrease of the band gap which corresponds to the reduction of the dissocaition energy in the present model. The transition from this nonmetallic to metallic conduction as experimentally observed around 1.4 Mbar [9] can be reproduced qualitatively [10].

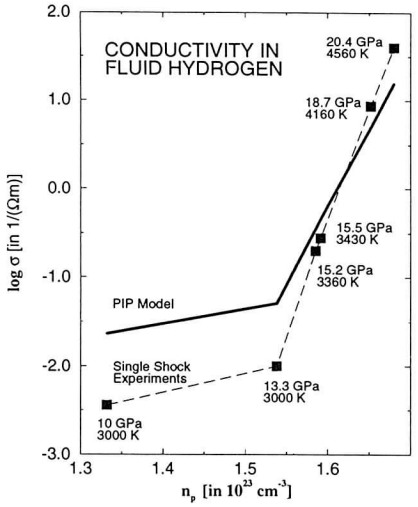

Figure 2: Conductivity in fluid hydrogen within the partially ionized plasma (PIP) model [6, 7] (solid line) compared with single-shock experiments [8] (dashed line).

References

[1] M. Ross, F.H. Ree, D.A. Young, J. Chem. Phys. **79**, 1487 (1983).
[2] A. Bunker, S. Nagel, R. Redmer, and G. Röpke, Phys. Rev. B **56**, 3094 (1997); Contrib. Plasma Phys. **37**, 115 (1997); Erratum *ibid.* **37**, 469-470 (1997).
[3] S. Nagel, R. Redmer, G. Röpke, M. Knaup, C. Toepffer, Phys. Rev. E **57** (May 1998).
[4] W.R. Magro, D.M. Ceperley, C. Pierleoni, and B. Bernu, Phys. Rev. Lett. **76**, 1240 (1996).
[5] T.J. Lenosky, J.D. Kress, L.A. Collins, and I. Kwon, Phys. Rev. B **55**, R11 907 (1997).
[6] H. Reinholz, R. Redmer, S. Nagel, Phys. Rev. E **52**, 5368 (1995).
[7] R. Redmer, Phys. Rev. E **57**, 3678 (1998).
[8] W.J. Nellis *et al.*, S.T. Weir, Phys. Rev. Lett. **68**, 2937 (1992).
[9] S.T. Weir, A.C. Mitchell, and W.J. Nellis, Phys. Rev. Lett. **76**, 1860 (1996).
[10] A. Bunker, S. Nagel, R. Redmer, and G. Röpke, in: Strongly Coupled Coulomb Systems (Plenum, New York, 1998).

Energy Relaxation in Strongly Correlated Plasmas

D.O. Gericke, M. Schlanges, S. Kosse
Institut für Physik, E.-M.-Arndt Universität, 17487 Greifswald, Germany

In the scenario of inertial confinement fusion, intensive lasers or energetic particle beams heat up the target. After such interactions the momentum distributions of the plasma particles are not Maxwellian. Especially, occupation of high energetic states occurs. Usually modells to describe relaxation towards the equilibrium are based on the first Born approximation (scattering cross section proportional to the square of the screened Coulomb potential) [1, 2]. This approximation is valid in the region of high or very low densities, $n > a_B^{-3}$ or $n < (e^2/kT)^{-3}$, only. Otherwise, strong correlation effects have to be taken into consideration. This can be done using the full T-matrix approach for the scattering rates [3].

For a first approach, it is possible to apply for the momentum distribution function the form $f(p,t) = f_0(p) + \delta f(p,t)$, where $f_0(p)$ is the equilibrium distribution. Then the time evolution of the pertubation $\delta f(p,t)$ is given by

$$\delta f(p,t) = \delta f(p,t_0)\, \mathrm{e}^{-t/\tau} \; . \qquad (1)$$

This is called the relaxation time approximation. The invers relaxation time τ^{-1} is given by the damping of the one-particle states $\Gamma(p\omega,t)$ which has to be taken on the energy shell (e.g. $\omega = p^2/2m$). For small pertubations, the damping can be calculated for equilibrium conditions. Applying the full T-matrix approach, we get in the non-degenerated case [3]

$$\Gamma(p) = \frac{4\pi}{(2\pi\hbar)^3} \frac{m_2^2 m_1}{m_{12}^3} \frac{n_2 \Lambda_2^3\, k_B T}{p} \int_0^\infty \mathrm{d}\overline{p}\; \overline{p}^2\, \sigma^{tot}(\overline{p}) \left[\mathrm{e}^{(-p/m_1 - \overline{p}/m_{12})^2 m_b/2k_BT} - \mathrm{e}^{(-p/m_1 + \overline{p}/m_{12})^2 m_2/2k_BT} \right] . \qquad (2)$$

In fig. 1 and 2, the electron–electron and the electron–proton contributions to the one-particle damping are plotted. The results following from the corresponding weak coupling theory (statically screened first Born approximation) are given for comparison. There are considerable deviations for small momenta $p = \hbar k$ between these two approximation schemes due to the strong correlation effects included in the full T–matrix approach.

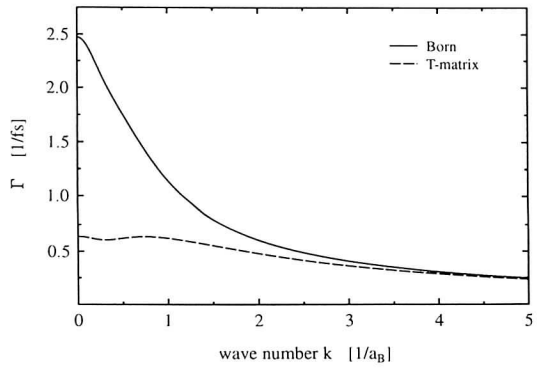

Figure 1: e–e contribution to the damping Γ for an equilibrium H–plasma with n=1·10^{21} cm^{-3} and T=19000 K

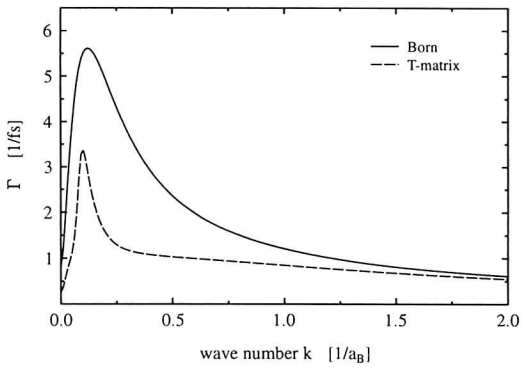

Figure 2: e–p contribution to the damping Γ for an equilibrium H–plasma with n=1·10^{21} cm^{-3} and T=19000 K

For strong pertubations, the relaxation time approximation cannot be applied, and one has to solve the kinetic equation. For these situations, we performed an analysis at the more general T–matrix level [3]. The collision integral can be reduced to a triple angle integration and one momentum integration. Results are shown in fig. 3. Here, the electron–electron contribution of the damping is plotted for a Gaussian electron distribution peaked at $p = \hbar/a_B$. The protons were considered to be in equilibrium with T=19000 K.

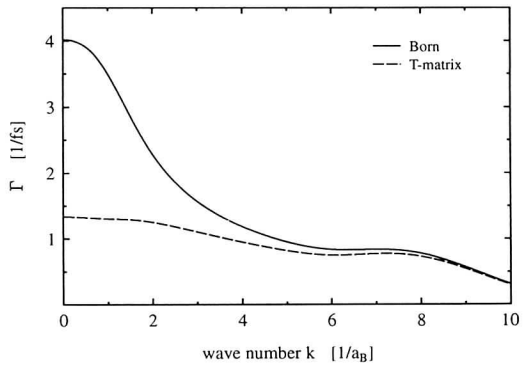

Figure 3: e–e contribution to the damping Γ for a nonequilibrium H–plasma with n=1·10^{21} cm^{-3}

References

[1] R. Binder, D. Scott, A.E. Paul, M. Lindberg, K. Henneberger, S.W. Koch, Phys. Rev. B **45** (1992)

[2] S. Kosse, M. Bonitz, M. Schlages, W.D. Kraeft, Contrib. Plasma Phys. **37** (1997)

[3] D.O. Gericke, S. Kosse, M. Schlanges, M. Bonitz, phys. stat. sol. (b) **206** (1998)

Collective Modes in Strongly Correlated Plasmas

P. Schmidt, G. Zwicknagel, P.-G. Reinhard and C. Toepffer
Institut für Theoretische Physik II, Universität Erlangen

We investigate excitations in strongly coupled one-component plasmas (OCP) with the help of molecular-dynamics (MD) computer simulations. As dynamical observables we study the velocity autocorrelation function $Z(t)$, the longitudinal $C_l(\vec{k},t)$ and the transversal current-current autocorrelation function $C_t(\vec{k},t)$ which are defined as averages of the single particle velocity $\vec{v}_1(t)$ and the current operator $\vec{j}(\vec{k},t) = \sum_j \vec{v}_j(t)\exp[i\vec{k}\cdot\vec{r}_j(t)]$, see [1]. Their spectral properties are best seen after Fourier transformation into frequency space where prominent peaks in the autocorrelation functions are related to collective modes. For instance, the longitudinal current correlation function $C_l(\vec{k},\omega)$ which is closely related to the dynamical structure factor exhibits always a peak near the plasma frequency which corresponds to the usual high-frequency plasmon mode. The transversal current correlation function $C_t(\vec{k},\omega)$, on the other hand, develops a low-frequency peak only for plasma parameters $\Gamma \gtrsim 100$ where a strongly coupled OCP supports a transversal acoustic (=shear) mode. The appearance of transversal collective shear modes indicates liquid behavior. In Fig. 1 we show the dispersion relations for the mentioned modes as deduced from the peaks in $C_{l,t}(k,\omega)$ for a

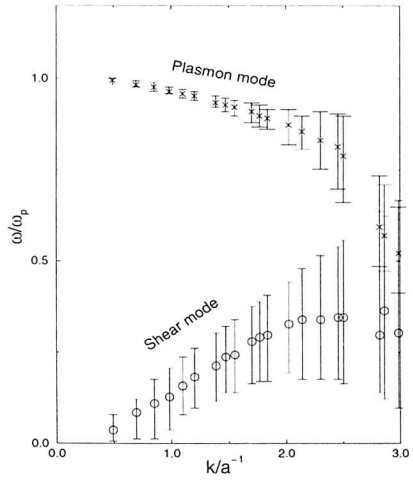

Figure 1: Dispersion relations for a OCP at $\Gamma = 158$ as obtained from MD-simulation results for $C_{l,t}(k,\omega)$.

OCP with $\Gamma = 158$. The transition from an ideal, gaseous regime for $\Gamma \ll 1$ through a liquid regime to the eventual Wigner crystallization is documented as well in the behavior of the velocity autocorrelation function (VAF). Its power spectrum, see Fig.2, shows a diffusive regime around zero frequency dominated by single particle collisions for $\Gamma \lesssim 1$ and a collective peak near the plasma frequency at larger values of Γ. For $\Gamma \gtrsim 100$ another prominent peak appears at a low, non-zero frequency which could be interpreted by a mode coupling model where the VAF is related to the current autocorrelation functions $C_{l,t}$ and the self-intermediate scattering function $S_s(k,t)$ via

$$Z(t) = \frac{m}{3k_B T}\int \frac{d^3k}{8\pi^3} S_s(k,t)\frac{C_l(k,t)+2C_t(k,t)}{nk^2}. \quad (1)$$

Relation (1) models the VAF as composed from the basic plasma modes, the longitudinal plasmon branch and the transversal acoustic branch. In Fig. 2 we compare the MD results for $Z(\omega)$ (solid curves) with the results from the mode coupling model (short dashed) where we employ the C_l, C_t, and S_s from the same MD simulations. The separate contributions of C_l and C_t to $Z(\omega)$ are shown as curves with long dashes. For large coupling $\Gamma = 137$ one can clearly distinguish the peak just below ω_p, resulting from the plasmon mode and the low frequency peak around $0.3\omega_p$. The agreement between the VAF $Z(\omega)$ and the short dashed curves from Eq.(1) clearly demonstrates that the peak in the VAF at low but finite frequency which arises for large Γ is due to the acoustic modes in the plasma. For a more extensive discussion of these questions and results see Ref.[1].

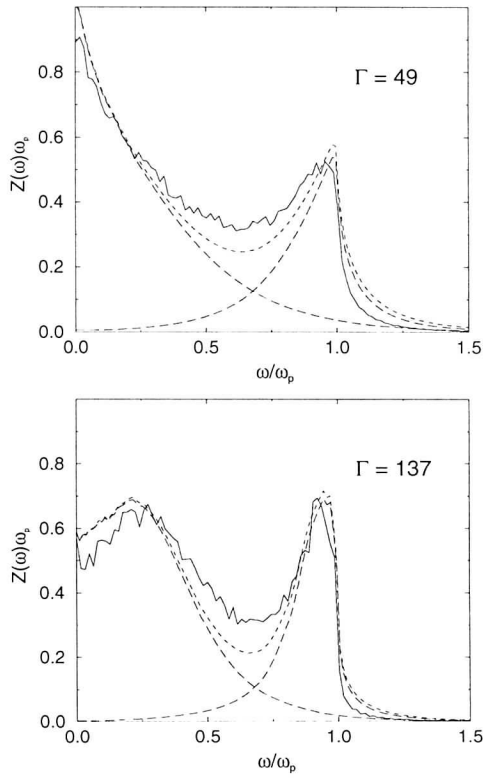

Figure 2: MD results for the VAF $Z(\omega)$ (solid curves) in comparison to the mode coupling model (1) (short dashed). The curves with the long dashes show the contributions from $C_l(k,\omega)$ and $C_t(k,\omega)$.

References

[1] P. Schmidt, G. Zwicknagel, P.-G. Reinhard and C. Toepffer, Phys.Rev.E **56** (1997) 7310.

Ionic Microfields in Strongly Correlated Plasmas

M. Lill, G. Zwicknagel, P.-G. Reinhard and C. Toepffer
Institut für Theoretische Physik II,
Universität Erlangen-Nürnberg

The broadening and shift of spectral lines emitted from atoms or ions in a plasma are of high interest in plasma diagnostics since widely used spectroscopic methods have direct access to these quantities. Due to the mutual interactions with the surrounding medium a proper description of these optical properties requires consideration of the underlying microscopic processes in the plasma. One important input data for a calculation of spectral line broadening is the precise knowledge of the distribution of the ionic microfields. To investigate the statistical properties of the microfields we use molecular dynamics (MD) computer simulations.

Figure 1 presents the results for the distributions $\boldsymbol{W}$ of the microfieldstrength $\boldsymbol{E}$ at a charged point in a one component plasma of ions with charge $\boldsymbol{Ze}$ and plasma parameters $\boldsymbol{\Gamma = \frac{Z^2e^2}{4\pi\varepsilon_0 k_B T}\left(\frac{4\pi n}{3}\right)^{1/3}}$ ranging from $\mathbf{0.01}$ to $\mathbf{100}$. For constant plasma density $\boldsymbol{n}$ we observe with decreasing temperature $\boldsymbol{T}$ (e.g. increasing $\boldsymbol{\Gamma}$) distributions whose maxima are shifted to lower electric fields. With decreasing kinetic energy very close collisions between charged particles connected with high electric fields become more rare.

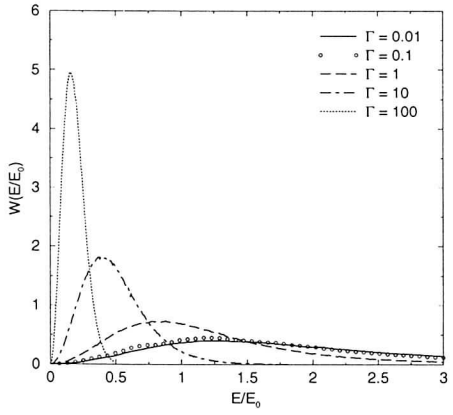

Figure 1: Distribution of the ionic microfield on a charged point for plasma coupling parameters ranging from $\boldsymbol{\Gamma = 0.01}$ to $\boldsymbol{\Gamma = 100}$. $\boldsymbol{E_0 = 2\pi\left(\frac{4}{15}\right)^{2/3}\left|\frac{Ze}{4\pi\varepsilon_0}\right| n^{2/3}}$

The obtained distributions coincide for $\boldsymbol{\Gamma \leq 0.01}$ with the model of Holtsmark [Hol19]. For large $\boldsymbol{\Gamma}$ figure 2 shows the comparison of the simulation results with the analytical models of Ecker [Eck58] and with the Single Harmonic Oscillator Model (SHO) [May47]. While the SHO shows quite good agreement with the MD results the model of Ecker overestimates the probability of high electric fields.

Figure 3 shows the results for the distributions of the microfields at a neutral point for plasma parameters from $\boldsymbol{\Gamma = 0.1}$ to $\boldsymbol{\Gamma = 100}$. It shows again a shift of the maximum of the microfield distribution with increasing $\boldsymbol{\Gamma}$

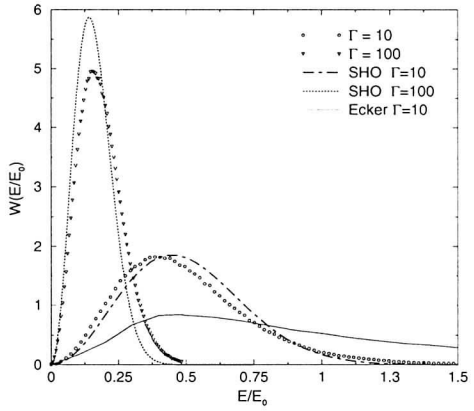

Figure 2: Distribution of the ionic microfield on a charged point. Comparison of the MD-Simulation data with the SHO-Model and the model of Ecker.

towards lower field strength. But compared with the field distribution on a charged point the shift of the distribution on a neutral point is much less pronounced. This is a consequence of the missing correlation between observation point and field producing charged particles which becomes particularly important in strongly correlated plasmas.

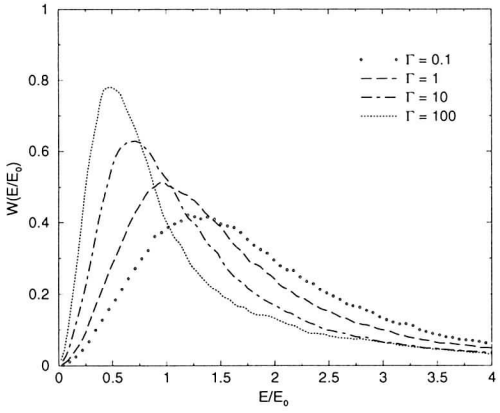

Figure 3: Distribution of the ionic microfield on a neutral point for plasma coupling parameters ranging from $\boldsymbol{\Gamma = 0.1}$ to $\boldsymbol{\Gamma = 100}$.

References

[Eck58] G. Ecker, K. G. Müller, Z. Physik **153**, 317 (1958)

[Hol19] J. Holtsmark, Ann. Physik **58**, 577 (1919)

[May47] H. Mayer, Los Alamos Scientific Labatory Report **LA-647** (1947) (unpublished)

Dielectric Properties of Hot and Dense Plasmas

Gerd Röpke, August Wierling
Universität Rostock, Fachbereich Physik, D-18051 Rostock

The dielectric function is one of the key quantities of hot and dense plasmas since it is related to the plasma conductivity, the dynamic structure factor as well as optical properties like spectral line profiles and reflectivity coefficients. In homogeneous, isotropic systems, the dielectric function is related to the electrical conductivity $\sigma(k,\omega)$ and the polarization function $\Pi(k,\omega)$ according to

$$\epsilon(k,\omega) = 1 + \frac{i}{\epsilon_0 \omega}\,\sigma(k,\omega) = 1 - \frac{1}{\epsilon_0 k^2}\,\Pi(k,\omega). \qquad (1)$$

For an ideal plasma, the Random Phase Approximation (RPA) has been a very successful approximation for the dielectric function describing collective properties such as plasmon excitation and dynamical screening. In dense plasmas, however, collisions have to be taken into account in the dielectric function. In [1] a multiple-moment approach to the dielectric function based on a generalized linear response theory has been developed allowing a systematic inclusion of collisions. It represents a unified theory of the dielectric function and the conductivity. Within this approach, the polarization function is given as a ratio of two determinants

$$\Pi(k,\omega) = i\,\frac{k^2}{\omega}\,\beta\,\Omega_0 \frac{\begin{vmatrix} 0 & M_{0n}(k,\omega) \\ M_{m0}(k,\omega) & M_{mn}(k,\omega) \end{vmatrix}}{|M_{mn}(k,\omega)|}. \qquad (2)$$

where M_{mn} are equilibrium correlation functions. These can be evaluated using standard techniques such as the thermodynamical Green's function method. Details can be found in [2]. The dielectric function has been studied for a two-component plasma at different plasma parameters. In [1], a plasma with solar core conditions (temperature $T = 98$ Ry, density $n = 8.9\,a_B^{-3}$) has been inspected, but analogous results apply for typical laser induced plasmas [5]. The polarization function (2) has been determined within a two-moment approach using the moments

$$b_1^c(p) = \frac{\hbar}{\sqrt{2m_c k_B T}} p_z \ ,$$
$$b_2^c(p) = \left(\frac{\hbar}{\sqrt{2m_c k_B T}}\right)^{3/2} \vec{p}^{\,2} p_z \ , \qquad (3)$$

and the correlation functions have been evaluated in Born approximation. Results for the imaginary part of the dielectric function as a function of frequency and wavenumber are presented in figure 1. For large wave numbers, the differences to the usual RPA are rather small, whereas significant differences occur in the long-wavelength-limit ($k \to 0$). In particular, the imaginary part is proportional to the inverse frequency in a certain frequency interval. According to (1), this is related to the dc-conductivity.

Special attention has been devoted to check exact known properties such as sum rules. Sum rules are closely related to conservation laws and can be used as an indicator for the consistency of perturbation expansions. It has been found, that the most prominent ones (f-sum rule, conductivity sum rule, perfect screening, cf. [4]) are obeyed by our approximation. In this respect, our approach is superior to an approach based on the Kubo-formula, where complicated vertex integral equations have to solved in order to ensure consistency [3].

Summarizing, a consistent approximation for the dielectric function beyond RPA taking into account collisions in Born approximation has been developed. The approach permits a systematic inclusion of nonideality effects. It can be augmented by enlarging the number of moments and evaluating the correlation functions involved beyond Born approximation. The dielectric function can be used for improved calculations of the refraction index, the reflectivity and absorption coefficients and further optical properties.

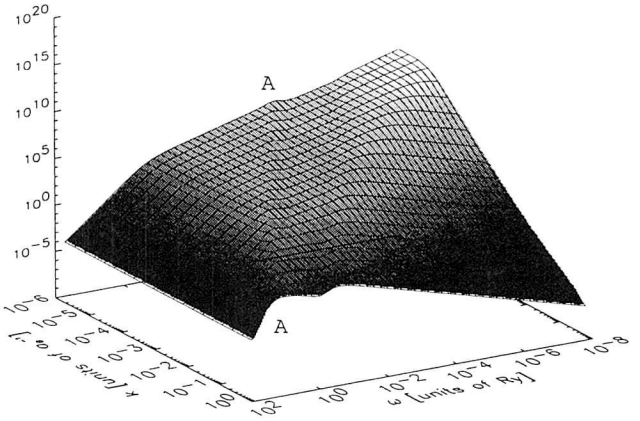

Figure 1: The imaginary part of the dielectric function for a hydrogen plasma (parameter values: temperature $T = 98$ Ry, density $n = 8.9\,a_B^{-3}$) as a function of frequency ω and wave number k. The letter A indicates the line of largest single-particle damping.

References

[1] G. Röpke and A. Wierling, Phys. Rev. E, appected for publication.
[2] G. Röpke, Phys. Rev. E **57**, 4673 (1998).
[3] G. Röpke and A. Wierling, Z. Phys. Chem. **204**, 159 (1998)
[4] G. Mahan , *Many-Particle Physics* (Plenum, New York, 1981).
[5] W. Theobald, R. Häßner, C. Wülker, and R. Sauerbrey, Phys. Rev. Lett. **77**, 298 (1996).

Dielectric Properties of Storage Ring Plasmas

Andreas Selchow, Klaus Morawetz
Universität Rostock, Fachbereich Physik, D-18051 Rostock

The storage ring plasmas (ion beam, electron beam in the cooler) are intermediate strongly coupled and non degenerated plasma with a tremendous anisotropy in temperature. One important prerequisite of obtaining dense and cold beams is strongly electron cooling [1]. Another plasma phenomena in dense beams are collective excitations (plasmons) which are detectable by the Schottky noise device [2]. Both items - the stopping power and the shape of the collective excitations - are related to the dielectric function $\epsilon(\vec{q},\omega)$.

We have investigated two dielectric function including collisions. At first we rederived the Mermin-DF [4] which is based on a relaxation ansatz of the Vlasov equation with respect to a local equilibrium distribution function

$$\left(\frac{\partial f(\vec{r},\vec{v},t)}{\partial t}\right)_{coll.} = -\frac{f(\vec{r},\vec{v},t)-\tilde{f}_0(\vec{r},\vec{v},t)}{\tau} . \quad (1)$$

This local distribution function is determined by the particle number conservation. Finally we get for a advanced relaxation DF

$$\epsilon_M\left(\vec{q},\omega+\frac{i}{\tau}\right) = 1+\frac{(1+\frac{i}{\omega\tau})\,(\epsilon(\vec{q},\omega+\frac{i}{\tau})-1)}{1+\frac{i}{\omega\tau}\frac{\epsilon(\vec{q},\omega+\frac{i}{\tau})-1}{\epsilon(\vec{q},0)-1}}) . \quad (2)$$

$\epsilon(\vec{q},\omega+\frac{i}{\tau})$ denotes here the Lindhard- or RPA DF with complex frequency, $\tau = 1/\lambda$ is the collision frequency one can obtain from classical plasma physics [3].

Following an idea of [2] we solved the Vlasov equation with Fokker-Planck collision integral. It describes the balance between dynamical friction and diffusion. Surprisingly we have found that the Mermin and the VFP DF seem to be identical. The limit of static (Debye) screening and the Drude behavior for asymptotic frequencies and consequently the lowest order sum rules are fulfilled. They have broadened plasmons shifted to lower frequencies than in RPA case. For $^{12}C^{6+}$ at densities $n \approx 10^{12}\mathrm{m}^3$ for $T \approx 10^4\mathrm{K}$ the differences to the RPA DF disappear.

Using the Mermin DF, which is numerically more easy to handle, as an input in the stopping power theory [5] we found that the Mermin stopping power becomes smaller than the Lindhard result, see Fig. 1. Since the friction is dependent on the square of density but only on temperature via the Coulomb logarithm we find a stronger dependence on the density however it does not reach the experimental, simulation and T-matrix results yet .

The second goal is to describe the plasmonic excitation which are visible in the Schottky noise. Modifying the Mermin DF (discreet wavenumbers respecting to the harmonic of excitations, shifted plasma frequency due to the influence of the beam tube) we compared in Fig. 2 the calculated Schottky noise with experimental date of a carbonium beam. It fits the date as excellent as the standard theory of Schottky noise, but is much easier to compute.

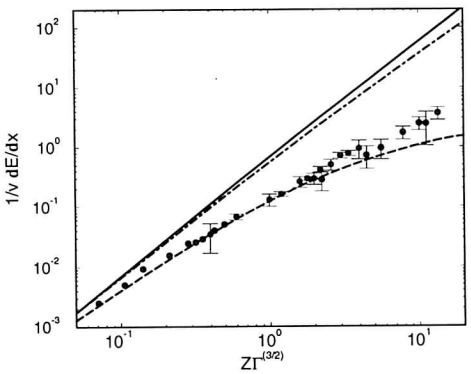

Figure 1: The normalized energy loss [Landau length L, thermal velocity v_t] $(Lv_t/T)1/v\frac{dE}{d\omega}$ for RPA(solid line), T-matrix result [5] (dashed line) and Mermin DF result (dot-dashed line). The filled circles are simulation results [6] which reproduce experimental data [7, 8].

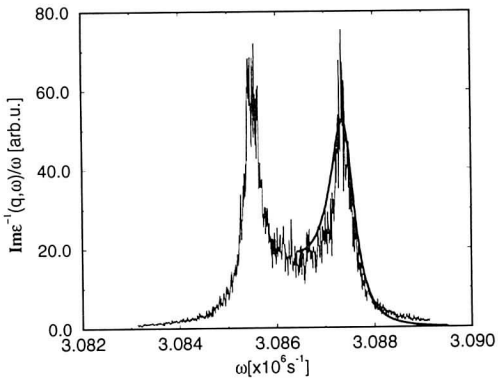

Figure 2: The Schottky spectra of a dense carbonium beam and the corresponding theoretical prediction. $(n = 8.3 \cdot 10^{13}\mathrm{m}^{-3}, T - \| = 11000\mathrm{K})$. Data from [9].

References

[1] H. Poth, Phys. Rep. **196** 135 (1990)
[2] V. Parkhomchuk, D. Pestrikov, Zh. Tech. Fis. **50** 1411 (1980) [russ.] (Sov. Phys. Tech. Phys. **25** 818 (1980))
[3] A. H. Sørensen, in: CERN Accelerator School, Hrsg. S. Turner, CERN 87-10 (1987)
[4] N. D. Mermin, Phys. Rev. **B1** 2362 (1970)
[5] K. Morawetz and G. Röpke, Phys. Rev. **E54** 1 (1996).
[6] G. Zwicknagel, C. Toepffer, P. Reinhard, Hyp. Int. **99** 285 (1996)
[7] A. Wolf *et.al.* Proc. Workshop on Beam Cooling and Related Topics, Montreaux, 1993 **CERN 94-03** Geneva, 1994, 416
[8] T. Winkler *et.al.*, Hyp. Int. **99** 277 (1996)
[9] K. Tetzlaff, diploma thesis **MPI-HV23-1997**

Formation of Correlations in Strongly Coupled Plasmas

K. Morawetz, Václav Špička and Pavel Lipavský
Fachbereich Physik, Universität Rostock, 18051 Rostock, Germany
and Institute of Physics, Academy of Sciences, Cukrovarnická 10, 16200 Praha 6, Czech Republic

Recent lasers allow to create a high density plasma within few femto seconds and observe its time evolution on a comparable scale [1]. We will discuss the formation of correlations in terms of correlation energy. To this end we can use a kinetic equation, which leads to the total energy conservation, i.e. non-Markovian kinetic equations of Levinson type [2, 3] which conserve total energy [4, 5]. During the first transient time period the screening is formed. This can be described by the non-Markovian Lenard - Balescu equation [6] instead of the static screened equation leading to the dynamical expression of the correlation energy.

We use Maxwell initial distributions at the high temperature limit, where the distributions are non-degenerated and we find

$$\begin{aligned}\frac{\partial}{\partial t}\frac{E_{\rm corr}^{\rm static}(t)}{n} &= -\frac{e^2\kappa T}{2\hbar}{\rm Im}\left[(1+2z^2){\rm e}^{z^2}{\rm erfc}(z)-\frac{2z}{\sqrt{\pi}}\right]\\ \frac{\partial}{\partial t}\frac{E_{\rm corr}^{\rm dynam}(t)}{n} &= -\frac{e^2\kappa T}{\hbar}{\rm Im}\left[{\rm e}^{z_1^2}{\rm erfc}(z_1)\right] \qquad (1)\end{aligned}$$

where we used $z=\omega_p\sqrt{t^2-it\frac{\hbar}{T}}$ and $z_1=\omega_p\sqrt{2t^2-it\frac{\hbar}{T}}$. This is the analytical quantum result of the time derivative of the formation of correlation for statically as well as dynamically screened potentials. For the classical limit we are able to integrate expression (1) with respect to times and arrive at

$$\begin{aligned}E_{\rm corr}^{\rm static}(t) &= -\frac{1}{4}e^2n\kappa\left\{1+\frac{2\omega_pt}{\sqrt{\pi}}-\left(1+2\omega_p^2t^2\right){\rm e}^{\omega_p^2t^2}{\rm erfc}(\omega_pt)\right\}\\ E_{\rm corr}^{\rm dynam}(t) &= -\frac{1}{2}e^2n\kappa\left\{1-\exp\left(\frac{\omega_p^2}{2}t^2\right){\rm erfc}(\frac{\omega_p}{\sqrt{2}}t)\right\}. \qquad (2)\end{aligned}$$

In Figs. 1, this formulae are compared with molecular dynamic simulations [7] for two values of the plasma parameter $\Gamma = 0.1$ and 1. In this region the static formula (2) well follows the major trend of the numerical result, see Fig. 1. The agreement is in fact surprising, because the static result underestimates the dynamical long time result of Debye- Hückel $\sqrt{3}/2\Gamma^{3/2}$ by a factor of two, which can be seen from the long time and classical limit $b^2=(\hbar\kappa)^2\frac{m_a+m_b}{8m_am_bT}\to 0$

$$\begin{aligned}E_{\rm corr}^{\rm dynam}(\infty) &= -\frac{e^2\kappa}{2}\frac{\sqrt{\pi}}{b}(1-{\rm e}^{b^2}{\rm erfc}(b))=-\frac{1}{2}e^2n\kappa+o(b)\\ E_{\rm corr}^{\rm static}(\infty) &= -\frac{e^2\kappa}{4}(1-\sqrt{\pi}\,{\rm erfc}(b))=-\frac{1}{4}e^2n\kappa+o(b). \qquad (3)\end{aligned}$$

The first result represents the Montroll correlation energy [8]. The explanation for this fact is that we can prepare the initial configuration within our kinetic theory such that sudden switching of interaction is fulfilled. However, in the simulation experiment we have initial correlations which are due to the set up within quasiperiodic boundary condition and Ewald summations. This obviously results into an effective statically screened Debye potential, or at least the simulation results allow for this interpretation.

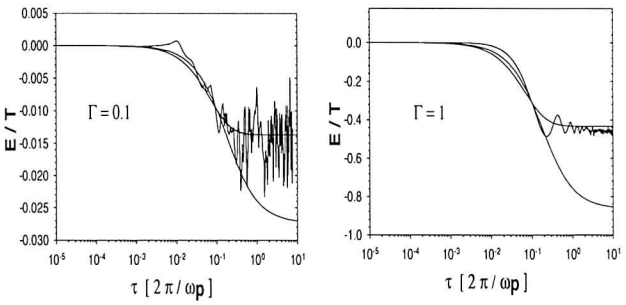

Figure 1: The formation of correlation energy due to molecular dynamic simulations [7] together with the result of (2) for a plasma parameter $\Gamma = 0.1$ (left) and $\Gamma = 1$ (right). The upper curve is the static and the lower the dynamical calculation of (2). The latter one approaches the Debye-Hückel result.

For $\Gamma = 1$, see Fig. 1, non-ideal effects become important and the formation time is underestimated within (2). This is due to non-ideality which was found to be an expression of memory effects [9] and leads to a later relaxation.

We are grateful to G. Zwicknagel who was so kind as to provide the data of simulations. Stimulating discussion with G. Röpke is acknowledged. This project was supported by the BMBF (Germany) under contract Nr. 06R0884, the Max-Planck Society, Grant Agency of Czech Republic under contracts Nos. 202960098 and 202960021, and the EC Human Capital and Mobility Programme.

References

[1] W. Theobald, R. Häßner, C. Wülker, and R. Sauerbrey, Phys. Rev. Lett. **77**, 298 (1996).

[2] H. Haug and A. P. Jauho, *Quantum Kinetics in Transport and Optics of Semiconductors* (Springer, Berlin Heidelberg, 1996).

[3] M. Bonitz and D. Kremp, Phys. Lett. A **212**, 83 (1996).

[4] K. Morawetz, Phys. Lett. A **199**, 241 (1995).

[5] M. Bonitz and et. al., J. Phys.: Condens. Matter **8**, 6057 (1996).

[6] K. Morawetz, Phys. Rev. E **50**, 4625 (1994).

[7] G. Zwicknagel, C. Toepffer, and P. G. Reinhard, in *Physics of strongly coupled plasmas*, edited by W. D. Kraeft and M. Schlanges (World Scientific, Singapore, 1995), p. 45.

[8] J. Riemann and et. al., Physica A **219**, 423 (1995).

[9] K. Morawetz, R. Walke, and G. Röpke, Phys. Lett. A **190**, 96 (1994).

APPENDICES

Meetings in 1997

In connection with the activities described in the Introduction a large number of discussion meetings and workshops have been arranged. After the first presentation of the working group results end of January 1997 at GSI, the program of the ***Hirschegg Winter School*** in February 1997 was devoted to a large part for the discussion of the HIDIF concept. In the second half of 1997 and continued until mid 1998 a number of working group meetings `Laser Facility´ were held.

An outstanding event was the biennial ***International Symposium on `Heavy Ion Inertial Fusion´*** organized by GSI in September 1997 in Heidelberg. It was held together with the *International Workshop on `Atomic Physics for Ion Driven Fusion´* organized by FZ Karlsruhe. Much of the results achieved iby summer 1997 were presented at this conference. The proceedings appeared in September 1998 in *Nuclear Instruments and Methods, Vol. A 415*. A short resumee about the conference and ist results, as it appeared in *GSI Nachrichten*, is given below.

Workshop and Symposium at Heidelberg, 22 – 27 September '97

Inertial confinement with heavy ion beams was the subject of a symposium on 'Heavy Ion Inertial Fusion', a promising option for a future energy production by thermonuclear fusion. Some 200 experts from the European Union, the U.S., Russia, Israel, Japan and China met to report on the progress made in this field. The four-day symposium was preceeded by the Workshop 'Atomic Physics for Ion Beam Fusion', which focused on the interaction of laser and particle beams with plasmas as well as on the investigation of matter under extreme conditions. These hitherto separate conferences were organised jointly for the first time by the FZ Karlsruhe and by GSI. The conference venue was the University of Heidelberg. The joint organisation of both conferences shall be maintained in future.

Major topics of the symposium were new trends in the field of target development, as well as further progress made in the study of the two driver concepts for heavy-ion beams, the high-frequency linear accelerator with storage rings, which is favoured in Europe, and the induction accelerator developed in the U.S. . In the last two years, a European study group (HIDIF: Heavy Ion Driven Inertial Fusion) consisting of accelerator experts from Germany, England, Russia and CERN, has worked out a driver concept which was presented and discussed at the conference. Supported by target experts from Italy, Spain, Germany, France and Russia, the study group also dealt with target developments adapted to this accelerator concept. A proposal to ignite the target by an intense laser pulse after compression of the Deuterium and Tritium (DT) fuel by the ion beam (Fast Ignitor) raises great interest because in this way the requirements concerning the accelerator could be reduced considerably. The study group will present an interim report by mid of this year.

Experimental work on the production of dense plasmas by ion beams is currently performed at the FZK and at GSI. At the heavy-ion synchrotron of GSI, beam dynamics studies and the investigation of the interaction of heavy-ion beams with dense plasmas play a major role. Following studies on inert gas crystals in the past years, recently a metal target could be transformed into a plasma for the first time and the hydrodynamic expansion be investigated.

In the field of theory, several simulation codes for the radiation-hydrodynamics of ion-created plasma were developed. Concerning the properties of matter under extreme conditions, recent results from the light-ion facility KALIF at the FZK were reported on the determination of the equation of state for various materials and on the investigation of Rayleigh-Taylor instabilities. The present upgrade of this facility, KALIF-HELIA, is expected to improve the experimental possibilities with light ions substantially.
Great importance was attached to the discussion of future experimental possibilities through the extension of already existing facilities at GSI and ITEP in Moscow, and particularly through the demonstration facility for the ignition of a DT-target by laser beams, the 'National Ignition Facility' (NIF), which is presently being installed in the U.S. . As a result of the current high intensity programme, GSI is going to increase the intensities for beams of the heaviest ion species by a factor of 50 to 2000. The goal of NIF, a Nd-glass-laser with a pulse energy of 2 MJ, is to demonstrate for the first time the ignition of a DT-filled fusion target by the year 2004. As NIF is funded out of the defense budget of the U.S. Department of Energy, there were debates already in advance of this project whether civil research, i. e. basic research in the field of hot dense plasmas and research on inertial confinement fusion, is granted an adequate share apart from military research. Representatives of the DOE and from Livermore have emphatically affirmed this, claiming it to be the declared policy of the U.S. . This scientific objective of NIF has become possible by the far-reaching declassification of inertial confinement fusion targets. The presentations and discussions of the conference confirmed the realisation of this policy.
At the end of the symposium, problems of energy production were discussed, especially the concepts of inertial fusion reactors recently investigated in the U.S. . Regarding the reactor design, the most important advantage compared to magnetic confinement fusion is the spatial separation of the driver from the reactor chamber. This gives much more flexibility for its construction, above all for the realisation of the liquid wall needed for cooling, neutron absorption, the breeding of Tritium. Another advantage is the much better access to the whole facility for service and maintenance. Due to these facts, the construction of a reactor with a life span necessary for an economically efficient exploitation of fusion energy appears technically possible - a problem which is still unsolved for the magnetic confinement fusion reactor.

Plasma Physics with Intense Heavy Ion Beams

(Working Group VI)

Concluding Remarks

For *energy generation by inertial confinement fusion* the heavy ion accelerator is considered the superior candidate for a reactor driver. Consequently, the focus of activities has to be in two areas, *accelerator physics and technology* and *target physics*, particularly the interaction of *heavy ion beams* with plasmas. *Theoretical predictions* are promising, however, the extrapolation from the present state of the art to the technology of energy generation requires an outstanding *experimental* effort for the verification of these predictions.

A future *accelerator facility at GSI* will play a crucial role for the progress in both areas and will define the milestones for the achievements towards ICF energy generation.

(1) For **plasma physics** the intensity requirements are based primarily on temperature and pressure achievable in an *extended sample* of matter at solid state density.

As a *first modest step* towards this aim the regime of **hydrodynamics** will be reached with the *new GSI injector* and a powerful *new rf-buncher for SIS* in a few years from now providing a specific deposition power in the order of several TW/g resulting in temperatures of up to 5 or 10 eV. Phenomena of high pressure physics at relatively low temperature, such as properties of matter, probably phase transitions, are accessible or expected in this regime.

With a *new GSI facility* the regime of **radiation physics** will be reached: Phenomena of radiation confinement and radiation transport, opacity measurements with its astrophysical relevance and in particular converter physics, one of the crucial issues of the heavy ion inertial confinement concept. This request would be satisfied with a beam intensity of 10^{13} particles per bunch and at adequate beam diameter and bunch length. One possibility would be a *synchrotron* of about 100 Tesla meter, which would achieve a specific deposition power of up to 1000 TW/g and temperatures of about 100 eV.

(2) Regarding **inertial fusion** the *next logical step* towards the driver accelerator would be a *storage ring* with an adequate high-current injector. With such a facility most accelerator-specific key issues of a driver could be investigated. Various storage ring scenarios have been proposed and are under discussion at GSI (including the European Study Group). A more detailed elaboration of concepts and costs is necessary before decisions can be made.

For the final aim of future energy generation, a facility just for *accelerator research and development* could be justified. Such a facility would also have a large potential for an ambitious plasma physics program. Experimental activities at such a facility would be an additional challenge to drive its operation to the extreme performance. It is a general experience that an accelerator facility needs a strong user community.

(3) A **laser facility** for diagnostic purposes is mandatory for the heavy ion plasma physics experiments. Moreover, a laser facility would play also an important role in plasma physics and atomic physics experiments. In particular *combined experiments* with laser and heavy ion beams should be considered and would open unique opportunities. Such a facility would not only extend and improve the general framework of experimental possibilities, it would also attract and strengthen a *user community* at an early stage, when high-power heavy ion beams are not yet available.

PARTICIPATING INSTITUTES

GSI
Gesellschaft für Schwerionenforschung
Planckstr. 1
64291 Darmstadt, Germany

Technische Universität Darmstadt
Institut für Angewandte Physik
Schloßgartenstr. 7
64289 Darmstadt, Germany

Technische Universität Darmstadt
Inst. für Theoret. Quantenelektronik
Hochschulstr. 4
64289 Darmstadt, Germany

Universität Erlangen
Physikalisches Institut, Abt. I
Erwin-Rommel-Str. 1
91058 Erlangen, Germany

Universität Erlangen
Institut für Theoretische Physik II
Staudtstr. 7
91058 Erlangen, Germany

Johann-Wolfgang-Goethe-Universität
Institut für Angewandte Physik
Robert-Mayer-Str. 2-4
60325 Frankfurt am Main, Germany

Johann-Wolfgang-Goethe-Universität
Institut für Theoretische Physik
Robert-Mayer-Str. 8-10
60325 Frankfurt am Main, Germany

Justus-Liebig-Universität Gießen
Inst. für Kernphysik (Strahlenzentrum)
Leihgesterner Weg 217
35392 Gießen, Germany

MPQ
Max-Planck-Institut für Quantenoptik
Hans-Kopfermann-Str. 1
85748 Garching, Germany

Technische Universität München
Physik-Department, E12
James-Franck-Str. 1
85748 Garching, Germany

Forschungszentrum Karlsruhe,
Institut für Neutronenphysik
und Reaktortechnik
76021 Karlsruhe, Germany

Forschungszentrum Jülich
Wilhelm-Johnen-Straße
52428 Jülich, Germany

Ernst-Moritz-Arndt-Universität
Fachbereich Physik
Domstr. 10a
17489 Greifswald, Germany

Universität Rostock
Fachbereich Physik
Universitätsplatz 3
18055 Rostock, Germany

Universität Rostock
MPG, AG 'Theoretische Vielteilchensysteme'
Universitätsplatz 3
18051 Rostock, Germany

L.P.G.P., Bat. 212
Universite Paris Sud
91405 Orsay Cedex, France

Rutherford Appleton Laboratory
Chilton, Didcot
Oxfordshire OX11 0QX, U.K.

CERN
1211 Geneva 23, Schwitzerland

DENIM, Madrid
Jose Gutierrez Abascal 2
28006 Madrid, Spain

Institute of Electrical Engineering
University of Naples
Via Claudio 21
80125 Naples, Italy

ENEA
Via E. Fermi 27
00044 Frascati RM, Italy

Institut for Chemical Physics (ICP)
142432 Chernogolovka, Russia

Institute for Theoretical and
Experimental Physics
Cheremushkinskaya Avenue 25
117259 Moscow, Russia

RFNC-VNIIEF, Sarov
37 Mir-Avenue
607200 Sarov, Russia

PUBLICATIONS

Experiments on the Interaction of Heavy Ion Beams with Dense Plasma
C. Stöckl, M.Roth, W. Süß, H. Wetzler, W. Seelig, M. Kulish, P. Spiller, J. Jacoby, D.H.H. Hoffmann
Fusion Technol. 31, 169 (1997)

Density Diagnostics of an Argon Plasma by Ion Beams and Spectroscopy
H. Wetzler, W. Süß, C. Stöckl, A.Tauschwitz, D.H.H. Hoffmann,
Laser and Particle Beams 15, 449-459 (1997)

Adiabatic Focusing and Channel Transport for Heavy Ion Fusion
A. Tauschwitz, S.S. Yu, R.O. Bangerter, J. Barnard, S. Eylon, T.J. Fessenden, S. Eylon, D.H.H. Hoffmann, J. Kwan, W. Leemans, M. de Magistris, C. Peters, L. Reginato, W.M. Sharp,
Proc. Int. Conf. On Laser Int. and Rel. Plasma Phen., Monterey, CA
AIP Conference Proceedings 406, 251 (1997)

Energy Deposition of Heavy Ions in Matter
M. Geißel, M. Roth, R. Bock, U. Funk, D.H.H. Hoffmann, U. Neuner, W. Seelig, S. Stöwe, W. Süß, A. Tauschwitz
Proc. Int. Workshop Subsecond Thermophysics, Aix-en-Provence, accepted for publication, 1997

Ion Beam Inertial Fusion
R. Bock
Atomic Physics Methods in Modern Research, Eds. K. Jungmann et al., Springer, Heidelberg, 1997, p. 211-230

Experimental Study to Accumulate, Accelerate and Focus a Massive Plasma Beam
J. Jacoby, C. Bickes, D.H.H. Hoffmann, C. Hofmann, J. Philipps
Proc. of the 10th IAEA Int. Workshop on Drivers for ICF, Osaka (1997)

Electrode Phenomena and Measurements of the Erosion Rate in High Current Pseudospark Switches
U. Pruckner, J. Christiansen, K. Frank, A. Goertler, D.H.H. Hoffmann, A. Schwandner, R. Tkotz
IEEE Trans. Plasma Sc. 25, 748 (1997)

Spatial and Time Characteristics of Current, High Voltage, Pseudospark Discharges
K. Frank, R. Stark, J. Christiansen, P. Felsner, A. Goertler, D.H.H. Hoffmann, U. Pruckner, A. Schwandner, M. Stetter, R. Tkotz, J. Urban
IEEE Trans. Plasma Sc. 25, 740 (1997)

The Role of Multi-electrode Geometry in the Generation of Pulsed Electron Beams in Preionization-Controlled Open-ended Hollow-cathode Transient Discharges
E. Dewald, M. Ganciu, B.N. Mandache, G. S. Musa, M.G. Nistor, A. M. Pointu, I.-I. Popescu, K. Frank, D.H.H. Hoffmann, R. Stark
IEEE Trans. Plasma Sc. 25, 279 (1997)

Pulsed Intense Hollow Cathode Beams Generated in Transient Hollow Discharches: Fundamentals and Applications
E. Dewald, K. Frank, D.H.H. Hoffmann, R. Stark, M. Ganciu, B.N. Mandache, I.-I. Popescu
IEEE Trans. Plasma Sc. 25, 272 (1997)

Vacuum Ultraviolet Rare Gas Light Source
J. Wieser, D. E. Murnick, A. Ulrich, H. A. Huggins, A. Liddle, W. L. Brown
Rev. Sci. Instr. 68, 1360 (1997).

Excimer Emission Spectra of Rare Gas Mixtures Using either a Supersonic Expansion or a Heavy- ion Excitation
T. Efthimiopoulos, D. Zouridis, A. Ulrich
J. Phys. D30, 1746 (1997).

Characterization and Recent Modifications of a compact 10 GHz Electron Cyclotron Resonance (ECR) Ion Source for Atomic Experiments
R. Irassl, P .Hathiramani, F .Britz, J.B .Greenwood, R.W McCullough, M. Schlapp, E. Salzborn
Physica Scripta T73, 380 (1997)

Observation of Interference in Charge Exchange Scattering in $He^{2+} + He^{+}$ Collisions
S. Krüdener, F. Melchert, K. v. Diemar, A. Pfeiffer, K. Huber, E.Salzborn, D.B. Uskov, L.P. Presnyakov
Phys. Rev. Lett. 79, 1002 (1997)

Charge Transfer in C^{3+} - He^{2+} Collisions
F. Melchert, S. Meuser. S. Krüdener, A. Pfeiffer, K. v. Diemar, E. Salzborn, E.Y. Sidky, C. D. Lin
J. Phys. B: At. Mol. Opt. Phys. 30, 697 (1997)

Equipartitioning and Halo due to Anisotropy
I. Hofmann
Proc. Particle Accelerator Conference, Vancouver, 1997, p.1852

A Symplectic Map Approach to the Space Charge Problem
G. Franchetti,I. Hofmann and G. Turchetti
Nonlinear and Stochastic Beam Dynamics: A Challenge to Theoretical and Computational Beam Physics, Lüneburg 1997, DESY Report

New Concept on the Application of Supersonic Gas Jets for Space Charge Neutralized Beam Transport in an ICF Reactor Chamber
P. Spiller, V.L. Varentsov
Laser and Particle Beams 15, 231 (1997)

The Dynamics of Space Charge Compensation
R. Becker
AIP Conf. Proceedings 391, Woodbury, New York 1997, p. 191

Designs of Recent Heavy Ion RFQ Accelerators
A. Schempp
AIP Conf. Proceedings 392, Woodbury, New York 1997. Vol 2 of 2, p. 1163

Interpretation for the Connecting Lines in the Projectional xx' Emittance in View of Liouville's Theorem
M. Sarstedt
Rev. Sci. Instrum. 68 (8), 3036 (1997)

Use of Charge Coupled-Device-Camera System for Optical Diagnostics of Intense Ion Beams
M. Sarstedt, R. Doelling, L. Wicke, H. Klein
Rev. Sci. Instrum. 68 (8), 2698 (1997)

Symmetrization in Indirectly Driven ICF Hohlraum Targets (I)
K.-H. Kang, J.A. Maruhn
Fusion Technology 31, 251 (1997)

Dynamic Effects on the Symmetrization in Indirectly Driven ICF Hohlraum Targets (II)"
K.-H. Kang, J.A. Maruhn
Fusion Technol. 31, 265 (1997)

Inertial Confinement Fusion Using Hohlraum Radiation Generated by Heavy Ion Clusters
N.A. Tahir, K.-J. Lutz, O. Geb, J.A. Maruhn, C. Deutsch
Phys. Plasmas 4, 796 (1997)

Development of Advanced Fuel Fusion Targets
N.A. Tahir, D.H.H. Hoffmann
Laser and Part. Beams 15, 575 (1997)

Inertial Fusion Driven By Intense Cluster Ions
C. Deutsch, A. Bret, S. Eliezer, J. Martenz - Val, N. A. Tahir
Fusion Technol. 31, 1 (1997) and in 'Current Trends in Inertial Fusion Research', Plenum Press, New York and London, Ed. E. Penarella 1997, p. 497 - 539.

Hohlraum Targets Driven By Cluster Ion Beams For Inertial Confinement Fusion
C. Deutsch, N. A. Tahir, O. Geb, J. A. Maruhn
Proc. of the 13th International Conf. on Laser Interaction and Realted Phenomena, AIP Conf. Proc. 406, Woodbury, New York (1997), Ed. G. H. Miley and E. M. Campbell, p. 189 - 197

ICF Related Research at MPQ
J. Meyer-ter-Vehn
13th International Conf. on Laser Interaction and Realted Phenomena, AIP Conf. Proc. 406, Woodbury, New York , 13 (1997), Ed. G. H. Miley and E. M. Campbell

Observation of VUV Radiation at Wavelengths in the ω_p - and $2\omega_p$- Wavelength Range Emitted from Femtosecond Laser Plasmas
U. Teubner, D. Altenbernd, P. Gibbon, E. Förster, A. Mysyrowicz, P. Audebert, J.-P. Geindre, J.C. Gauthier, R. Lichters, J. Meyer-ter-Vehn
Optics Communications 144, 217 (1997)

Positron and γ-photon Production and Nuclear Reactions in Cascade Processes Initiated by Sub-terawatt Femtosecond Laser
P.L. Shkolnikov, A.E. Kaplan, A. Pukhov, J. Meyer-ter-Vehn
Appl. Phys. Letters 71, 3471 (1997).

Laser Hole Boring into Overdense Plasma and Relativistic Electron Currents for Fast Ignition of ICF Targets
A. Pukhov, J. Meyer-ter-Vehn
Phys. Rev. Letters 79, 2686 (1997)

Selfsimilar Solutions of Gas Dynamics with Exponential Time Dependence
V. Simonsen, J. Meyer-ter-Vehn
Phys. Fluids 9, 1462 (1997)

Experimental Observation of Relativistic Self-channelling of an Intense Laser Pulse in a Preformed Plasma
M. Borghesi, A.J. MacKinnon, L. Barringer, R. Gaillard, L. Gizzi, C. Meyer, O. Willi, A. Pukhov, J. Meyer-ter-Vehn
Phys. Rev. Letters 78, 879 (1997)

Ion-ion Correlations in Dense Plasma Derived from a Quasimolecular Thomas-Fermi Model
H.-D. Frey, J. Meyer-ter-Vehn
Contrib. Plasma Physics 37, 77 (1997)

Calculation of the X-ray Absorption Fine Structure in Shock-compressed Matter
H.-D. Frey, J. Meyer-ter-Vehn
Contrib. Plasma Physics 37, 89 (1997)

Relativistic Wave-Breaking in Warm Plasma
Z.M. Sheng, J. Meyer-ter-Vehn
Phys. Plasmas 4, 493 (1997)

Optical Probing of Laser-induced Indirectly-driven Shock Waves in Aluminum
M. Basko, Th. Löwer, V.N. Kondrashov, A. Kendl, R. Sigel, J. Meyer-ter-Vehn
Phys. Rev. E56, 1019 (1997)

Fast Electron Transport in High Intensity Short Pulse Laser-solid Experiments
A. R. Bell, J.R. Davies, S. Guerin, H. Ruhl
Plasma Phys. Control. Fusion 39, 653 (1997)

Ejection Energy of Photoelectrons in Strong Field Ionization
D. Bauer
Phys. Rev. A 55, 2180 (1997)

A Two-dimensional, Two-electron Model Atom in a Laser Pulse: Exact Treatment, Single Active Electron-analysis
D. Bauer
Phys. Rev. A 56, 3028 (1997)

Fast Ignitor: Fluid Dynamics of Channel Formation and Laser Beam Propagation
S. Hain, P. Mulser
Laser and Particle Beams 15, 541 (1997)

Reduced Fractional Absorption and Second Harmonic Emission in Laser-produced Plasmas
H. Ruhl, R. A. Cairns
Phys. Plasmas 4, 2246 (1997)

Analytical Results of the Boltzmann Equation
C. Toepffer, C. Cercignani
Contrib. Plasma Phys. 37, 279 (1997)

Towards Ordered Beams: Longitudinal Cooling vs. Shear
M. Seurer, C. Toepffer
Hyperfine Interactions 108, 333 (1997)

Stopping of Ions and Local Electron Densities at Strong Coupling
G. Zwicknagel, Q. Spreiter, C. Toepffer
Hyperfine Interactions 108, 131 (1997)

Cooling of Particle Beams: Intrabeam Scattering, Envelope Instability and Shear
M. Seurer, C. Toepffer, V. Variale, A. Pisent, L. Tecchio, A. Burov
Nucl. Inst.and Meth. in Phys.Res. A 395, 275 (1997)

Longitudinal and Transversal Collective Modes in Strongly Correlated Plasmas
P. Schmidt, G. Zwicknagel, P.-G. Reinhard, C. Toepffer
Phys. Rev. E 56, 7310 (1997)

Dynamic Screening Effects on Rate Coefficients of Dense Plasmas
Th. Bornath, M. Schlanges, F. Morales, R. Prenzel
J. Quant. Spectr. Rad. Transfer 58, 501 (1997)

Dielectric Function of Femtosecond Laserproduced Plasmas
R. Fehr, D.O. Gericke, W.D. Kraeft, M. Schlanges, W. Theobald, R. Hässner, R. Sauerbrey
SILASI- Report 1996-1997

T-matrix Approximation of the Stopping Power
D.O. Gericke, M. Schlanges, W.D. Kraeft
Laser and Particle Beams 15, 523 (1997)

Self Energy and Two Particle States in Dense Plasma
W.D. Kraeft, R. Fehr
Contrib. Plasma Phys. 37, 173 (1997)

Numerical Solution of the Quantum Landau Equation for a Dense Plasma
S. Kosse, M. Bonitz, M. Schlanges, W.D. Kraeft
Contrib. Plasma Phys. 37, 499 (1997)

Diffusion and Heat Transport in a Dense Partially Ionized Plasma
T. Ohde, Th. Bornath, M. Bonitz, M. Schlanges
Contrib. Plasma Phys. 37, 229 (1997)

Density Expansion of the Equation of State for a Multi-Component Quantum Plasma
J. Riemann, M. Schlanges, W.D. Kraeft
Laser and Particle Beams 15, 533 (1997)

Lenard-Balescu-Type Kinetic Equation for Composite Particles in Dense Quantum Plasmas
M. Schlanges, Th. Bornath
Contrib. Plasma Phys. 37, 239 (1997)

Exact Solution of Selfconsistent Vlasov Equation
K. Morawetz
Phys. Rev. C 55, 1015 (1997) rapid comm.

Medium Modification of Two-particle Scattering in Nonideal Bose Systems
H. Stein, K. Morawetz, G. Röpke
Phys. Rev. A 55, 1945 (1997)

Quasiparticle Transport Equation with Collisional Delay:I. Phenomenological Approach
V. Spicka, P. Lipavsky, K. Morawetz
Phys. Rev. B 55, 5084 (1997)

Quasiparticle Transport Equation with Collisional Delay:II. Quantum Statistical Approach
V. Spicka, P. Lipavsky, K. Morawetz
Phys. Rev. B 55, 5095 (1997)

Debye-Onsager-Relaxation-Effect beyond Linear Response and Antiscreening in Plasma Systems
K. Morawetz
Contrib. Plasma Phys. 37 (2+3), 195-211 (1997), errata 37, 4

Stopping Power in Strongly Coupled Plasmas
K. Morawetz
Laser and Particle Beams 15, 507-521 (1997)

Debye-Onsager-Relaxation-Effect beyond Linear Response
K. Morawetz
Proceedings of the International Conference on Strongly Coupled Coulomb Systems, SCCS'97, Boston

Formation of Binary Correlations in Plasma
K. Morawetz, V. Spicka, P. Lipavsky
Proceedings of the International Conference on Strongly Coupled Coulomb Systems, SCCS'97, Boston

CONFERENCE CONTRIBUTIONS

Heidelberg, Germany: 12th International Symposium on Heavy Ion Inertial Fusion, September 24 - 27, 1997 jointly with **8th International Workshop on Atomic Physics for Ion-Driven Fusion, September 22 - 23, 1997**

Symposium Contributions (Talks and Posters):

I. Hofmann
HIDIF - An Approach to High Rep-rate Inertial Fusion

M. Stetter
High-density Plasma Physics with Heavy Ion Beams

K. Frank, C. Bickes, U. Ernst, E. Eberle
Low-pressure Pseudospark Switches for ICF Pulsed Power

M. de Magistris, A. Tauschwitz
Particle Optics for a Current Carrying Beam Focusing and Transport System

G. Rumolo, I. Hofmann
Measurement and Interpretation of Longitudinal Instabilities in the ESR
Comparison between Theory and Simulations for Longitudinal Instabilities of Coasting Beams

R. Bär, I. Hofmann, P. Moritz, U. Oeftiger
Measurement of Space-Charge Induced Frequency Shifts of Quadrupolar Beam Oscillations in the SIS

R.W. Hasse, I. Hofmann
Space-Charge Limit of Multiturn Injection in HIDIF by 2D and 3D PIC Simulation

G. Franchetti, I. Hofmann, G. Turchetti
Nonlinear Transverse Beam Dynamics and Space Charge Effects in the HIDIF Ring

U. Oeftiger, I. Hofmann, R.W. Müller, W. Pirkl
Longitudinal Particle Dynamics in a Heavy Ion Driven Ignition Facility

R.W. Müller, P. Strehl
Protection of Storage Rings and Ion-beam devices from Melting

P. Spiller
Optics of Final Beam Transport and Focusing for a Heavy Ion Driven Ignition Facility (HIDIF)

J. D`Avanzo, I. Hofmann, P. Spiller
Beam-Beam Space Charge Effects in the HIDIF Target Chamber

H. Deitinghoff, G. Parisi, K. Bongardt, M. Pabst
A Heavy Ion DTL Design for HIDIF

A. Firjahn-Andersch, J. Madlung, A.Schempp, H. Zimmermann
Progress of the Two-Beam Funneling Experiment

A. Jakob, K. Reidelbach, J. Pozimski, R. Dölling, H. Klein
Diagnostic of the Compensation Process of Ion Beams with a Time-Resolving Ion Energy Spectrometer

A. Schempp
Increasing the Effective Linac Current by Postfunneling

A. Schempp
The Injector for the HIDIF Driver Linac

M. Weber, K. Volk, P. Beller, A. Lakatos, A. Maaser, H. Klein
Development of a Bi+ Source for a Heavy Ion Driven Ignition Facility

J. Maruhn
Exploration of Possible Target Experiments with Intense Heavy Ion Beams

K.-J. Lutz, F. Illenberger, J.A. Maruhn
3D Viewfactor Simulations of frankfurt and Russian HIF-Targets

N.A. Tahir, D. H.H. Hoffmann, J.A. Maruhn
Design and Simulation of Double Shell Inertial Fusion Targets
Development of Trtium Poor and Advanced Fuel Fusion Targets

J. Meyer-ter-Vehn
On Fast Ignition of Fusion Targets

P. Mulser, S. Hain, F. Cornolti
Beam Generated Ablation Pressure

V.Vatulin et al.
Numerical and Experimental Studies of Heavy Ion Target Design with Converters on Side Wall of the Chamber.

Vakhlamova L.L., Vinokurov O.A., Ermolovich B.F., Ryabikina N.A., Shagaliev R.M.
Numerical Studies on Conversion Efficiency of High-Speed Ion Beam Energy into X-radiation.

Vatulin V.V., Vakhlamova L.L., Vinokurov O.A, Ryabikina, N.A, Shagaliev R.M.
2D Simulation of X-ray Transfer in Targets in Kinetic Approximation.

S. Skrypnik, B. Voronin, V. Vatulin, V. Yermolovich, E. Shaporenko, A. Kazarin, S. Kibkalo
Numerical Simulation of Operation of the Target with Converters on Side Surface of the Casing

E.G. Vasina, V.M. Chekshin
An Approach to View Factor Calculation for Radiation Transfer Simulation in 2D Axisymmetric Geometries

A.A. Bazin, V.V. Vatulin, Yu.A. Dementyev, V.F. Mironova, G. I. Skidan, E.N. Tikhomirova, B.P. Tikhomirov
Application of View-Factor Method in Calculations of Radiation Transport in Targets

N.V.Zidkov
Experimental Investigations for Interest of Inertial Fusion on the Laser Installation ISKRA-5

Workshop Contributions (Talks and Posters):

C. Stöckl
Interaction of Heavy-Ion Beams with Laser Plasmas

S. Stöwe
Heavy Ion Heated Lead Targets - Induced Hydrodynamic Motion and Pressure Waves

M. Roth, C. Stöckl, M. Geißel, W. Seelig
Energy Loss of Heavy Ions in Laser Produced Plasma

W. Süß, D.H.H. Hoffmann, C. Stöckl, M. Roth
Charge State Measurements of Heavy Ions Passing a Laser Produced Plasma with High Time Resolution

O. Iwase, M. Roth, C. Stöckl, M. Geißel
Plasma Diagnostics for Laser-produced Plasma

M. Geißel
Future Possibilities for Plasma Diagnostics at GSI

K. Weyrich
Heavy Ions for Simulating Fusion Neutron Induced Radiation Damage in SiC

U. Funk
High Energy Density in Solid Rare Gas Crystals and Solid Hydrogen

J. Jacoby
Swift Ion Plasma Interaction Experiments at Erlangen

E. Dewald, K. Frank, D.H.H. Hoffmann, M. Ganciu
Pulsed Intense Electron Beams Produced in Pseudospark and PCOHC for Beam-Plasma Interaction Experiments

M. Engelbrecht, H.-P- Flierl, D.H.H. Hoffmann
Development of Efficient Plasma Stripper Targets

E. Eberl, S. Jelinek, Y. Latteyer, A. Tauschwitz
XUV-amplification in an Argon Z-pinch Plasma

H.-P. Flierl, M. Engelbrecht, M.-P. Engelhardt, A. Meineke
The Energy Loss of Fully Stripped Light Ions Traversing a Hydrogen Plasma

A. Golubev, M. Basko, A. Fertman, A. Kozodaev
Dense Plasma Diagnostics by Fast Proton Beams

V. Mintsev, V. Gryaznov, M. Kulish, V. Fortov
About Measurements of Stopping Power in Expolisvely Driven Plasma Targets

M. Kulish, V. Gryaznov, A. Mezhiba, V. Mintsev
Optical Properties of Dense Xenon Plasma

F. Melchert
Beam Loss in Storage Rings Caused by Ion-ion Collisions

P.-G. Reinhard
High Energy Density in Hydrogen - Transition to a Metallic Fluid

J. D`Avanzo, I. Hofmann, M. Lontano
Nonlinear Ion Stopping in Dense Plasmas

A.J. Kemp, J. Meyer-ter-Vehn, A. Oparin
General-purpose Equation-of-State, Based on the QEOS Description

M. Knaup
Hydrogen under Extreme Conditions

G. Zwicknagel
Correlation Effects in Cluster Ion-Beam Stopping

C. Deutsch, N. Tahir, O. Geb, J.A. Maruhn
Hohlraum Targets Driven by Cluster Ions for Inertial Confinement Fusion

M.Schlanges, D.O.Gericke, W.D. Kraeft
Kinetic Theory for the Stopping Power of Dense Plasmas

K. Morawetz, V. Spicka, P. Lipavsky
Formation of Correlations in Strongly Coupled Plasma
Stopping Power in Dense Plasmas and Field Effects beyond Response
Nonlocal Corrections to the Landau Theory of Quasiparticle Transport

Portland, Oregon, USA: Int. Conf. on Lasers, December 2-6, 1996, (Proc.: Ed.: V. J. Corcoran and T. A. Goldman, STS- Press Mc. Lean, VA, USA (1997) 434-440)

M. Salvermoser, A. Ulrich
Recombination Laser Schemes Combining Heavy Ion Beam and Discharge Excitation

Osaka, Japan: IAEA Technical Committee Meeting on Drivers and Ignition Facilities for Inertial Fusion, March 10-14, 1997

Th. Löwer, V. Kondrashov, M. Basko, R. Sigel, A. Kendl, J. Meyer-ter-Vehn
Optical Probing of Laser-induced Shock Waves in Aluminum and Silicon

Vancouver, Canada: Particle Accelerator Conference, May 12-16, 1997

I. Hofmann
Equipartitioning and Halo due to Anisotropy

H. Deitinghoff, A. Parisi
Considerations on Particle Dynamics in a Heavy Ion DTL

A. Firjahn-Andersch, J. Madlung, A.Schempp, H. Zimmermann
A Two-Beam-RFQ for Ion Beam Funneling

A. Jakob, K. Reidelbach, J. Pozimski, R. Dölling, H. Klein
Diagnostic of the Compensation Process of Ion Beams with a Time-Resolving Ion Energy Spectrometer

J. Pozimski, R. Dölling, A. Jakob, P. Groa, H. Klein
Gabor Plasma Lens Focusing for LEBT Systems

V.A. Andreev, A.A. Kolomiets, V.I. Pershin, V.N. Sidorenko, R.M. Vengrov, S.G. Yaramyshev, O.V. Ershov, G. Parisi
Development of the ITEP 27 MHz Heavy Ion RFQ

Lüneburg, Germany: Nonlinear and Stochastic Beam Dynamics: A Challenge to Theoretical and Computational Beam Physics, 1997

G. Franchetti, I. Hofmann, G. Turchetti.
A Symplectic Map Approach to the Space Charge Problem

Michigan, U.S.A.: Space-Time Workshop at NSCL, May 28-31, 1997

K. Morawetz, P. Lipavsky, V. Spicka
Transport Theory with Nonlocal Corrections

Berchtesgaden, Germany: Fusion `97, June 3-9, 1997, (Proc. Fusion: Plasma Phys. 39, suppl. Contr. Fusion 12B, 39 (1997))

J. Meyer-ter-Vehn
Prospects of Inertial Confinement Fusion

Vienna, Austria: 20th International Conference on the Physics of Electronic and Atomic Collsions, July 23-29,1997

R. IraáI, F. Britz, M. Pawlowsky, M. Schlapp, J.B. Greenwood, R.W. McCullough, E. Salzborn
Upgrade and Investigation of a fully Permanent 10 GHz Electron Cyclotron Resonance Ions Source for Atomic Physics Experiments

K. Bajajova, C.Wohlfahrt, S.Krüdener, F. Melchert, K. v.Diemar, A. Pfeiffer, K. Huber, E. Salzborn
Charge Exchange in Collisions Between Singly Charged Heavy Ions

B.Uskov, L.P.Prcsnyakov, E Salzborn, H.Iawara
Double to Single Detachment Ratio of H-Ions in Collisions with Multiply Charged Ions

Boulder, Colorado USA: Workshop on Nonneutral Plasmas, July 29 - August 1, 1997

C. Toepffer
Longitudinal and Transversal Collective Excitations in Strongly Correlated Plasmas
Simulation of Crystallization in Storage Rings

Varenna, Italy: International Conference on Superstrong Fields in Plasmas, August 27 - September 2, 1997

R. R. E. Salomaa, S. J. Karttunen, P. Mulser, T. J. H. Pättikangas, W. Schneider
Generation of Superhot Electrons by Intense Field Structures

Boston, USA: International Conference on Strongly Coupled Coulomb Systems, August 3 - 10, 1997

C. Toepffer
Wave Packet Molecular Dynamics (WPMD) Simulations of Hydrogen Under Extreme Conditions

D.O. Gericke, M. Schlanges, W.D. Kraeft, Th. Bornath
Kinetic Approach to the Stopping Power

M. Schlanges, Th. Bornath
Kinetic Theory of Ionization and Recombination Rates for Dense Quantum Plasmas

D. Kremp, W.D. Kraeft, M. Schlanges
Bound States in Dense Non-Equilibrium Plasmas

R. Fehr, W.D. Kraeft
Spectral Properties in Dense Plasmas

R. Prenzel, Th. Bornath, M. Schlanges
Ionisation Kinetics in a Dense Carbon Plasma

Tomsk, Russia: Third International Conference on Atomic and Molecular Pulsed Lasers, September 22 - 26, 1997

A. Ulrich, J. Wieser, D. E. Murnick
Excimer Formation Using Low Energy Electron Beam Excitation

J. Wieser, A. Ulrich, M. Salvermoser, H. Shaw, D. E. Murnick, H. Dahi
Light Sources Using Energy Transfer from Excimer to Line Radiation

Taormina, Italy: Int. Conf. on Ion Sources '97, September 7 - 13, 1997

R. Dölling
Space Charge Compensation in Low Energy Positive Ion Beams

M. Weber, K. Volk, P. Beller, A. Lakatos, A. Maaser, H. Klein
Development of a Bi+ Source for Heavy Ion Fusion

P. Mulser, D. Bauer, S. Hain, F. Cornolti
Ultraintense Laser-Solid Interaction Phenomena

H. Ruhl, F. Cornolti, F. Califano, A. Macchi
Kinetic Approach to Superintense Laser-Solid Interaction

Long Beach, CA, USA: 13th Interdisciplinary Laser Science Conference (ILS-XIII), October 12-17, 1997

D. E. Murnick, H. Dahi, A. Ulrich, J. Wieser
Efficient Bright UV and VUV Light Sources

DIPLOMA- AND PHD-THESIS

M. Geißel
Plasmadiagnostik an einer wandstabilisierten Argon-Plasmalinse
Diploma-Thesis, TH Darmstadt, March 1997

M. Roth
Experimentelle Bestimmung des Energieverlustses schwerer Ionen in lasererzeugten Plasmen
PhD-Thesis, TU Darmstadt, December 1997

M. Engelbrecht
Messung und Simulation von Energieverlust und Ladungsverteilung schwerer Ionen nach Wechselwirkung mit Plasmen und Gasen
Diploma-Thesis, Universität Erlangen-Nürnberg, 1997

M. P. Engelhardt
Aufbau eines Flugzeitspektrometers zur Energieverlustmessung von Ionen
Diploma-Thesis, Universität Erlangen-Nürnberg, 1997

J. F. Philipps
Spektroskopische Diagnostik einer veränderlichen Wasserstoffgasentladung
Diploma-Thesis, Universität Erlangen-Nürnberg, 1997

C. Hofmann
Plasmadynamik und Impulsübertragung bei der Beschleunigung von Gasentladungsplasmen
Diploma-Thesis, Universität Erlangen-Nürnberg, 1997

M. Salvermoser
Untersuchung von Rekombinationslaserschemata bei Anregung mit hochenergetischen Schwerionenstrahlen,
PhD-Thesis, TU München, December 1997

A. Bechtold
Aufbau eines Schwerionen-RFQ-Beschleunigers mit hohem Tastverhältnis
Diploma-Thesis, Universität Frankfurt, 1997

R. Kölbel
Aufbau und Inbetriebnahme eines Bunchers für variable Teilchenenergien
Diploma-Thesis, Universität Frankfurt, 1997

J. Pozimski
Untersuchungen zum Transport raumladungskompensierter niederenergetischer und intensiver Ionenstrahlen mit einer Gabor-Plasma-Linse
PhD-Thesis, Universität Frankfurt, 1997

F. Illenberger
Adaptive Gitterrechnungen zur Strahlungshydrodynamik
Diploma-Thesis, Universität Frankfurt, October 1997

I. Zahn
Lineare und nichtlineare Abschirmung und Stoßfrequenzen bewegter Ionen im Plasma
Diploma-Thesis, TH Darmstadt, February 1997

D. Bauer
Dynamik der Feldionisation im intensiven Laserpuls
PhD-Thesis, TH Darmstadt, July 1997

M. Walter
Bremskraft auf schwere Ionen in einem anisotropen, magnetisierten Elektronenplasma
Diploma-Thesis, TU München, May 1997

T. Gherega
Numerische Simulation von räumlich eindimensionalen und zweidimensionalen Plasmen mittels finiter Differenzen
PhD-Thesis, TU München, September 1997

R. Fehr
Spektrale Eigenschaften in dichten Plasmen
PhD-Thesis, Universität Greifswald, 1997

AUTHOR INDEX